Multiresponsive and supramolecular field-effect transistors

Tim Leydecker

Tim Leydecker. Multiresponsive and supramolecular field-effect transistors. Other. Université de Strasbourg, 2015. English. NNT : 2015STRAF056 . tel-02003634

HAL Id: tel-02003634
https://theses.hal.science/tel-02003634

Submitted on 1 Feb 2019

UNIVERSITÉ DE STRASBOURG

ÉCOLE DOCTORALE DES SCIENCES CHIMIQUES
UMRS 7006 – Institut de science et d'ingénierie Supramoléculaires

THÈSE

présentée par :

Tim LEYDECKER

soutenue le : **11 Décembre 2015**

pour obtenir le grade de : **Docteur de l'université de Strasbourg**
Discipline/ Spécialité : Chimie

Multiresponsive and supramolecular field-effect transistors

THÈSE dirigée par :

M. SAMORÌ Paolo	Professeur, Université de Strasbourg, France

RAPPORTEURS :

M. LAZZARONI Roberto	Professeur, Université de Mons, Belgique
M. MARLETTA Giovanni	Professeur, Université de Catania, Italie

---

Autres membres du jury :

M. HEISER Thomas	Professeur, Université de Strasbourg, France Examinateur interne

RESUME DE LA THESE

Le sujet de cette thèse est l'optimisation performances des transistors à effet de champ organiques (OFET) et l'intégration de fonctionnalités supplémentaires dans des OFET par mélange des composants moléculaires, chacun conférant une caractéristique bien distincte.

Les semi-conducteurs organiques ont fait l'objet d'une activité de recherche approfondie au cours des dernières décennies, car ils représentent des composants clés pour les applications technologiques dans l'opto-électronique tels que l'électronique de grande échelle, les écrans et les senseurs[1-7]. Ils présentent de nombreux avantages par rapport à leurs homologues inorganiques (ajustement de leurs propriétés physiques par le biais fonctionnalisation chimique, traitement à faible coût en utilisant des conditions douces, intégration sur des supports flexibles, etc.)[8]. Toutefois, pour une mise sur le marché, la plupart des semi-conducteurs organiques déposés en solution doivent encore atteindre des mobilités à effet de champ comparables à ceux du silicium amorphe. Ces mobilités faibles résultent de la faible cristallinité des couches semi-conductrices en raison d'une taille de grain typique qui est normalement beaucoup plus faible que la longueur de canal du dispositif.[9] En outre, les propriétés des dispositifs organiques sont fortement dépendants de leur interface étant donné l'importance que les interfaces métal / semi-conducteur et diélectrique / semi-conducteur jouent dans la détermination de la mobilité du transistor à effet de champ ainsi que la tension de seuil.[10-11] Par conséquent, une ingénierie de l'interface optimale est nécessaire, car elle affectera la mobilité et la tension seuil.

Les petites molécules semi-conductrices ont démontré des performances électriques intéressantes, en partie en raison de leur tendance prononcée à former des domaines cristallins par rapport à leurs homologues polymères.[12-18] En particulier, les dispositifs d'oligothiophènes hexaméthyl-substitués, tels que le di-hexylquaterthiophene (DH4T) sont des systèmes modèles facilement accessibles qui ont fait leurs preuves pour afficher une grande résistance à l'environnement, en raison de leur assemblage dense et de chaînes hexyles agissant comme une couche de passivation en plus de leur performance de transport de charges dans les transistors. Pour des films sublimés le plus forte mobilité observée (μ) est de 0,09 cm² / Vs. En ce qui concerne les films déposés par solution, les valeurs les plus élevées de mobilité

trouvées dans la littérature sont de µ = 0,043 cm² / Vs pour les dispositifs imprimés par jet d'encre et de µ = 0,012 cm² / Vs pour les films déposés par enduction centrifuge, révélant une grande marge pour l'amélioration d'un point de vue de la fabrication des dispositifs.[19-21] La morphologie et la cristallographie de films DH4T ont été plus récemment étudiées par Thierry et al., montrant comment DH4T peut s'auto-assembler en une structure cristalline hautement ordonnée. Dans leur étude, l'ordre cristallin dans les domaines produits par sublimation sous vide était similaire à celui trouvé dans des domaines cristallins issus d'une solution. Les dispositifs par solution de haute mobilité peuvent être produits donc si le processus cinétique régi par la croissance du film est contrôlée pour obtenir de grands domaines cristallins, éliminant ou réduisant l'effet de joints de grains, qui sont préjudiciables pour le transport de charge.[22-24]

Initialement, cette molécule prototype a été testée dans trois solvants chlorés différents à savoir le chloroforme ($CHCl_3$), le 1,2-dichlorobenzène (DCB) et le chlorobenzène (CB). Le choix du solvant a été jugée crucial pour les performances du dispositif. En particulier, la caractérisation morphologique multi-échelle, de centaines d'µm jusqu'à l'échelle nanométrique, a été réalisée à la fois par microscopie optique (OM) et à force atomique (AFM). Les morphologies des films préparés par déposition de goutte de solution de 1 mg / ml de DH4T dans du chloroforme, du chlorobenzène (CB) et du dichlorobenzène (DCB) ont été comparées. La surface des films de DH4T déposés à partir de solution dans le chloroforme est constituée de petits cristaux rarement reliés entre eux, tandis que les films obtenus en utilisant le chlorobenzène ou le dichlorobenzène comme solvant affichent des domaines cristallins plus grands et plus uniformes sur les images OM. Tous les films englobés dans cette étude présentent un haut degré de cristallinité tel que confirmé par analyse par diffraction à incidence rasante des rayons X. L'uniformité de film sans présence de défauts sur une plus grande échelle pour les films de chloro- et dichlorobenzène diminue significativement la présence des joints de grains. Inversement, les films déposés à partir $CHCl_3$ présentent une très forte rugosité de surface à échelle méso, tandis que les films préparés à partir de CB ont montré une diminution de la rugosité. Les films préparés à partir de solutions DCB exposées une rugosité encore plus faible.

La procédure qui présentait la meilleure mobilité, à savoir 70 µL de DH4T à 5 mg / ml dans le DCB et une vitesse d'évaporation de 0,1, sera désigné comme la «procédure optimisée ». Elle a été reproduite avec succès sur plus de 110 dispositifs avec l'hexaméthyldisilazane (HMDS) en tant que traitement de surface. Il convient de noter, en dépit du fait que la déposition par goutte est une technique de dépôt qui est censé conduire à des performances inégales de dispositif à dispositif en raison de la variation d'épaisseur dans le plan xy, la présence de grands cristaux plats couvrant des centaines de micromètres a permis la fabrication de dispositifs dont les caratéristiques électriques dont la mobilités avec des écarts types qui sont absolument comparables à ceux obtenus pour des films produits par enduction centrifuge. De manière significative, contrairement aux dispositifs HMDS fonctionnalisés préparés par la procédure optimisée, les courbes de sortie n'indiquent pas la présence d'une résistance de contact élevée lorsque l'octadécyltrichlorosilane (OTS) est utilisé pour fonctionnaliser la surface du diélectrique d'oxyde de silicium. Les dispositifs ont démontré des mobilités allant jusqu'à 0,10 cm² / Vs et des rapports I_{on} / I_{off} jusqu'à 5×10^7. Lorsque la procédure optimisée est utilisé, les cristallites comblent facilement l'espace entre les électrodes source et drain. En outre, la morphologie des cristallites, suivant le profil des électrodes, semble indiquer l'absence de sites de nucléation dans la région inter-électrodique. Cela indique que la formation de cristallites ne commence pas dans le solvant mais seulement plus tard, ces structures "atterrissant" sur les électrodes et s'étendant par auto-assemblage.

Afin de démontrer cette hypothèse, DH4T a été mélangé avec une molécule similaire, DH2T (dihexylbithiophene). 7 échantillons ont été produits, avec des quantités croissantes de DH2T dans le mélange, et les performances électriques ont été mesurées. Les trois scénarios d'assemblage extrêmes sont les suivants: (a) un film entièrement mélangé avec présence d'impuretés DH2T l'intérieur des grains de DH4T, conduisant à une diminution probable de cristallinité; (b) une séparation de phase horizontale avec les îlots de DH2T entourés par du DH4T et (c) la ségrégation verticale de phase avec une couche de molécule la plus légère et la plus soluble (DH2T) sur le dessus. De manière surprenante, les données obtenues par TOF-SIMS indiquent que la couche de DH2T est présente à l'interface entre le diélectrique et la couche semi-conductrice (l'interface étant de 50:50 DH4T: DH2T sur un mélange 99: 1). Ce résultat tend à confirmer l'idée que la nucléation de cristallites DH4T ne se produit pas dans la région du canal, mais plutôt dans la partie supérieure de la goutte de solution déposée sur les électrodes. Les performances électriques ont été testées pour les films résultants des solutions mixtes. Une forte baisse de performances électriques a été constatée lors de l'addition de très petites quantités de DH2T au mélange (0.1%). DH2T étant une petite molécule isolante, la baisse des performances électriques prouve la présence de DH2T à l'interface avec le diélectrique. Cela montre que le test électrique peut être utilisé comme un outil non destructif de caractérisation de l'interface.

Nous avons employé les connaissances acquises sur les (macro)molécules et l'auto-assemblage multi-composant afin d'intégrer une nouvelle fonctionnalité dans un dispositif semi-conducteur par voie de mélange. Parmi les différentes classes de molécules, les systèmes photochromiques ont montré des résultats prometteurs en tant que commutateurs moléculaires, mais très peu de caractéristiques des (semi)conductivité ainsi qu'une fatigue non négligeable. La commutation optique entre deux états adressables indépendamment conduit à des changements à la fois au niveau moléculaire et l'échelle macroscopique. Au niveau moléculaire, nous observons des changements structurels et électroniques, des changements réversibles de la géométrie, des moments dipolaires, de la conjugaison π, de réversibles, de la bande interdite, etc.[25] La modification des propriétés macroscopiques lors de la commutation comprennent des changements dans la forme, le comportement de l'agrégation et de la conductance. La molécule que nous avons choisi est un diaryléthène (DAE-Me), synthétisé dans le cadre d'une collaboration à long terme, par le groupe du professeur Stefan Hecht à l'Université Humboldt de Berlin. Étant donné que ces diaryléthènes alkyle-substitués ne présentent pas de comportement semi-conducteur, ils ont été mélangés avec un polymère semi-conducteur bien connu, à savoir P3HT. La HOMO de P3HT se trouve entre celles du DAE-Me ouvert et la forme fermée. En raison de ce fait, lorsque le diaryléthène est dans la forme ouverte, son HOMO agit comme un centre de diffusion.[26-27] Néanmoins, lorsque le diaryléthène est dans la forme fermée, les charges se retrouvent piégés réduisant ainsi le courant $| I_{DS} |$ obtenu. Etant donné que le diaryléthène est thermodynamiquement stable dans les deux formes, cet effet a été utilisé afin de stocker des informations et de créer des mémoires à plusieurs niveaux.

Un montage de laser avec des temps d'éclairage de 3 ns à haute intensité a été utilisé afin d'enquêter sur la commutation photo-induite sur les moments pertinents dans l'électronique moderne par irradiation. Une impulsion laser de 3-ns (λ = 313 nm) à intensité modulable a irradié l'échantillon toutes les dix secondes conduisant à une diminution progressive du courant contrôlée par le nombre d'impulsions. Chaque impulsion générant un palier de diminution de courant ΔI_{DS} en raison de l'augmentation du nombre de molécules de diaryléthène dans la forme ouverte, qui ont basculé vers leur forme fermée. Nous avons réussi à construire un dispositif de 400 niveaux d'intensité de courant, pour atteindre une capacité de stockage de données sur huit bits (256 niveaux). Par réduction de l'intensité lumineuse en utilisant des filtres, nous avons montré que la hauteur des marches est fonction de la densité de puissance surfacique parce que le nombre de molécules subissant une isomérisation est directement lié à la densité des photons frappant la zone active du dispositif. Par conséquent, afin d'augmenter le nombre de paliers, l'intensité lumineuse peut être modulée d'une intensité faible à élevée. Le nombre de paliers serait seulement limité par le bruit dans le signal (conduisant à 5000 étapes pour l'expérience présentée) pour un nombre maximal théorique d'étapes égal au nombre de diaryléthènes dans le mélange.

Dans l'intérêt de démontrer la possible mise en œuvre des mémoires dans les applications électroniques novatrices, toute la procédure a été transférée sur un substrat flexible, la abandonnant sur les couches rigides inorganiques à base de silicium pour des couches polymères de polyéthylène téréphtalate (PET), le poly (méthacrylate de méthyle)) (PMMA) et le poly (4-vinylphénol) (PVP). Les dispositifs ont été caractérisés électriquement et les mobilités sont comparables à celles sur oxyde de silicium (supérieures à 10^{-3} cm² / Vs). Les capacités de commutation ont été testées sur plusieurs cycles de commutation dynamiques. Nous avons constaté que les dispositifs pouvaient être basculés de la forme fermée à ouverte et vice-versa. Des courbes dynamiques I_{DS}-temps avec de petites étapes d'illumination à 313 nm indiquent la capacité de l'appareil à fonctionner comme une mémoire multi-niveaux de 4 bits (16 niveaux distincts). En outre, la caractérisation électrique a été réalisée sur le dispositif après les étapes successives de flexion (rayons de courbure de 29 mm, 17,5 mm, 10 mm, 8 mm et 6 mm). Après flexion, les performances étaient encore comparables à celles observées avant flexion à chaque rayon de courbure pendant 60 secondes, avec des pertes mineures en termes de courant et un léger changement dans la tension de seuil, prouvant qu'avec de l'optimisation, la mémoire organique 3-terminaux étudiée peut être utilisée dans l'électronique flexible.

Visant une enquête plus approfondie sur l'implémentation de fonctions par le biais de mélanges, deux polymères, IIDDT-C3 et N2200, ont été sélectionnés pour leurs fortes capacités de transport de charge respectivement de type p et de type n, ainsi qu'une légère ambipolarité. Les deux polymères contenant des squelettes de thiophène et des chaînes alkyle similaires à nos molécules modèles DH4T et P3HT, elles démontraient ainsi un bon potentiel de mélange. L'objectif de cette étude en cours est la fabrication de dispositifs ambipolaires. Des dispositifs avec des quantités différentes de IIDDT-C3 dans le mélange ont été produits, avec de bonnes performances électriques. Un dispositif ambipolaire parfaitement équilibré a été produit à un mélange 50/50 de IIDDT-C3 et N2200. Cette approche est très intéressante car elle permet l'ambipolarité à la demande et pourrait être adaptée à d'autres polymères à mobilités plus élevés.

En résumé, notre étude comparative sur la structure par rapport à la fonction dans des OFETs basés sur DH4T en solution a révélé que par l'optimisation des conditions de formation d'un film par un choix judicieux de la méthode de traitement, de type de solvant, de la fonctionnalisation des interfaces et en particulier en réglant la vitesse d'évaporation du solvant il est possible de conduire l'auto-assemblage moléculaire vers la formation d'architectures hautement ordonnées présentant des caractéristiques électriques améliorées. De manière significative, leur utilisation comme composants électro-actifs dans des OFETs conduit à des performances de électriques qui sont au-delà de l'état de l'art pour les transistors basés sur DH4T, même lorsque comparé à ceux produits par sublimation faits avec la même molécule. En particulier, les mobilités de type p atteignant 0,10 cm² / Vs et des ratios I_{on} / I_{off} supérieurs à 10^7 ont été atteints. Nos résultats confirment sans ambiguïté que l'adaptation des interfaces est la clé de bonnes performances électriques. Notre méthode de traitement pour fabriquer des dispositifs à haute mobilité est compatible avec les applications de grande échelle offrant ainsi une voie vers l'électronique organique qui satisfait l'équilibre nécessaire entre la performance et la facilité de fabrication. Combiner le matériau avec DH2T a donné des informations supplémentaires sur le processus de cristallisation de DH4T qui se déroule au-dessus des électrodes. Ces résultats ont été confirmés par TOF-SIMS ainsi que la caractérisation électrique des films produits à partir de mélanges DHnT.

En mélangeant un polymère semi-conducteur avec une petite molécule photochromique, nous avons montré qu'il était possible de construire des dispositifs de mémoire à 3 terminaux ayant des caractéristiques remarquables. Surtout, la possibilité de définir plusieurs niveaux de courant distincts ouvre la voie à des mémoires à haute densité, avec des unités de mémoire 8-bits (256+ niveaux). Le temps d'éclairage utilisé pour le montage laser était à l'échelle de la nanoseconde, une échelle de temps qui est nécessaire pour l'électronique de la vie réelle. Il a été montré que cette approche pourrait être appliquée aussi sur des substrats flexibles. En outre, les très bonnes capacités de conservation des données des dispositifs et la fiabilité après plusieurs cycles d'écriture-effacement rend cette approche idéale pour l'électronique de l'avenir. Etant donné que cette approche est très polyvalente et non limité à une paire précise de molécules, en vue d'une alternative à l'encapsulation, le P3HT sensible à l'air pourrait être remplacé par un semi-conducteur de type p différent avec des niveaux d'énergie similaires, menant à des courants potentiellement plus élevés (d'où un nombre accru de niveaux possibles). En outre, les électrodes peuvent être imprimées à faible coût, sur de grandes surfaces pour une production de masse facilitée. En mélangeant deux polymères, il fut possible d'obtenir l'ambipolarité à la demande avec un rapport de mobilités

« type p / type n » allant de 10^{-2} et 10^{3}. Cette approche pourrait être adaptée à d'autres paires de semi-conducteurs et fait partie d'une étude en cours avec d'autres polymères.

Toutes ces études ont démontré que conférer à un matériau des fonctionnalités supplémentaires par mélange est une approche très efficace, réduisant les coûts et les difficultés de traitement par rapport aux techniques reposant sur l'utilisation de couches distinctes de matériaux. La sélection minutieuse des conditions de traitement (solvant, concentration, rapport de mélange, traitement de la surface, etc.) conduisent à de bonnes performances électriques pour chaque matériau et mélange étudié.

ABSTRACT

The topic of this thesis is the optimization of organic field-effect transistor (OFET) performances and the integration in OFET of additional functionalities through blending molecular components each one imparting a well-distinct characteristic to the material.

Organic semiconductors have been the focus of an extensive research activity during the past decades because they represent key active components for technological applications in opto-electronics such as large-area electronics, displays and sensing. They hold numerous advantages when compared to their inorganic counterparts (tunability of their physical properties via chemical functionalization, their low cost processing using mild conditions integration onto flexible supports, etc.). However, in order to enter the marketplace, most of the solution-processable organic semiconductors still need to reach field-effect mobilities comparable to those of amorphous silicon. These low device mobilities arise from the poor crystallinity of the semiconducting layers due to a typical grain size which is normally much smaller than the channel length of the device. Furthermore, organic devices' properties are strongly interface-dependent given the importance that metal/semiconductor and dielectric/semiconductor play in determining the field-effect transistor’s mobility as well as threshold voltage. Hence, optimal interface engineering is required because it will ultimately affect mobility and threshold voltage.

Small semiconducting molecules have proven to exhibit interesting electrical performances, partly due to their pronounced tendency to form crystalline domains when compared to their polymeric counterparts. In particular, hexamethyl-substituted oligothiophene based devices, such as di-hexylquaterthiophene (DH4T) are easily accessible model systems that have proven to display a high resistance to the environment, due to their dense packing and hexyl chains working as a passivation layer in addition to their charge transport performance in transistors. For vacuum deposited films the highest observed mobility (μ) amounted to 0.09 cm^2/Vs. As far as solution-processed films are concerned, the highest reported mobility values amounted to μ=0.043 cm^2/Vs for ink-jet printed devices and of μ=0.012 cm^2/Vs for spin-coated films, indicating that there is much room for improvement

on the processing side. Morphology and crystallographic parameters of DH4T films have been more recently investigated by Thierry et al. showing how DH4T can self-assemble into a highly ordered crystalline structure. In their study, the crystalline order within domains produced by vacuum sublimation was similar to that found in crystalline domains grown from solution. High mobility solution-processed devices can be therefore produced if the kinetically governed process of film growth is controlled to achieve large crystalline domains, eliminating or reducing the effect of grain boundaries, which are detrimental for the charge transport.

Initially this prototypical molecule was tested in three different chlorinated solvents namely chloroform ($CHCl_3$), 1,2-dichlorobenzene (DCB) and chlorobenzene (CB). The choice of the solvent was found to be crucial for the device performance. In particular, multiscale morphological characterization, from the hundreds-of-µm down to sub-µm scale, was carried out both by optical (OM) and atomic force (AFM) microscopy. The morphologies of DH4T films prepared by drop-casting from 1 mg/mL DH4T solution in chloroform, chlorobenzene (CB) and dichlorobenzene (DCB) were compared. The surface of the DH4T films deposited from chloroform solution consists of small crystals often not interconnected, whereas the films obtained using chlorobenzene or dichlorobenzene as a solvent display larger and more uniform crystalline domains in OM images. All films encompassed in this study exhibit high degree of crystallinity as confirmed by grazing incidence X-ray diffraction analysis. The film uniformity without presence of defects over a larger scale for chloro- and dichlorobenzene films does significantly decrease the occurrence of grain boundaries. Conversely, films deposited from $CHCl_3$ displayed very high surface roughness on the mesoscale, while films prepared from CB showed a decreased roughness. Films prepared from DCB solutions exhibited an even smaller roughness.

The procedure that exhibited the best mobility, i.e. 70 µL of DH4T at 5 mg/mL drop-cast from DCB, evaporation rate of 0.1, will be referred to as the “optimized procedure”. It has been successfully reproduced on over 110 devices using hexamethyldisilazane (HMDS) as a surface treatment. Noteworthy, in spite of the fact that drop-casting is a deposition technique which is supposed to lead to uneven device-to-device performances due to thickness variation in the x-y plane, the presence of large flat crystals spanning over hundreds of micrometers allowed for the fabrication of devices whose electrical parameters featured mobilities with standard deviations which were absolutely comparable to those achieved in spin-coated films. Significantly, in contrast to HMDS-functionalized devices prepared with the optimized procedure, output curves do not indicate the presence of a high contact resistance when octadecyltrichlorosilane (OTS) is used to functionalize the surface of the dielectric silicon oxide. The devices exhibit mobilities up to 0.10 cm²/Vs and I_{on}/I_{off} up to 5×10^7.

When the optimized procedure is used, the crystallites readily bridge the source and drain electrodes. Furthermore, the morphology of the crystallites, bridging and following the profile of the electrodes, seems to suggest the absence of nucleation sites in the interelectrodic region. This indicates that the formation of the crystallites does commence in the solvent and only later these structures "land" on the electrodes and expand via self-assembly.

In order to demonstrate this hypothesis, DH4T was blended with a similar molecule, DH2T (dihexylbithiophene). 7 samples were produced, with increasing amounts of DH2T in the blend, and the electrical performances were measured. The three extreme assembly scenarios are: (a) a fully blended film with presence of the DH2T impurities within the DH4T grains, leading to a likely decrease of crystallinity; (b) a horizontal phase segregation with islands of DH2T surrounded by DH4T and (c) vertical phase segregation with a layer of the lightest and most soluble molecule (DH2T) on top. Surprisingly, data from TOF-SIMS measurements indicate that the DH2T layer is present at the interface between dielectric and within the semiconducting layer (the interface being 50:50 DH4T:DH2T on a 99:1 blend). This result tends to corroborate the idea that the nucleation of DH4T crystallites does not happen within the interchannel region, but rather at the top of the solution drop deposited on the electrodes. The electrical performances were tested for the films resulting of blended solutions. A strong decrease of electrical performances was found upon addition of very small quantities of DH2T to the blend. Since DH2T is a insulating small molecule, the drop in electrical performances proves the presence of the DH2T at the interface with the dielectric. This shows that electrical testing can be used as a non-destructive tool of characterization of the interface.

We profited of the knowledge acquired on (macro)molecules and multicomponent self-assembly in order to to incorporate a novel functionality into a semiconducting device via blending. Among various classes of molecules, photochromic systems have shown promising results as molecular switches, but very little (semi)conducting characteristics and not negligible fatigue. Optical switching between two independently addressable states leads to changes both at the molecular and the macroscopic scale. At the molecular level, we observe reversible structural and electronic changes in the geometry, dipole moments, π-conjugation, bandgap, etc. Modifications of macroscopic properties upon switching include changes in shape, aggregation behavior and conductance. The molecule we have chosen is diarylethene (DAE-Me), synthesized, in the frame of a long-term collaboration, by the group of Prof. Stefan Hecht at Humboldt University Berlin. Given that these alkyl substituted diarylethenes did not display any semiconducting behavior, they have been blendend with a well-known semiconducting polymer, i.e. P3HT. The HOMO level of P3HT sits in-between that of DAE-Me in the open and the closed form. Because of this reason when the diarylethene is in the open form, its HOMO acts as a scattering center. On the other hand, when the diarylethene is in the closed form, charges get trapped reducing thereby resulting the $|I_{DS}|$ current. Since the diarylethene is thermodynamically stable in both forms, this effect was used in order to store information and build multilevel memories.

A laser-setup with illumination times of 3 ns at high intensity was used in order to investigate the photo-induced switching upon irradiating times relevant in modern electronics. A 3-ns laser pulse (λ = 313 nm) at modulable intensity was shone on the sample every ten seconds leading to a progressive current decrease controlled by the number of pulses. Each pulse generated a ΔI_{DS} step decrease owing to the increasing number of diarylethene molecules in the open form which are turned into their closed form. We have successfully built a 400 current-intensity levels device, reaching a data storage capacity over 8 bit (256 levels). By reduction of the light intensity using filters, we have shown that the step height is dependent on the areal power density because the number of molecules undergoing isomerization is directly linked to the density of the photons hitting the active area of the device. Therefore, in order to increase the number of steps, the light intensity could be modulated from low to high. The number of steps would only be limited by the noise in the signal (leading to 5000 steps in the presented experiment) for a theoretical maximum number of steps equal to the number of diarylethenes in the blend.

In the interest of demonstrating possible implementation of the memory-devices into novel electronic applications, the whole procedure was transferred onto a flexible substrate, trading the rigid inorganic silicon based layers for polymeric sheets of polyethylene terephtalate (PET), Poly(methyl methacrylate)) (PMMA) and poly(4-vinylphenol) (PVP). The devices were electrically characterized and the measured field-effect mobilities were comparable to those on silicon oxide (exceeding 10^{-3} cm²/Vs). Switching capabilities were tested over multiple dynamic switching cycles. We have found that the devices could be switched closed and back open. Dynamic I_{DS}-time curves with small illumination steps at 313 nm indicate the ability of the device to work as a 4-bit multilevel memory (16 distinct levels). Furthermore, electrical characterization was performed on the device after successive bending steps (bending radii of 29 mm, 17.5 mm, 10 mm, 8 mm and 6 mm). Post-bending performances were still comparable to those observed before bending at each bending radius for 60 seconds, with only minor losses in terms of current and a slight shift in the threshold voltage, proving that with further optimization, the studied organic 3-terminal memory devices could be introduced into flexible electronics.

Aiming further investigation of function implementation through blending, two polymers, IIDDT-C3 and N2200, were selected for their strong capabilities of respectively p-type and n-type charge transport, as well as slight ambipolarity. Both polymers contain thiophene backbones and alkyl chains similarly to our model molecules DH4T and P3HT, therefore demonstrating good blending potential. The objective of this ongoing study is the fabrication of ambipolar devices. Devices with different quantities of IIDDT-C3 in the blend were produced, with good electrical performances. A perfectly balanced ambipolar device was produced at a 50/50 blend of IIDDT-C3 and N2200. This approach is very interesting as it allows ambipolarity on demand and could be adapted to other polymers with higher mobilities.

In summary, our comparative study on the structure vs. function relationship in solution processed DH4T based OFETs revealed that by optimizing the conditions of film formation via judicious choice of processing method, solvent type, interfaces functionalization and in particular by tuning the rate of solvent evaporation it is possible to drive the molecular self-assembly towards the formation of highly ordered low-dimensional architectures exhibiting enhanced electrical characteristics. Significantly, their use as electroactive components in OFETs led to device performances that are beyond the state-of-the-art for DH4T-base transistors, even when compared to vacuum processed OFETs made with the same molecule. In particular, *p*-type mobilities as high as 0.10 cm^2/Vs and I_{on}/I_{off} currents exceeding 10^7 were achieved. Our results unambiguously confirm that the tailoring of interfaces is key. Our processing method to achieve high mobility devices is compatible with large-area applications thus providing a pathway towards organic electronics that satisfies the needed balance between performance and processability. Blending the material with DH2T gave additional insight into the crystallization process of DH4T that takes place above the electrodes. Those results were confirmed by TOF-SIMS as well as electrical characterization of the films produced from DHnT blends.

By blending a semiconducting polymer with a photochromic small molecule, we have shown that it is possible to build 3-terminal memory-devices with impressive characteristics. Above all, the ability to define many distinct current-levels paves the way for high-density memories, with 8-bit memory units (256+ levels). Illumination times using the laser-setup were in the ns rage, a timescale that is necessary for real-life electronics. It has been shown that this approach could be implemented also onto flexible substrates. Furthermore, the very good data-retention capabilities of the devices and the reliability after many write-erase cycles makes this approach ideal for the electronics of the future. Since this approach is very versatile, as an alternative to encapsulation, the air-sensible P3HT could be replaced by an alternative p-type semiconductor with similar energy levels, leading to potentially higher currents (hence an increased possible number of steps). Additionally, the electrodes could be printed for facilitated low-cost, large-area mass production. By blending two polymers it was possible to achieve ambipolarity on demand with any kind of p/n ratio ranging from 10^{-2} to 10^{3}. This approach could be adapted to other *p*-type/*n*-type pairs and is part of an ongoing study with other polymers.

All these studies have demonstrated conferring to a material additional functionalities via blending is a very efficient approach, reducing costs and processing difficulties as compared to techniques relying on the processing of separate layers of materials. The careful selection of processing conditions (solvent, concentration, blend ratio, surface treatment, etc.) lead to good electrical performances of each material and blend.

REFERENCES

1. Sirringhaus, H.; Brown, P. J.; Friend, R. H.; Nielsen, M. M.; Bechgaard, K.; Langeveld-Voss, B. M. W.; Spiering, A. J. H.; Janssen, R. A. J.; Meijer, E. W.; Herwig, P.; de Leeuw, D. M., Two-Dimensional Charge Transport in Self-Organized, High-Mobility Conjugated Polymers. *Nature* **1999,** *401* (6754), 685-688.
2. Orgiu, E.; Samorì, P., 25th Anniversary Article: Organic Electronics Marries Photochromism: Generation of Multifunctional Interfaces, Materials, and Devices. *Adv. Mater.* **2014,** *26* (12), 1827-1845.
3. Tobjörk, D.; Österbacka, R., Paper Electronics. *Adv. Mater.* **2011,** *23* (17), 1935-1961.
4. Xu, Y. Y.; Zhang, F.; Feng, X. L., Patterning of Conjugated Polymers for Organic Optoelectronic Devices. *Small* **2011,** *7* (10), 1338-1360.
5. Dimitrakopoulos, C. D.; Malenfant, P. R. L., Organic Thin Film Transistors for Large Area Electronics. *Adv. Mater.* **2002,** *14* (2), 99-117.
6. Nomoto, K.; Hirai, N.; Yoneya, N.; Kawashima, N.; Noda, M.; Wada, M.; Kasahara, J., A High-Performance Short-Channel Bottom-Contact OTFT and Its Application to AM-TN-LCD. *IEEE Trans. Electron Devices* **2005,** *52* (7), 1519-1526.
7. Torsi, L.; Farinola, G. M.; Marinelli, F.; Tanese, M. C.; Omar, O. H.; Valli, L.; Babudri, F.; Palmisano, F.; Zambonin, P. G.; Naso, F., A Sensitivity-Enhanced Field-Effect Chiral Sensor. *Nat. Mater.* **2008,** *7* (5), 412-417.
8. Arias, A. C.; MacKenzie, J. D.; McCulloch, I.; Rivnay, J.; Salleo, A., Materials and Applications for Large Area Electronics: Solution-Based Approaches. *Chem. Rev.* **2010,** *110* (1), 3-24.
9. Shtein, M.; Mapel, J.; Benziger, J. B.; Forrest, S. R., Effects of Film Morphology and Gate Dielectric Surface Preparation on the Electrical Characteristics of Organic-Vapor-Phase-Deposited Pentacene Thin-Film Transistors. *Appl. Phys. Lett.* **2002,** *81* (2), 268-270.
10. Cornil, J.; Beljonne, D.; Calbert, J. P.; Brédas, J. L., Interchain Interactions in Organic Pi-Conjugated Materials: Impact on Electronic Structure, Optical Response, and Charge Transport. *Adv. Mater.* **2001,** *13* (14), 1053-1067.
11. Liscio, A.; Orgiu, E.; Mativetsky, J. M.; Palermo, V.; Samorì, P., Bottom-up Fabricated Asymmetric Electrodes for Organic Electronics. *Adv. Mater.* **2010,** *22* (44), 5018-5023.
12. Halik, M.; Klauk, H.; Zschieschang, U.; Schmid, G.; Ponomarenko, S.; Kirchmeyer, S.; Weber, W., Relationship between Molecular Structure and Electrical Performance of Oligothiophene Organic Thin Film Transistors. *Adv. Mater.* **2003,** *15* (11), 917-922.
13. Payne, M. M.; Parkin, S. R.; Anthony, J. E.; Kuo, C. C.; Jackson, T. N., Organic Field-Effect Transistors from Solution-Deposited Functionalized Acenes with Mobilities as High as 1 Cm(2)/V-S. *J. Am. Chem. Soc.* **2005,** *127* (14), 4986-4987.
14. Sergeyev, S.; Pisula, W.; Geerts, Y. H., Discotic Liquid Crystals: A New Generation of Organic Semiconductors. *Chem. Soc. Rev.* **2007,** *36* (12), 1902-1929.
15. Leufgen, M.; Rost, O.; Gould, C.; Schmidt, G.; Geurts, J.; Molenkamp, L. W.; Oxtoby, N. S.; Mas-Torrent, M.; Crivillers, N.; Veciana, J.; Rovira, C., High-Mobility Tetrathiafulvalene Organic Field-Effect Transistors from Solution Processing. *Org. Electron.* **2008,** *9* (6), 1101-1106.
16. Mas-Torrent, M.; Masirek, S.; Hadley, P.; Crivillers, N.; Oxtoby, N. S.; Reuter, P.; Veciana, J.; Rovira, C.; Tracz, A., Organic Field-Effect Transistors (OFETs) of Highly Oriented Films of Dithiophene-Tetrathiafulvalene Prepared by Zone Casting. *Org. Electron.* **2008,** *9* (1), 143-148.
17. Gao, P.; Beckmann, D.; Tsao, H. N.; Feng, X.; Enkelmann, V.; Baumgarten, M.; Pisula, W.; Müllen, K., Dithieno 2,3-D;2 ',3 '-D ' Benzo 1,2-B;4,5-B ' Dithiophene (DTBTD) as Semiconductor for High-Performance, Solution-Processed Organic Field-Effect Transistors. *Adv. Mater.* **2009,** *21* (2), 213-216.
18. Cavallini, M.; D'Angelo, P.; Criado, V. V.; Gentili, D.; Shehu, A.; Leonardi, F.; Milita, S.; Liscio, F.; Biscarini, F., Ambipolar Multi-Stripe Organic Field-Effect Transistors. *Adv. Mater.* **2011,** *23* (43), 5091-5097.
19. Generali, G.; Dinelli, F.; Capelli, R.; Toffanin, S.; di Maria, F.; Gazzano, M.; Barbarella, G.; Muccini, M., Correlation among Morphology, Crystallinity, and Charge Mobility in Ofets Made of Quaterthiophene Alkyl Derivatives on a Transparent Substrate Platform. *J. Phys. Chem. C* **2011,** *115* (46), 23164-23169.

20. Song, D. H.; Choi, M. H.; Kim, J. Y.; Jang, J.; Kirchmeyer, S., Process Optimization of Organic Thin-Film Transistor by Ink-Jet Printing of DH4T on Plastic. *Appl. Phys. Lett.* **2007,** *90* (5), 053504.
21. Garnier, F.; Hajlaoui, R.; El Kassmi, A.; Horowitz, G.; Laigre, L.; Porzio, W.; Armanini, M.; Provasoli, F., Dihexylquaterthiophene, a Two-Dimensional Liquid Crystal-Like Organic Semiconductor with High Transport Properties. *Chem. Mater.* **1998,** *10* (11), 3334-3339.
22. Granstrom, E. L.; Frisbie, C. D., Field Effect Conductance Measurements on Thin Crystals of Sexithiophene. *J. Phys. Chem. B* **1999,** *103* (42), 8842-8849.
23. Someya, T.; Katz, H. E.; Gelperin, A.; Lovinger, A. J.; Dodabalapur, A., Vapor Sensing with Alpha,Omega-Dihexylquarterthiophene Field-Effect Transistors: The Role of Grain Boundaries. *Appl. Phys. Lett.* **2002,** *81* (16), 3079-3081.
24. Dabirian, R.; Palermo, V.; Liscio, A.; Schwartz, E.; Otten, M. B. J.; Finlayson, C. E.; Treossi, E.; Friend, R. H.; Calestani, G.; Müllen, K.; Nolte, R. J. M.; Rowan, A. E.; Samorì, P., The Relationship between Nanoscale Architecture and Charge Transport in Conjugated Nanocrystals Bridged by Multichromophoric Polymers. *J. Am. Chem. Soc.* **2009,** *131* (20), 7055-7063.
25. Nougaret, L.; Kassa, H. G.; Cai, R. G.; Patois, T.; Nysten, B.; van Breemen, A. J. J. M.; Gelinck, G. H.; de Leeuw, D. M.; Marrani, A.; Hu, Z. J.; Jonas, A. M., Nanoscale Design of Multifunctional Organic Layers for Low-Power High-Density Memory Devices. *Acs Nano* **2014,** *8* (4), 3498-3505.
26. Borjesson, K.; Herder, M.; Grubert, L.; Duong, D. T.; Salleo, A.; Hecht, S.; Orgiu, E.; Samori, P., Optically Switchable Transistors Comprising a Hybrid Photochromic Molecule/N-Type Organic Active Layer. *Journal of Materials Chemistry C* **2015,** *3* (16), 4156-4161.
27. Orgiu, E.; Crivillers, N.; Herder, M.; Grubert, L.; Patzel, M.; Frisch, J.; Pavlica, E.; Duong, D. T.; Bratina, G.; Salleo, A.; Koch, N.; Hecht, S.; Samori, P., Optically Switchable Transistor Via Energy-Level Phototuning in a Bicomponent Organic Semiconductor. *Nature Chemistry* **2012,** *4* (8), 675-679.

TABLE OF CONTENTS

SYMBOLS AND ABBREVIATIONS

AFM	Atomic force microscopy
Ag	Silver
Au	Gold
$\mathbf{C_{10}}$	1-decanethiol
CB	Chlorobenzene
$\mathbf{CHCl_3}$	Chloroform
$\mathbf{C_i}$	Dielectric capacitance
Cr	Chrome
DAE	Diarylethene
DAE-Me	1,2-Bis(2-methyl-5-p-tolylthiophen-3-yl)cyclopent-1-ene
DAE-Me_c	DAE-Me in the closed form
DAE-Me_o	DAE-Me in the open form
DCB	1,2-dichlorobenzene
DH2T	Dihexylbithiophene
DH4T	Dihexylquaterthiophene
DH6T	Dihexylsexithiophene
DHnT	Hexyl-terminated thiophene oligomers
$\boldsymbol{\varepsilon}$	Permittivity
$\mathbf{e^-}$	Electron
$\boldsymbol{\varepsilon_0}$	Vacuum permittivity
$\mathbf{E_c}$	Conduction band
$\mathbf{E_f}$	Fermi level
$\mathbf{E_g}$	Band gap
$\boldsymbol{\varepsilon_r}$	Relative permittivity
$\mathbf{E_v}$	Valance band
eV	Electronvolt
$\mathbf{E_{vac}}$	Vacuum level
$\mathbf{FC_{10}}$	1H,1H,2H,2H-perfluorodecanethiol
FET	Field-effect transistor
GIXD	Grazing incident X-ray diffraction
$\mathbf{h^+}$	Electron-hole
HMDS	Hexamethyldisilazane
HOMO	Highest occupied molecular orbital
$\mathbf{I_{DS}}$	Drain-source current
IE	ionization energy
$\mathbf{I_{GS}}$	Leakage current
IIDDT-C3	poly[1,1'-bis(4-decyltetradecyl)-6-methyl-6'-(5'-methyl-[2,2'-bithiophen]-5-yl)-[3,3'-biindolinylidene]-2,2'-dione]
$\mathbf{I_{off}}$	Lowest I_{DS} value
$\mathbf{I_{on}}$	Highest I_{DS} value
$\mathbf{I_{on}/I_{off}}$	I_{on}-to-I_{off} ratio
$\boldsymbol{k_B}$	boltzman constant
L	Channel length
LUMO	Lowest unoccupied molecular orbital
MTR	Multiple trap and release model
OFET	Organic field-effect transistor
OM	Optical microscopy
OTFT	Organic thin-film transistor
OTS	Octadecyltrichlorosilane

P	Pressure
P(NDI2OD-T2)	Poly[N,N'-bis(2-octyldodecyl)-naphthalene-1,4,5,8-bis(dicarboximide)-2,6-diyl]-alt-5,5'-(2,2'-bithiophene)
P3HT	Poly (3-Hexylthiophene)
PCD-TPT	Polythiadiazolopyridinediyl(4,4-dihexadecyl-4H-cyclopentadithiophenediyl) thiadiazolopyridinediyl(4,4-dihexadecyl-4H-cyclopentadithiophenediyl)
PDVT-8	Poly[2,5-bis(2-octyldodecyl)pyrrolo[3,4-c]pyrrole-1,4(2H, 5H)-dione-alt 5,5′-di(thiophen-2-yl)-2,2′-(E)-2-(2-(thiophen-2-yl)vinyl)thiophene]
PET	Polyethylene terephthalate
PMMA	Poly(methylmethacrylate)
PVP	Poly(4-VinylPhenol)
$R_{channel}$	Channel resitance
$R_{contact}$	Contact resistance
RPM	Rounds per minute
R_{rms}	Root-mean-squared roughness
R_t	Tunneling resistance
R_{total}	Total resitance
SAM	Self-assembled monolayer
Si	Silicon
SiO_2	Silicon dioxide
SNR	Signal-to-noise ratio
T	Temperature
TLM	Transfer length method
ToF-SIMS	Time of Flight Secondary Ion Mass Spectrometry
UPS	Ultraviolet photoelectron spectroscopy
V_{ab}	Charge-transfer integral
V_{DS}	Drain-source voltage
V_{GS}	Gate-source voltage
VRH	Variable range hopping
V_{Th}	Threshold voltage
W	Channel width
W/L	width-to-length ratio
W_f	Work function
XRD	X-ray diffraction
α	Tilt angle
ΔG_{evap}	Gibbs free energy of evaporation
ΔG_{l}	Molar Gibbs free energy (liquid)
ΔG_{m}	Gibbs free energy of mixing
ΔG_{v}	Molar Gibbs free energy (vapor)
ΔH_{m}	Enthalpy of mixing
ΔS_{m}	Entropy of mixing
λ	Reorganizational energy
μ	Field effect mobility
μ_{eff}	Effective mobility
μ_n	Electron field effect mobility
μ_p	Hole field effect mobility
μ_p/μ_n	*p*-type-to-*n*-type mobility ratio
τ	Trapping time
τ_{tr}	Average trapping time on shallow traps
$\varphi_{b.}$	Schottky barrier
χ	Electron affinity

Chapter 1. Introduction

1.1. Background

The blending of two materials in order to form a new one, with improved characteristics, is not a recent idea in human history. From artifacts produced from copper based alloys seven thousands of years ago [1] to modern polymer blends with improved thermal and mechanical properties, [2] blending has always been a go-to approach for many applications. Nevertheless, in the field of electronics, very pure single component materials are often privileged, due to their often superior performances, and addition of a secondary material is mostly limited to very small amounts, for doping purposes. [3-5] These inorganic electronic devices have demonstrated tremendous calculation capabilities, shaping the modern world. The first field-effect transistors, at the foundation of the logic gates necessary for data processing, were patented by Julius Edgar Lilienfeld first (in 1926) [6] and later by Oskar Heil in 1934, [7] but without any practical application. The first semiconducting devices were developed by the team of William Shockley at Bell Labs in 1947, opening the gates for an uninterrupted research in electronics, [8,9] with the first integrated circuit, developed by Jack Kilby, emerging in 1958. [10] Starting from less than ten transistors integrated in the early sixties, hundreds of millions of transistors now compose our processors, the central data processing units of our computers. As their power increased and their fabrication cost decreased, their potential for applications exploded, and microchips are now integrated in countless devices. From phones to tombstones, cars and pet-collars, everyday objects are transformed into controllable, connected, “smart” devices, which can collect and process data.

Unfortunately, electronics are still facing multiple limitations for future implementation. Silicon-based technologies tend to be very expensive and power consuming to produce, since microchips are fabricated on wafers grown from liquid silicon. Also, silicon-based chips are non-flexible and show no transparency. All these drawbacks have lead to parallel research on organic semiconductors as a replacement for inorganic technologies. The first field-effect transistor fabricated using an organic material as active semiconductor (polythiophene) was reported in 1987 by Koezuka and co-workers. [11] Since then, numerous polymers and small molecules based on thiophene units featuring semiconducting properties were synthetized, and viable organic field-effect transistors were fabricated. Novel materials integrating long conjugated systems with a wide variety of chemical functions were produced. Among them, some displayed all the characteristics lacking in their inorganic counterparts: flexibility, transparency, easily processing from the solution.

Regrettably, the "perfect" material has not emerged yet, each molecular material featuring very few strongly positive aspects, and a large variety of drawbacks such poor electrical performances, opacity, weak mechanical properties, air sensitivity or low solubility in the preferred solvents. While most of the research effort is still focused on the synthesis of novel materials, other approaches can lead to high-performing organic field-effect transistors. Two in particular stand out. First, the fabrication of the devices can be optimized, by careful selection of the processing techniques and consideration of the interfaces that determine the interplay between materials for improved electrical characteristics. Second, one particular strength of organic materials, the possibility to blend it in the solution, can be exploited. Two or more well established materials can be combined in the solution for the fabrication of devices with improved performances, and even completely new functions.

1.2. Aims of the thesis

While device optimization through developments of advanced processing techniques and tuning of injection barriers has always followed the study of organic materials, [12-14] blending organic materials for improved and new properties in electronics has only started to be thoroughly investigated since the mid-1990s. This approach yielded good results for augmentation of the electroluminescence of organic light emitting diodes and photovoltaics. [15-17] The concept was further extended to organic field-effect transistors with aims of improvement of electrical performances and implementation of novel features in organic devices. [18,19]

In the work presented in this thesis, we will try to reach further in these directions and produce devices with the highest possible performances, using mostly small molecules and polymers available commercially. We will not limit ourselves to a single pair of molecules to be blended, but consider blends with sets of molecules that share similarities, in order to obtain a wider study that can be applied in multiple cases. We will consider blends composed of a family of small molecules (oligothiophenes) in order to explore the consequences of the presence of similar molecules on the crystallinity and electrical performances of a semiconductor film. Films produced from polymer blends with radically different electrical characteristics and molecular structures for potential ambipolar transistors will be investigated. The presented work will be linked to real-world applications by the fabrication of a photoswitchable multilevel memory device based on a blend of a semiconducting polymer and a photochromic small molecule. We will aim to demonstrate the viability of such a technology by implementation onto a flexible substrate and measurement of long-term volatility.

In order to increase the performances of field-effect transistors produced from the solution, a large diversity of processing techniques have been developed, often by means of complex experimental setups (such as Langmuir Schaefer) that could not realistically be implemented into industrial applications. The works presented in this thesis will avoid such techniques and rely on simple processing of semiconducting materials that mimic industry-viable processes, such as ink-jet printing. Nevertheless, all transistors presented in this thesis will be fabricated upon careful investigation of the ideal interface tuning for optimal charge transport.

1.3. Structure of the Thesis

The thesis is composed of nine chapters. The work is arranged in the following order:

- Chapter 1 aimed to introduce the topic of the thesis and placed it in the scientific context.
- Chapter 2 will focus on charge transport in solid materials. It will try to provide a glimpse on some theoretical aspects of charge transport in organic materials and charge injection across interfaces.
- Chapter 3 will present the materials employed in the thesis, their properties and characteristics.
- Chapter 4 will discuss organic field-effect transistors, their particular features and the their electrical characterization.
- Chapter 5 will present the experimental techniques for device fabrication and the instruments used for sample characterization.
- Chapter 6 will focus on the optimization of films of dixehylquaterthiophene for improved electrical performances. It will focus on the control of the rate of evaporation and the functionalization of surfaces. It will explore the effect of blending of small semiconducting molecules for increased charge transport.
- Chapter 7 will center on a wide range of polymers with different electrical characteristics, blended for the fabrication of ambipolar transistors. It will demonstrate exceptional

performances for multiple polymer combinations. It will center on both electrical and morphological characterization in order to provide convincing explanations for the observed performances.

- Chapter 8 will spotlight field-effect transistors based on a polymer and a small photochromic molecule for photoswitchable memory applications. It will explore the fabrication and characterization of non-volatile multilevel memories with hundreds of discernible current levels. It will demonstrate the implementation of these devices on a transparent flexible polyethylene terephtalate substrate, and prove the ability to perform properly upon multiple bendings.
- Chapter 9, the conclusion, will summarize the work presented in the thesis, and give short term and long term outlooks.

1.4. References

1 Thornton, C. P., Lamberg-Karlovsky, C. C., Liezers, M. & Young, S. M. M. On pins and needles: Tracing the evolution of copper-base alloying at Tepe Yahya, Iran, via ICP-MS analysis of common-place items. *J. Archaeol. Sci.* **29**, 1451-1460 (2002).
2 Utracki, L. A. & Wilkie, C. *Polymer Blends Handbook*. (Springer, 2010).
3 Zulehner, W. The Growth of Highly Pure Silicon-Crystals. *Metrologia* **31**, 255-261 (1994).
4 Moskalyk, R. R. Gallium: the backbone of the electronics industry. *Miner. Eng.* **16**, 921-929 (2003).
5 Jeon, H. G., Inoue, M., Hirarnatsu, N., Ichikawa, M. & Taniguchi, Y. A modified sublimation purification system using arrays of partitions. *Org. Electron.* **9**, 903-905 (2008).
6 Lilienfeld, J. E. Method and apparatus for controlling electric currents. U.S. patent (1926).
7 Heil, O. Improvements in or relating to Electrical Amplifiers and other Control Arrangements and Devices. U.K. patent (1934).
8 Bardeen, J. & Brattain, W. H. The Transistor, A Semi-Conductor Triode. *Phys. Rev.* **74**, 230 (1948).
9 Shockley, W. & Pearson, G. L. Modulation of Conductance of Thin Films of Semi-Conductors by Surface Charges. *Phys. Rev.*, 232 (1948).
10 Kilby, J. S. Miniaturized Electronic Circuits. U.S. patent (1964).
11 Koezuka, H., Tsumura, A. & Ando, T. Field-Effect Transistor with Polythiophene Thin-Film. *Synthetic. Met.* **18**, 699-704 (1987).
12 Law, K. Y. Organic Photoconductive Materials - Recent Trends and Developments. *Chem. Rev.* **93**, 449-486 (1993).
13 Brown, A. R., Deleeuw, D. M., Lous, E. J. & Havinga, E. E. Organic N-Type Field-Effect Transistor. *Synthetic. Met.* **66**, 257-261 (1994).
14 Katz, H. E. Organic molecular solids as thin film transistor semiconductors. *J. Mater. Chem.* **7**, 369-376 (1997).
15 Park, J. Y. *et al.* The electroluminescent and photodiode device made of a polymer blend. *Synthetic. Met.* **79**, 177-181 (1996).
16 Ferenczi, T. A. M. *et al.* Organic Semiconductor: Insulator Polymer Ternary Blends for Photovoltaics. *Adv. Mater.* **23**, 4093 (2011).
17 Falke, S. M. *et al.* Coherent ultrafast charge transfer in an organic photovoltaic blend. *Science* **344**, 1001-1005 (2014).
18 Park, B. *et al.* High-performance organic thin-film transistors with polymer-blended small-molecular semiconductor films, fabricated using a pre-metered coating process. *J. Mater. Chem.* **22**, 5641-5646 (2012).
19 Lee, W. H. & Park, Y. D. Organic Semiconductor/Insulator Polymer Blends for High-Performance Organic Transistors. *Polymers* **6**, 1057-1073 (2014).

Chapter 2. Charge transport in organic materials

2.1. Introduction

This chapter will attempt to give a general overview on charge carriers and charge transport in on organic materials. It will discuss the presence of electrons in solids, and review the different types of materials depending on their energetic levels. It will consider the various interfaces between materials and how they affect charge carrier transport. In this chapter, we will also focus on the effect of impurities at the surface and within the materials. Finally, we will point out the optimal conditions for charge transport in organic materials.

2.2. Charges in materials

2.2.1. *Energetic levels*

In the case of an electron not bound to an atom, such as a free electron in the gas phase, its energy is not limited to a strict value. [1] In an isolated atom, the energy of the electrons can only equal well defined discrete values, [2] which correspond to atomic orbitals. Any atom joining to form a molecule combines its atomic orbitals to form molecular orbitals, each of which equals a discrete energy level. [3] As more atoms are brought together, the molecular orbitals widen and their energetic levels form quasi-continuums instead of taking discrete values. These specific intervals where the energy of an electron can equal any value are represented as bands, and separated by band-gaps (**Figure 2.1**). [4] While the higher occupied energetic levels broaden into large energy-bands, the inner atomic electrons do not interact significantly with neighboring atoms, and their energy levels stay very close to their original values.

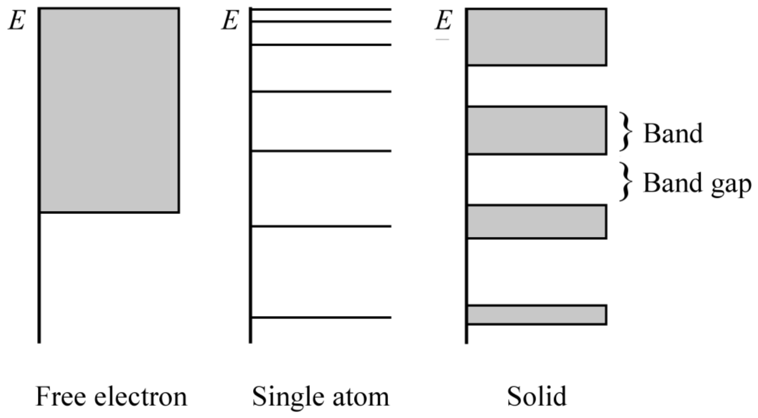

Figure 2.1: Representation of the possible energetic levels of an electron in different states at 0 K.

The Fermi-Dirac distribution $f(\epsilon)$ describes the distribution of particles (electrons in our case) over the possible energy states of the system. [5] It describes the probability of an electron to occupy a state with the energy ϵ. It allows determination of the average number of electrons occupying the state:

$$f(\epsilon) = \frac{1}{e^{(\epsilon - \mathrm{E_F})/(k_B \mathrm{T})} + 1} \qquad \textbf{Eq. 2.1}$$

with T the temperature in K and k_B the Boltzmann constant. The Fermi level, $\epsilon = E_F$, is defined as the level with 50% chance of occupancy as determined from the Fermi-Dirac distribution. The Fermi level is represented alongside the bands in energy diagrams, as to determine the occupancy of the bands. All bands with energies below the Fermi level are filled, while those above are unoccupied. The highest occupied band (immediately below E_F) is named the valence band (E_v), while the lowest unoccupied band (immediately above E_F) is referred to as the conduction band (E_c), as represented in **Figure 2.2**. If the Fermi level is located within a band, valence and conduction band are overlapping. The vacuum level is the energy of a free stationary electron that is outside of any material. The energy required to extract an electron from the valence band maximum to the vacuum level is the ionization energy (IE). [6] If the valence band and conduction band are overlapping, the IE corresponds to the energy required to extract an electron from the Fermi level to the vacuum level and is called the work function (W_f).

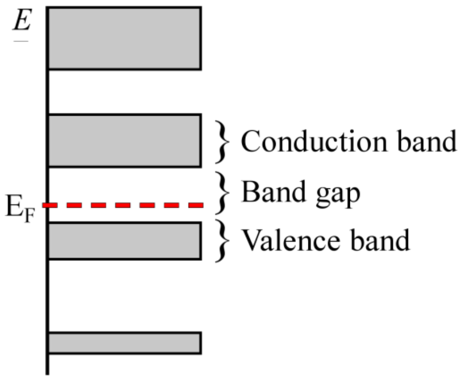

Figure 2.2: Representation of the valence and conduction bands for a Fermi level within a band gap.

2.2.2. Charges and charge transport

The absence of one electron in the valence band is commonly referred to as an electron hole, and will be will be mentioned as a “hole” during the whole thesis. Holes are generated when an electron leaves the valence band for the conduction band (electron-hole pair generation). [7] Holes differ greatly from electrons as electrons (e^-) are negatively charged and holes (h^+) positively charged. In order to be potentially mobile, electrons at the highest occupied energy level, E_F, have to be able to access a slightly higher energy level to provide net motion in a particular direction. Conversely, holes are potentially mobile if they are able to access a lower energy level. In the case of a valence and conduction band overlap (absence of band gap E_g at the Fermi level), both electron and hole transport are easily achieved since the Fermi level is present inside the continuum of allowed energy levels. Materials offering this characteristic are conductive. If the Fermi level is within a broad band gap far from the valence and conduction bands, charges cannot move within the material that is an insulator. If the Fermi level is within a band gap, but close to either the valence or the conduction band, charge mobility is potentially reachable under specific conditions, and the material is a semiconductor (**Figure 2.3**). If the Fermi level is close to the conduction band, electrons are potentially mobile and the solid is an *n*-type semiconductor. Conversely, potential hole movement due to proximity of the Fermi level to the valence band is characteristic of a *p*-type semiconductor. [8]

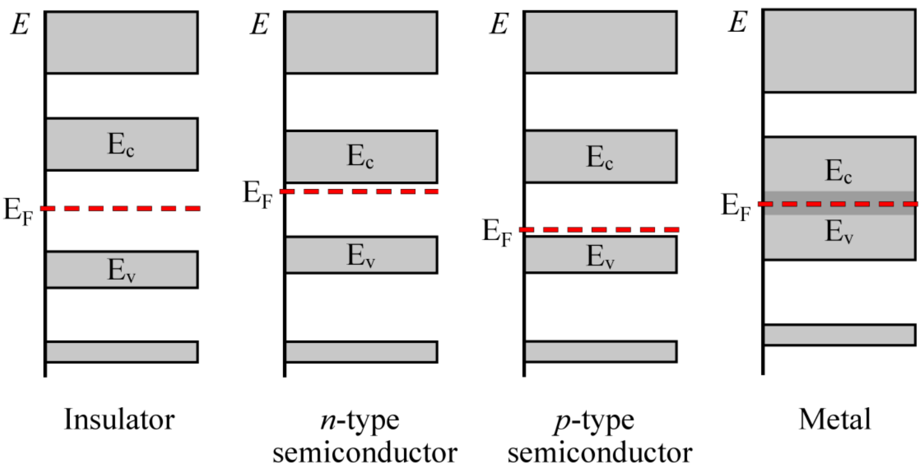

Figure 2.3: Energy diagrams for insulators, semiconductors and metals.

2.2.3. Static and mobile charge carriers

Charge carriers (holes or electrons) are mobile within the solid in the case of a metal. If a strong electric field is applied on a metal, the electron density that responds to the applied field is so important that the electric field cannot penetrate far into the solid. [9] In the case of insulators, the electric field is widespread into the solid and can lead to the polarization of the material (called a dielectric). [10] This is due to the charges that, unable to flow within the material, are only displaced towards or opposite of the field, creating an internal electric field reducing the overall field within the dielectric itself. The resistance of the dielectric to convey the electrical field is the permittivity (ε), that is often given in terms of relative permittivity (ε_r) according to the equation:

$$\varepsilon = \varepsilon_r \mathcal{E}_0 \qquad \textbf{Eq. 2.2}$$

with ε_0 the vacuum permittivity, in F/cm. The capacitance is directly related to the permittivity, and is function of the thickness and shape of the dielectric solid. In the case of a flat layer, the capacitance C_i is calculated following the equation:

$$C_i = \varepsilon_r \varepsilon_0 \frac{A}{d} \qquad \textbf{Eq. 2.3}$$

with A in cm² the area of the dielectric where the potential is applied and d the thickness of the dielectric, in cm.

Semiconductors behave as insulators where charges cannot move freely in the solid. Nevertheless, under application of an electric field, the energy levels available to electrons are altered and electrons and holes become mobile in respectively *n*-type and *p*-type semiconductors. This effect is named the field-effect and will be exploited for field-effect transistors as will be discussed in chapter 4. Unlike in the case of metals, the electric field is propagated into the semiconductor, but not as well as in the case of insulators. Therefore, two regions are defined, the bulk region and the interface region, where the electric field is the strongest and charge transport is possible.

Charge movement within the metal or semiconductor solid can be conditioned by application of an electric potential. Electrons will move towards positive potential while holes will do the opposite.

2.2.4. Charge transport in organic semiconductors

Organic molecules are defined as compounds that contain a skeleton of carbon atoms on which are attached hydrogen, oxygen or nitrogen atoms. [11] Carbon can form different type of bonds according to the hybridization theory of atomic orbitals. Its 6 electrons are split between inner and outer shells. In the most inner shell $1s^2$ there are two electrons, other four are placed two in the second s orbital ($2s^2$) and two more in the p orbital. These four external orbitals can undergo hybridization forming an excited orbital state generated by a linear combination of s and p orbital wave functions.

This hybrid orbital called sp has a lower energy with respect to un-hybridized p orbital because electrons can be disposed in it with parallel spins. Of particular interest is when hybridization occurs between 2p orbital, p_x and p_y, with the s orbital. This allows a bond formation where a conjugated π- electron system is formed by un-hybridized p_z orbitals of sp^2 carbon atoms in a molecule as shown in **Figure 2.4**. In this configuration, two carbons each share one electron from their sp hybrid shell resulting in σ bond, and a free p_z electron perpendicular to the plane of the C and H atoms, forming a π bond. Hence, there is a double bond between the carbons, the addition of a strong σ bond and a weaker π bond. The electron conduction can occur due to the change in weak π orbital overlap. In conjugated systems, electrons can delocalize within the molecule, leading to molecular orbitals that can spread through large areas of the molecule. Conjugated systems may also include other atoms, such as sulfur.

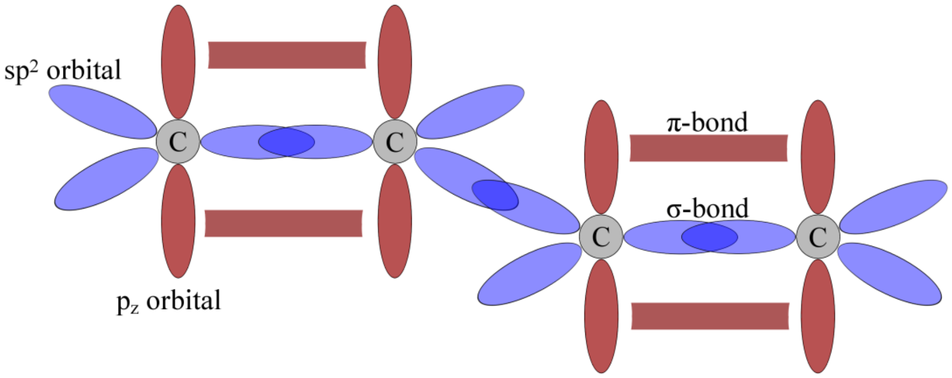

Figure 2.4: Cartoon representing 4 carbon atoms in a conjugated system, with their outer-shell molecular orbitals.

In organic molecules, the highest occupied and lowest unoccupied energy levels are the HOMO (Highest Occupied Molecular Orbital) and the LUMO (Lowest Unoccupied Molecular Orbital). The σ bond is very strong and is formed by low energy orbitals, while the π bond is more fragile due to weaker p_z orbital overlap. Therefore, the HOMO of organic semiconductors stems from electrons in π bonds. Organic semiconductors are divided into two categories: small molecules and polymers. While in a single small molecule, the energetic levels of the HOMO and LUMO are single states, band-like energy levels separated by a band gap (E_g) are observed for small molecules in crystalline domains and polymers, as were described previously in **Figures 2.2** and **2.3**. In the case of small molecules in crystalline domains, this is due to intermolecular interactions. Polymers are very long molecules with a high number of atomic orbitals that interact, resulting in broad energy bands.

While inorganic materials such as silicon form a very tight crystalline lattice due to the covalent bonding between atoms, molecular crystals are structures held together by relatively weak forces: van der Waals interactions and hydrogen bonds, resulting result from the attraction between dipoles on different molecules. [12] Consequently, organic molecules are separated by a greater distance than atoms within an inorganic crystal. Furthermore, organic molecules do not have a perfect symmetry like atoms in inorganic lattices. Therefore, within a molecular crystal, charge transport is affected by the directionality of molecules in regards to the applied electric field. An example is given in **Figure 2.5**, where the observed mobility of charges was dependant on the orientation of the crystal. The largest observed mobility was along the b-axis. While for a perfect mono-crystal, the orientation would always be the same in the whole crystal, a polycrystalline solid consists of multiple crystalline domains with different molecular orientations, with different charge transport characteristics.

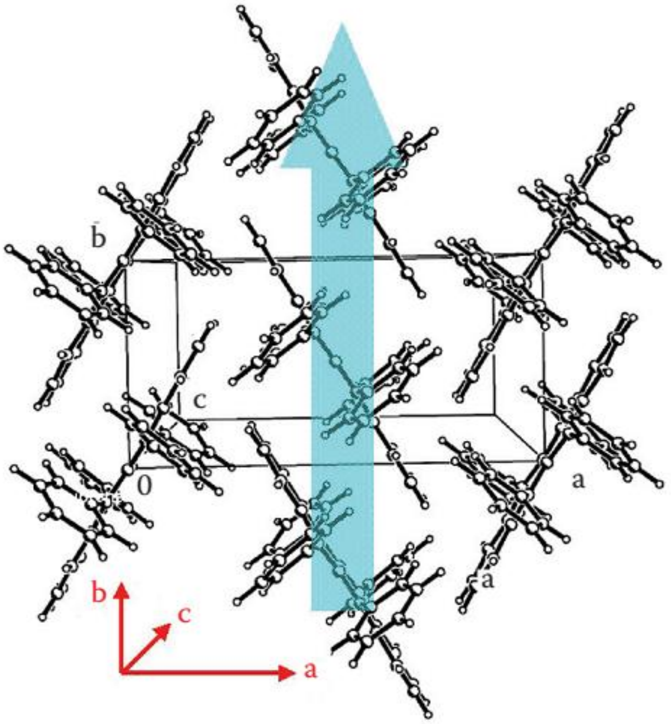

Figure 2.5: Packing of molecules in rubrene crystals. The crystal facets used for the FET fabrication correspond to the a–bcrystallographic plane. Reproduced from Sundar et al. [13]

Therefore, 3 types of charge transport are present in polycrystalline organic semiconductors: intra-molecular, inter-molecular and inter-grain transport (**Figure 2.6**). Charges travel through the molecule, by delocalization of an electron within a conjugated system. In that case, charge transport is highly related to the orientation of the molecule compared to the electric field. [14] In order to move from one molecule to the next, charges need to cross a gap in the material. This effect is called hopping. In the case or inter-molecular transport within a crystalline domain, the covered distances are relatively small (below 1 nm). Nevertheless, the hopping aptitude is variable and not only depends greatly on the distance but also on the alignment and interactions between the molecules. [15] The third type of charge transport, inter-grain transport, is the hopping of charges between crystalline domains. It is dependent on the general crystallinity of the material. In general for charges to be mobile, crystalline “islands” should not be separated by wide gaps without (semi)conducting material. Ideally, the whole solid should be a single crystal for optimal charge transport, without defects or amorphous regions.

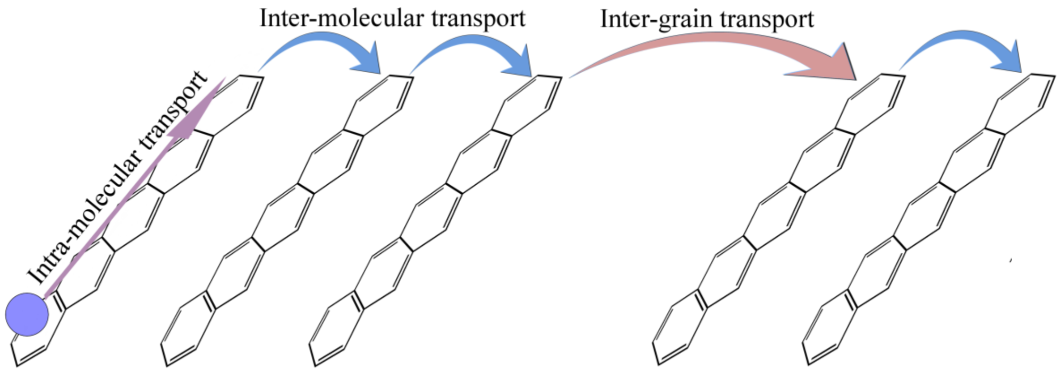

Figure 2.6. Intra-molecular, inter-molecular and inter-grain charge transport. Example for pentacene.

2.2.5. *p-type and n-type organic semiconductors*

Organic semiconductors can in principle transport both holes and electrons within their conjugated system. Their ability to transport either holes or electrons is dependent on their specific molecular structure, the different chemical groups attached on their conjugated backbone. A molecule such as pentacene, substituted with multiple electron donor hydrogen atoms, will have a highly electronegative conjugated system, leaving much affinity for holes, leading to *p*-type transport ability. Conversely, the same molecule substituted with strongly electron-withdrawing fluorine groups instead of hydrogen atoms (perfluoropentacene), will be favorable for electron transport. [16]

Nevertheless, most of the semiconducting organic materials operate in the *p*-type mode, and examples of n-type operation with good charge transport characteristics are relatively rare. [17] This "asymmetry" between *n*- and *p*-type carriers is due to several reasons: the HOMO bandwidth being typically larger than the LUMO bandwidth, [18] a stronger trapping of n-type polarons, [19] and a larger Schottky barrier for electron injection into organic semiconductors from the most commonly used high work function metals, which will be discussed in section *2.3*.

2.2.6. *The polaron model*

While the polaron model was introduced first for inorganic semiconductors, [20-22] it was later extended by Holstein and by Fesser et al. to molecular crystals and conjugated polymers. [23,24] Charge transport in organic semiconductors can be described by the concept of small polarons, the electronic states resulting from interaction of charge with lattice polarization at a length scale comparable to the lattice constant. [25-27] A charge carrier residing on a molecular site tends to polarize its neighboring region. As the resulting formed polarization cloud moves with the charge, the traveling entity is no longer a naked charge, but a polaron: a charge carrier together with the induced polarization, considered as one entity. In organic conjugated solids, they result from the deformation of the conjugated chain under the action of the charge.

The stability of the polaron is dependent on two factors: the average residence time of a charge on a molecule and the time necessary for the polarization cloud to form around the charge. The residence time is dependent on the width of the allowed energetic band where the charge resides, while polarization time is correlated with the energy of an electron transistion (the energy of the band gap). While the polarization time is similar for inorganic and organic structures (estimated in the order of 10^{-15} s), the residence time in molecular systems is estimated to be greater by two orders of magnitude compared to their inorganic counterparts (10^{-14} s v. 10^{-16} s), due to the much narrower bands of organic molecules. As a consequence, in inorganic systems, charge carriers move so fast that the polarization cloud does not have enough time to form. Conversely, in molecular solids, the electronic polaron has enough time to form, and the energy levels of a charged molecule are significantly shifted with respect to that of a neutral molecule.

2.2.7. Defects in the semiconductor crystal: the multiple trap-and-release model

Defects present in organic crystals create localized electronic states in the HOMO–LUMO gap, that can act as traps for charges. The effect of these states on charge transport depends on their energy. Two cases are considered. First, if the energy of a localized state is close to the energetic level of the HOMO or LUMO band (within a few k_BT, k_B being the Boltzmann constant), respectively for *p*-type and *n*-type transport, these states act as shallow traps. A polaron trapped in a shallow trap, which is characterized with a finite trapping time, τ, can be thermally activated and released into the band. Conversely a localized state further away from the HOMO or LUMO act as a deep trap, and a polaron that is trapped in this state cannot be release by thermal excitations. Shallow and deep traps are illustrated in **Figure 2.7**.

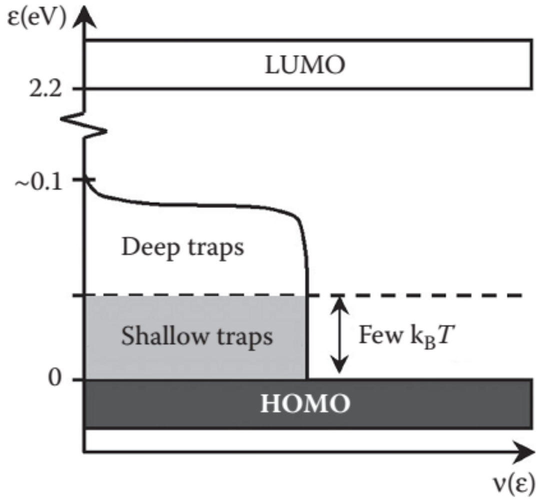

Figure 2.7: Schematic diagram of the energy distribution of localized electronic states, in the energy gap between the HOMO and LUMO bands in the rubrene single-crystal OFETs. Reproduced from Podzorov et al. [28]

The effect of shallow traps on the channel conductivity can be described by the Multiple Trap and Release (MTR) model. [29] The Multiple Trapping and Release model was first developed by Shur and Hack [30] to describe charge transport in hydrogenated amorphous silicon, and later extended to organic semiconductors by Horowitz et al. [31,32] In this model, mobile charges can be momentary trapped by shallow traps, the number being correlated with the density of traps and the temperature. The description of the effect of trapping can be described using two approaches. First, it can be considered that all carriers that were field induced contribute to the current flow at any time, but their effective mobility (μ_{eff}) is reduced compared to a trap-free system (μ_0):

$$\mu_{eff} = \mu_0(T)\frac{\tau(\mathrm{T})}{\tau(\mathrm{T}) + \tau_{\mathrm{tr}}(\mathrm{T})} \qquad \textbf{Eq. 2.4}$$

with $\tau_{tr}(T)$ the average trapping time on shallow traps and $\tau(T)$ the average time that a polaron spends diffusively traveling between the consecutive trapping events. The other approach assumes that only a fraction of the field induced charge carriers (n_{eff}) are moving at any given moment, but these carriers are moving with a trap-free mobility:

$$n_{eff} = n\frac{\tau(\mathrm{T})}{\tau(\mathrm{T}) + \tau_{\mathrm{tr}}(\mathrm{T})} \qquad \textbf{Eq. 2.5}$$

These two approaches are equivalent for describing the conductivity σ in a material, which depends on a product of n and μ, and the distinction between these approaches can only becomes clear in the Hall effect measurements, in which the density and the intrinsic mobility of truly mobile carriers can be determined independently. From the first approach we can conclude that the intrinsic regime of conduction is only realized when $\tau >> \tau_{tr}$, where $\mu_{eff} \approx \mu_0$. In this case, the dependence σ(T) reflects the temperature dependence of the intrinsic mobility $\mu_0(T)$. Conversely, when $\tau << \tau_{tr}$, the transport is dominated by shallow trapping processes. It is to be underlined that in the MTR, all the trapping processes are temperature dependant, as shown in equations **2.4**. and **2.5**.

2.2.8. Marcus theory

The MRT model is an accurate depiction of charge transport in organic crystals, it applies to well-ordered materials, prototypes of which are vapor deposited small molecules like pentacene or oligothiophenes, where thermally activated charge transport is often observed. It is yet not reliable for disordered films. Hopping is a thermally activated tunneling of carriers between localized states. This means that charge carriers occupy one state at time and hop from a state to another one with a frequency depending on temperature. The rate limiting step is the intermolecular hopping between two adjacent molecules. In the absence of external forces, the rate, k, of electron or hole hopping between adjacent sites a and b (with respectrive energies ϵ_a and ϵ_b) can be described by the Marcus theory: [33]

$$k_{ab} = \frac{|V_{ab}|^2}{\hbar} \sqrt{\frac{\pi}{\lambda k_B T}}\, exp\left[-\frac{(\lambda + \epsilon_b - \epsilon_a)^2}{4\lambda k_B T}\right] \qquad \textbf{Eq. 2.6}$$

In **Eq. 2.6**, V_{ab} is the charge-transfer integral, λ is the reorganization energy, k_B is the Boltzmann's constant, T is the absolute temperature, and h is the Planck's constant. For a fixed T, the charge hopping rate k depends critically on two material parameters, namely, V_{ab} and λ.

The transfer integral V_{ab} is the electronic coupling factor. In organic semiconductors V_{ab} is strictly dependent on the overlapping of electronic states. Therefore, it is related to the supra-molecular interactions occurring between conjugated chains. Distance between stacked chains is a major factor governing the transfer integral and stronger interactions lead to an increased hopping rate. On the other hand, the reorganization energy λ is an intra-molecular property that is specific to every molecule. When a charge moves, reorganization occurs in the polymer, compensating the novel electronic structure of the molecule. From the equation, we notice that the transfer rate does not increase indefinitely with more favorable energy differences, the exponential term being maximal at $\Delta\epsilon = -\lambda$. In other words, the energy difference between sites should compensate the reorganization energy.

2.2.9. Variable range hopping transport in organic semiconductors

The Variable Range Hopping (VRH) model, as described by Vissenberg et al, [34] accounts for hopping in positionally and energetically disordered systems of localized states.

In a highly disordered organic solid, percolation theory developed by Hammersley in 1957 applies: within the material, several paths of molecules with the adequate intermolecular distance and orientation are present. Nevertheless, a large portion of the material is not perfectly connected in all directions. Hopping only accounts for charge transport governed by the thermally activated tunneling of carriers between localized states. Variable range hopping, on the other hand states that a carrier may either hop over a small distance with high activation energy or hop over a long distance with a low activation energy.

In Vissenbergs VRH model, the conductivity σ is dependent not only on the effective temperature (T_0), number of states per unit volume (N_t), fraction of the localized state occupied by a carrier (δ) and molecular overlap governing the thermally actived tunneling process between two localized states (α), but also the critical number of bonds per site in the percolation network (B_c):

$$\sigma(\delta, T) = \sigma_0 \left(\frac{\pi \, N_t \, \delta \, (T_0/T)^3}{(2\alpha)^3 \, B_c \, \Gamma(1 - T/T_0)\Gamma(1 + T/T_0)} \right)^{T_0/T} \qquad \textbf{Eq. 2.7}$$

2.2.10. Charge transport in polymers

Conjugated polymers are organic macromolecules that consist of tens to hundreds of covalently bound molecular building blocks that are arranged in a chainlike structure. Evidently, conjugated polymeric semiconductors differ greatly from small molecules, as their length is orders of magnitude larger. The elastic arrangement of molecules in their backbone supports collective vibration modes, phonons. The electronic structure of polymers is a consequence of the interplay between π-

electron delocalization along the polymer backbone and strong electron-phonon coupling. The electron-phonon coupling corresponds to the induced electron-lattice induced vibrations.

In a perfectly straight polymer chain, the HOMO and LUMO states of the neutral polymer would be fully delocalized along the polymer chain and exhibit significant broadening with estimated bandwidths of several electron volts. [35] However, as a result of the strong electron-phonon coupling and the disorder-induced finite conjugation length, charges introduced into the polymer interact strongly with certain molecular vibrations and are able to lower their energy with respect to the extended HOMO/LUMO states by forming localized polaron states surrounded by a region of molecular distortion. [36]

Polymer chains are semi-flexible: rigid at length scales comparable to their persistence length and flexible at larger length scales. Conjugated polymer chains have many degrees of conformational freedom and interact weakly with each other, resulting in complex microstructures in the solid state. If the spacing between neighboring crystallites is only a few persistence lengths, a chain that exits one ordered region and enters another does not suffer large bends in its backbone and retains significant conjugation. In the polymeric solids heterogeneous microstructures, the ordered regions are largely responsible for charge transport, since charges must overcome an energy barrier to move from ordered to amorphous regions [37] as represented in **Figure 2.8**. Owing to its reduced conjugation length, the amorphous fractions of polymers have a larger bandgap compared to the crystalline aggregates. This energetic offset hinders carrier migration into the amorphous regions, and it is energetically and statistically favorable for charges at the order/disorder interface to migrate back into the ordered regions. Considering that charge transfer is favored in the crystalline domains, and charge transport is mostly realized within the chains of the polymer, two important factors are to be considered: the crystallinity and the nature of the chain (length, rigidity). [38]

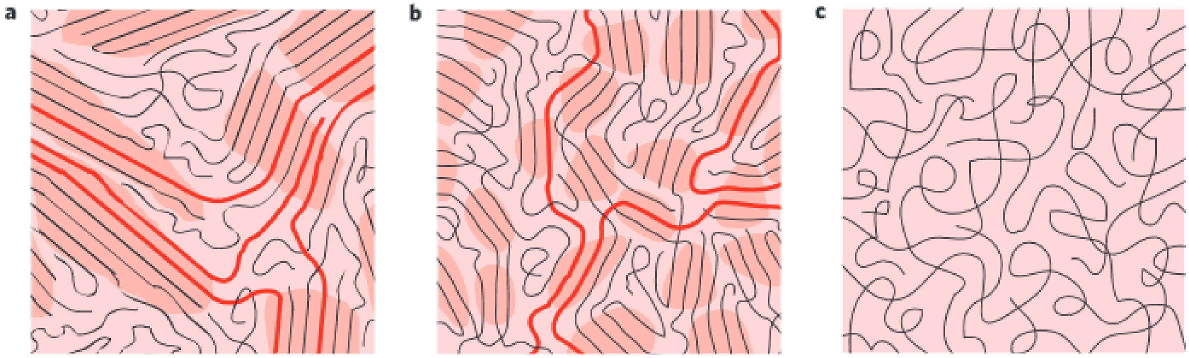

Figure 2.8: **Schematics of the microstructure of the polymer P3HT** (a) semi crystalline polymer film, (b) disordered aggregates, and (c) a completely amorphous film. Figure reproduced from Noriega et al. [37]

2.3. *Interfaces*

2.3.1. *Metal-semiconductor junctions*

Charge carriers may travel through a junction, from one material to another. It is for instance possible to inject charges from a metal (the source) into a semiconductor, and back into a metal again (the drain), by applying an electrical potential between source and drain. The interface energy barrier is given by the energy offset between the molecular orbital of the semiconductor and the Fermi-level of the metal. Before contact, both the metal and semiconductor are in their normal state and their Fermi-levels are misaligned. Upon contact, the work function of the metal and the ionization energy of the semiconductor align. [39,40] In the case of the work function of the metal higher than the IE of the semiconductor, electrons will flow from the semiconductor into the metal, lowering the semiconductor Fermi-level (depletion). Conversely, a lower W_f will result in the decrease of the Fermi-level of the metal (accumulation), by electron-flow from the metal to the semiconductor. [41] The difference between the vacuum level of the semiconductor and conduction band is the electron affinity χ (**Figure 2.9**).

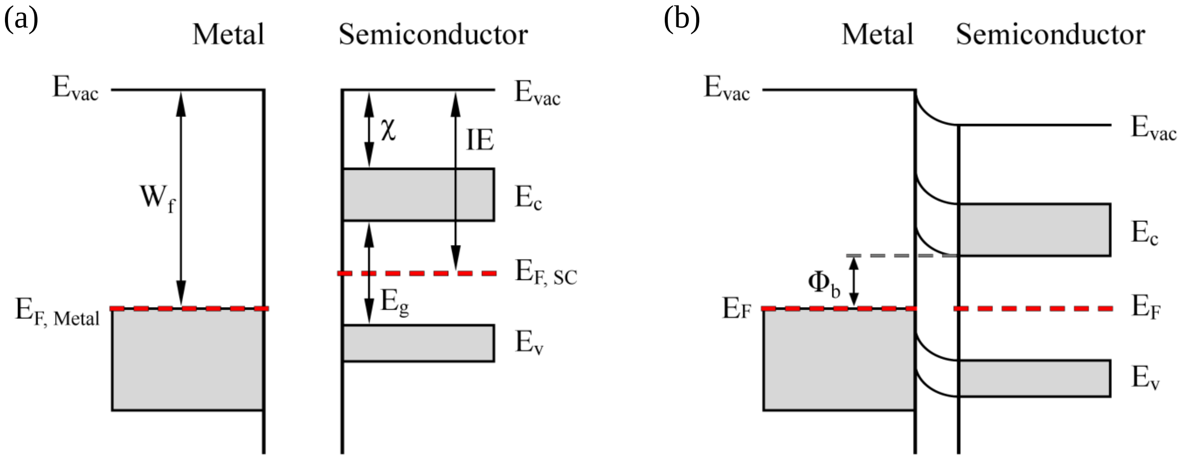

Figure 2.9: Metal/semiconductor junction, example for $W_f > IE$. (a) Energy diagram of a metal and a semiconductor, not joined. (b) Energy diagram of the same metal and semiconductors after junction.

If a gap is present between the surface of the metal and the surface of the semiconductor, the exchanged charges will create an electric field within the gap. Upon closing the gap, the vacuum levels of both sides mismatch. The energy barrier Φ_b (Shottky barrier) is the energy a charge carrier needs to move from the E_F of the metal into the conduction band of the semiconductor:

$$\Phi_b = E_C - E_F \qquad \textbf{Eq. 2.8}$$

Three possible configurations are conceivable depending on the energy levels of the metal and semiconductor: W_f > IE, W_f = IE and W_f < IE. In the first case, due to electron depletion, the contact region is unable to supply enough charge carriers to the bulk of the semiconductor, and the contact is injection-limited for electrons. On the other hand, there is a hole surplus in the contact region so the metal is able to provide any charge flow required by the bulk of the semiconductor (ohmic contact for holes). If W_f and IE are equal, the Fermi levels are already aligned and no charge redistribution is needed (neutral contact). In the third case, the electrons are accumulated in the semiconductor (Ohmic contact for electrons). As a result, in order to facilitate injection of electrons from a metal into a semiconductor, a metal with a work function lower than the IE of the semiconductor is recommended. In the case of hole injection into the semiconductor, a metal W_f higher than the IE of the semiconductor is preferred.

2.3.2. Tuning the energy levels of a metal surface with self-assembled monolayers

As described above, depending on the work function of the metal and the IE of the semiconductor, hole or electron transport can be favored or hindered. We have seen that in order to increase the n-type conduction, a metal with a low work function is preferable; while a high work function is better for *p*-type conduction. This can be arranged by the choice of the right metal. For example, a metal with a high work function such as gold ($W_f \approx$ 4.7-5 eV) is often selected to be used with *p*-type semiconductors. Nevertheless, the selected metal should be easily processable and inert, leaving often few possibilities, and the IE of the semiconductor could still be superior to the work function of the metal. In order to face these injection problems, the metal can be functionalized by chemisorption of Self-Assembled Monolayers (SAMs) on the surface. Among SAMs, thiolated molecules are widely used for the functionalization of a gold surface. [42,43] The growth of the monolayer can be produced by immersion of the metal layer into a solution containing the thiol-substituted molecules to be chemisorbed. As the thiol groups approach the surface, the sulfur forms a chemical bond with the gold, and the chemisorbed molecules lie down on the surface of the gold layer. Once the substrate is fully covered, a “nucleation” phase starts where molecules tilt-up, creating islands with a dense phase of upright molecules. Other thioated molecules of the solution bond with the metal, leading to a dense monolayer. [44,45] While the coverage can be homogeneous upon the whole surface, the formation of areas with different orientations can be observed, especially if the SAM covered metal is defect-rich. [46]

The formation of a self-assembled monolayer has great impact on the surface of the metal, and varies depending on the chemisorbed molecule. Depending on the interaction of the SAM with a solution deposited on it, the wettability can be tuned. [47,48] Furthermore, the ability to stack molecules in crystals over the metal can be affected by the SAM. [49] In terms of injection, two major effects derive from the formation of a monolayer on the metal. First, the SAM represents a layer of often non-conductive molecules that act as a gap between the source and the semiconductor, as illustrated in **Figure 2.10**. An additional potential due to the gap between metal and semiconductor that need to be overcome by the electrons emerges from the dipole moment between metal and SAM. The second effect is a modification of the work function of the metal due to the formation of the metal-SAM bond. The bond dipole is strongly dependent on the chosen metal so for a given fixed metal, the work function shift is mostly defined by molecular dipole. [50] Therefore, by careful selection of the chemical function on the SAM it is possible to increase or decrease the work function of the metal. [51]

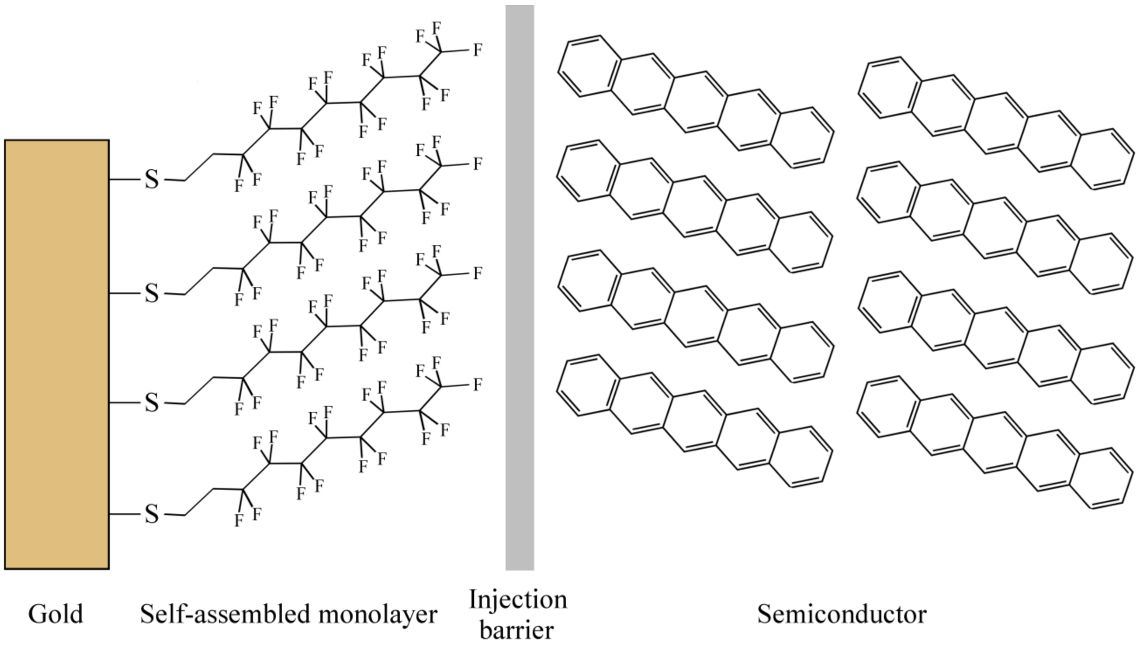

Figure 2.10: Cartoon illustrating a metal-semiconductor junction. Illustration for gold functionalized with a self-assembled monolayer of fluorinated alkanethiols.

The chemisorption of a SAM on a metal adds an insulating barrier that charges must overcome to be injected in the semiconductor. The physical process that allows charges to overcome the barrier is tunneling, and a longer distance to cover is synonym of a larger tunneling resistance R_t. Naturally, the tunneling resistance is also dependent on the chemical nature of the backbone of the chemisorbed molecule. Consequently, the tunneling resistance is defined by:

$$R_t = R_0 e^{-\beta L} \qquad \textbf{Eq. 2.9}$$

with R_0 the effective contact resistance, L the thickness of the SAM and β the exponential factor associated with the nature of the molecular backbone of the molecule chemisorbed on the metal. In summary, the optimal SAM for charge injection should be as short and tightly packed as possible, with the appropriate functions to shift the work function of the metal.

2.3.3. Charge transport at the semiconductor-dielectric interface

When an electric field is applied on a semiconductor through a dielectric, charge carriers present in the semiconductor will travel towards the dielectric. The affected charges will depend on the potential that is applied, with holes moving towards negative potential and electrons towards positive potential. Charge carriers will therefore accumulate at the interface between dielectric and semiconductor, and this region will be the location of most of the charge transport. In order to optimize electrical performances, it is of capital importance to create a dielectric surface that is adapted to charge transport. While the obvious approach is to decrease surface roughness and remove adsorbed impurities that could interfere with charge transport, the use of SAMs on the dielectric surface can also provide improvements in the mobility of charges. The formation of a SAM on a dielectric is similar to the process described for metal functionalization. The adequate SAM on a dielectric can impact the crystallization process of the semiconductor through modification of the wettability and modification of the surface energy. In the case of the commonly used dielectric silicon dioxide (SiO_2), molecules are chemisorbed on the surface using silane or silazane groups. [52]

2.4. Effect on impurities in the semiconductor: Doping and trapping

If the semiconductor is in direct proximity of a second material, charges present in the semiconductor might interact with it. Charge carrier trapping is the transfer of a charge carrier from the delocalized states of the semiconductor to a localized state in the second material. [53] The trap states can be localized within the semiconductor, on an unsaturated bond of an atom at the semiconductor-dielectric interface, or within the surrounding environment. In order for a charge carrier to be trapped into a molecule, the process has to be energetically favorable. For electrons, charges will only flow in the trap if the LUMO of the trap is lower than the LUMO of the semiconductor. Conversely, holes will be trapped if the HOMO of the trap is higher than the HOMO of the semiconductor.

Doping refers to the introduction of small quantities of impurities into a material in order to tune its electrical properties. Doping is commonly used for inorganic semiconductors. In the case of silicon, small quantities of electron acceptors (such as boron) can be used for *p*-type doping, while small quantities of electron donors (such as phosphorus) can be introduced for *n*-type doping. [54] Upon addition of these impurities, some energy states within the band gap can be allowed: donor impurities create states near the conduction band while acceptor impurities add states close to the valence band. [55] These additional states lead to better conduction in the material for the target type of transport. In organic semiconductors, doping is performed by oxidation or reduction of the semiconductor by addition of chemical reactants in order to favor the generation of charge carriers. Compared to inorganics, doping in molecular materials occurs by addition of much larger quantity of dopants. The presence of oxygen can lead to oxidative doping of an organic semiconductor, resulting in increased charge carrier concentration and reduced charge transport characteristics. [56] In order to avoid oxygen doping, organic materials are usually tested in an oxygen-free environment.

2.5. Conclusions

In this chapter, charge carrier transport in solid materials was discussed. Energy levels of materials were considered for the classification of solids into categories depending on their electrical features. We have determined the ideal conditions for charge transport within organic semiconductors and concluded that organic small molecules should be tightly packed in large crystalline domains, while polymers benefit greatly from smaller domains where charge carriers hop from one chain to the next. Upon discussion regarding charge injection from one material to another, we have determined that the HOMO and LUMO levels should be carefully considered, and that it is possible to tune the energetic levels of surfaces through functionalization with self-assembled monolayers. The impact of the presence of impurities in or at the interface of a semiconductor was reviewed. It was determined that while charge trapping and doping were often detrimental effects, those effects can be controlled.

2.6. References

1 Shi, X., Li, L., Evans, C. M. & Findley, G. L. Energy of the quasi-free electron in argon, krypton and xenon. *Nucl. Instrum. Meth. A.* **582**, 270-273 (2007).

2 Lin, C. C. & Anderson, L. W. Studies of Electron-Excitation of Rare-Gas Atoms into and out of Metastable Levels Using Optical and Laser Techniques. *Adv. Atom. Mol. Opt. Phy.* **29**, 1-32 (1991).

3 Brookes, N. J., Ariafard, A., Stranger, R. & Yates, B. F. Reactivity of CO2 towards Mo[N(R)Ph](3). *Dalton Trans.*, 9266-9272 (2009).

4 Hoddeson, L. H. & Baym, G. The Development of the Quantum-Mechanical Electron Theory of Metals - 1900-28. *P. Roy. Soc. A* **371**, 8-23 (1980).

5 Chakraborty, P. K., Biswas, S. K. & Ghatak, K. P. On the modification of the Fermi-Dirac distribution function in degenerate semiconductors. *Physica B* **352**, 111-117 (2004).

6 Bieri, G., Burger, F., Heilbronner, E. & Maier, J. P. Valence Ionization Energies of Hydrocarbons. *Helv. Chim. Acta.* **60**, 2213-2233 (1977).

7 Rana, F. Electron-hole generation and recombination rates for Coulomb scattering in graphene. *Phys. Rev. B* **76** (2007).

8 Irie, T., Endo, S. & Kimura, S. Electrical-Properties of P-Type and N-Type Cuinse2 Single-Crystals. *Jpn J. Appl. Phys.* **18**, 1303-1310 (1979).

9 Black, C. T. & Welser, J. J. Electric-field penetration into metals: Consequences for high-dielectric-constant capacitors. *IEEE T. Electron. Dev.* **46**, 776-780 (1999).

10 Resta, R. Macroscopic Polarization in Crystalline Dielectrics - the Geometric Phase Approach. *Rev. Mod. Phys.* **66**, 899-915 (1994).

11 Farges, J. P. *Organic Conductors: Fundamentals and Applications*. (CRC Press, 1994).

12 Goodwin, A. L. Organic Crystals Packing Down. *Nat. Mater.* **9**, 7-8 (2010).

13 Sundar, V. C. *et al.* Elastomeric transistor stamps: Reversible probing of charge transport in organic crystals. *Science* **303**, 1644-1646 (2004).

14 Kinder, L., Kanicki, J., Swensen, J. & Petroff, P. Structural ordering in F8T2 polyfluorene thin-film transistors. *P. Soc. Photo-Opt. Ins.* **5217**, 35-42 (2003).

15 Liu, L. *et al.* The relationship between intermolecular interactions and charge transport properties of trifluoromethylated polycyclic aromatic hydrocarbons. *Org. Electron.* **15**, 1896-1905 (2014).

16 Sakamoto, Y. *et al.* Perfluoropentacene: High-performance p-n junctions and complementary circuits with pentacene. *J. Am. Chem. Soc.* **126**, 8138-8140 (2004).

17 Gao, X. K. & Hu, Y. B. Development of n-type organic semiconductors for thin film transistors: a viewpoint of molecular design. *J Mater Chem C* **2**, 3099-3117 (2014).

18 da Silva, D. A., Kim, E. G. & Bredas, J. L. Transport properties in the rubrene crystal: Electronic coupling and vibrational reorganization energy. *Adv. Mater.* **17**, 1072-+ (2005).

19 Karl, N. *Charge-carrier mobility in organic crystals, in Organic electronic materials*. 283-326 (Springer-Verlag, 2001).

20 Yamashita, J. & Kurosawa, T. On electronic current in NiO. *J. Phys. Chem. Solids* **5**, 34-43 (1958).

21 Pekar, S. I. Issledovanija po Elektronnoij Teorii Kristallov. *gostekhizdat moskva* (1951).

22 Landau, L. D. Über die Bewegung der Elektronen in Kristalgitter. *Phys. Z. Sowjetunion* **3**, 644-645 (1933).

23 Fesser, K., Bishop, A. R. & Campbell, D. K. Optical-Absorption from Polarons in a Model of Polyacetylene. *Phys. Rev. B* **27**, 4804-4825 (1983).

24 Holstein, T. Studies of polaron motions - part i: the molecular crystal model. *Ann. Phys.* **8**, 325-342 (1959).

25 Holstein, T. Polaron motion. II. "Small" polaron. *Ann. Phys.* **8**, 343 (1959).

26 Pope, M. & Swenberg, C. E. *Electronic processes in organic crystals and polymers, 2nd ed.*, (Oxford University Press, 1999).

27 Silinsh, E. A. & Apek, V. *Organic molecular crystals: Interaction, localization and transport phenomena*. (AIP Press, 1994).

28 Podzorov, V. *et al.* Intrinsic charge transport on the surface of organic semiconductors. *Phys. Rev. Lett.* **93** (2004).

29 Horowitz, G. Organic thin film transistors: From theory to real devices. *J Mater Res* **19**, 1946-1962 (2004).

30 Shur, M. & Hack, M. Physics of Amorphous-Silicon Based Alloy Field-Effect Transistors. *J Appl Phys* **55**, 3831-3842 (1984).

31 Horowitz, G., Hajlaoui, M. E. & Hajlaoui, R. Temperature and gate voltage dependence of hole mobility in polycrystalline oligothiophene thin film transistors. *J Appl Phys* **87**, 4456-4463 (2000).

32 Horowitz, G., Hajlaoui, R. & Delannoy, P. Temperature-Dependence of the Field-Effect Mobility of Sexithiophene - Determination of the Density of Traps. *J Phys Iii* **5**, 355-371 (1995).

33 Marcus, R. A. Electron-Transfer Reactions in Chemistry - Theory and Experiment. *Rev. Mod. Phys.* **65**, 599-610 (1993).

34 Vissenberg, M. C. J. M. & Matters, M. Theory of the field-effect mobility in amorphous organic transistors. *Phys. Rev. B* **57**, 12964-12967 (1998).

35 van der Horst, J. W., Bobbert, P. A., Michels, M. A. J., Brocks, G. & Kelly, P. J. Ab initio calculation of the electronic and optical excitations in polythiophene: Effects of intra- and interchain screening. *Phys. Rev. Lett.* **83**, 4413-4416 (1999).

36 Bredas, J. L., Beljonne, D., Coropceanu, V. & Cornil, J. Charge-transfer and energy-transfer processes in pi-conjugated oligomers and polymers: A molecular picture. *Chem. Rev.* **104**, 4971-5003 (2004).

37 Noriega, R. *et al.* A general relationship between disorder, aggregation and charge transport in conjugated polymers. *Nat. Mater.* **12**, 1037-1043 (2013).

38 Sirringhaus, H. *et al.* Two-dimensional charge transport in self-organized, high-mobility conjugated polymers. *Nature* **401**, 685-688 (1999).

39 Ishii, H. *et al.* Kelvin probe study of band bending at organic semiconductor/metal interfaces: examination of Fermi level alignment. *Phys. Status Solidi A* **201**, 1075-1094 (2004).

40 Zhang, Z. & Yates, J. T. Band Bending in Semiconductors: Chemical and Physical Consequences at Surfaces and Interfaces. *Chem. Rev.* **112**, 5520-5551 (2012).

41 Lange, I. *et al.* Band Bending in Conjugated Polymer Layers. *Phys. Rev. Lett.* **106** (2011).

42 Harder, P., Grunze, M., Dahint, R., Whitesides, G. M. & Laibinis, P. E. Molecular conformation in oligo(ethylene glycol)-terminated self-assembled monolayers on gold and silver surfaces determines their ability to resist protein adsorption. *J. Phys. Chem. B* **102**, 426-436 (1998).

43 Tour, J. M. *et al.* Self-Assembled Monolayers and Multilayers of Conjugated Thiols, Alpha,Omega-Dithiols, and Thioacetyl-Containing Adsorbates - Understanding Attachments between Potential Molecular Wires and Gold Surfaces. *J. Am. Chem. Soc.* **117**, 9529-9534 (1995).

44 Kumar, A., Biebuyck, H. A. & Whitesides, G. M. Patterning Self-Assembled Monolayers - Applications in Materials Science. *Langmuir* **10**, 1498-1511 (1994).

45 Sellers, H., Ulman, A., Shnidman, Y. & Eilers, J. E. Structure and Binding of Alkanethiolates on Gold and Silver Surfaces - Implications for Self-Assembled Monolayers. *J. Am. Chem. Soc.* **115**, 9389-9401 (1993).

46 Vericat, C., Vela, M. E., Benitez, G., Carro, P. & Salvarezza, R. C. Self-assembled monolayers of thiols and dithiols on gold: new challenges for a well-known system. *Chem. Soc. Rev.* **39**, 1805-1834 (2010).

47 Lee, B. S. *et al.* Imidazolium ion-terminated self-assembled monolayers on Au: Effects of counteranions on surface wettability. *J. Am. Chem. Soc.* **126**, 480-481 (2004).

48 Biebuyck, H. A. & Whitesides, G. M. Self-Organization of Organic Liquids on Patterned Self-Assembled Monolayers of Alkanethiolates on Gold. *Langmuir* **10**, 2790-2793 (1994).

49 Clevenger, M. B., Zhao, J. N. & McDevitt, J. T. Use of a self-assembled monolayer for the preparation of crystalline organic superconductor high-T-c superconductor structures. *Chem. Mater.* **8**, 2693-& (1996).

50 Heimel, G., Romaner, L., Zojer, E. & Bredas, J. L. The interface energetics of self-assembled monolayers on metals. *Acc. Chem. Res.* **41**, 721-729 (2008).

51 Campbell, I. H. *et al.* Controlling charge injection in organic electronic devices using self-assembled monolayers. *Appl. Phys. Lett.* **71**, 3528-3530 (1997).

52 Ulman, A. Formation and structure of self-assembled monolayers. *Chem. Rev.* **96**, 1533-1554 (1996).

53 Cordones, A. A. & Leone, S. R. Mechanisms for charge trapping in single semiconductor nanocrystals probed by fluorescence blinking. *Chem. Soc. Rev.* **42**, 3209-3221 (2013).

54 Zhang, S. B., Wei, S. H. & Zunger, A. Intrinsic n-type versus p-type doping asymmetry and the defect physics of ZnO. *Phys. Rev. B* **63** (2001).

55 Umebayashi, T., Yamaki, T., Itoh, H. & Asai, K. Band gap narrowing of titanium dioxide by sulfur doping. *Appl. Phys. Lett.* **81**, 454-456 (2002).

56 Schafferhans, J., Baumann, A., Wagenpfahl, A., Deibel, C. & Dyakonov, V. Oxygen doping of P3HT:PCBM blends: Influence on trap states, charge carrier mobility and solar cell performance. *Org. Electron.* **11**, 1693-1700 (2010).

Chapter 3. Molecules and materials

3.1. Introduction: small molecules, oligomers, polymers

Two categories of molecules are used for organic electronics: small molecules and polymers. The former are monodispersed whereas the latter are polydispersed. As a result the former can more easily undergo aggregation forming crystalline architectures whereas the latter can also crystallize but only to a certain degree and are therefore often called semicrystalline. Upon solvent evaporation, crystalline lamellas of polymers are surrounded by amorphous regions. Polymers are characterized by a molecular weight (distribution). The processing methods of small molecules and polymers are different. Methods such as thermal evaporation are mostly reserved to small molecules, and in general, mono-crystals are specific to small molecules. Whether small molecule or polymer, the conjugated system is of paramount importance for charge transport, and is often based on a conjugated monomer, such as aromatic thiophene units. Since the synthesis of polythiophene was described in 1982, oligomers and polymers of thiophene derivatives have been extensively investigated. [1] Oligomers are molecules consisting of a few monomer units, while polymers usually contain from a few dozen to a few hundreds of monomers, leading to a very high molecular weight of tens of kDa.

This chapter will focus on the description of the small molecules and polymers used in the thesis. It will review *p*-type and *n*-type semiconductors, as well as photochromic molecules. Furthermore, processing from the solution will be discussed in terms of blending and solubility, and phase segregation will be considered.

3.2. Studied semiconductors

3.2.1. Oligothiophenes

Oligothiophenes (OTs) represent one of the most promising classes of semiconductive materials for field-effect transistor fabrication owing to their charge transport characteristics and environmental stability.[2-4] However, unsubstituted OTs are insoluble in the usual solvents and can be deposited only by vacuum evaporation, which is slow, expensive and hardly applicable for large scale production. The high charge mobility and poor solubility of oligothiophenes is linked to the great molecular ordering and side-by-side stacking of aromatic molecules. It was demonstrated that the introduction of hexyl groups in the α- and ω-positions (see **Figure 3.1**) leads to an increase of solubility (good solubility for α-,ω-dihexylbithiophene, DH2T, and α-,ω-dihexylquaterthiophene, DH4T, but less than 1 mg/mL for α-,ω-dihexylsexithiophene, DH6T).[5] Solubility of sexithiophene could be further improved by functionalization via hexyl groups in the β-position, but films based on β-,β‘-DH6T were completely amorphous and the charge transport ability was greatly reduced.[6] Thefore, the studied molecules in this theses were DH2T, DH4T and DH6T, in their α-,ω-hexyl substituted form.

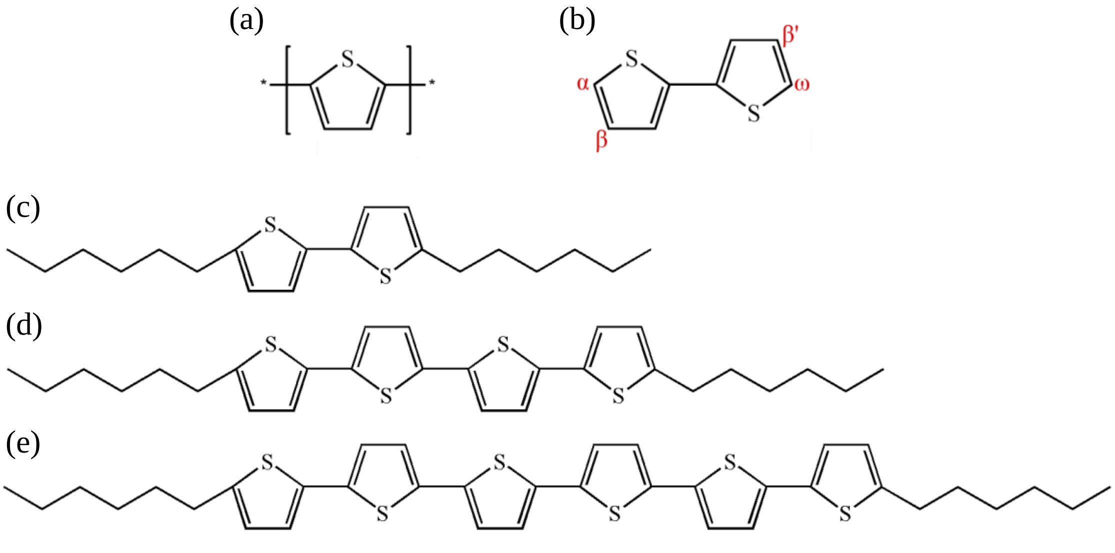

Figure 3.1: Thiophene oligomers and hexyl-terminated thiophene oligomers. (a) Thiophene monomer. (b) Bithiophene with α-, β-, ω- and β‘- substitution sites. (c) α-,ω-dihexylbithiophene (DH2T). (d) α-,ω-dihexyl-quaterthiophene (DH4T). (e) α-,ω-dihexylsexithiophene (DH6T).

3.2.2. Polymers

3.2.2.1. P3HT, a p-type semiconducting polymer

Small molecules, due to their high inclination to form crystalline lattices, have been widely investigated for organic field-effect transistors, and still yet retain the highest reported electrical characteristics to date. [7] But these materials are seriously challenged by longer polymeric chains that exhibit interesting mechanical characteristics that could find many potential applications. Polymers with ability to transport holes are the most common semiconducting polymers. They include polymers based on long conjugated thiophene chains, alkyl-substituted for increased solubility (for example PQT-12 [8]), often with intercalated groups between thiophene units, such as thienothiophene in polymers like PBTTT-C14 [9]. Other intercalated groups include fluorine (in F8T2 [10]), carbazole (in PCB-R [11]) and cyclopentadithiophene (in PCPDT [12]), among many others.

Poly(3-Hexylthiophene) (P3HT, **Figure 3.2**) is a simple polymer based on the thiophene monomer substituted with a hexyl chain. It is a much studied and well established *p*-type semiconducting polymer. It is highly soluble and forms polycrystalline architectures consisting of crystalline domains surrounded by amorphous matrixes. The intermolecular distance is largely reduced in the crystalline domains, and hopping is therefore favored as compared to the amorphous areas of the film. Two major aspects of improvement of electrical performances of P3HT are the increase of the size of crystalline domains for facilitated inter-molecular transport and the increase of the length of the polymeric chains for improved intra-molecular transport. The ideal scenario would be a single P3HT crystal bridging the interelectrodic gap. In the case of a highly regioregular material, the interdigitated stacking of P3HT in crystalline domains is favored, and chain bending is inhibited. Therefore, highly regioregular P3HT with high molecular weight (50 kDa) has been used in the works presented in this thesis. The structure of P3HT films is very interesting for blending, as upon solvent evaporation, the other molecules tend to be expelled from the crystalline domains (where most hopping occurs) into the amorphous regions of the film. P3HT is a polymer with a very wide range of use in different applications, ranging from organic field-effect transistors to solar cells when blended with an *n*-type material such as PCBM. [13]

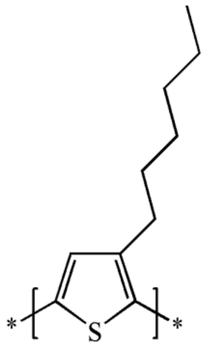

Figure 3.2: Chemical formula of Poly(3-Hexylthiophene).

3.2.2.2. *Other p-type semiconducting polymers*

While P3HT remains one of the most used *p*-type semiconductors for organic electronics and one of the more established building blocks for these applications, in the last few years several materials have successfully challenged it, by displaying greater electrical performances and air-stability. Among those, three are studied in this thesis: IIDDT-C3 (Poly[1,1'-bis(4-decyltetradecyl)-6-methyl-6'-(5'-methyl-[2,2'-bithiophen]-5-yl)-[3,3'-biindolinylidene]-2,2'-dione]), [14] PDVT-8 (poly[2,5-bis(2-octyldodecyl)pyrrolo[3,4-c]pyrrole-1,4(2H, 5H)-dione-alt 5,5′-di(thiophen-2-yl)-2,2′-(E)-2-(2-(thiophen-2-yl)vinyl)thiophene]) [15] and PCD-TPT (Poly[[1,2,5]thiadiazolo[3,4-c]pyridine-4,7-diyl(4,4-dihexadecyl-4H-cyclopenta[2,1-b:3,4-b']dithiophene-2,6-diyl)[1,2,5]thiadiazolo[3,4-c]pyridine -7,4-diyl(4,4-dihexadecyl-4H-cyclopenta[2,1-b:3,4- b']dithiophene-2,6-diyl)]) [16] (**Figure 3.3**). These polymers share some characteristics with P3HT, as they all contain thiophene groups in their conjugated systems and alkyl chains are present for improved solubility. IIDDT-C3 is based on an isoindigo core coupled to two thiophene groups. The combination of the electron-rich and electron-poor blocks is effective for increase π-π stacking between polymer chains, for an improved crystallinity in the solid phase. [17] Furthermore, the presence of the electron-rich thiophene groups compensates the isoindigo core and helps to increase the HOMO level of the polymer. A similar design is adopted in the polymer PDVT-8, pyrrolopyrroledione blocks separated by thiophene-based chains. PCD-TPT was designed for great rigidity with dihexadecylcyclopentadithiophene groups around the thiadiazolopyridine units. Interestingly, not only all these polymers proved better *p*-type semiconducting performances, they also exhibit some electron-transport properties, making them slightly ambipolar.

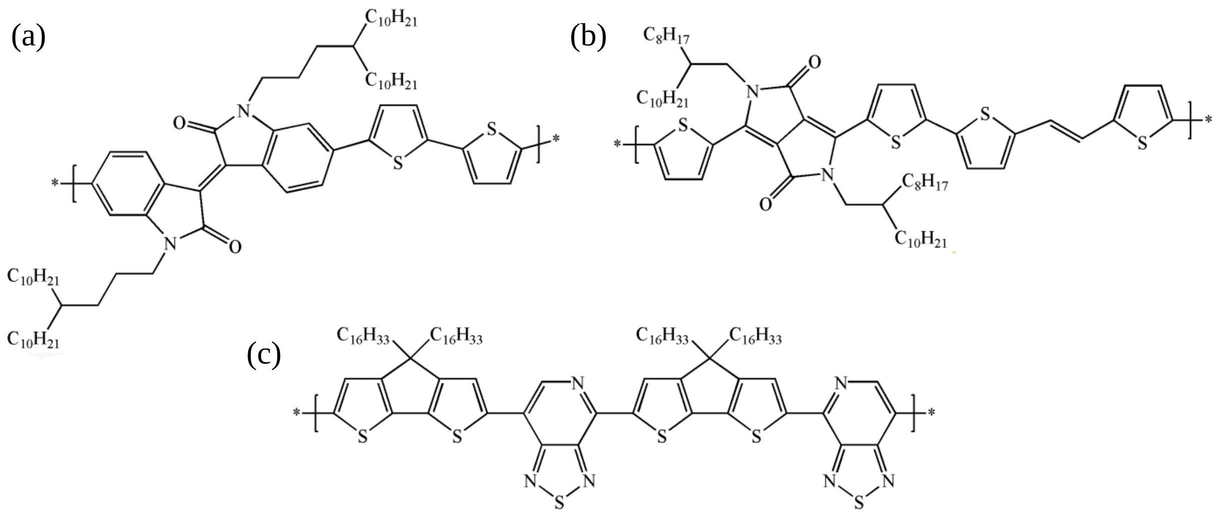

Figure 3.3: Chemical formulae of the studied *p*-type polymers. (a) IIDDT-C3. (b) PDVT-8. (c) PCDTPT.

3.2.2.3. P(NDI2OD-T2), an n-type semiconducting polymer:

The first discovered organic materials with semiconducting properties were all materials with hole transport capabilities. The main strategy followed by synthetic chemists for developing *n*-type organic semiconductors is to reduce the electron density along the π-conjugation in the neutral state. Functional groups such as fluorides, nitriles, amides and imides, are attached onto the π-conjugated backbone. Using this approach, low-lying LUMO and HOMO energy levels to efficiently inject electrons are obtained and, at the same time, molecules with low reorganization energy are stabilized. Nevertheless, *n*-type materials are still lacking behind their *p*-type counterparts, and most of the organic *n*-type semiconductors are small molecules. Well performing *n*-type polymers are still relatively rare. The best performing *n*-type polymers to date are based either on benzothiadiazole groups (for example F8BT [18]) and perylene diimides (for example PDIC8-EB [19]).

P(NDI2OD-T2) (poly[N,N'-bis(2-octyldodecyl)-naphthalene-1,4,5,8-bis(dicarboximide)-2,6-diyl]-alt-5,5'-(2,2'-bithiophene) (**Figure 3.4**) was selected as *n*-type semiconductor to be used in combination of the aforementioned *p*-type semiconductors for the work presented in chapter 7. The conjugated system is comprised of a naphthalene diimide core and two thiophene units. The aliphatic chains are tailored for optimal solubility and stacking, leading to one of the best performing *n*-type semiconductors. [20] While it is predominantly an *n*-type semiconductor, it has some very minor *p*-type charge transport capabilities.

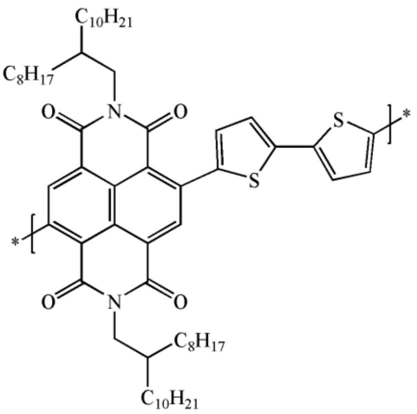

Figure 3.4: Chemical formulae of the studied *n*-type polymer P(NDI2OD-T2).

3.3. Photochromic molecules

Organic molecules differ greatly from inorganic systems. The wide variety of organic molecules exhibit specific characteristics, such as flexibility, transparency and solubility in various solvents. Among all features, their chemical reactivity is one of their most obvious yet remarkable, as it leaves much room for tunability of various physical and chemical properties including the electrical performances, as it was described previously with SAMs. A photochromic organic molecule is a chemical system that can change its state when subjected to illumination. [21] After irradiation at a specific wavelength, a reversible transformation occurs in the molecule affecting its geometry and/or conjugation. [22-24] As an example of these molecules, we can cite azobenzenes, which switch from the more linear *trans* isomer to the more bulky *cis* form when illuminated, leading to possible energetic changes. [25]

Diarylethenes are molecules composed of two aromatic substituents, bridged by an olefinic bond. More specifically, the typically used diarylethenes are bisthienylethenes. They are composed of two thiophene groups at each side of the olefinic bond, is rigidified by a cyclopentane unit, as illustrated in **Figure 3.5**. Upon irradiation with UV light, a bond is created by delocalization in the conjugated system, resulting in a modification of the energetic levels of its HOMO and LUMO. [22] The new form is stable but the photochromic molecule will return to its original state upon irradiation with visible light. Noteworthy, it is a bi-stable system: both forms are stable and the molecule can be synthesized in either one of the two forms. Furthermore, the molecules occupy a similar space in both forms; therefore, switching of the diarylethenes can be performed in a tightly packed solid.

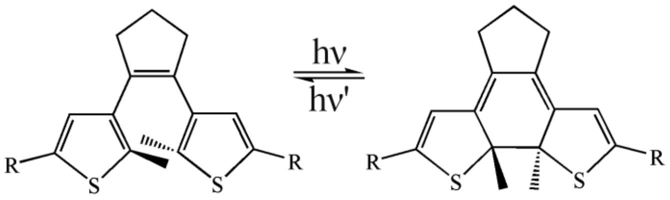

Figure 3.5: Chemical formula of the diarylethene's switchable core in its two stable forms.

If a semiconductor is in contact with the switchable molecules electronic or electrostatic interactions between the two systems can take place. In particular, charge carriers might get trapped into the switchable molecule, if it is energetically favorable. In the case of a switchable molecule with two HOMO levels for each form that are higher and lower than the HOMO level of the semiconductor, the switchable molecule might act as a trap for holes in one form and not the other, as described in **Figure 3.6**. Conversely, tunable LUMO levels can make a molecule switch from scattering center to charge trap for electrons. This effect can be exploited to tune the charge transport characteristics of a semiconductor upon irradiation at the adequate wavelengths.

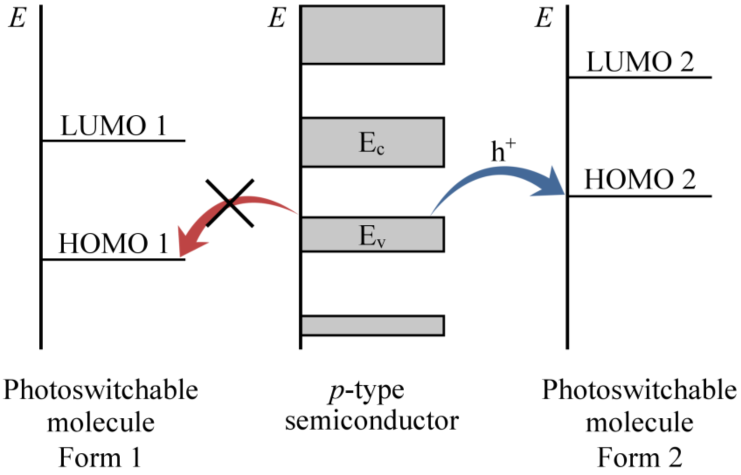

Figure 3.6: Diagram representing charge transfer from a semiconductor into a photoswitchable molecule.

3.4. Mixing components

While inorganic semiconductors for electronic applications are produced by growth from the pure molten material (with added dopant impurities), organic electronics are fabricated using evaporation techniques (only possible for small molecules) or deposited from the solution with techniques such as drop-casting, spin-coating, ink-jet printing, dip-coating and spray-coating, among others. When solution processed materials are considered, solubility and ability to blend should be examined. The basic thermodynamic relationship governing mixtures established by Gibbs is: [26]

$$\Delta G_m = \Delta H_m - T\Delta S_m \qquad \textbf{Eq. 3.1}$$

with ΔG_m the Gibbs free energy of mixing, ΔH_m the enthalpy of mixing ΔS_m the entropy of mixing and T the temperature. In order for spontaneous mixing to occur, ΔG_m should be negative. The enthalpy of mixing is always positive; therefore, in ideal solutions the components are always miscible in any proportions. An ideal solution is defined by mixing of small molecules where the cohesive interactions and the adhesive interactions are equal in strength: there is no enthalpy of mixing (ΔH_m= 0). A regular solution is a solution that diverges very little from an ideal solution. The entropy of mixing is considered equal to that of the ideal solution with the same composition, due to the lack of strong specific interactions. The enthalpy of mixing is nevertheless non-zero, and mixing will be favored only if $\Delta H_m < T\Delta S_m$. The miscibility of different components is dependent on the mixing ratio and intermolecular interaction and can be represented in phase diagrams, an example being given in **Figure 3.7**.

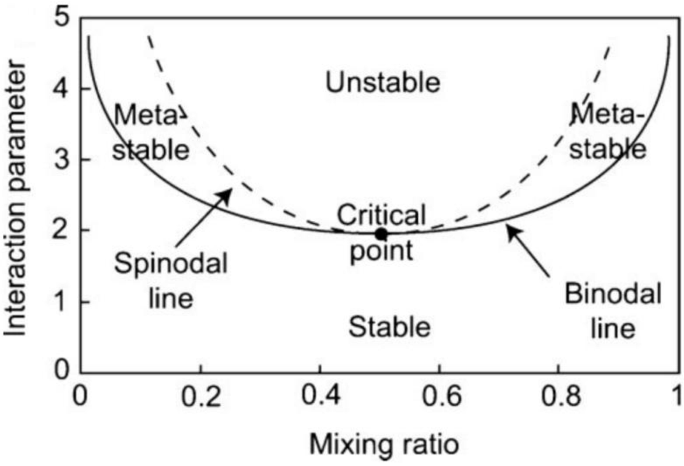

Figure 3.7: Phase diagram of a two-component blend as described by the regular solution model. Reproduced from Jones et al. [27]

In order to adequately describe solutions of small molecules with specific intermolecular interaction, group contribution theory can be applied. The different chemical functions of the molecules present in the blend will interact, and the sum of all interactions approximately corresponds to the global interactions, and the enthalpy can be evaluated. Considering mixing in terms of chemical functions is a very practical approach, since it opens the way for the design of molecules with particular chemical functions, that will favor or prevent blending or solubility in certain solvents. Organic semiconductors are often designed with intermolecular and molecule/solvent consideration, in order to favor solubility in organic solvents and packing.

Nevertheless, considering only the intermolecular interactions stemming from the functional groups of the molecules is insufficient for large molecules, such as polymers. The basic theory for estimating the miscibility of blends including polymers was developed by Flory and Huggins and is thus referred to as the Flory-Huggins theory. [28,29] The equation describing the Gibbs free energy of mixing resulting from their analysis is the Flory-Huggins equation:

$$\Delta G_m = k_b T V \left[\frac{\varphi_1}{V_1}\ln\varphi_1 + \frac{\varphi_2}{V_2}\ln\varphi_2\right] + \varphi_1\varphi_2\chi_{12}k_b T V/\nu_r \qquad \textbf{Eq. 3.2}$$

with V the total volume, V_i the molecular volume of component i, φ_i the volume fraction of component i, k_B Boltzmann's constant, χ_{12} the Flory-Huggins interaction parameter and υ_r the interacting segment volume. In this equation, the first term accounts for the combinatorial entropy of mixing and the second for the enthalpy of mixing. The Flory-Huggins Equation was successfully applied to demonstrate the basic reason for decreased miscibility of solvent-polymer mixtures compared to solvent-solvent mixtures as the combinatorial entropy of mixing is decreased. In polymer-polymer mixtures, the combinatorial entropy of mixing approaches insignificant values in the limit of high molecular weight polymer mixtures. Therefore, to achieve miscibility, a negative heat of mixing ($\chi_{12} < 0$), and consequently negative enthalpy must be obtained. In order to increase the miscibility if the condition $\Delta G_m < 0$ is reached, the temperature can be increased.

3.5. Phase segregation

In most cases solutions with mixed molecules in the original volume are used. Nevertheless, a perfectly mixed initial solution with more than one component does not necessarily result in a homogeneous solid material once the solvent is evaporated. The final solid resulting from the blended solution can have different domains composed of the different molecules initially present in the blend, an effect called phase segregation (or phase separation). Phase segregation can occur on either the vertical scale (z-scale), the horizontal scale (xy-scale) or both. An illustration of vertical and horizontal phase segregation is presented in **Figure 3.8**. There are many consequences of phase segregation on charge transport in organic materials. While in a perfectly homogeneously blended solid, the charge transport is similar over a long distance compared to the size of the molecules in the film, the transport properties vary greatly when the films is composed of islands of single components. If charge transport is favored in one material compared to the others, charges travelling in the film might follow a path composed only of that material. Furthermore, in the case of vertical phase segregation, if the charge transport is performed at the interface between the solid and the layer below, the other material might have no influence at all on the charge transport. Controlled phase segregation can be employed for applications that require two separate layers of materials with different charge transport properties, for example semiconductor and dielectric for organic thin-film transistors or *p*-type and *n*-type semiconductors for organic solar cells. Furthermore, fabrication of phase segregated solids is an interesting approach for fabrication of ultra-thin films and encapsulating layers.

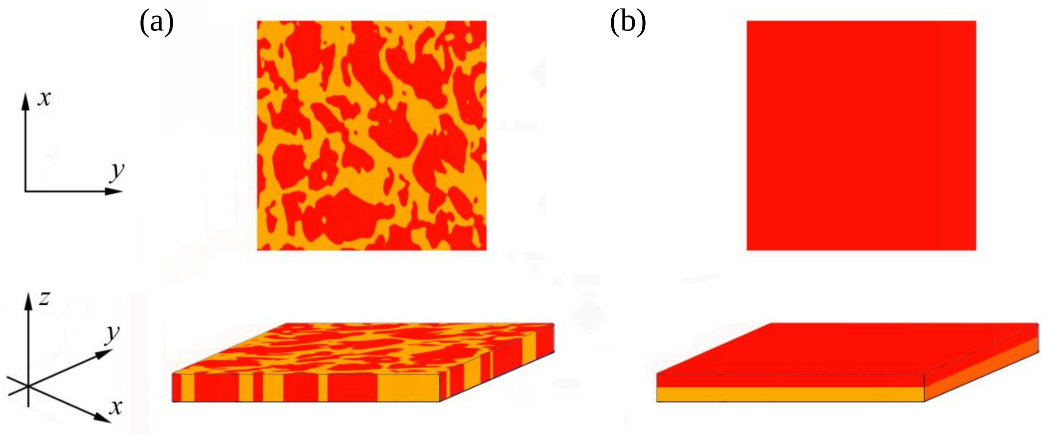

Figure 3.8: Cartoon representing examples of phase segregated solids. (a) Horizontal phase segregation. (b) Vertical phase segregation.

In the case of small molecules, phase segregation is often provoked by the difference in solubility of the initially mixed molecules. If one of the molecules aggregates first and deposits at the bottom of the solution, a layer of that molecule could form. This would result in both vertical and horizontal phase segregation. Another source of phase segregation in small molecules is the formation of small pure crystalline domains that assemble upon increase of the concentration by solvent removal. This can produce horizontally segregated films, and is favored when the solvent removal process is very slow for optimized crystal growth (formation of the thermodynamic product over the kinetic product). The interfaces should also be carefully considered. If one of the molecules has a higher affinity of the surface where the solution is deposited, a film of one molecule can form at that surface, leading to vertical phase segregation. Additionally, a layer of one phase often forms at the film/atmosphere surface due to the growth of a wetting layer.

In solution, the solvent molecules dilute the polymer/polymer interactions and the system forms a single phase. Upon film deposition, the solvent evaporates and as the solvent concentration decreases the interactions between polymer chains increase, increasing the driving force for phase separation. As the solvent concentration decreases, however, the polymer chains become less mobile and once a glass transition is encountered the morphology is frozen. Nevertheless, these frozen morphologies may be unstable to further phase separation, if additional processing steps are applied. Solvent vapor in the atmosphere or heating above the glass transition (annealing) are commonly employed techniques to favor additional phase segregation of the frozen morphology. It is noteworthy to mention that since phase segregation is often to be avoided, solvent vapor treatment and annealing should be employed with care in multi-component films.

Two distinctly different phase separation processes can be observed with initially miscible polymer mixtures subjected to solvent removal (evaporation or non-solvent addition): Nucleation and Growth [30] and Spinodal Decomposition. [31] The concept of nucleation refers to the first step of the creation of a new phase, and growth to the expansion of said phase. In the case of nucleation and growth, the system is in the meta-stable region of the phase-separation diagram (see **Figure 3.7**), it is therefore stable to small fluctuations in concentration. Phase separation then relies upon on the formation of a single component droplet of a certain minimum radius before further phase separation resulting in an overall lowering of the free energy of the system. This droplet may theoretically be formed through thermal fluctuation or through a reduction in the nucleation barrier by the presence of impurity particles that can be present in the original solution. Therefore, in order to avoid phase segregation, the purity of the initial compounds should be carefully considered. Spinodal decomposition, on the other hand, occurs when the system is in the unstable region of the phase diagram, after a greater amount of solvent is evaporated. In the unstable region, small fluctuations in composition lower the free energy, and phase separation proceeds immediately by the random composition fluctuations.

3.6. Conclusions

Organic materials offer a great variety of options for the fabrication of electronics. From small molecules to large molecular weight polymers, many interesting properties are can be taken advantage of such as *p*- or *n*-type charge transport, photo-switching and solubility in organic solvents. When the materials are processed from the solution, parameters such as solubility and surface affinity should be carefully considered. Furthermore, in the case of blends of materials, the phase segregation is a very important factor that depends on multiple parameters such as temperature, solubility and nature of interfaces.

3.7. References

1 Kagan, C. R. & Andry, P. *Thin-film transistors*. (Marcel Dekker, 2003).

2 Chesterfield, R. J. *et al.* High electron mobility and ambipolar transport in organic thin-film transistors based on a pi-stacking quinoidal terthiophene. *Adv. Mater.* **15**, 1278 (2003).

3 Facchetti, A., Mushrush, M., Katz, H. E. & Marks, T. J. n-type building blocks for organic electronics: A homologous family of fluorocarbon-substituted thiophene oligomers with high carrier mobility. *Adv. Mater.* **15**, 33 (2003).

4 Halik, M. *et al.* Relationship between molecular structure and electrical performance of oligothiophene organic thin film transistors. *Adv. Mater.* **15**, 917 (2003).

5 Barbarella, G. *et al.* Solid-state conformation, molecular packing, and electrical and optical properties of processable beta-methylated sexithiophenes. *J. Am. Chem. Soc.* **121**, 8920-8926 (1999).

6 Garnier, F. *et al.* Molecular Engineering of Organic Semiconductors - Design of Self-Assembly Properties in Conjugated Thiophene Oligomers. *J. Am. Chem. Soc.* **115**, 8716-8721 (1993).

7 Yuan, Y. B. *et al.* Ultra-high mobility transparent organic thin film transistors grown by an off-centre spin-coating method. *Nat. Commun.* **5** (2014).

8 Pandey, R. K., Singh, A. K. & Prakash, R. Directed Self-Assembly of Poly(3,3 '''-dialkylquarterthiophene) Polymer Thin Film: Effect of Annealing Temperature. *J Phys Chem C* **118**, 22943-22951 (2014).

9 Li, L. H., Kontsevoi, O. Y., Rhim, S. H. & Freeman, A. J. Structural, electronic, and linear optical properties of organic photovoltaic PBTTT-C14 crystal. *J. Chem. Phys.* **138** (2013).

10 Lee, S. H. *et al.* Simultaneous Improvement of Hole and Electron Injection in Organic Field-effect Transistors by Conjugated Polymer-wrapped Carbon Nanotube Interlayers. *Sci Rep-Uk* **5** (2015).

11 Drolet, N. *et al.* 2,7-carbazolenevinylene-based oligomer thin-film transistors: High mobility through structural ordering. *Adv. Funct. Mater.* **15**, 1671-1682 (2005).

12 Horie, M. *et al.* Cyclopentadithiophene-benzothiadiazole oligomers and polymers; synthesis, characterisation, field-effect transistor and photovoltaic characteristics. *J Mater Chem* **22**, 381-389 (2012).

13 Vanlaeke, P. *et al.* P3HT/PCBM bulk heterojunction solar cells: Relation between morphology and electro-optical characteristics. *Sol. Energ. Mat. Sol. C* **90**, 2150-2158 (2006).

14 Lei, T., Dou, J. H. & Pei, J. Influence of Alkyl Chain Branching Positions on the Hole Mobilities of Polymer Thin-Film Transistors. *Adv. Mater.* **24**, 6457-6461 (2012).

15 Chen, H. J. *et al.* Highly p-Extended Copolymers with Diketopyrrolopyrrole Moieties for High-Performance Field-Effect Transistors. *Adv. Mater.* **24**, 4618-4622 (2012).

16 Luo, C. *et al.* General Strategy for Self-Assembly of Highly Oriented Nanocrystalline Semiconducting Polymers with High Mobility. *Nano Lett.* **14**, 2764-2771 (2014).

17 Lei, T. *Design, Synthesis, and Structure-Property Relationship Study of Polymer Field-Effect Transistors*. 23-57 (Springer, 2015).

18 Kietzke, T. *et al.* Novel approaches to polymer blends based on polymer nanoparticles. *Nat. Mater.* **2**, 408-U407 (2003).

19 Hahm, S. G. *et al.* High-Performance n-Channel Thin-Film Field-Effect Transistors Based on a Nanowire-Forming Polymer. *Adv. Funct. Mater.* **23**, 2060-2071 (2013).

20 Rivnay, J. *et al.* Unconventional Face-On Texture and Exceptional In-Plane Order of a High Mobility n-Type Polymer. *Adv. Mater.* **22**, 4359 (2010).

21 Orgiu, E. & Samori, P. 25th Anniversary Article: Organic Electronics Marries Photochromism: Generation of Multifunctional Interfaces, Materials, and Devices. *Adv. Mater.* **26**, 1827-1845 (2014).

22 Orgiu, E. *et al.* Optically switchable transistor via energy-level phototuning in a bicomponent organic semiconductor. *Nat. Chem.* **4**, 675-679 (2012).

23 El Gemayel, M. *et al.* Optically switchable transistors by simple incorporation of photochromic systems into small-molecule semiconducting matrices. *Nat. Commun.* **6** (2015).

24 Borjesson, K. *et al.* Optically switchable transistors comprising a hybrid photochromic molecule/n-type organic active layer. *J. Mater. Chem. C* **3**, 4156-4161 (2015).

25 Crivillers, N. *et al.* Photoinduced work function changes by isomerization of a densely packed azobenzene-based SAM on Au: a joint experimental and theoretical study. *Phys. Chem. Chem. Phys.* **13**, 14302-14310 (2011).

26 Small, P. A. Some factors affecting the solubility of polymers. *J. Appl. Chem.* **3**, 71-80 (1953).

27 Jones, A. L. & Richards, R. W. *Polymers at surfaces and interfaces*. (Cambridge university press, 1999).

28 Huggins, M. L. Solutions of long chain compounds. *J. Chem. Phys.* **9** (1941).

29 Flory, P. J. Thermodynamics of high polymer solutions. *J. Chem. Phys.* **9**, 660-661 (1941).

30 Mcmaster, L. P. Aspects of Liquid-Liquid Phase-Transition Phenomena in Multicomponent Polymeric Systems. *Adv. Chem. Ser.*, 43-65 (1975).

31 Cahn, J. W. Phase separation by spinodal decomposition in isotropic systems. *J. Chem. Phys.* **43**, 93-99 (1965).

Chapter 4. Organic electronics

4.1. Semiconductors in electronics

Semiconductors are at the core of electronics. They are widely used for the fabrication of a wide variety diodes (point-contact diodes, junction diodes, light-emitting diodes), photonic devices (solar cells, photo-detectors) and transistors (switches, amplifiers). Transistors are of particular interest since they are the basis of logic gates, and therefore data processing circuits. Organic semiconductors have been the focus of an extensive research activity during the past decades because they represent key active components for now market mature technological applications (displays, sensors).[1-6] Numerous are the advantages they hold when compared to their inorganic counterparts including the tunability of their physical properties via chemical functionalization,[7-9] their low cost processing[10,11] using mild conditions (low temperature and ambient pressure) and up-scalable approaches even on flexible supports.[12] While transistors are very interesting for all their (potential) applications, they are also widely used in research as a tool of testing of the electrical properties of (organic) semiconductors.

4.2. Field-effect transistors

4.2.1. Basic operation of an organic field-effect transistor

A Field-Effect Transistor (FET) is a device based on three electrodes (source, drain and gate), a dielectric and a semiconductor. If the transistor is based on an organic semiconductor, it is called an organic Field-Effect Transistors (OFET). The electrodes source and drain are in contact with the semiconductor: upon application of a drain-source potential (V_{DS}), charges potentially flow through the semiconductor (I_{DS} current). The inter-electrode area where charges are transported within the semiconductor is called channel. The gate electrode is separated from the other electrodes and the semiconductor by the dielectric (**Figure 4.1**), in order to avoid charge transport between source and drain electrodes through the gate. The potential applied between source and gate is the V_{GS} potential and the current flowing through the dielectric is the leakage current I_{GS}, that is to be avoided in field-effect transistors. Upon application of a positive (or negative) V_{GS} potential, negative (or positive) charges are attracted to the semiconductor/dielectric interface, into the channel.

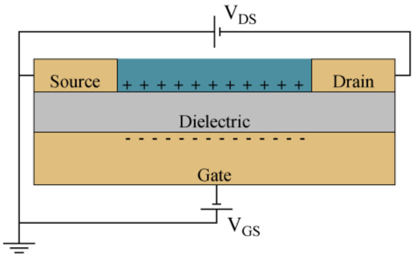

Figure 4.1: Field-effect transistor, example for the bottom-contact, bottom-gate geometry.

4.2.2. Field-effect transistor geometries

The elements of the FET described above can be staked in different ways (geometries). The major difference between devices operating at different geometries is the contribution of charge transport and injection to the overall device performance. In the case of the bottom-contact, bottom-gate geometry (**Figure 4.2, a**), source and drain electrodes are placed directly on the dielectric surface, and the charges are flowing only in the very first few layers of semiconductor that is adjacent to the dielectric surface. The dielectric being present directly on the flat gate, it can be very thin for optimal capacitance. It can be functionalized easily before deposition of the semiconductor. Furthermore, since the semiconductor is the last deposited layer, a device with electrodes and dielectric can be mass-produced or purchased in advance, leading to a facile and very reproducible device fabrication. In order to improve the injection from the source and drain electrodes into the semiconductor, the top-contact, bottom-gate geometry can be adopted (**Figure 4.2, b**). In that configuration, the source and drain electrodes are deposited over the semiconductor, while retaining the dielectric and gate at the bottom. In the staggered geometry, the injection is facilitated due to (i) the large contact area between the source electrode and the semiconductor and (ii) the formation a more intimate semiconductor/electrode interface due to the diffusion of metal atoms within the soft active layer following thermal evaporation. One major drawback is the impossibility to functionalize the source and drain electrodes. The third possible geometry is the bottom-contact, top-gate configuration (**Figure 4.2, c**). In that geometry, transistors are usually fabricated over a substrate. Source and Drain electrodes are deposited first, and may be functionalized for improved charge injection. The semiconductor is deposited afterwards. The dielectric is present over the semiconductor, and needs to be of a greater thickness to avoid gate leakage, since the semiconductor and electrodes beneath do not represent a perfectly flat film. The gate is finally present over the dielectric. While this geometry leads to particularly good transport at the semiconductor/dielectric interface it is the one that requires the highest number of production steps, and possible failure due to source/gate short circuit. Furthermore, the dielectric surface cannot be functionalized. The fourth possible geometry is the top-contact, top-gate configuration (**Figure 4.2, d**). In this geometry, the source and drain electrodes are over the semiconductor. Since charges are attracted to the gate on top, this configuration is not recommended in most cases as compared to the bottom-contact, top-gate geometry.

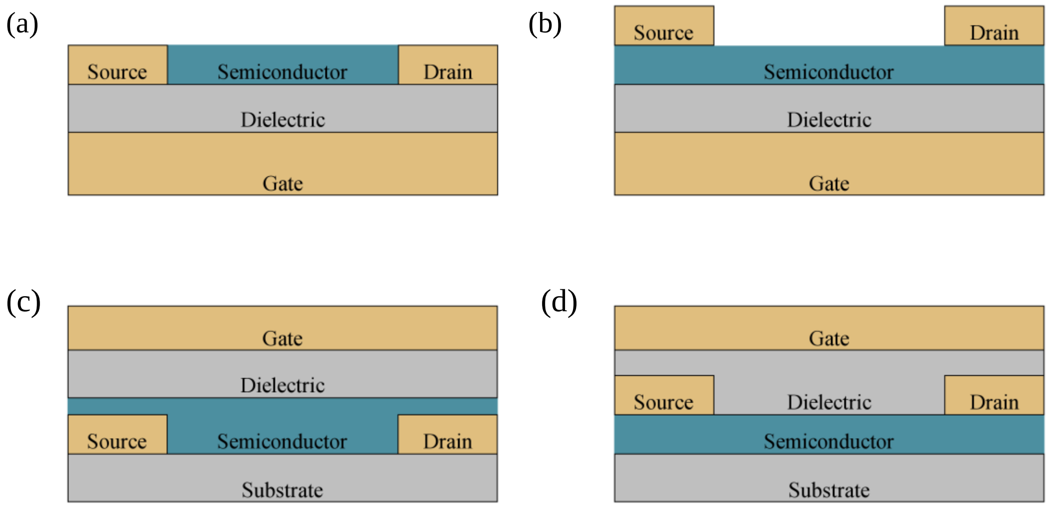

Figure 4.2: Field-effect transistor geometries. (a) Bottom-contact, bottom-gate geometry. (b) Top-contact, bottom-gate geometry. (c) Bottom-contact, top-gate geometry. (d) Top-contact, top-gate geometry.

4.2.3. Measurement of electrical characteristics

In order to determine the electrical characteristic of a semiconductor, two plots are traced: the transfer curve and the output curves. An output curve ($I_{DS}V_{DS}$) designates the plot of the source-drain current as a function of the drain-source potential. Commonly, multiple output curves for different gate-source potentials are drawn. In the output curves, two regions are defined, corresponding to two operation regimes of the FET. At low V_{DS}, the linear region, where I_{DS} increases linearly with V_{DS} and at higher V_{DS}, the saturation region, where I_{DS} is constant. From the different output curves at different V_{GS}, the I_{on}-I_{off} ratio (I_{on}/I_{off}) can be determined. The I_{on}/I_{off} corresponds to the ratio between the highest and lowest observed current at fixed V_{DS}. A higher I_{on}/I_{off} is synonym of a good ability to switch on and off the device, while a poor I_{on}/I_{off} is associated with a badly switching transistor. A transfer curve ($I_{DS}V_{GS}$) designates the plot of the source-drain current as a function of the gate-source potential. Usually, two transfer curves are represented: one in linear regime, and one in saturation regime. In the case of *n*-type semiconductor, negative charge carriers will start to travel in the semiconductor starting from a certain gate-source voltage, the threshold voltage (V_{Th}).

The presence of a threshold voltage has multiple reasons. First, the presence of shallow traps in the semiconductor that need to be filled before mobile charge can be induced in the channel. [13] Second, charged states or dipoles are present at the dielectric surface, and an additional gate voltage might be necessary to induce the formation of the channel. [14] An increase of the V_{GS} over the V_{Th} will result in an increase of the I_{DS} current. In *p*-type semiconductors, the I_{DS} current is negative and charge transfer will increase with higher negative V_{GS}. Once the threshold voltage is reached, the I_{DS} current increases linearly with the V_{GS} at lower V_{DS} (linear regime), while at higher V_{DS} (saturation regime), the I_{DS} current increases quadratically with V_{GS}. The I_{on}/I_{off} may be extracted from the transfer curves, and corresponds to the I_{DS} measured at the highest (I_{on}) divided by the lowest I_{DS} value (I_{off}).

In order to fabricate powerful data processing units, transistors with fast charge-transporting capabilities are required. The speed at which charges move in the semiconductor upon application of a gate voltage is the field-effect mobility μ_{FET} (that will be noted μ for convenience in the rest of this thesis). It can be extracted from the transfer curves. In a transistor, the I_{DS} is dependent on the capacitance of the dielectric (C_i), the threshold voltage, the field-effect mobility, the length (L) and the width (W) of the channel and the operating regime (linear or saturation), giving the two equations for *n*-type semiconductors (in the case of *p*-type semiconductors, the currents are negative since hole currents are conventionally negative):

$$I_{DS} = \mu_{LIN} C_i \frac{W}{L} [(V_{GS} - V_{TH}) V_{DS}] \qquad \textbf{Eq. 4.1}$$

$$I_{DS} = \frac{1}{2}\mu_{SAT} C_i \frac{W}{L}(V_{GS} - V_{TH})^2 \qquad \textbf{Eq. 4.2}$$

From these equations, we can conclude that the width-to-length ratio (W/L) plays a major role in the value of the I_{DS}. Since higher I_{DS} currents are easier to measure and process in output and transfer curves, the W/L is usually maximized by an interdigitated geometry of the source and drain. From the equations **4.1** and **4.2**, the mobility in linear and saturation regime is extracted:

$$\mu_{LIN} = \left(\left[\frac{\partial I_{DS}}{\partial V_{GS}}\right]_{V_{DS}=const.}\right)\frac{L}{W}\frac{1}{C_i}\frac{1}{|V_{DS}|} \qquad \textbf{Eq. 4.3}$$

$$\mu_{SAT} = 2\left(\left[\frac{\partial\sqrt{|I_{DS}|}}{\partial V_{GS}}\right]_{V_{DS}=const.}\right)^2 \frac{L}{W}\frac{1}{C_i} \qquad \textbf{Eq. 4.4}$$

These equations allow the easy determination of the mobility of the charge carriers in a transistor. Nevertheless, they are not an accurate representation of the mobility solely within the semiconductor, but they consider the total resistance R_{total}: both the resistance of the channel region and the resistance of the electrode-semiconductor contact:

$$R_{total} = R_{channel} + R_{contact} \qquad \textbf{Eq. 4.5}$$

The contact resistance ($R_{contact}$) is independent on the channel length, whereas the channel resistance ($R_{channel}$) increases linearly with the channel length. Therefore, multiple transistors can be fabricated with varying channel lengths, and their total resistance can be plotted as a function of L. An example is given in **Figure 4.3**. $R_{contact}$ can be extrapolated from the plot, at L = 0. The value of the contact resistance can then be deducted from the total resistance for each channel length, allowing the calculation of the mobility within the channel. This method is referred to as the Transfer Length Method (TLM).

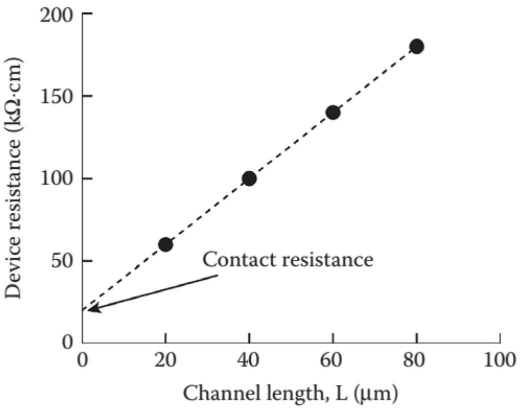

Figure 4.3: Example of a total resistance versus channel length plot with extrapolation used to determine the contact resistance. Reproduced from Sirringhaus et al. [15]

4.2.4. *Ambipolar field-effect transistors*

Ambipolar field-effect transistors are transistors capable of both *p*- and *n*-type transport. Ambipolar materials are strongly researched, due to their potential for the development of next-generation light-emitting devices, integrating the ability of both photogeneration and current modulation (device switching) in a single-device architecture. [16] In ambipolar transistors, both holes and electrons can contribute to the net electrical current, leading to a modification of the current equations **Eq. 4.1** and **Eq. 4.2**. In saturation regime, the I_{DS} current is:

$$I_{DS} = \frac{1}{2}\mu_{SAT,n} C_i \frac{W}{L}\left(V_{GS} - V_{TH,n}\right)^2 + \frac{1}{2}\mu_{SAT,p} C_i \frac{W}{L}\left(V_{GS} - V_{TH,p}\right)^2 \qquad \textbf{Eq. 4.6}$$

The threshold voltage being extracted similarly to how it was described for unipolar semiconductors, separately for *p*-type and *n*-type transport. A significant contribution of both holes and electrons is only present close to the region between $V_{Th,p}$ and $V_{Th,n}$. The *p*-type mobility and *n*-type mobilities are therefore extracted in the V_{GS} regions of the transfer curves where the contribution of the other charge transport is negligible, and **Eq. 4.1** and **Eq. 4.2** are valid.

4.2.5. *Bias stress and current decay*

Upon creation of a carrier channel in a field-effect transistor by application of V_{GS}, the V_{Th} of the transistor changes over time, a phenomenon known as bias stress effect. In the case of a *p*-type semiconductor, a negative gate-source voltage is applied, causing the threshold voltage to shift towards more negative values, while a positive gate-source voltage is applied to *n*-type semiconductor based transistors, inducing a positive threshold voltage shift. [14] The bias stress effect is attributed to the trapping of carriers from the gate bias-induced conduction channel into localized electronic states. These trap states may be located either within the semiconductor, at the semiconductor/dielectric interface, or within the gate dielectric. The longer the gate bias is applied, the more carriers are trapped, and a larger shift in threshold voltage is observed. Trapped carriers still contribute to the charge balance in the transistor, but not to the I_{DS}, resulting in a shift in threshold voltage. Depending on the physical characteristics of the trap states, trapped carriers either return to mobile states once V_{GS} is removed, or they remain trapped until physically eliminated, for example, by thermal annealing.

While the shift in V_{Th}, and consequently I_{DS} at fixed V_{GS} is often minimal during the standard plotting of output and transfer curves, devices that endure several minutes of constant V_{GS} and V_{DS} biasing show signs of a decay of the $|I_{DS}|$ current. This is the case of the devices described in chapter 8, that underwent over one hour of constant V_{DS} and V_{GS} biasing. In order to separate the interesting signal $\Delta I_{DS,\ switch}$, i.e. the decrease in current due to the switching of diarylethene, and $\Delta I_{DS,\ decay}$, i.e. the decrease in current due to bias-induced decay, the decay was fitted for each I_{DS}-time plot. The decay was fitted from the curve itself before the first irradiation, from 200 s to the first irradiation. The decay was fitted using the following equation:

$$\Delta I_{DS,decay}(t) = A_1 \times e^{-t/t_1} + A_2 \times t \qquad \textbf{Eq. 4.7}$$

with *t* being the time expressed in seconds. The average time constant $t_{1,\ average}$ was found to be 432 ± 20 s. The values of fitting parameters extracted from a blank P3HT I_{DS}-time curve and the most important I_{DS}-time graphs presented in chapter 8 are reported in **Table T4.1**. An example of curve taken from chapter 8 before and after fitting is given in **Figure 4.4**.

Table T4.1: Fitting parameters

	A_1 / A	**A_2 / A**	**t_1**	**R^2 (exp)**	**R^2 (lin)**
Blank P3HT	-3.338×10^{-4}	6.051×10^{-8}	433.16	0.99895	0.99983
Figure 8.11*	-5.373×10^{-5}	6.943×10^{-9}	418.57	0.99994	0.99842
Figure 8.12*	-4.619×10^{-7}	4.037×10^{-11}	443.28	0.99991	0.99818
Figure 8.23 (a)*	-5.713×10^{-6}	4.400×10^{-10}	457.69	0.95111	0.76410
Figure 8.23 (b)*	-1.354×10^{-6}	1.912×10^{-10}	407.63	0.97637	0.91260

*figure numbers from chapter 8.

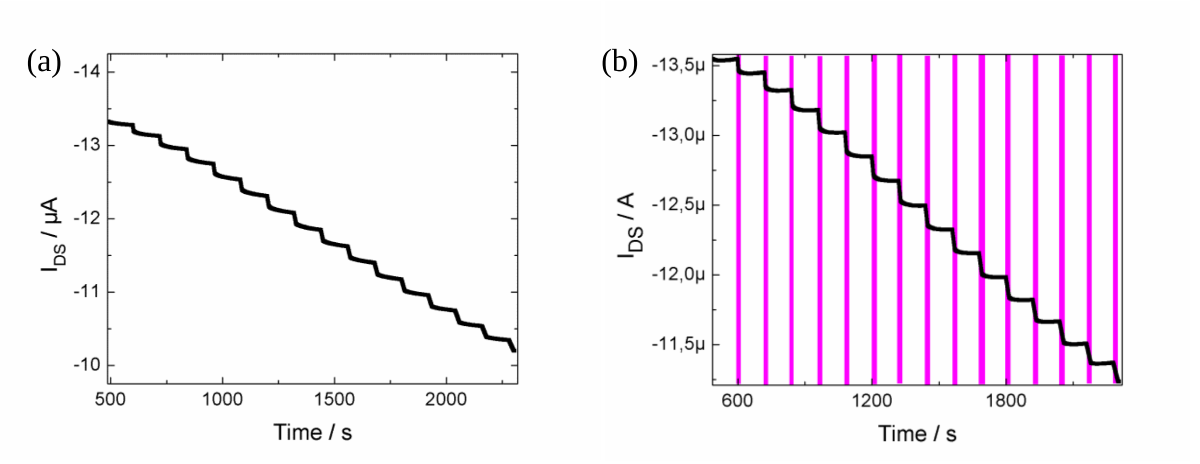

Figure 4.4: Experimental dynamic I_{DS}-time curves recorded in devices assembled on a polyethylene terephthalate substrate (Figure 8.23, b). (a) Uncorrected graph. (b) Graph corrected from the bias-stress induced decay.

4.2.6. Signal-to-noise ratio

Noise, as the random fluctuations in electrical current, is a characteristic of all electronic circuits. While in the case of transfer and output curves, the difference in I_{DS} between each point is very large compared to the noise induced by the circuit or testing device, the value of I_{DS} varies slightly (in the range of tens to hundreds of pA) between measurement points at constant V_{DS} and V_{GS}. In order to determine the “readability” of an electrical information, the value of the signal is compared to the root mean squared value of the noise amplitude. This section aims to give details of how the signal-to-noise ratio was calculated for the values reported in chapter 8.

The SNR (Signal-to-Noise Ratio) was extracted from the 400-step I_{DS}-time measurement curve. The ratio is calculated using the following equation:

$$\mathrm{SNR} = \frac{A_{\mathrm{signal}}}{\mathrm{RMS}\ A_{\mathrm{noise}}} \qquad \textbf{Eq. 4.8}$$

with A_{signal} the step height and RMS A_{noise} the root mean square of A_{noise} the noise amplitude. In order to determine ½ A_{noise} the noise half-amplitude, 3 times 80 consecutive current points between two illuminations were taken from the I_{DS}-time measurements: once at the beginning of the experiment (**Figure 4.5, a**), once in the middle of the experiment (**Figure 4.5, b**) and one at the end **(Figure 4.5, c**).

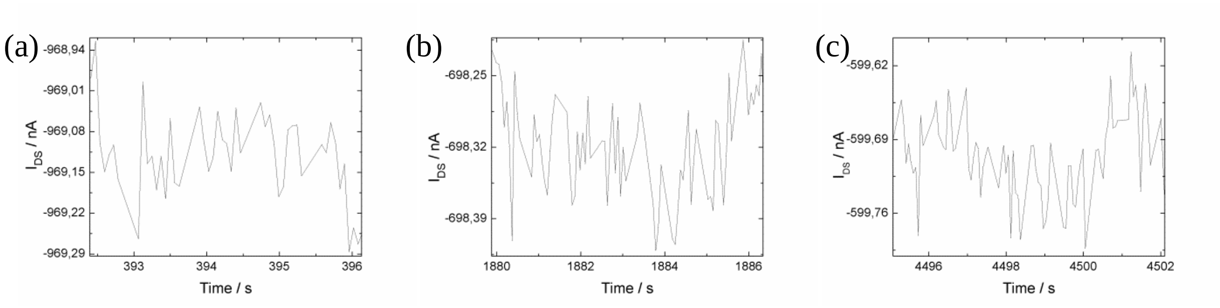

Figure 4.5: I_{DS}-time curves for Signal-to-noise calculations. I_{DS}-time curve (a) before illumination; (b) after 150 illumination steps, and (c) after full experiment (400 illumination steps).

The value of the current was subtracted from the average current over the 80 current points, leading to 3 × 80 values of ½ A_{noise}:

$$A_{noise} = 2 \times |I_{DS} - Average\ (I_{DS})| \qquad \textbf{Eq. 4.9}$$

A_{noise} was calculated as 2 times the absolute value of ½ A_{noise}. RMS A_{noise} the root mean square of A_{noise} was calculated:

$$\text{RMS A}_{\text{noise}} = \sqrt{\frac{1}{80}\left[\left(A_{noise,1}\right)^2 + \left(A_{noise,2}\right)^2 + \cdots + \left(A_{noise,80}\right)^2\right]} \qquad \textbf{Eq. 4.10}$$

Finally, the 3 calculated RMS A_{noise} values over 80 points were averaged.

4.2.7. Flexibility

Among the advantages of organic electronics, flexibility is always listed as an important feature. While the tangible need for flexible or purposely curved everyday electronics remains debatable, those devices are often suffering from involuntary mechanical constraints, such as a person accidentally sitting down on a phone or letting it fall on the ground. Furthermore, multiple applications could arise in the health industry such as biocompatible flexible sensors. In the never-ending back-and-forth competition for marketing exposure, cheap electronics integrated into flexible substrates could easily find their way onto everyday commodities, from video-games on cereal boxes to electronic-augmented clothing.

While measuring the resistance to bending of transistors on a flexible substrate should revolve around thousands of bending and unbending processes performed on a specific robotized setup, a more convenient approach was adopted in the bending experiments of chapter 8. In order to determine the effect of successive bends on the electrical performances, the flexible devices were first tested prior to any bending. Once the electrical characterization performed, the sample was bent a first large bending radius of 29 mm for one minute, made flat again and tested a second time. These steps were replicated four times with the bending radius decreased each time, down to 6 mm (**Figure 4.6**). The bending was performed by attaching the sample on a round cylinder, making sure that it was well strapped in order to ensure the actual bending of the whole sample, and not only the substrate around the device. It is noteworthy to mention that while this study does not account for resistance over thousands of bends, it serves as a good proof of concept for flexible electronics.

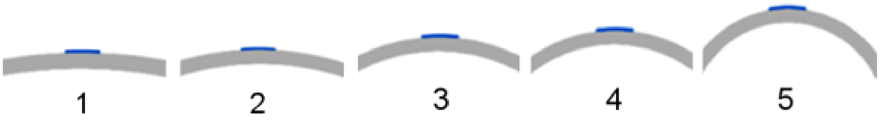

Figure 4.6: Integration of the memory unit onto a flexible PET substrate. Cartoon depicting the bending radii (1: 29.0 mm, 2: 17.5 mm, 3: 10.0 mm, 4: 8.0 mm, and 5: 6.0 mm).

4.3. Organic memories

Memories are a very important aspect of modern computers, and are usually split into two categories: volatile and non-volatile. The first type, often based on capacitors (such as dynamic random access memory), is used for short-term storage of data, and needs to be electrically refreshed by rewriting of the same data multiple times every second. While these kinds of memory find great many applications such as cache memory in processors, the second type, non-volatile memory is widely used for permanent data storage (hard drives, memory sticks…). The current trend tends to leave behind all forms of disk-based analogic memories for more reliable, easier to downscale and less power-consuming digital memories, that rely mostly on field-effect transistors. Unlike in fields such as

LEDs and solar cells, organic based technologies for digital data-storage has not yet entered the mass fabrication stage, and flash memories produced today are all based on inorganic MOSFETs (Metal-Oxide-Semiconductor Field-Effect Transistors). While standard memories may only store a single value out of two possibilities (either a “0” or a “1”, 1-bit storage), multilevel memories are devices where the addressable states are more numerous (such as a 3-bit storage memory with 8 distinct levels). Multilevel memories are believed to be the key for further miniaturization in electronics.

The important characteristics that a memory should exhibit are the following: long retention times, high switching ratio and easy programming. The switching ratio is the ratio between the measured current of the memory in the “on” state and the memory in the “off” state. If the two states are too close, misreading of the information could happen due to a slight unintentional change in current. The memory should be also easy to program: in the case of electrical programming, the necessary applied voltage should be acceptable for integration into everyday electronics. To date, numerous successful attempts to organic storage units are reported in literature, relying on a wide variety of different approaches, and the two following sections will give a summary of the performances of the memories reported in these research articles.

4.3.1. Electrical programming

2-Terminal and 3-terminal resistive switching memories based on polymers, organic small molecules and ferroelectric materials have shown impressive switching ratios up to 10^8 and low programming voltages. [17-19] Unfortunately, this approach relies on two stable states of polarization therefore it is ill suited for multilevel memories. [20] On the other hand, memories designed around electrets, i.e. dielectric materials (usually polymers) exhibiting quasi-permanent electric charge or dipole polarization, have displayed ability to perform as multilevel memories with different applied programming voltages. Although the observed switching ratios over 10^8 push them at the forefront of research on organic memories, [21,22] their unacceptably high programming voltages (up to ± 200 V) and most importantly their low retention times ($<10^4$ s) represent still major obstacles towards their integration into everyday electronics. [23,24] Storing charges in a metal or semiconductor layer exploiting the principle of the floating gate located within the dielectric can be achieved with metallic nanoparticles, with each particle counting as a charge-storage site independent and isolated from other sites. While not extensively explored, this approach is relevant for the fabrication of multilevel memories exhibiting acceptable programming voltages (up to ± 40 V) but thus far is accompanied by disappointing retention times for long-term multilevel storage (10^4 s). [25]

4.3.2. Photoprogramming

As compared to electrical programming of organic memories, photoprogramming offers the fundamental advantage of having the photo-writing being orthogonal to the electrical readout. Photochromic molecules have shown promising results as molecular switches, but rather mediocre (semi)conducting behavior and not negligible fatigue. [26-28] Most studies on organic memories based on photochromic molecules have focused on three types of photochromic systems: azobenzenes, spiropyrans, and diarylethenes (DAEs). [29-32] Optical switching between two independently addressable states leads to changes both at the molecular and at the macroscopic scale. At the molecular level, one observes reversible modifications of the geometrical and electronic structure, including changes in dipole moment, π-conjugation, band-gap, etc.,[33] which can be translated into respective adaptations of macroscopic properties upon switching, including changes in shape, aggregation behavior and conductance. While conductance changes are often a sought-after property, concomitant morphological changes at the meso-scale could lead to stability issues, in particular since maintaining high order in the film is crucial for device performance. Therefore, the optimal solution consists of a photochromic molecule in which the two switching states exhibit simultaneously (i) the lowest possible change in supramolecular organization, (ii) the largest modulation of the electronic properties, (iii) sufficient stability of both interconverting isomers, (iv) a fast switching induced by the light stimulus, and (v) an efficient switching in the solid state. All of these characteristics can be met by DAEs. [34] In earlier studies, organic memories based on layered device architectures composed of DAE and triarylamine derivatives proved to be a valuable approach for the production of organic multilevel memories with 30 reported current-levels. [35,36] However, the fabrication of multi-layers clearly requires multi-step processing, and the devices need several minutes of irradiation at high intensity in order to obtain a sufficient switching yield, making them unsuitable for applications in the electronic industry. Furthermore, electrical switching exhibited a limited reversibility.

4.4. Conclusions

While the applications for organic semiconductors are seemingly unlimited, transistors are among the most extensively used. In this chapter we have reviewed how transistors can be used as a testing device for organic semiconductor performances, in particular mobility, I_{on}/I_{off}, threshold voltage and contact resistance values from output and transfer curves. The current decay emerging from prolonged biasing and the noise in electrical current measurement were discussed. Furthermore, we explored device flexibility and multiple approaches for organic memory fabrication.

4.5. References

1 Sirringhaus, H. *et al.* Two-dimensional charge transport in self-organized, high-mobility conjugated polymers. *Nature* **401**, 685-688 (1999).

2 Bredas, J. L., Beljonne, D., Coropceanu, V. & Cornil, J. Charge-transfer and energy-transfer processes in pi-conjugated oligomers and polymers: A molecular picture. *Chem. Rev.* **104**, 4971-5003 (2004).

3 Xu, Y. Y., Zhang, F. & Feng, X. L. Patterning of Conjugated Polymers for Organic Optoelectronic Devices. *Small* **7**, 1338-1360 (2011).

4 Dimitrakopoulos, C. D. & Malenfant, P. R. L. Organic Thin Film Transistors for Large Area Electronics. *Adv. Mater.* **14**, 99-117 (2002).

5 Nomoto, K. *et al.* A high-performance short-channel bottom-contact OTFT and its application to AM-TN-LCD. *IEEE Trans. Electron. Dev.* **52**, 1519-1526 (2005).

6 Torsi, L. *et al.* A sensitivity-enhanced field-effect chiral sensor. *Nat. Mater.* **7**, 412-417 (2008).

7 Yoon, M. H., Facchetti, A. & Marks, T. J. sigma-pi molecular dielectric multilayers for low-voltage organic thin-film transistors. *Proc. Natl. Acad. Sci. U.S.A.* **102**, 4678-4682 (2005).

8 Nouchi, R. & Kubozono, Y. Anomalous hysteresis in organic field-effect transistors with SAM-modified electrodes: Structural switching of SAMs by electric field. *Org. Electron.* **11**, 1025-1030 (2010).

9 Mei, Y. C. *et al.* High Mobility Field-Effect Transistors with Versatile Processing from a Small-Molecule Organic Semiconductor. *Adv. Mater.* **25**, 4352-4357 (2013).

10 Forrest, S. R. The path to ubiquitous and low-cost organic electronic appliances on plastic. *Nature* **428**, 911-918 (2004).

11 Yan, H. *et al.* A high-mobility electron-transporting polymer for printed transistors. *Nature* **457** (2009).

12 Arias, A. C., MacKenzie, J. D., McCulloch, I., Rivnay, J. & Salleo, A. Materials and Applications for Large Area Electronics: Solution-Based Approaches. *Chem. Rev.* **110**, 3-24 (2010).

13 Zschieschang, U., Weitz, R. T., Kern, K. & Klauk, H. Bias stress effect in low-voltage organic thin-film transistors. *Appl Phys a-Mater* **95**, 139-145 (2009).

14 Pernstich, K. P. *et al.* Threshold voltage shift in organic field effect transistors by dipole monolayers on the gate insulator. *J Appl Phys* **96**, 6431-6438 (2004).

15 Bao, Z. & Locklin, J. *Organic Field-Effect Transistors*. (CRC Press, 2007).

16 Muccini, M. A bright future for organic field-effect transistors. *Nat. Mater.* **5**, 605-613 (2006).

17 Nili, H. *et al.* Nanoscale Resistive Switching in Amorphous Perovskite Oxide (a-SrTiO3) Memristors. *Adv. Funct. Mater.* **24**, 6741-6750 (2014).

18 Han, Y., Cho, K., Park, S. & Kim, S. Resistive Switching Characteristics of HfO2-Based Memory Devices on Flexible Plastics. *J. Nanosci. Nanotechno.* **14**, 8191-8195 (2014).

19 Zhang, W. B. *et al.* Thermally-stable resistive switching with a large ON/OFF ratio achieved in poly(triphenylamine). *Chem. Commun.* **50**, 11856-11858 (2014).

20 Heremans, P. *et al.* Polymer and Organic Nonvolatile Memory Devices. *Chem. Mater.* **23**, 341-358 (2011).

21 Chiu, Y. C. *et al.* High performance nonvolatile transistor memories of pentacene using the electrets of star-branched p-type polymers and their donor-acceptor blends. *J. Mater. Chem. C* **2**, 1436-1446 (2014).

22 Baeg, K. J. *et al.* High-Performance Top-Gated Organic Field-Effect Transistor Memory using Electrets for Monolithic Printed Flexible NAND Flash Memory. *Adv. Funct. Mater.* **22**, 2915-2926 (2012).

23 Chiu, Y. C. *et al.* Multilevel nonvolatile transistor memories using a star-shaped poly((4-diphenylamino)benzyl methacrylate) gate electret. *NPG Asia Mater.* **5** (2013).

24 Chou, Y.-H., Chang, H.-C., Liu, C.-L. & Chen, W.-C. Polymeric charge storage electrets for non-volatile organic field effect transistor memory devices. *Polym. Chem.* **6**, 341-352 (2015).

25 Zhou, Y., Han, S. T., Sonar, P. & Roy, V. A. L. Nonvolatile multilevel data storage memory device from controlled ambipolar charge trapping mechanism. *Sci. Rep.* **3** (2013).

26 Orgiu, E. & Samori, P. 25th Anniversary Article: Organic Electronics Marries Photochromism: Generation of Multifunctional Interfaces, Materials, and Devices. *Adv Mater* **26**, 1827-1845 (2014).

27 Hayakawa, R., Higashiguchi, K., Matsuda, K., Chikyow, T. & Wakayama, Y. Optically and Electrically Driven Organic Thin Film Transistors with Diarylethene Photochromic Channel Layers. *ACS Appl. Mater. Inter.* **5**, 3625-3630 (2013).

28 Matsui, N. & Tsujioka, T. Carrier mobility of photochromic diarylethene amorphous films. *Org. Electron.* **15**, 2264-2269 (2014).

29 Nishimura, K. *et al.* Solution electrochemiluminescent cell with a high luminance using an ion conductive assistant dopant. *Jpn. J. Appl. Phys., Part 2* **40**, L1323-L1326 (2001).

30 Andersson, P., Robinson, N. D. & Berggren, M. Switchable charge traps in polymer diodes. *Adv. Mater.* **17**, 1798-1803 (2005).

31 Raimondo, C. *et al.* Optically switchable organic field-effect transistors based on photoresponsive gold nanoparticles blended with poly(3-hexylthiophene). *Proc. Natl. Acad. Sci. U.S.A.* **109**, 12375-12380 (2012).

32 Taguchi, M., Nakagawa, T., Nakashima, T., Adachi, C. & Kawai, T. Photo-patternable electroluminescence based on one-way photoisomerization reaction of tetraoxidized triangle terarylenes. *Chem. Commun.* **49**, 6373-6375 (2013).

33 Russew, M. M. & Hecht, S. Photoswitches: From Molecules to Materials. *Adv. Mater.* **22**, 3348-3360 (2010).

34 Irie, M., Fulcaminato, T., Matsuda, K. & Kobatake, S. Photochromism of Diarylethene Molecules and Crystals: Memories, Switches, and Actuators. *Chem. Rev.* **114**, 12174-12277 (2014).

35 Shallcross, R. C., Korner, P. O., Maibach, E., Kohnen, A. & Meerholz, K. Photochromic Diode With a Continuum of Intermediate States: Towards High Density Multilevel Storage. *Adv. Mater.* **25**, 4807-4813 (2013).

36 Korner, P. O., Shallcross, R. C., Maibach, E., Kohnen, A. & Meerholz, K. Optical and electrical multilevel storage in organic memory passive matrix arrays. *Org. Electron.* **15**, 3688-3693 (2014).

Chapter 5. Experimental techniques

5.1. Device fabrication

5.1.1. Substrate preparation

5.1.1.1. Fraunhofer substrates

Bottom-contact bottom-gate configuration transistors purchased from IPMS Fraunhofer Institute were used. They consisted of n^{++}-Si substrates covered by 230 nm of thermally grown SiO_2 as the gate dielectric (15 nF capacitance). Basic substrates and pre-patterned substrates with pairs of gold electrodes with interdigitated geometry as the source and drain were used. In both cases they were hexamethyldisilazane (HMDS) treated and protected with a layer of dicing resist. The first step consisted in the removing of the dicing resist through washing of the sample. It was a multiple-step procedure, with first a rough rinsing of the dicing resist using acetone, followed by immersion into an acetone bath. The immersed sample was placed for 20 minutes in an ultra-sonic cleaner, removed, dried under nitrogen flow, and re-immersed in an isopropanol bath placed for 20 minutes in an ultra-sonic cleaner. The sample was finally removed and dried under nitrogen flow. After this procedure, the sample was dicing resist-free but still functionalized with HMDS, that can be removed by UV-Ozone cleaning.

5.1.1.2. UV-Ozone cleaning

If undesired molecules were adsorbed on the surface of the substrate, the sample was placed in a Novascan PSD ozone cleaner and irradiated with intense short ultraviolet wavelengths using a mercury vapor lamp (184.7 and 253.7 nm) in the presence of oxygen. The ozone cleaning consists of multiple steps (**Figure 5.1**). First, the irradiated at 184.7 nm dioxygen is dissociated into oxygen radicals and ozone molecules. Under 253.7 nm irradiation, oxygen radicals interact with the adsorbed layer on the substrate, and produce volatile molecules, mostly CO_2 and H_2O, that leave the surface. Each substrate was irradiated for 5 minutes followed by 25 minutes of resting time before the substrate was removed from the UV-Ozone cleaner.

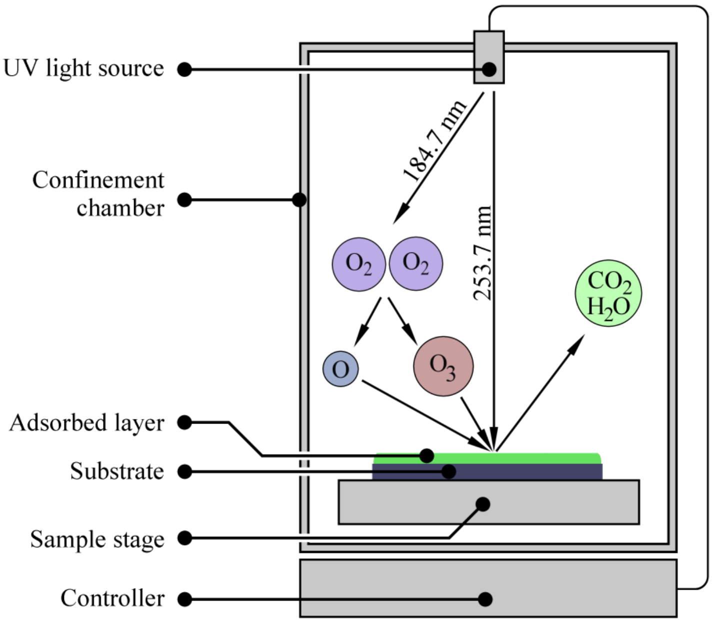

Figure 5.1. Schematic of a UV-Ozone cleaner

5.1.1.3. Polyethylene terephtalate substrates

Polyethylene terephtalate (PET) substrates were used for flexible applications. Large square sheets of PET commercialized under the name Melinex (thickness 175 µm) were purchased from Teijin DuPont. They were cut into square 2.25 cm² sheets and attached to glass substrates to mimic the rigid silicon-based substrates from Fraunhofer for device fabrication. They were cleaned using ethanol and dried under nitrogen flow.

5.1.1.4. Metal evaporation

In order to deposit metal films (Au, Ag, Cr), a physical vapor deposition setup was used (Plassis ME300B and Plassis ME400B, **Figure 5.2**). The source material (a metal in our case) is vaporized and re-condensates on the sample. The chamber is first pumped using a rotary pump, then jointly combined with a turbo pump in order to be put the chamber in ultra-high vacuum ($P < 10^{-9}$ bar). The low pressure ensures that the adsorption of residual gases on the surface during film formation is minimal, in order to obtain pure films. The metal is then heated by applying a strong electric current (typically between 130 A and 200 A) until the melting point is reached. When the metal is in a liquid phase, an equilibrium between the molar Gibbs free energy of the liquid (ΔG_l) and the vapor (ΔG_v) is formed ($\Delta G_l = \Delta G_v$), meaning that the metal is evaporated until the equilibrium is reached. The Gibbs free energy of evaporation (ΔG_{evap}), is defined by:

$$\Delta G_{evap} = \Delta G_v - \Delta G_l \qquad \textbf{Eq. 5.1}$$

When the temperature of the liquid is increased (upon increasing the current), $\Delta G_{evap} < 0$: the vapor state is favored and the thermally activated vapor pressure is increased, leading to an increased deposition rate. The vapor pressure of the evaporated metal P_M can be calculated : $\log(P_M)$ is linearly correlated with the temperature T, following the equation:

$$\log(P_M) = 5.006 + C + \frac{B}{T} \qquad \textbf{Eq. 5.2}$$

with B and C being empirical parameters that are tabulated for most metals.

In order to produce a very homogeneous film of pure material, the evaporation is first stabilized at the desired rate before the shutter is opened and the covering of the film can start. The crystal detector, a quartz microbalance evaluates the mass variation by measuring the change in frequency of a quartz crystal resonator. Thus, the evaporation rate can be evaluated and adjusted in real time for optimal depositions.

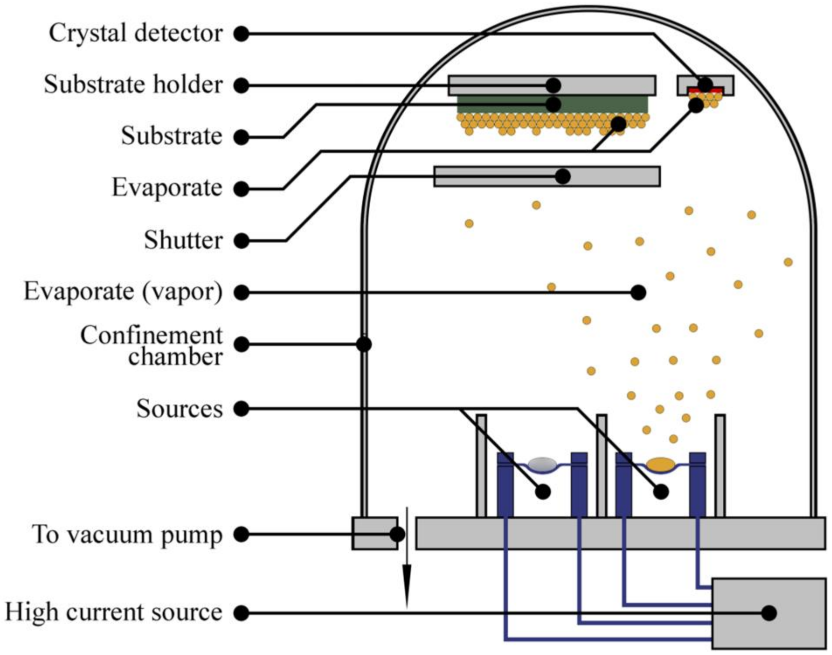

Figure 5.2: Schematic of the physical vapor deposition setup.

In the case of the deposition of source and drain electrodes on a silicon oxide substrate, a thin layer (3 nm) of chromium was evaporated first on the substrate. This intermediate layer was deposited to ensure optimal adherence of the electrodes on the substrate. Interdigitated gold source and drain electrodes were evaporated using a shadow mask covering the substrate, with channel lengths of 60, 80, 100 and 120 µm and W = 10 mm. For top-gate transistors, an aluminum gate electrode was evaporated, using a shadow mask. **Table T5.1.** lists the most common experimental conditions and parameters used for electrode evaporation. The evaporation was performed inside a glovebox when the organic material was deposited beforehand. In order to avoid short-circuit in top-gate transistors, the source/drain electrodes are evaporated thinner than in other geometries.

Table T5.1. Experimental conditions of metal evaporation for different transistor geometries.

Electrodes	Geometry	Metal	Thickness / nm	Rate / nm/s	Glovebox
Source/Drain	Bottom-contact	Au	60	0.02-0.1	No
Source/Drain	Top-contact	Au	60	0.02-0.1	Yes
Source/Drain	Top-gate	Au	40	0.02-0.1	No
Gate	Bottom-contact	Au	60	0.02-0.1	No
Gate	Top-gate	Al	200	1-3	Yes

5.1.1.5. Self-assembled monolayer treatments

Self-Assembled Monolayer (SAM) treatment relies on the adsorption of a single layer of the molecule on the treated surface. Depending on the target surface, used SAMs were either thiol-terminated (for interaction with gold electrodes) or silane terminated (for interaction with SiO_2 surfaces). Depending on the used SAMs, the effect on the surface varies. In particular, the work function and the wetting of the surface can be tuned. Also, the surface can be passivated, and the formation of larger crystallic domains can be favored.

Two self-assembled monolayers, hexamethyldisilazane (HMDS) and octadecyltrichlorosilane (OTS), were used for dielectric treatment. OTS treatment consisted of a 12-hours immersion of the ozone-treated wafer into a 10 mM solution of OTS in toluene including 30 min of heating at 60 °C at the beginning of the immersion. The samples were afterwards rinsed multiple times with toluene and heated for 60 min at 60 °C. HMDS was spin coated at 1500 RPM on the substrate and annealed for 1 hour at 100 °C.

Two self-assembled monolayers, 1-decanethiol (C_{10}) and 1H,1H,2H,2H-perfluorodecanethiol (FC_{10}), were used for electrode treatment. The procedure was similar for both SAMs: the ozone-treated wafer was immersed 12 hours into a 1mM solution of the SAM in absolute ethanol. The wafer was afterwards washed with clean ethanol and annealed 1 hour at 60°C.

5.1.2. Organic materials

5.1.2.1. Semiconductor and diarylethene solution preparation

Organic semiconductors were moved directly after reception to a nitrogen-filled glovebox, where they were kept at all times. Diarylethenes were kept protected from light in a fridge outside of the glovebox. Anhydrous solvents were purchased and kept in the glovebox. Vials, caps, spatulas and magnetic stirrers used for solution preparation were introduced in the glovebox after removal of the possible dust and water by nitrogen flow.

Solution preparation consisted of addition of the selected material into the previously weighted vial in nitrogen atmosphere. The vial was then weighted again and the mass of the introduced material was calculated. The adequate volume of solvent was added using an Eppendorf micropipette. The solution was stirred, and if described in the manuscript, heated on a hotplate. In the case of diarylethenes, the material was weighted in air before being introduced in the glovebox. For the preparation of blends of solutions, separate solutions were prepared at the same concentration and blended into a new vial at the adapted ratio, then stirred for several minutes.

5.1.2.2. Dielectric solution preparation

All the organic dielectrics used were kept in air atmosphere. Dielectric preparation varied between polymers. In the case of poly(methyl methacrylate) (PMMA, purchased from Sigma-Aldrich, Mw = 120 kDa), 70 mg of material and 1 mL of ethyl acetate were introduced into a vial in nitrogen atmosphere, and stirred for 30 minutes at 55°C . The hot solution was filtered using 0.2 µm filters (Acrodisc LC 13). Poly(4-vinylphenol) (PVP, purchased from Sigma-Aldrich, Mw = 25 kDa) solutions were fabricated using 100 mg of PVP for 1 mL of 1-Methoxy-2-propanol, and stirred for 1 hour at 100°C. The solution was used unfiltered. Cytop CTL 809M and its fluorinated solvent were purchased from Ashai Glass Japan. A 9/1 Cytop/solvent solution was prepared and shaken vigorously. The solution was kept overnight in the fridge before being moved to the glovebox.

5.1.2.3. Solution deposition

Drop casting is the simplest among the deposition methods, yet very interesting as it shares similarities with ink-jet printing, making it a good approach for experiments that could be integrated into industrial procedures. It consists of the application of a drop of the solution or dispersion directly onto the substrate. The volume of deposited material is depending on the size and wetting of the substrate. For a standard 2.25 cm² substrate, the volume was ranging from 50 µL to 200 µL. After evaporation of the solvent, a film is formed. Drop casting has the drawback of creating films that are often very thick and can be very inhomogeneous.

Spin-coating was used in order to form thinner and more homogeneous films. It consists in the high-speed rotation of the sample (from 1000 to 4000 RPM with acceleration up to 4000 $\text{RPM}\cdot\text{s}^{-1}$) after deposition of a drop of the solution or dispersion onto the substrate. The substrate is maintained to the spin-coater through vacuum, and therefore this approach is only viable for rigid substrate. In the case of a flexible substrate such as polyethylene terephthalate (PET), the substrate has to be first attached to a rigid surface. The rotation speed and acceleration have to be adapted depending on the solvent, since a small drop of low boiling point solvent could evaporate soon after deposition. Also, the target thickness of the film has to be considered in the choice of rotation speed, with thinner films produced from higher rotation speeds.

5.2. Characterization techniques

5.2.1. Surface characterization

5.2.1.1. Atomic Force Microscopy

In order to represent the surface of the sample at the nanometer scale, an Atomic Force Microscopy (AFM) setup was used (**Figure 5.3**).

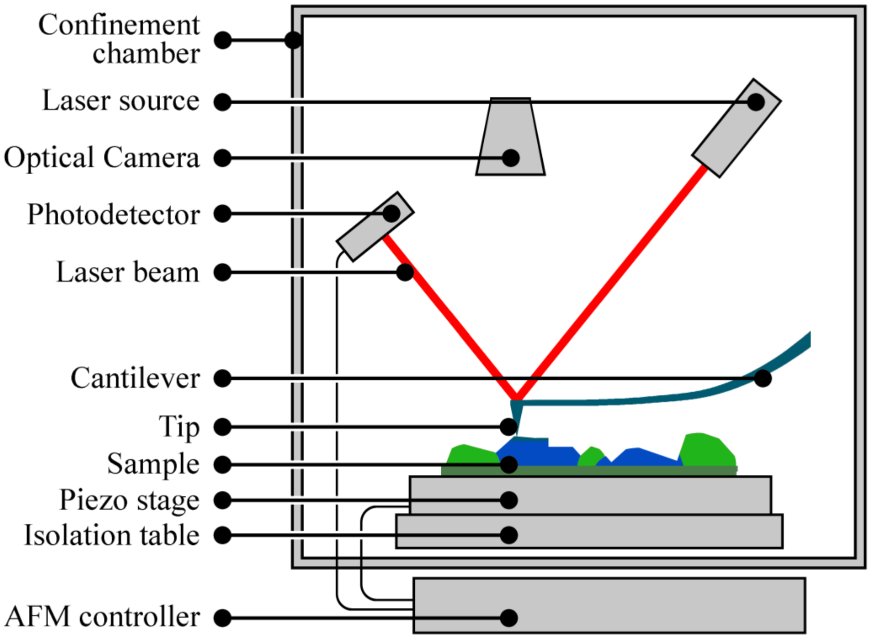

Figure 5.3: Atomic force microscopy setup.

The AFM consists of a tip, mounted on an oscillating cantilever, scanning the surface. A laser beam hits the rear side of the cantilever, causing a reflection, recorded by a photo-diode system. The AFM measurement can be performed in two modes: contact or tapping. Since the contact mode scratches the surface, our experiments were always performed in the tapping mode. In order to increase the quality of the results obtained during AFM experiments, each spot is being recorded and analyzed twice (trace, retrace). In constant-height mode, each time the amplitude is increased or reduced the tip is automatically respectively lowered or raised, to avoid either loss of contact or damaging of the tip and sample. The topography of the surface induces changes in the amplitude of the oscillations. Such a change is measured point by point. Upon integrating measurements carried out on N × N points forming a square array, an image can be drawn providing a direct map of the topography of the surface of the studied sample.

The setting of the height of the sample relative to the tip is performed by the optical focusing of the surface, using a camera. The tip is then carefully moved towards the surface, until focused. Once the tip is fully focused, it is considered close enough to the surface. This step precedes the adjustment of the laser reflection, which should hit the photo-diode in its center. Exterior noises have to be avoided. Exterior noise can have three major sources: acoustic, mechanic and electrostatic. In order to prevent low data-quality from each noise source, the AFM setup is fixed on a vibration isolation table within an acoustic isolation enclosure acting as a Faraday cage as well.

The obtained image corresponds to the height of the surface at each of the coordinates. The arbitrary color system shows high surfaces in light brown, whereas a darker brown is used for low surfaces (**Figure 5.4**.). If the tip interacts with the surface, there can be a delay in the oscillations. This delay is plotted as a function of the x and y position, giving the phase image. Depending on the material, the delay varies (as an example we can cite the important difference between hydrophobic and hydrophilic surfaces). Therefore, there is useful data that can be extracted even from a flat surface using an AFM technique. Mechanical proprieties can also be measured by AFM: data on the adhesion of the tip to the surface can be collected from the delay of the oscillation rate.

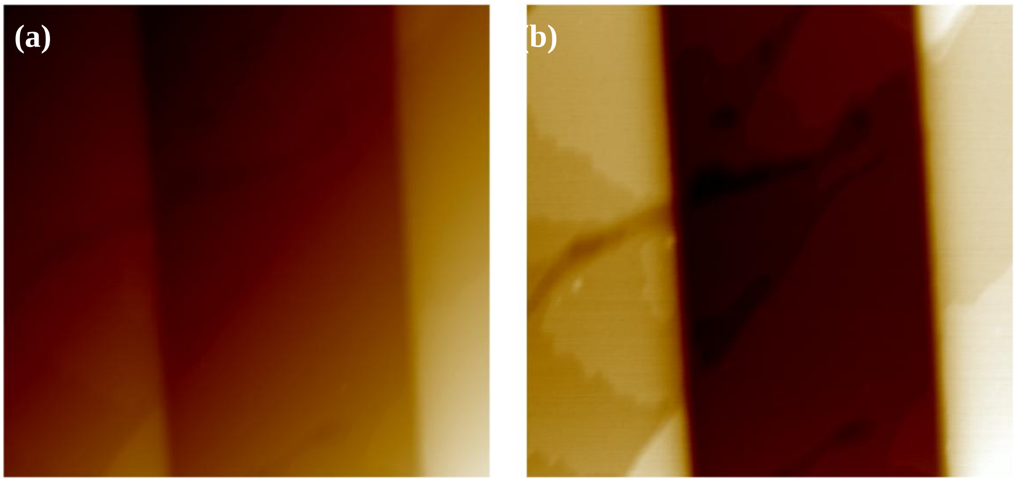

Figure 5.4. Example of a AFM image before and after plane-fitting. (a) Raw AFM measurement, z-scale: 2µm, xy-scale: 40 µm. (b) The same measurement, after plane-fitting, z-scale: 80 nm, xy-scale: 40 µm.

The starting image obtained from the AFM experiment is usually very rough, and needs treatment before conclusions can be reached. One major attribute of most surfaces explored with AFM is the 3 orders of magnitude size difference between the *xy*-scale (µm) and the *z*-scale (nm). Therefore, a very slight tilt or curvature of the tested sample has a major impact on the z-scale. In order to adjust for that problem, the plane is first fitted to get exploitable data. The second parameter to be taken into account is the size of the samples (several cm²) compared to the size of the tested area (several µm²).

Thus, multiple images have to be taken at different points of the sample to ensure that the observed topography is representative of the sample. Furthermore, in the case of transistors, it is crucial to probe the surface within the channel between source and drain, as this is where the charge transport takes place and it could differ from the surface around the device. Contrarily to some microscopy techniques such as optical microscopy that are only effective for data-collection at the xy-scale, atomic force microscopy allows quantitative measurement of the surface topography. Consequently, the height of nano-sized objects (fibers, nano-crystals) can be easily determined. Additionally, the root mean square surface roughness (R_{rms}) can be calculated, using the formula:

$$\mathrm{R_{rms}} = \sqrt{\frac{1}{n}[(\mathrm{R_1})^2 + (\mathrm{R_2})^2 + \cdots + (\mathrm{R_n})^2]} \qquad \textbf{Eq. 5.3}$$

with R the height of each of the n probed coordinates. The values of the roughness obtained by these means can be directly compared to the roughness of other samples, if the surface area it was calculated from is identical in each case.

5.2.1.2. Mechanical contact profilometer

In order to determine the thickness of deposited films, a thin line of material was removed from the film. The profile perpendicular to the line was probed using a mechanical contact profilometer (KLA-Tencor Alpha-Step IQ). The Alpha-Step IQ is a stylus-based scanning instrument with a maximum scan length of 10 mm (**Figure 5.5**). It has a transductive sensor that registers the vertical motion of the stylus. Since the sensor is very precise and sensible, the setup is placed on an isolation table. The sample is placed on the rotary sample stage, and moved under the stylus. An optical camera is used to correct the placement of the sample, and the stylus is lowered until it touches the surface of the film. The surface is probed at a speed of 10-100µm/s across the gap in the material, while the vertical motion sensor measures the height of the sample.

Once the profile is measured, the two sides of the pristine film around the gap are set at the same height (h_0), and the height of the gap (h_G) is obtained. The difference between h_0 and h_G accounts for the depth of gap and equals the thickness of the probed film. Multiple measurements of the thickness are taken across the whole sample to ensure that the film's thickness is uniform, and the average value of the thickness is calculated. This method is very reliable as it is not dependant on the z-axis tilt of the film.

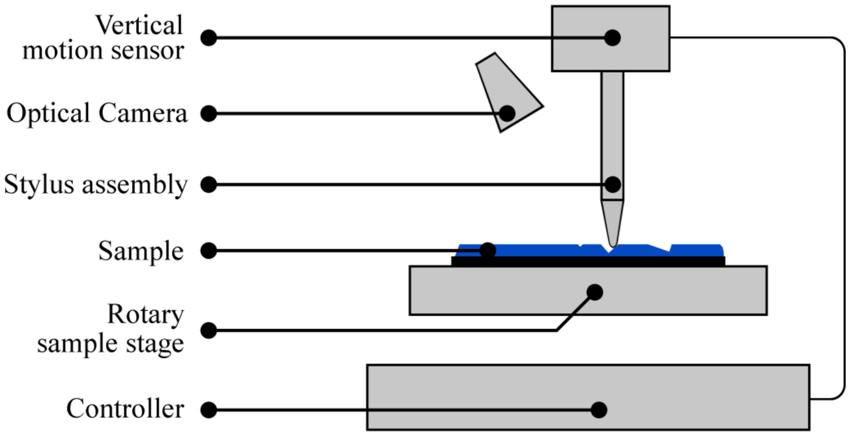

Figure 5.5: Schematic of a mechanical contact profilometer.

5.2.1.3. Contact angle

The contact angle was measured by means of a drop shape analyzer instrument (Krüss DSA 100, **Figure 5.6**). This setup is very powerful for the determination of the wetting of various films for multiple solvents, and was used as a tool of comparison between uncoated and self-assembled monolayer treated surfaces.

First, the sample to be tested is placed on the mobile sample stage, and the syringe is washed and filled with the desired solvent, in order to reproduce the same conditions as during the preparation of the sample for other experiments. A 5 µL drop of solvent is deposited onto the sample, and the optical camera is aligned and focused on the drop. The camera takes a picture of the deposited drop and the instrument software determines the position of the base of the sample and the shape of the drop of solvent. The angle between the surface and the tangent of the drop at the contact with the surface is measured and corresponds to the contact angle. The experiment is reproduced multiple times and an average value of the contact angle is calculated.

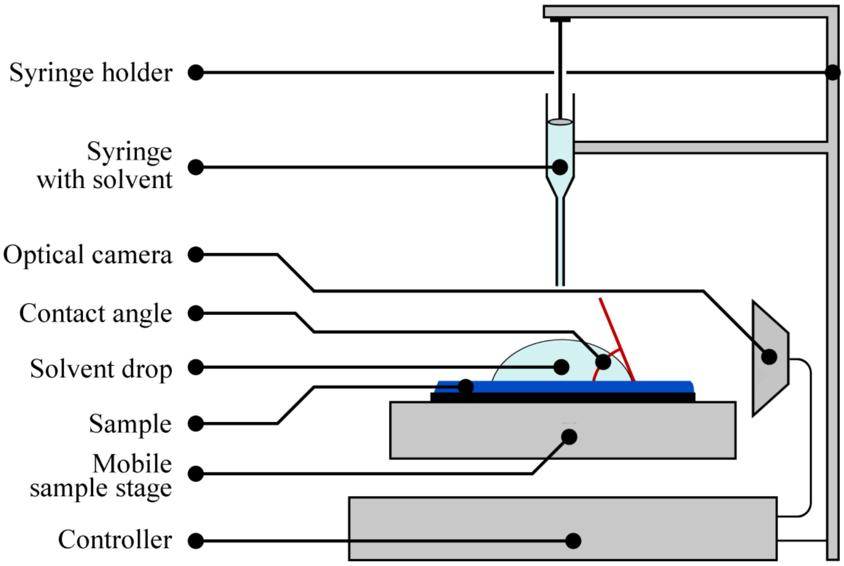

Figure 5.6: Schematic of a drop-shape analyzer setup

5.2.2. Ambient photoelectron spectroscopy

The determination of the Ionization Energy (IE) of the studied semiconductors and the work function of the electrodes was performed using a photoelectron spectrometer setup (RIKEN AC-2, **Figure 5.7**), which operates under ambient conditions. The spectrometer consists of a UV light source (deuterium arc lamp), coupled with a spectrometer, emitting light at a progressive selected wavelength (200-300 nm). The beam is focused on the surface of the sample. If the energy of the photons is sufficient to ionize the molecule, an electron is emitted from the surface towards the detector, which counts the number of emitted electrons.

The number of emitted electrons is plotted as a function of the energy of the photons in the UV-beam. The plot shows two distinct sections: a flat section at low energies, where very little emitted electrons are counted and a linear section, with increasing electron yields. The IE corresponds to the intersection between flat and linear areas of the plot.

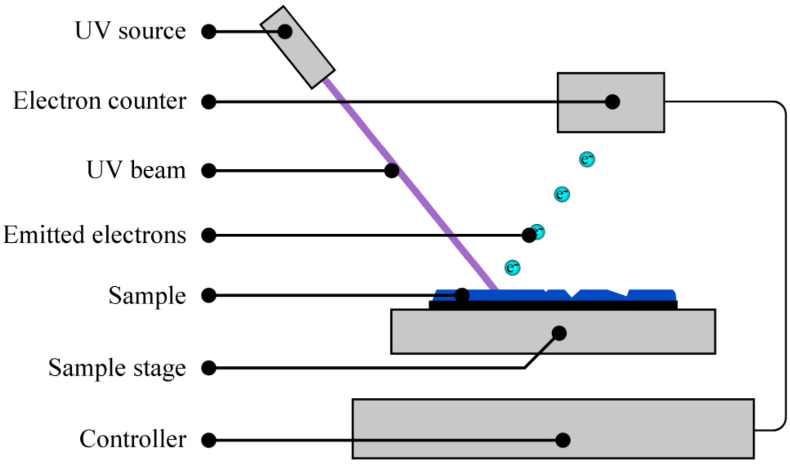

Figure 5.7: Schematic of an ambient photoelectron spectrometer.

5.2.3. Electrical characterization

5.2.3.1. Probe-station

The electrical characterization of all devices was performed using a Keithley 2636A Dual-channel System Source Meter (for testing of devices illuminated under short-pulse laser, a Keithley 2400 was used). The electrical characterization took place under nitrogen atmosphere in a glovebox, and unless specified otherwise, in the dark. The sample was placed on the sample stage of a Cascade Microtech M150 probestation (**Figure 5.8**) and electrically connected to the Keithley though sample stage and up to 3 tungsten probes. Connection was ensured using the mobile sample stage, micro-positioners and a camera integrated to the probe-station. The source meter was controlled using the softwares Labtracer and Labview (for hysteresis measurements).

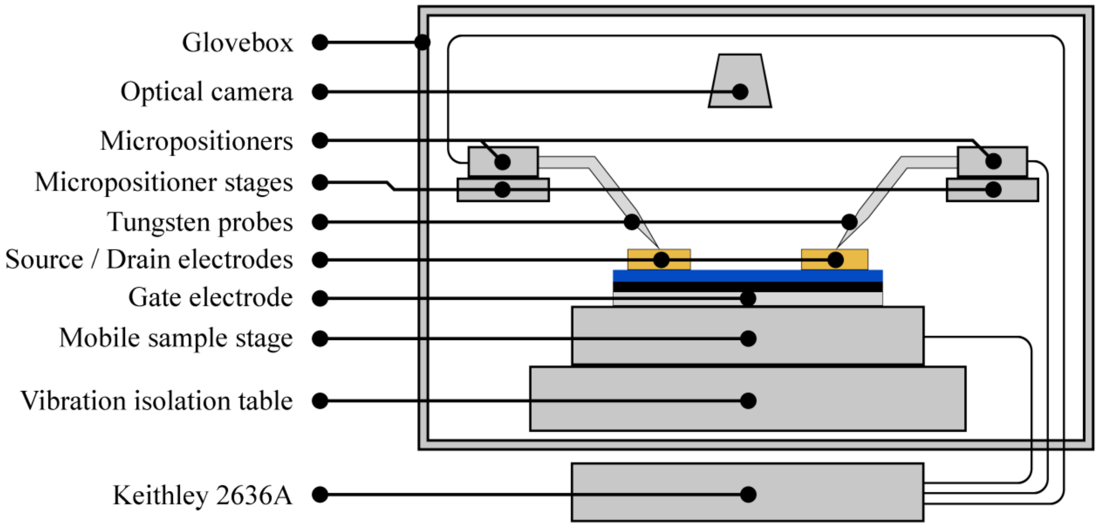

Figure 5.8: Electrical characterization setup for bottom-gate bottom-contact transistors.

5.2.3.2. Light irradiation set-ups

For electrical characterization during illumination, the probestation previously described was complemented by a monochromator (Polychrome V, Till Photonics). The wavelength and intensity of the irradiation was controlled using the software Polycon. The range of possible wavelengths was 300 – 700 nm, and the intensity could be tuned up to 74 μJcm^{-2} per second of irradiation at 313 nm, with the optical fiber located at 1cm of the target device. Illumination times could be programmed with microsecond precision. Short-pulse laser irradiation consisted of 3 ns pulses at controllable wavelength, using an Ekspla NT342. The intensity was 85±17 μJcm^{-2} for each 3 ns pulse at 313 nm. A schematic of the different illumination setups for the different applications is given in chapter 8.

Chapter 6. Solution processed field-effect transistors based on oligothiophene films with performances exceeding those of vacuum sublimed films

6.1. Introduction

Small semiconducting molecules have been the target of a wide research endeavor in the last decades, and have proven to exhibit interesting electrical performances, partly due to their more pronounced tendency to form crystalline domains when compared to their polymeric counterparts.[1-7] Among all organic small molecules, pentacene, rubrene and C_8-BTBT have so far exhibited the largest carrier mobilities, up to μ=43 cm²/Vs in off-center spin-coated C_8-BTBT film[8-10] In addition to the above-mentioned families of small molecules, a substantial activity has been devoted since over two decades to oligothiophenes as promising candidates for charge transport.[11-14] Initially they were deposited by means of thermal evaporation,[15,16] until substituted moieties were synthesized making it possible to process them from solution.[17,18] In particular, hexamethyl-substituted oligothiophene (DHnT) based devices, such as di-hexylquaterthiophene (DH4T) are easily accessible model systems that have proven to display a high resistance to the environment, due to their dense packing and hexyl chains working as a passivation layer[19-21] in addition to their charge transport performance in transistors.[22] Indeed, a previous work reported mobilities up to 0.23 cm^2/Vs for thermally evaporated DH4T.[23] However, these performances have only been achieved for a particular channel's width-to-length ratio of 1.5 and by using vacuum deposition as a preparation technique. Clearly such a low W/L is not optimal for low-power devices given that very high operating voltages must be applied in order to achieve the same output currents one can measure in devices featuring high W/L ratio. On the other hand, for vacuum deposited films the highest observed mobility amounted to 0.09 cm^2/Vs even when a higher width-to-length ratio was used.[24] As far as solution-processed films are concerned, the highest reported mobilty values amounted to $\mu = 0.043$ cm^2/Vs for ink-jet printed devices[25] and of $\mu = 0.012$ cm^2/Vs for spin-coated films,[26] indicating that there is much room for improvement on the processing side. Further, the statistical deviation of the average mobilities as well as the number of measured samples are seldom reported thereby lessening the reliability of the estimated materials properties. The I_{on}/I_{off} ratio reported in the literature for this material usually ranges between 10^5 and 10^7 [23-25] providing evidence for the good switching ability of the devices. Morphology and crystallographic parameters of DH4T films have been more recently investigated by Thierry *et al*. showing how DH4T can self-assemble into a highly ordered crystalline structure.[27] In their study, the crystalline order within domains produced by vacuum sublimation was similar to that found in crystalline domains grown from solution. High mobility solution-processed devices can be therefore produced if the kinetically governed process of film growth is controlled to achieve large crystalline domains,[28] eliminating or reducing the effect of grain boundaries, which are detrimental for the charge transport.[29-31]

In this chapter, we will focus on two routes for device performance improvement of solution processed DH4T transistors. The first part of the study will highlight performance boost by attaining a control over the kinetics of the self-assembly process via the optimization of the solvent evaporation rate combined with a careful choice of the source/drain and gate dielectric surface functionalization. The second part of the study will exploit the opposite of the “ideal” conditions, using DHnT molecules processed using the worst performing solution (chloroform), and demonstrate how dramatic improvements in electrical characteristics can be achieved through blending.

6.2. Methods

6.2.1. Device fabrication

The tested DH4T molecule was purchased from Polyera under the name ActivInk P0400. DH2T was purchased from Sigma Aldrich. DH6T was synthesized by Melucci’s group (ISOF- CNR, Bologna). All molecules were used as received, without further purification. Solvents were purchased from Sigma Aldrich and used as provided. Bottom-contact bottom-gate configuration transistors purchased from Fraunhofer Institute were used. They consist of on n^{++}-Si substrates with 230 nm of thermally grown SiO_2 as the gate dielectric and pre-patterned pairs of gold electrodes with interdigitated geometry as the source and drain, as illustrated in **Figure 6.1**. All samples were prepared and measured in a N_2 filled glovebox to avoid oxidative doping of the materials and ensure reproducibility of the experiments. Solution preparation, HMDS treatment and electrode functionalization were performed under nitrogen atmosphere. Electrode functionalization was performed by immersion a 4 mM solution of either 1-decanethiol (C_{10}) or 1*H*,1*H*,2*H*,2*H*-perfluorodecanethiol (FC_{10}) (**Figure 6.2**) in ethanol for 12 hours. C_{10} has been selected to increase the wetting abilities of the wafer. Substrates were thoroughly rinsed by squirting 100 µL of absolute ethanol for 5 times. HMDS and OTS, were both purchased from Sigma-Aldrich (**Figure 6.3**). HMDS was spin coated at 1500 RPM on the substrate and annealed for 1 hour at 100 °C. OTS treatment consisted of a 12-hours immersion of the ozone-treated wafer into a 10 mM solution of OTS in toluene with 30 min of heating at 60 °C at the beginning of the immersion. The samples were afterwards rinsed with toluene and heated for 60 min at 60 °C. The solution was prepared by dissolving DHnT in 1,2-dichlorobenzene. The solution was afterwards stirred and heated at 100 °C for 1 hour. 70 µL of the cold solution were drop-cast on the substrate. Drop-casting was chosen as the deposition technique since, compared to spin-coating, it is more similar to the ink-jet printing process used in real device fabrication.

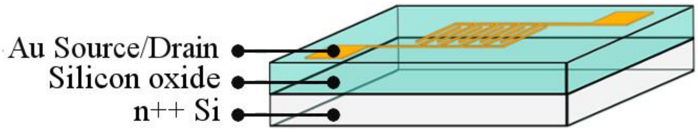

Figure 6.1: Bottom-gate devices on silicon oxide. Schematic representation of the pre-patterned bottom-contact bottom-gate wafer used for all the devices in this chapter.

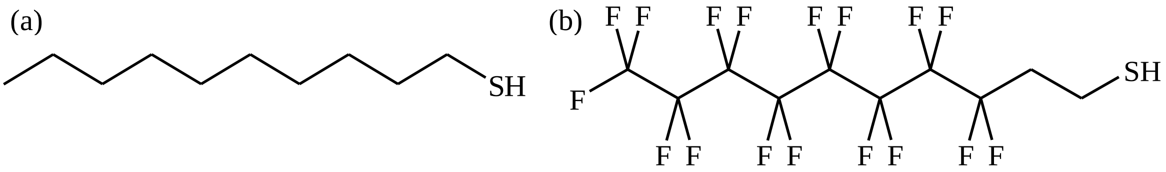

Figure 6.2: Molecular structures for electrode functionalization. Chemical formulae of (a) 1-decanethiol (C_{10}) and (b) 1*H*,1*H*,2*H*,2*H*-perfluorodecanethiol (FC_{10}) used for electrode functionalization.

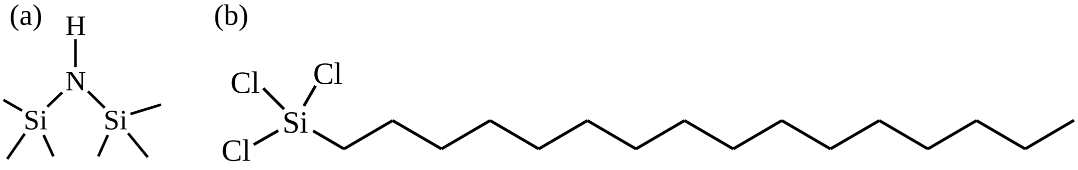

Figure 6.3: Molecular structures of SAMs for dielectric treatment. Chemical formulae of (a) hexamethyldisilazane (HMDS) and (b) Octadecyltrichlorosilane (OTS) used for dielectric treatment.

6.2.2. Device characterization

OFET properties were evaluated under positive or negative gate bias to explore the majority charge carrier type and device performance. Experimental data were analyzed using standard field-effect transistor equations (for *p-type* semiconductors):

$$I_{DS} = -\frac{W}{2L}\mu C_{TOT}(V_{GS} - V_{Th})^2 \qquad \textbf{Eq. 6.1}$$

where I_{DS} is the source-drain current, V_{GS} is the gate voltage, C_0 is the capacitance per unit area of the dielectric layer, V_{Th} is the threshold voltage, and μ is the field-effect mobility in the saturation region. The mobilities were determined in the saturation regime, *i.e.* at $V_{DS} = -60$ V from the slope of plots of $(I_{GS})^{1/2}$ versus V_{GS}. In all the characterized sets, the voltage range was kept constant for both I_{DS} – V_{DS} and I_{DS} –V_{GS} to ensure full comparison among different samples.

In order to evaluate the contact resistance ($R_{contact}$), the conductivity as a function of the channel length has been measured for >110 devices. By subtracting the parasitic contribution of the contact resistance from the total measured resistance ($R_{measured} = R_{total} = R_{channel} + R_{contact}$) the field-effect mobility values could be adjusted.

For each device (2.5 µm, 5 µm, 10 µm and 20 µm channels) the inverse of the transconductance (g_m) which takes into account the whole resistive contribution coming from both material and contacts has been extracted from the I_{DS}-V_{GS} graphs in the linear regime.

$$R_{TOT} = (g_m)^{-1} = \left(\frac{\partial I_{DS}}{\partial V_{GS}}\right)^{-1} \qquad \textbf{Eq. 6.2}$$

R_{total} values have been plotted as a function of the channel length for 4 samples at each V_{DS} = -20 V and V_{DS} = -25 V. The resistance calculated at channel length (L) = 0 µm is the contact resistance contribution to the total resistance.

An ambient photoelectron spectrometer working at ambient conditions was employed to determine the ionization energy (IE) of the DHnT films and the work function of the different SAM-functionalized gold electrodes.

6.2.3. Atomic Force microscopy (AFM)

The morphology of the large crystallites has been mapped by performing topographical AFM imaging in tapping mode in air environment using a Veeco Dimension 3100 operating on a Nanoscope IV control unit. When multiple layers form one on top of the other, we can evaluate the height of each step by performing a high amount of step-height measurements. Once the size of the layer in known, we can evaluate the tilt angle (α) of the molecule towards the surface:

$$\alpha = \theta - \arccos\left(\frac{h}{l}\right) \qquad \textbf{Eq. 6.3}$$

with *h* the height of the layer, *l* the length of the molecule (estimated value via energy minimization) and θ the angle difference between the straight up position and the surface (90°).

6.2.4. Ultraviolet photoelectron spectroscopy

The ionization energy value of the different SAMs and of DHnT were measured by a Photoelectron Spectrometer, AC-2, by RKI Instruments working at ambient conditions. The analyzed films were realized following the same experimental procedures as those employed in the realization of FET devices in order to ensure full consistency with the films that were electrically characterized. Ionization energy values of gold without treatment and treated with different thiols are reported in the **Table T6.1**.

Table T6.1: Ionization energy measured by ambient photoelectron spectrometer.

Procedure	IE (eV)
Bare Au	4.80
Au FC_{10} treated	5.43
Au C_{10} treated	4.32

FC_{10}: 1H,1H,2H,2H-perfluorodecanethiol ; C_{10}: undecanethiol.

6.3. DH4T transistors

Initially this prototypical molecule (DH4T) was tested in three different chlorinated solvents namely chloroform ($CHCl_3$), 1,2-dichlorobenzene (DCB) and chlorobenzene (CB) (**Figure 6.4**). The choice of the solvent was found to be crucial for the device performance. In particular, multi-scale morphological characterization, from the hundreds-of-μm down to sub-μm scale, was carried out both by optical (OM) and atomic force (AFM) microscopy, therefore supporting the electrical and structural characterization presented later in the manuscript.

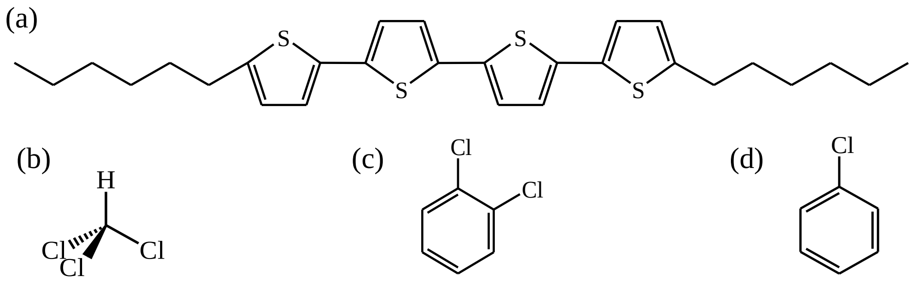

Figure 6.4: Molecular structures of DH4T and the 3 tested solvents. Chemical formulae of (a) dihexylquaterthiophene (DH4T), (b) chloroform, (c) dichlorobenzene and (d) chlorobenzene.

Figure 6.5 compares the morphologies of DH4T films prepared by drop-casting a 100 µL drop on a SiO_2/Si-n^{++} substrate from 1 mg/mL concentrated solution in chloroform, chlorobenzene (CB) and dichlorobenzene (DCB). The surface of the DH4T films deposited from chloroform solution (**Figure 6.5, a** and **6.5, d**) consists of small crystals often not interconnected, whereas the films obtained using chlorobenzene or dichlorobenzene as a solvent (**Figure 6.5, b** and **6.5, e, 6.5, c** and **6.5, f**) display larger and more uniform crystalline domains in OM images. The film uniformity without presence of defects over a larger scale for chloro- and dichlorobenzene films does significantly decrease the occurrence of grain boundaries. Conversely, films deposited from $CHCl_3$ displayed very high surface roughness on the mesoscale (R_{RMS} - of 165 nm), while films prepared from CB showed a decreased roughness (R_{RMS} = 22 nm). Films prepared from DCB solutions exhibited an even smaller roughness (with R_{RMS} = 7 nm).

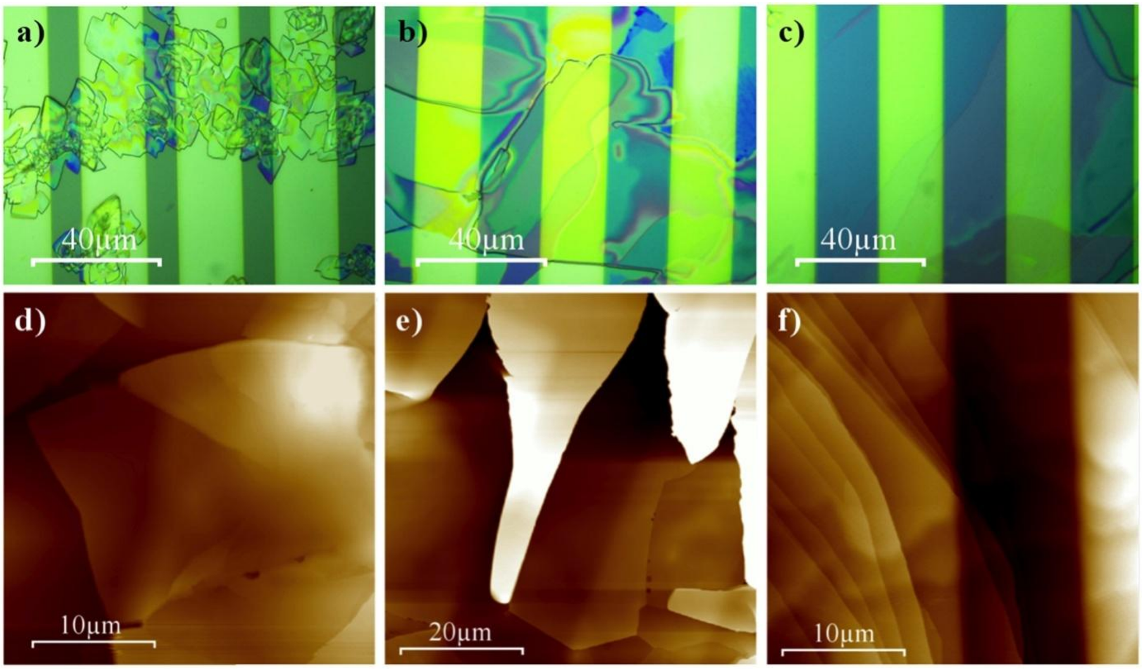

Figure 6.5: Optical microscopy and atomic force microscopy. Top panel: Optical microscope images of DH4T films produced by drop-casting solutions in (a) $CHCl_3$, (b) CB, (c) DCB. Bottom panel: Tapping Mode AFM topography images of DH4T films produced by drop-casting solutions in (d) $CHCl_3$, (e) CB, and (f) DCB. Z-scales: (d) 2 µm, (e) 500 nm, (f) 120 nm.

Optical microscope images confirm that when the optimized procedure (described below) is used, the crystallites processed from DCB solvent are large enough to easily bridge the source-drain electrodes for channel lengths up to 20 µm (**Figure 6.6**). For longer channel lengths such as 60 µm, the crystallites are only slightly larger than the channel, leading to the presence of more grain boundaries within the channel. The flat crystalline samples prepared from CB exhibit a greater roughness and more grain boundaries are present whilst those from chloroform tend to form extremely rough aggregates (**Figure 6.5**).

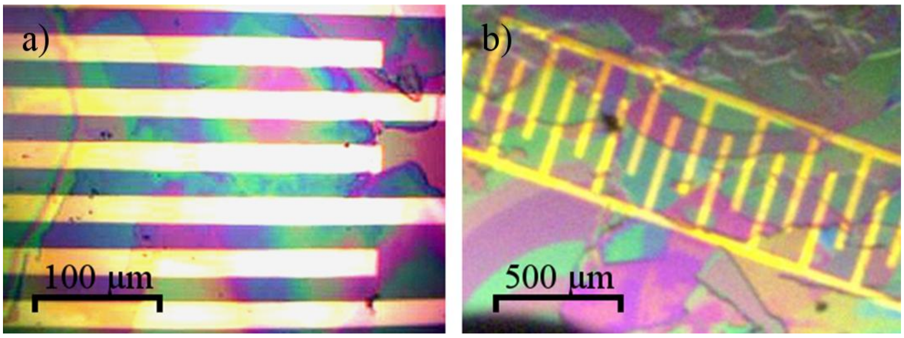

Figure 6.6: Optical microscope images of DH4T thin film organic field-effect transistors based on the optimized procedure. (a) DH4T drop-casted on 20-µm-channel electrodes. (b) DH4T drop-casted on 60-µm-channel electrodes.

When employed as the active layer in a bottom-contact bottom-gate FET with Au source and drain electrodes, drop-cast films from solution in $CHCl_3$ exhibited two orders of magnitude lower mobility and I_{on}/I_{off} when compared to those obtained by using DCB and CB as a solvent, as highlighted in the graphs of **Figure 6.7** . A careful concentration-dependent study was carried out in order to find out the concentration giving the highest mobility (**Table T6.2**). The best mobility was recorded when a 5 mg/mL solution was drop-cast from DCB (0.038 cm^2/Vs)**.** Furthermore, the evaporation rate of the solvent was found being a critical parameter when producing DH4T-based OFETs by solution processing. A three-fold improvement of the charge carrier mobility in drop-cast films was achieved when the evaporation rate was slightly reduced (by a factor of 2) by means of a top cover with a controlled aperture surface. However, when the evaporation rate was more extensively reduced (tightly sealed cover) a drop in mobility appeared up to a factor of ten. As can be seen on the OM images (**Figure 6.8**), the evaporation rate of 0.1 produced the film with the least amount of defects. This is due to the solvent-vapor annealing[32] caused by the tightly sealed cover.

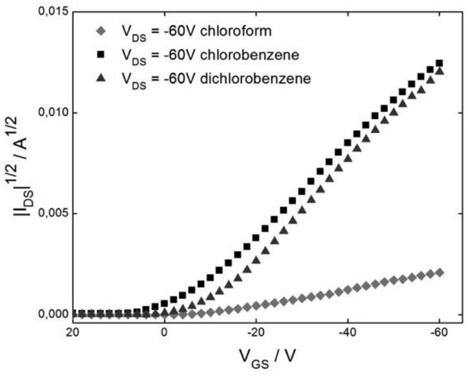

Figure 6.7: Comparative $I_{DS}V_{GS}$ graphs of drop-casted DH4T films in saturation regime, for chloroform, chlorobenzene and dichlorobenzene.

Table T6.2: Detailed correlation between DH4T processing conditions, solvent employed, and electrical performances. All films were drop-cast on HMDS-treated silicon oxide and untreated gold electrodes.

Solvent	**Self-assembled monolayer**	**Volume of DH4T casted, Concentration**	**Evaporation rate [Butyl acetate = 1]**	**Average[f] mobility [cm²/Vs]**	**I_{on}/I_{off}**	**Average[f] threshold voltage [V]**
$CHCl_3$	HMDS	100 µL, 1 mg/mL	11.6	6.85×10^{-5}	10^{1}-10^{4}	-12
CB[a]	HMDS	100 µL, 1 mg/mL	0.2[c]	1.09×10^{-3}	10^{1}-10^{4}	-7
DCB[b]	HMDS	100 µL, 1 mg/mL	0.2[c]	6.63×10^{-3}	10^{4}-10^{6}	-8
DCB[b]	HMDS	70 µL, 5 mg/mL	0.2[c]	8.80×10^{-3}	10^{4}-10^{5}	-37
DCB[b]	HMDS	100 µL, 3.5 mg/mL	0.2[c]	1.11×10^{-2}	10^{4}-10^{5}	-36
DCB[b]	HMDS	70 µL, 10 mg/mL	0.2[c]	4.34×10^{-4}	10^{1}-10^{3}	-14
DCB[a]	HMDS	70 µL, 2 mg/mL	0.02[e]	7.70×10^{-4}	10^{2}-10^{3}	-45
DCB[b]	HMDS	70 µL, 5 mg/mL	0.02[e]	3.33×10^{-3}	10^{4}-10^{5}	-39
DCB[b]	HMDS	100 µL, 3.5 mg/mL	0.02[e]	2.00×10^{-3}	10^{3}-10^{5}	-43
DCB[b]	HMDS	70 µL, 5 mg/mL	0.1[d]	2.58×10^{-2}	10^{4}-10^{5}	-39
DCB[b]	OTS	70 µL, 5 mg/mL	0.1[d]	6.14×10^{-2}	10^{7}	-10

[a] Chlorobenzene; [b] dichlorobenzene; [c] solvent left to evaporate at normal rate (evaporation taking between 12 h and 18 h); [d] solvent left to evaporate at slow rate (evaporation taking between one and two days); [e] solvent left to evaporate at very slow rate (evaporation taking between one and 5 and 7 days); [f] average over at least 16 devices.

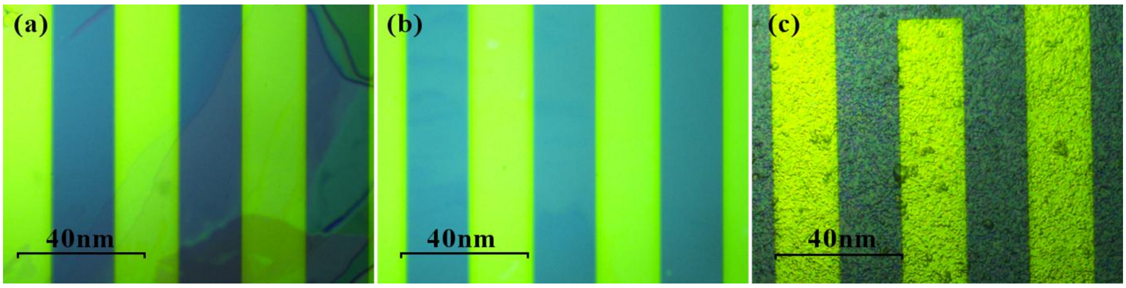

Figure 6.8: Optical microscope images of DH4T drop-cast from dichlorobenzene. (a) normal evaporation rate of 0.2, uncovered (b) evaporation rate reduced to 0.1 using a glass cover (c) evaporation rate reduced to 0.02 using a tightly sealed glass cover. Butyl acetate = 1.

The procedure that exhibited the best mobility, i.e. 70 µL of DH4T at 5 mg/mL drop-cast from DCB, evaporation rate of 0.1, will be referred to as the "*optimized procedure*". It has been successfully reproduced on > 110 devices using hexamethyldisilazane (HMDS) as a surface treatment. Noteworthy, in spite of the fact that drop-casting is a deposition technique which is supposed to lead to uneven device-to-device performances due to thickness variation in the x-y plane, the presence of large flat crystals spanning over hundreds of micrometers allowed for the fabrication of devices whose electrical parameters featured mobilities with standard deviations which were absolutely comparable to those achieved in spin-coated films (**Table T6.3**). In very few instances (less than 3% of the cases), the presence of non-functioning devices could be ascribed to the insufficient coverage of the device upon deposition of the material. As highlighted by AFM and OM, the major differences in mobility between the above-mentioned cases would all stem from the occurrence of grain boundaries in the crystalline films which exhibited a highly crystalline nature of the film as confirmed by GIXD analysis (**Figures 6.9** and **6.10**).

Table T6.3: Optimized procedure using HMDS, for channel lengths comprised between 2.5 µm and 20 µm.

Sample	**Functioning devices**[a]	**Average**[b] **mobility [cm²/Vs]**	**Average**[b] **I_{on}/I_{off}**	**Average**[b] **threshold voltage [V]**
DCB08	16	$2.58 \pm 1.52 \times 10^{-2}$	2×10^5	-39 ± 5
DCB11	16	$2.68 \pm 0.97 \times 10^{-2}$	5×10^5	-34 ± 4
DCB12	16	$2.73 \pm 1.40 \times 10^{-2}$	5×10^6	-19 ± 9
DCB13	14	$4.10 \pm 1.50 \times 10^{-2}$	6×10^6	-29 ± 9
DCB14	16	$2.80 \pm 1.25 \times 10^{-2}$	2×10^6	-28 ± 7
DCB15	16	$3.05 \pm 1.19 \times 10^{-2}$	6×10^5	-29 ± 8
DCB16	15	$3.29 \pm 1.99 \times 10^{-2}$	1×10^6	-32 ± 6

[a] number of functioning devices (out of 16 devices per sample for small channels, out of 8 devices for large channels); [b] average over all functioning transistors.

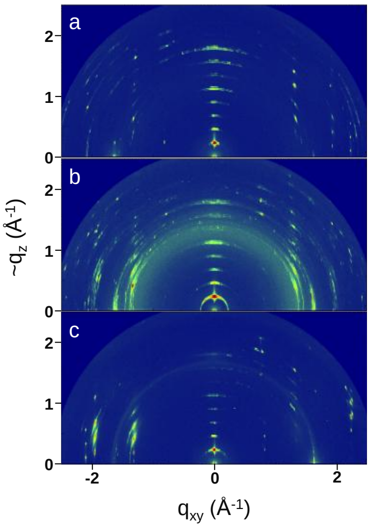

Figure 6.9: 2D GIXD patterns of DH4T drop-casted on bare Si. (a) chloroform used as a solvent ; (b) dichlorobenzene used as a solvent ; (c) using the optimized procedure (HMDS).

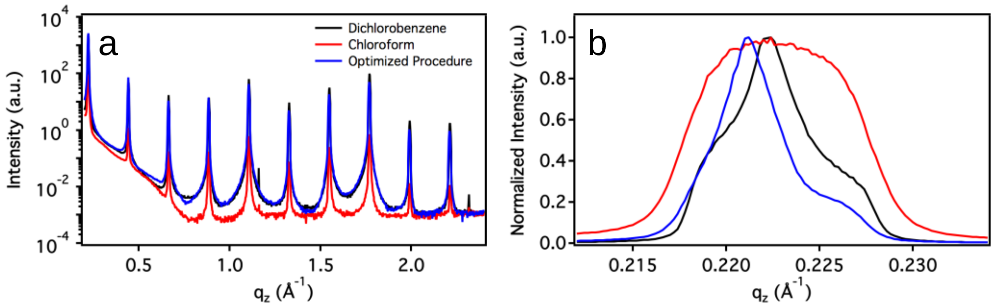

Figure 6.10: GIXD measurements. (a) Diffraction pattern of DH4T drop-casted on bare Si along the q_z direction showing a high number of (00L) peaks up to fairly large q values. (b) Analysis of a specific region shows an overlap of several (001) peaks, which is indicative of the polycrystalline nature of the drop-casted films.

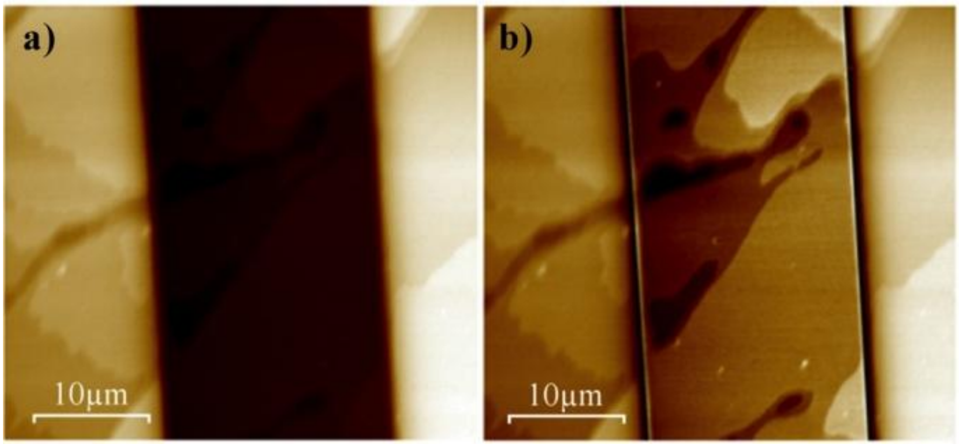

Figure 6.11: Tapping Mode topography AFM images of DH4T crystallites in a 20 µm channel. (a) Unmodified image; (b) linear height flattening introduced in the image to show differences between channel and electrodes. a,b) Z-scales=70 nm.

When the optimized procedure is used (**Figure 6.11**), the crystallites readily bridge the source and drain electrodes. Furthermore, the morphology of the crystallites, bridging and following the profile of the electrodes, seems to suggest the absence of nucleation sites in the interelectrodic region. This indicates that the formation of the crystallites does commence in the solvent and only later these structures “land” on the electrodes and expand via self-assembly.

In addition to the effects of the solvent and its evaporation rate on the electrical performances, a thorough physico-chemical analysis of the metal/semiconductor interface was performed. In particular, the gold electrodes were functionalized with either 1-decanethiol ($CH_3(CH_2)_9$-SH) or 1*H*,1*H*,2*H*,2*H*-perfluorodecanethiol ($CF_3(CF_2)_7CH_2CH_2$-SH) forming chemisorbed self-assembled monolayers (SAM). By means of an ambient photoelectron spectroscopy, we measured an ionization energy of 5.20 ± 0.02 eV for DH4T films, whilst the work function of uncoated gold, 1-decanethiol-functionalized gold and perfluorodecanethiol-functionalized gold resulted 4.80 ± 0.20 eV, 4.32 ± 0.02 eV and 5.43 ± 0.02 eV, respectively. Interestingly, the best energy match for injecting holes in the HOMO of DH4T should be attained when perfluorodecanethiol SAMs are employed, followed by uncoated gold and 1-decanethiol-functionalized electrodes. However, both mobility and currents were found being slightly higher when functionalized electrodes were utilized, revealing that the affinity of the semiconductor for the surface and the physical interface metal/electrode play a key role (**Table T6.4**). Investigating the shape of the output curves (**Figure 6.12**), no notable difference in injection capacity was found between the untreated electrodes and the two used SAMs. The surface energy of SAM-functionalized electrodes is lower than in uncoated gold as revealed through contact angle measurements using DCB as liquid. Among the three difference cases, the best performing devices were ultimately those bearing SAM-functionalized source and drain electrodes, owing to a lower surface energy and higher surface affinity of the DH4T molecules. To verify the latter statement we performed contact angle measurements by using solutions of DH4T in DCB (5 mg/mL) as performed in the case of the corresponding devices. The experiment did not reveal appreciable differences with respect to the former contact angle measurements performed with pure DCB (**Figure 6.13**).

Table T6.4: Comparison of different 5mg/mL DH4T films drop-casted from dichlorobenzene using HMDS. FC_{10}: 1H,1H,2H,2H-perfluorodecanethiol ; C_{10}: 1-decanethiol.

Treatment	**Channel length / µm**	**Average mobility / cm²/Vs**	**I_{on}/I_{off}**	**Average threshold voltage / V**
none	2.5-20	8.80×10^{-3}	10^4-10^5	-37
C_{10}	2.5-20	1.08×10^{-2}	10^5-10^6	-16
FC_{10}	2.5-20	1.04×10^{-2}	10^3-10^6	-10

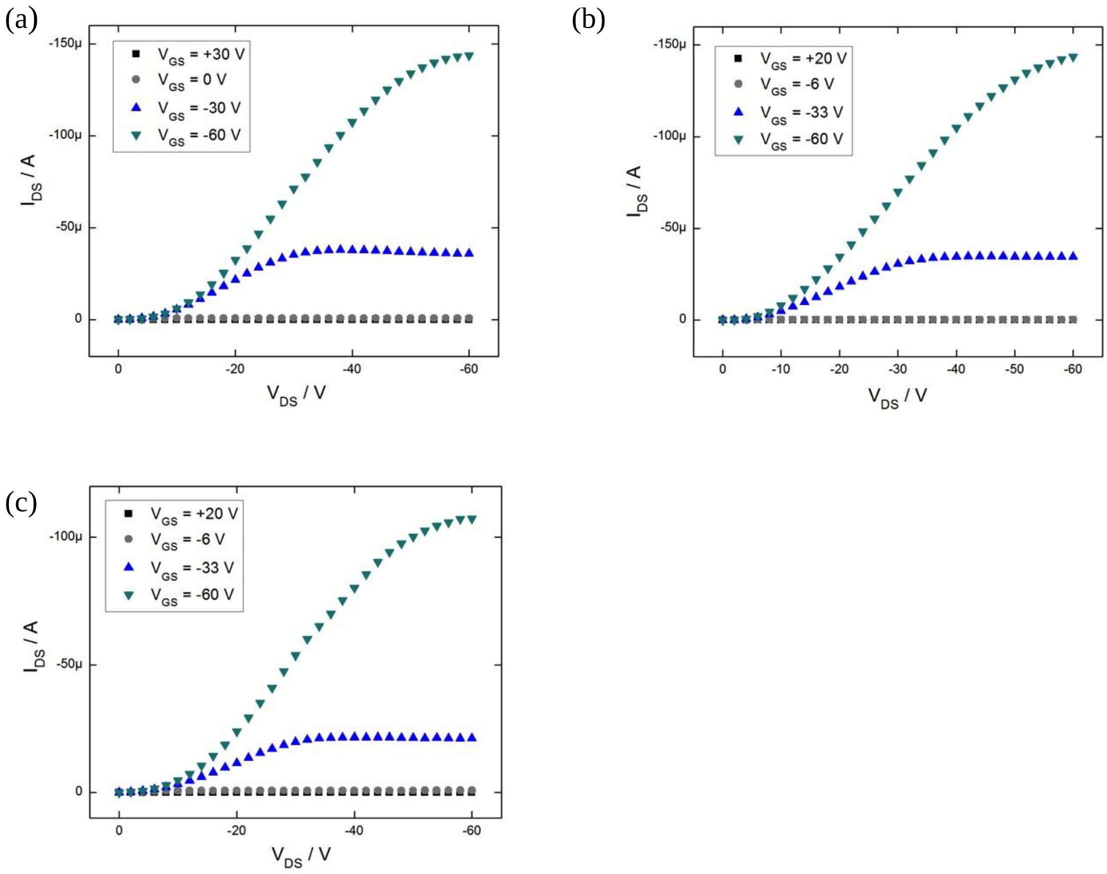

Figure 6.12: $I_{DS}V_{DS}$ plots of DH4T films on untreated (a), 1-decanethiol treated (b) and 1H,1H,2H,2H-perfluorodecanethiol treated (c) electrodes.

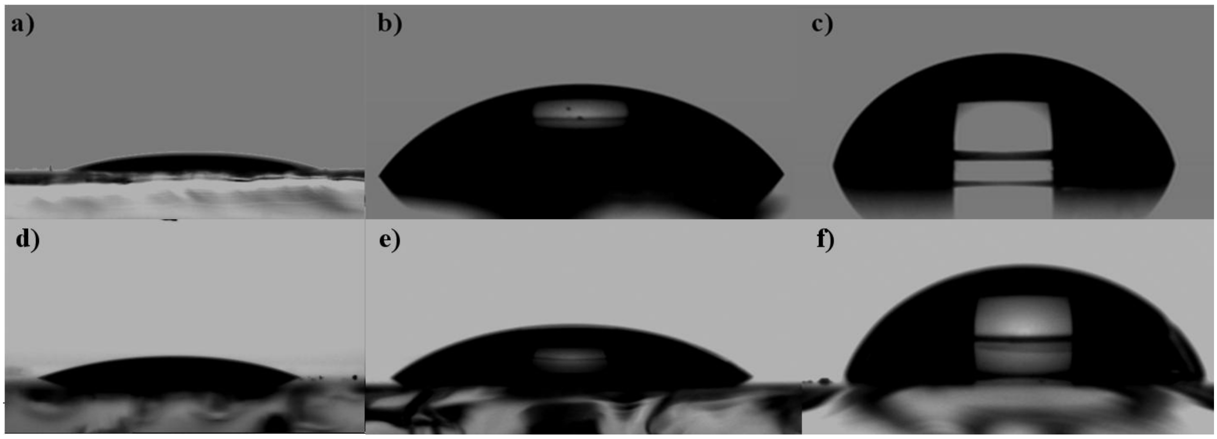

Figure 6.13: Dichlorobenzene contact angle measurements, with contact angle values: (a): uncoated gold (19.2°); (b) 1-decanethiol (57.8°); (c): 1H,1H,2H,2H-Perfluorodecanethiol (76.8°). Dichlorobenzene with DH4T at 5mg/mL contact angle measurements: (d) uncoated gold (18.4°); (e) 1-decanthiol (45.3°); (f) 1H,1H,2H,2H-Perfluorodecanethiol (72.6°).

In addition, all films encompassed in this study exhibit high degree of crystallinity as confirmed by GIXD analysis (**Figure 6.9 and 6.10**); interestingly, the structural order within thin films does not differ significantly between samples fabricated under different preparation conditions. We want to point out here that, in general, OFETs probe only the dielectric-semiconductor interface[33] while GIXD probes the bulk crystalline structure, which may differ from that of the interfacial layer.[34] Because DH4T tends to crystallize into relatively flat platelets, here we assume that the interface exhibits the same crystalline structure as that of the bulk crystal. Most probably, the difference in mobility does not stem from the crystalline order of the film but rather from the difference in the crystallite size as a result of each specific preparation condition. In other words, a high number of small crystals translates into a high number of grain boundaries, which strongly limit charge transport.

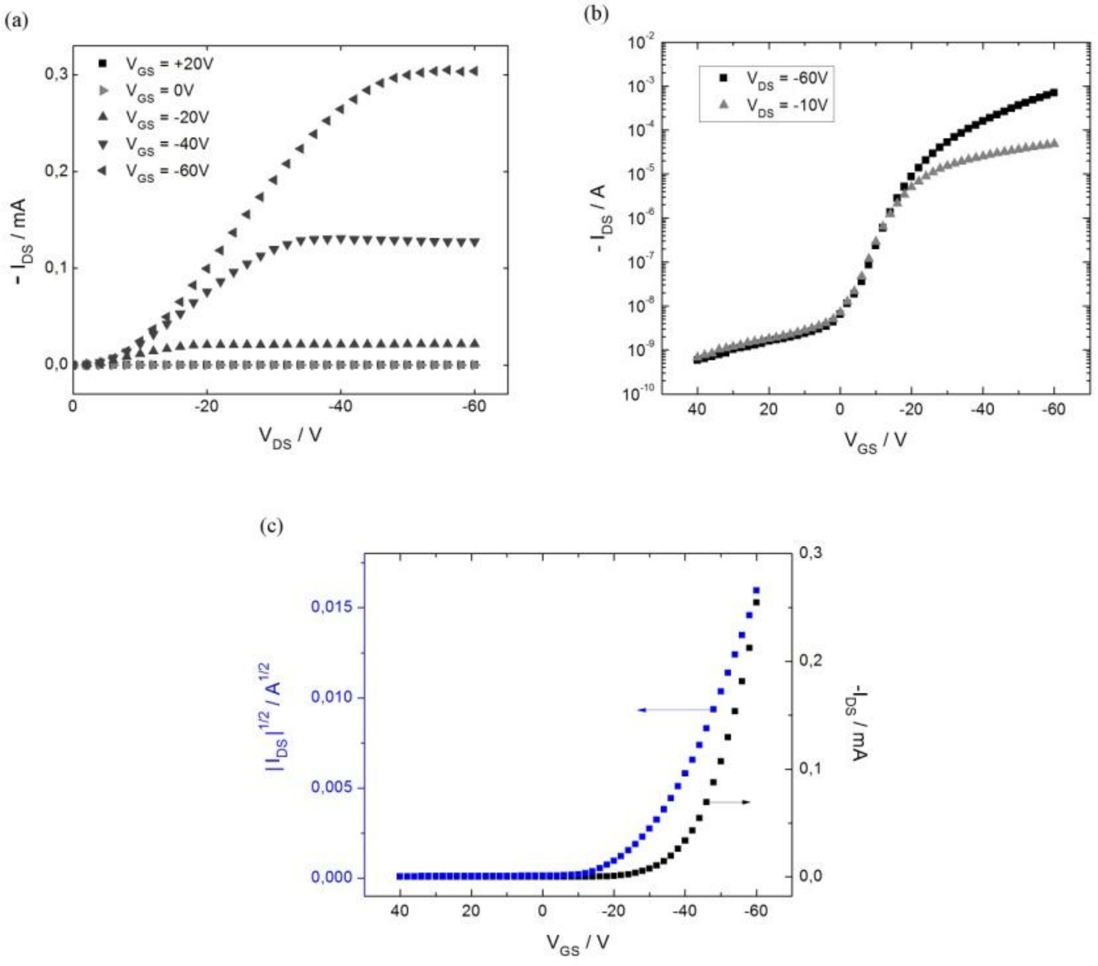

Figure 6.14: DH4T OFET based on the *optimized procedure* using HMDS and 1-decanethiol treated electrodes. (a) Output characteristics. (b) Transfer characteristics of the same device in the linear and saturation region (log scale). (c) I_{DS} vs. V_{GS} and Sqrt(I_{DS}) vs. V_{GS} in saturation regime (V_{DS} = - 60V, L = 20 µm, W = 10 mm).

Furthermore, even the devices prepared with the optimized procedure based on the use of HMDS and 1-decanethiols to functionalize the interface of the organic semiconducting material with the dielectrics and electrodes, respectively, show an unfavorable charge injection, as evidenced from the non-linearity of the output curve at low source-drain voltage (**Figure 6.14**). For channel length comprised between 2.5 µm and 20 µm, hole mobility of about 0.06 cm²/Vs is observed on > 110 devices, with an average I_{on}-I_{off} ratio of ~10^5 (**Table T6.3**). The highest hole mobility observed amounts to 0.08 cm²/Vs and the highest I_{on}-I_{off} ratio is of ~5×10^7. It is worth pointing out that we did not observe any electron (*n*-type) transport in any device.

Further, when the size of the channel reaches 60 µm and over, we observed a 4- and 10-fold decrease in mobility and I_{on}/I_{off}, respectively (see SI). The amount of devices with observable semiconducting characteristics is considerably lower as well (37% compared to 97%). The threshold voltage is not affected by the change of the channel length.

The average contact resistance value extracted from I_{DS}-V_{GS} graphs in the linear regime is reported in **Table T6.5** and amounted to ~100 kΩ (103 kΩ) (See SI). By using the $R_{contact}$ value of 103 kΩ, the mobility was adjusted using $R_{channel}$ instead of R_{total} provided that $R_{channel} = R_{total} – R_{contact}$ (**Tables T6.6 and T6.7**). The obtained values are plotted as a function of the channel length. We notice that values of the mobility adjusted for $R_{contact}$ ~ 100 kΩ are uniform over all the channel lengths revealing that mobility is an intrinsic parameter of the material and its value should not depend on a specific channel length. When mobilities are corrected for the contact resistance, we observe an average mobility topping 0.05 cm²/Vs for the small channels (2.5 µm and 5 µm) (**Figure 6.15**).

Table T6.5: Contact resistance. Values for each sample at V_{DS} = -20V and V_{DS} = -25V.

Sample	**$R_{contact}$ (V_{DS} = - 20 V) / kΩ**	**$R_{contact}$ (V_{DS} = - 25 V) / kΩ**	**Average $R_{contact}$ / kΩ**
DCB11	99	71	85
DCB12	90	76	83
DCB13	110	103	106
DCB15	160	114	137
Average (σ)	115	91	103

Table T6.6: Correction factors. (contact resistance).

L / µm	**$\mu_{uncorrected}$ / cm²/Vs**	**$\mu_{corrected}$ cm²/Vs**	**$\mu_{corrected}/\mu_{uncorrected}$ (R = 103kΩ)**
2.5	5.31×10^{-3}	1.34×10^{-2}	2.61
5	7.40×10^{-3}	1.33×10^{-2}	1.80
10	9.31×10^{-3}	1.29×10^{-2}	1.39
20	1.14×10^{-2}	1.38×10^{-2}	1.21

Table T6.7: Mobility values corrected for contact resistance.

L / µm	Uncorrected mobility / cm²/Vs	Mobility corrected for $R_{contact}$ = 103 kΩ
2,5	1.95×10^{-2}	5.00×10^{-2}
5	2.84×10^{-2}	5.01×10^{-2}
10	3.13×10^{-2}	4.38×10^{-2}
20	3.72×10^{-2}	4.49×10^{-2}

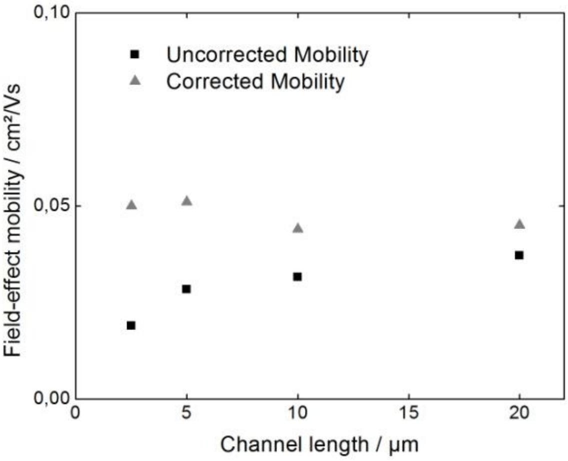

Figure 6.15: Average field-effect mobility in the saturation regime as a function of the channel length. The devices were prepared according to the *optimized procedure* on 1-decanethiol treated gold electrodes.

Significantly, in contrast to HMDS-functionalized devices prepared with the *optimized procedure*, output curves do not indicate the presence of a high contact resistance when octadecyltrichlorosilane (OTS) is used to functionalize the surface of the dielectric silicon oxide (**Figure 6.16**). The devices exhibit mobilities up to 0.10 cm²/Vs and I_{on}/I_{off} up to 5×10^7 (**Table T6.8**). The average threshold voltage was found to be -12 V in the saturation regime and -9 V in the linear regime, which is 2- to 3-fold smaller in absolute value if compared to HMDS-treated devices. Figure 5c shows that the transfer curve is bent at high gate voltages. This would indicate that the device is prone to bias stress. Notably, HMDS-treated devices were found to exhibit a more pronounced bias stress when measured at the same V_{GS}-V_{Th} (**Figure 6.17**). These findings were confirmed by I_{DS}-time curves (**Figure 6.18**). However, the gate voltage was swept up to -60 V also in OTS-treated FETs for the sake of consistency with the HMDS case. Given that OTS-treated devices showed lower (in absolute value) threshold voltage, the above-mentioned bias stress can be ascribed to the higher V_{GS}-V_{Th} value employed when testing OTS-treated samples.

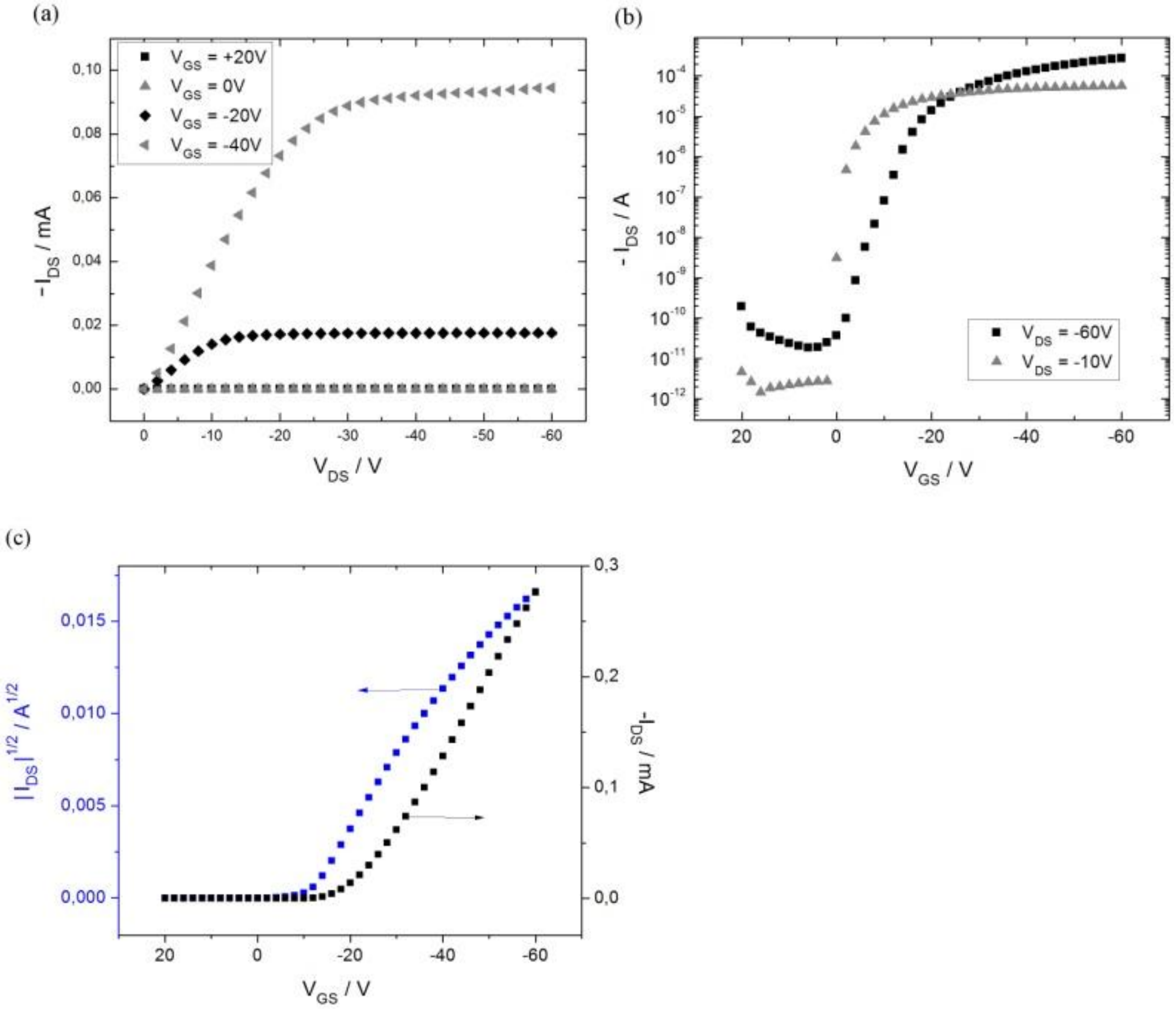

Figure 6.16: DH4T OFET based on the *optimized procedure* using OTS and 1-decanethiol treated electrodes. (a) Output characteristics. (b) Transfer characteristics of the same device in the linear and saturation region, plotted in logarithmic scale. (c) I_{DS} vs. V_{GS} and Sqrt(I_{DS}) vs. V_{GS} in saturation regime (V_{DS} = - 60 V, W = 10 mm, L = 20 µm).

Table T6.8: Optimized procedure using OTS.

Sample	**Average$^{a)}$ mobility [cm²/Vs]**	**Average$^{a)}$ I_{on}/I_{off}**	**Average$^{a)}$ threshold voltage [V]**
DCB22	$6.12 \pm 2.65 \times 10^{-2}$	1×10^{7}	-10 ± 5
DCB23	$6.14 \pm 0.85 \times 10^{-2}$	1×10^{7}	-13 ± 3

$^{a)}$average over all functioning transistors.

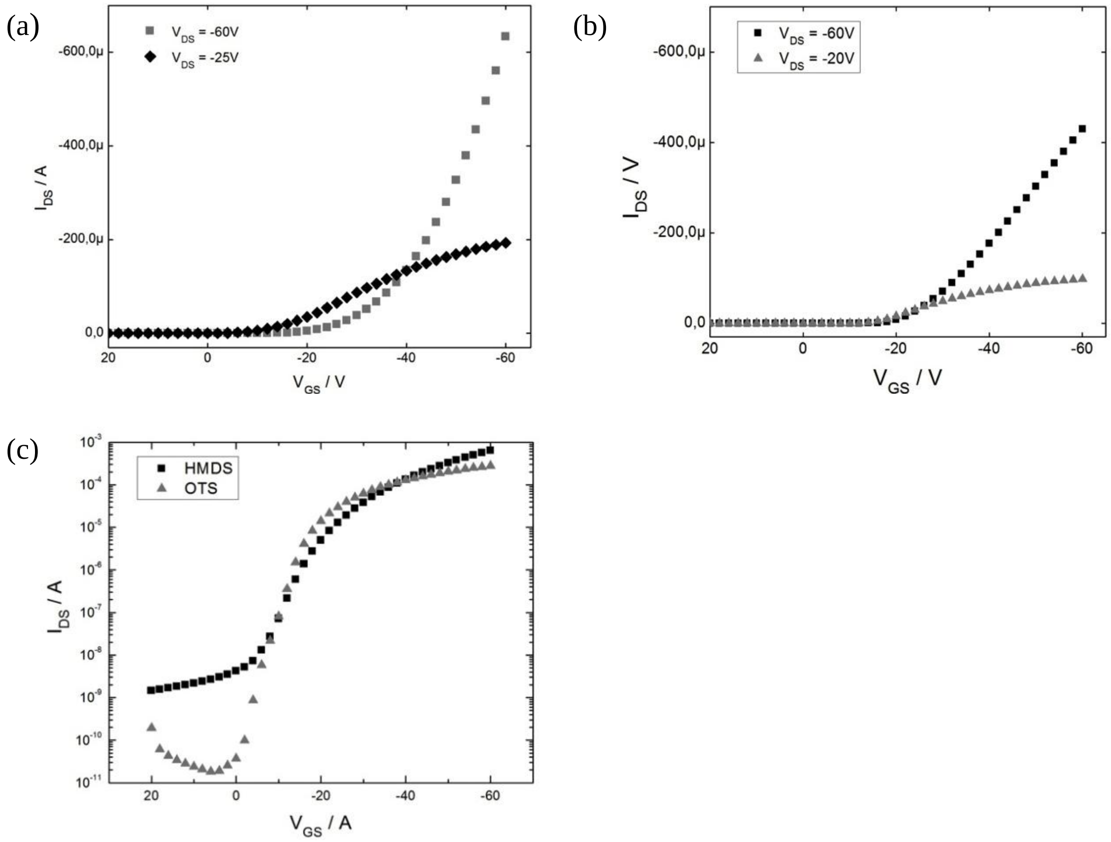

Figure 6.17: $I_{DS}V_{GS}$ graphs of DH4T films produced by following the optimized procedure in linear and saturation regime, for (**a**) HMDS, and (**b**) OTS treated silicon oxide test patterns. (**c**): $I_{DS}V_{GS}$ graph of DH4T films produced by following the optimized procedure in saturation regime, for HMDS- and OTS- treated silicon oxide test patterns.

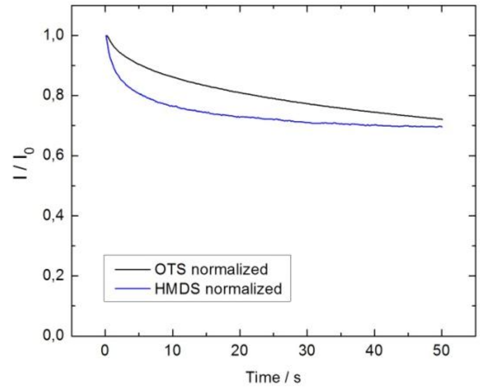

Figure 6.18: Normalized I_{DS} vs. time curves for OTS- vs. HMDS-treated FETs biased at $V_{GS} - V_{Th}$ = - 20 V, V_{DS} = - 60V, prepared with the optimized procedure. I_0 is the current value at t = 0 sec. (L = 20 µm and W = 10mm; V_{DS} = - 60V).

The reason for these improved electrical performances cannot stem from chemical difference in the oxide treatment given that both OTS and HMDS are methyl-terminated. However, the performances on organic transistors are in general improved in terms of threshold voltage and mobility when OTS is utilized.[35] Surprisingly, the dielectric substrate treatment seems to affect the charge injection as can be observed in the output curves. Several points could be brought up in order to explain this unexpected trend: (i) the DH4T film thickness of OTS-treated devices is thinner than that measured over HMDS ones (tens vs. hundreds of nm) as confirmed by the AFM and profilometer (also, the roughness is lower, as shown in **Table T6.9**). (ii) This difference in thickness could lead to higher OFF current in HMDS-treated devices. In addition, the average OFF current increase of ca. two orders of magnitude can be ascribed to the more favored and unavoidable presence of water molecules on the surface of HMDS vs. OTS-treated silicon oxide which stems from the larger surface energy of the former. (iii) AFM imaging of films recorded on HMDS-treated substrates showed to exhibit thinner crystalline planes, lying on top of each other, which are formed during the evaporation of the residual solvent (**Figure 6.19**). During the solvent evaporation the crystals will have a certain affinity for the surface. The better interaction of the DH4T crystals for OTS- vs. HMDS-treated surface promotes formation of thickest multi-layered crystals in the latter case. As a result, the thinner crystalline layers adapt more easily to the pre-patterned electrode geometry, therefore improving the semiconductor/electrode interface quality when OTS is used. The presence of more interfacial defects can be further verified by looking at the sub-threshold slope and the resulting amount of interfacial traps which is ca. 10 times lower in OTS-functionalized devices (see **Table T6.10**).

Table T6.9: RMS roughness of various DH4T films. Values obtained from AFM measurements. Averages were acquired over 10 spots, each of them of 100 µm² area.

Solvent	Functionalization	Evaporation rate (butyl acetate = 1)	Average R_{rms} (nm)	Standard deviation (nm)
CHCl3	HMDS	11.6	165.2	41.6
CB	HMDS	0.2	21.6	7.3
DCB	HMDS	0.2	7.1	1.9
DCB	HMDS	0.1	2.8	0.9
DCB	OTS	0.1	1.5	0.3

Table T6.10. Subthreshold slope calculated in the case of OTS- vs. HMDS-treated transistors. In addition, the corresponding number of interfacial traps is shown.

L [µm]	S (V dec^{-1}) OTS	N_{traps} (cm^{-2}) OTS	S (V dec^{-1}) HMDS	N_{traps} (cm^{-2}) HMDS
20	6,5	$1,12\times10^{13}$	109	$1,89\times10^{14}$
10	7,5	$1,30\times10^{13}$	110	$1,91\times10^{14}$
5	7,2	$1,24\times10^{13}$	85	$1,48\times10^{14}$
2.5	9,0	$1,56\times10^{13}$	101	$1,75\times10^{14}$

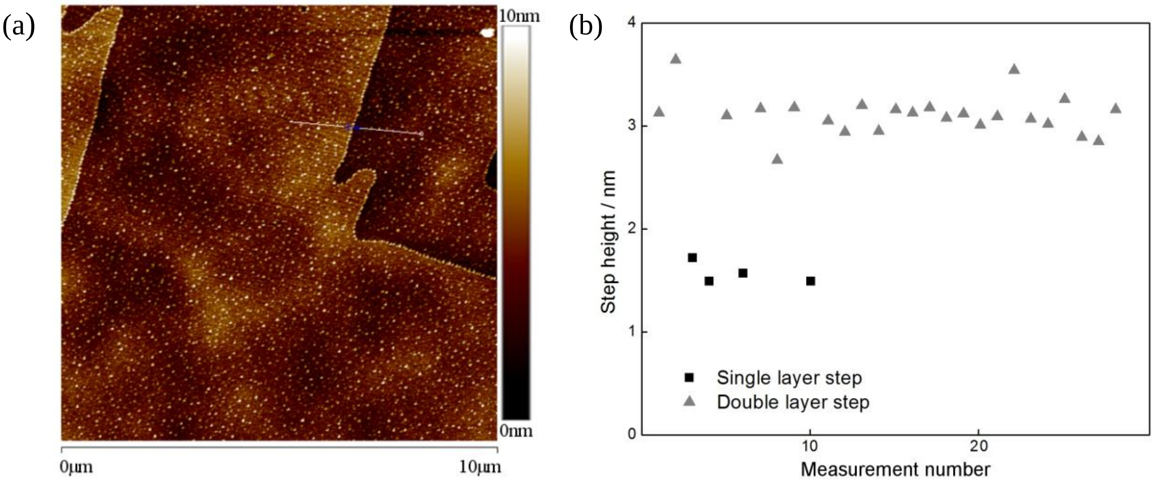

Figure 6.19. Atomic force microscopy of DH4T films on OTS, using the optimized procedure. (a) Topography AFM images of a DH4T optimized procedure OTS film. (b) Step height measurements. This graph shows the result of measurements of 25 steps (average over 3 measurements each). Higher steps have been left out (3 or more layers). The calculated average layer size is of 1.54 nm. The tilt angle (α) of the molecule towards the surface was calculated using equation **Eq. 4.3**, (using as parameters h = 1.54 nm; l = 3.05 nm and θ = 90°). A tilt angle value of 30° was found, consistently with a similar value (24.2°) reported in literature. [36]

6.4. Blends including DH4T

In section *6.3.* we have demonstrated that a careful selection of solvent and evaporation rate lead to major improvements of the electrical performances of the tested semiconductor. In order to further improve the electrical characteristics of the material, we introduced other materials within the same family of semiconductors, DHnT [22]. The additional molecules were DH2T and DH6T (**Figure 6.20**). Unfortunately, the purchased DH6T that was used at first did feature very low purity, and some experiments could not be performed again in time, explaining the lack of data for some films containing DH6T. It is noteworthy to mention that even though the DHnT oligomers differ greatly in terms of electrical characteristics [37-39], these small molecules share many similarities, being based on thiophene groups with two hexyl chains for improved solubility in organic solvent. Two are the effects we aimed at unraveling via blending DH4T with similar oligothiophenes with different lengths. On the one hand, smaller oligomers like DH2T could be expected to fill the intercrystal regions. On the other hand the variation of the oligothiophene length could be accompanied with a vertical phase segregation which could affect drastically the OFET performance in bottom-gate bottom-contact devices.

(a)

(b)

(c)

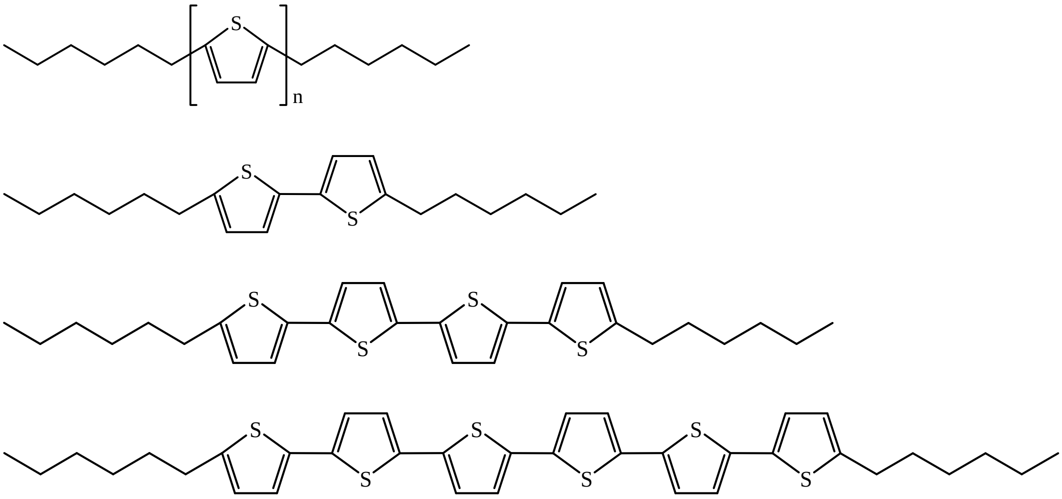

Figure 6.20: Molecular structures of DHnT molecules and P3HT. Chemical formulae of (a) the general DHnT structure, (b) dihexylbithiophene (DH2T), (c) dihexylquaterthiophene (DH4T), (d) dihexylsexithiophene (DH6T) and (e) poly(3-hexylhexylthiophene) (P3HT).

First we fabricated transistors using the optimized procedure on HMDS given in the previous section. We introduced small amounts of DH2T, a molecule that exhibited no charge transport properties when tested in a transistor. Not surprisingly, even small amounts of DH2T added to the DH4T resulted in a strong decrease of the mobility (**Figure 6.21**). This can explained by (i) DH2T acting as an inhibitor for DH4T crystal formation (ii) DH2T acting as a trap for charges in the channel, and/or (iii) the DH2T forming a thin layer at the interface with the dielectric, where most of the charge transport is performed by the transistor.

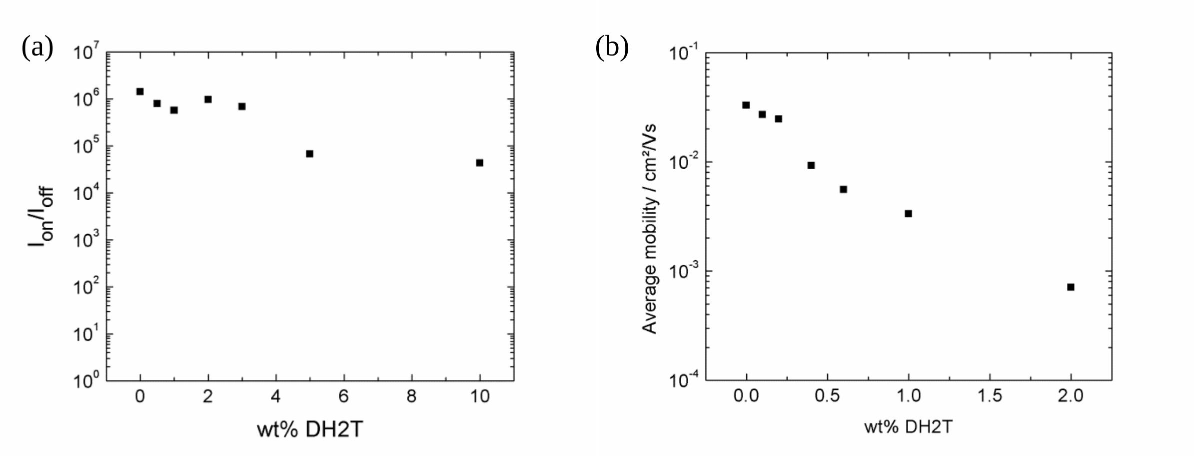

Figure 6.21: Electrical characteristics as a function of the amount of DH2T added to DH4T (optimized procedure using HMDS). Both the values of (a) the I_{on}/I_{off} and (b) the mobility as a function of wt% DH2T were obtained from transfer curves (average over 8 transistors with L = 2.5 µm; 5 µm; 10 µm; 20 µm).

Experimental data from GXRD performed by Salleo's group at Stanford University showed that addition of small amounts of DH2T into the DH4T solution does not result in films with decreased

DH4T crystallinity (**Figure 6.22**). These findings contradict the proposition that DH2T is responsible for a lower crystallinity in the formed film. Therefore, the position on the z-scale of the DH2T was investigated by means of Time of Flight Secondary Ion Mass Spectrometry (ToF-SIMS) measurements, performed at University of Catania by Prof. Licciardello's group. From the ToF-SIMS analysis, we can conclude the on the top of the sample, only DH4T is present (**Figure 6.23**, first 100 seconds). Once we reach the interface between semiconductor and dielectric, there is progressively more DH2T to be found with the DH4T, while at no point a pure DH2T film is observed. This can be due to the very small quantities of DH2T that were introduced. Nevertheless, it is clear that DH2T is present at the semiconductor-dielectric interface, where most charges move from the source to the drain electrode, confirming proposition (iii). The very slow evaporation of the solvent in the optimized procedure is providing enough time for the DH2T and DH4T to phase segregate. Therefore, the same blend was produced, using either dichlorobenzene at normal evaporation rate or chloroform as solvents.

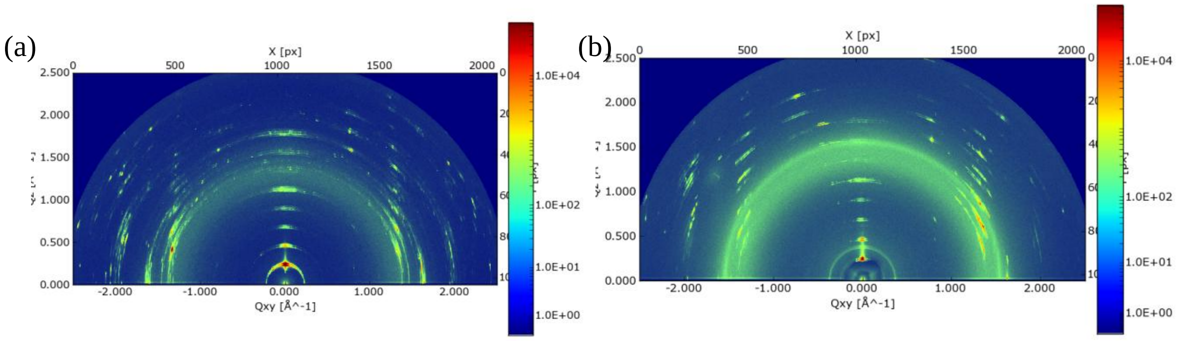

Figure 6.22: 2D GIXD patterns of films drop-casted on bare Si. (a) Pure DH4T dropcasted from dichlorobenzene ; (b) DH2T/DH4T blend containing 2% DH2T and 98% DH4T.

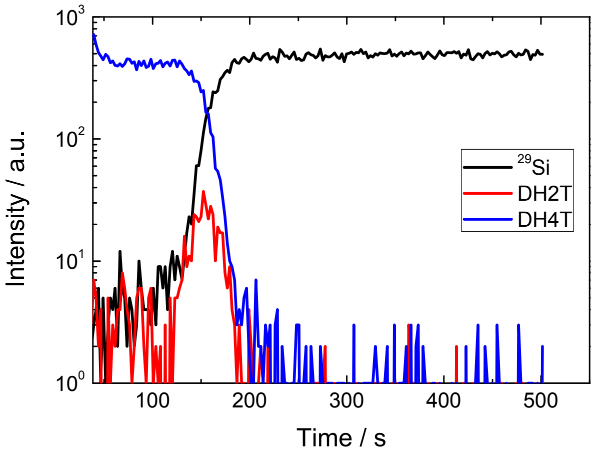

Figure 6.23: ToF-SIMS on bare Si, of a film resulting from a drop-cast of a DH4T/DH2T blend in dichlorobenzene. (2% wt DH2T)

The electrical performances of samples produced from DH4T/DH2T blends in chloroform and DCB (without reduction of the evaporation rate) were tested. The mobilities as function of the amount of DH2T are reported in **Figure 6.24**. A small increase of the mobilities at low quantities of DH4T was observed in both cases. Consistently with results obtained in the previous section, mobilities of devices produced from DCB were higher than the mobilities of the devices produced from $CHCl_3$. Unfortunately, the increases in electrical performances were rather modest, which can easily be explained by the absent charge-transport characteristics of DH2T, due to a very wide band gap of 3.6 eV, as reported by Facchetti et al. [40]

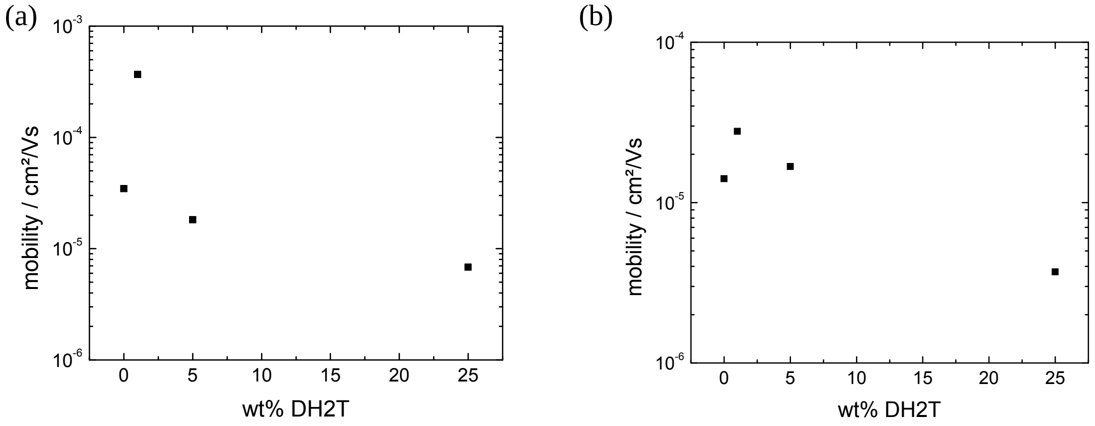

Figure 6.24: Mobilities as a function of the amount of DH2T added to DH4T. Mobilities of films deposited from (a) dichlorobenzene and (b) chloroform. The mobility as a function of wt% DH2T were obtained from transfer curves (average over 8 transistors with L = 2.5 µm; 5 µm; 10 µm; 20 µm).

In order to further improve electrical characteristics of DH4T in chloroform, various amounts of DH6T were added, to form a new blend. Electrical characteristics are reported in **Figure 6.25**. While mobilities of DH4T and DH6T are only one order of magnitude apart ($\mu_{DH4T} = 3.4 \times 10^{-5}$ cm²/Vs; $\mu_{DH6T} = 4.6 \times 10^{-6}$ cm²/Vs), the I_{on}/I_{off} ratio is different by 4 orders of magnitude, DH6T being a very poor semiconductor with an I_{on}/I_{off} of 20. An impressive improvement of charge-transport capabilities has been observed upon addition of 10% of DH4T to the DH6T solution. A 50-fold and 300-fold increase in mobility compared to respectively DH4T and DH6T was found. In terms of I_{on}/I_{off}, the most favorable blend was with even amounts of each component ($I_{on}/I_{off} = 5 \times 10^5$), a 4 order of magnitude increase compared to DH6T, with values rather close to DH4T both in terms of mobility and on/off ratio. $I_{DS}V_{GS}$ curves are presented in linear and logarithmic scale in **Figure 6.26**. We observe that both in terms of currents and curve-shape, samples ranging from 100% DH4T to 50% DH4T have very similar transfer curves, demonstrating a very minor effect of the DH6T on the charge transport mechanism in the device. On the other hand, even small amounts of DH4T (5-10%) added to the blend result in major changes in mobility, I_{on}/I_{off} and threshold voltage. These results are very intriguing since the highest observed mobilities would be expected to be at best equal to the mobilities of DH4T or DH6T, if the materials were completely phase-segregated. While the high I_{on}/I_{off} could be explained by DH6T aggregates surrounded by DH4T areas, the observed mobility is probably due to a complete change in crystallinity of either DH4T, DH6T or both upon blending.

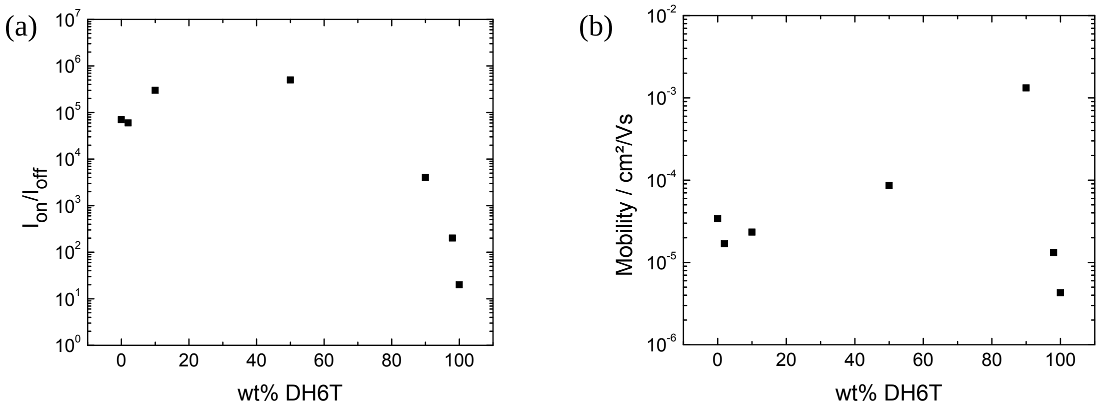

Figure 6.25: Electrical characteristics as a function of the amount of DH6T added to DH4T. Both the values of (a) the I_{on}/I_{off} and (b) the mobility as a function of wt% DH2T were obtained from transfer curves (average over 8 transistors with L = 2.5 µm; 5 µm; 10 µm; 20 µm).

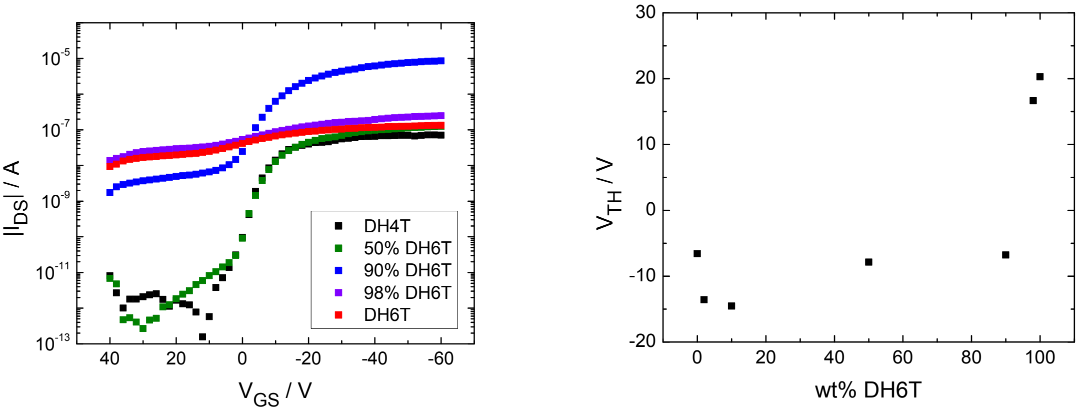

Figure 6.26: Transfer curves and threshold voltages as a function of the amount of DH6T added to DH4T. All the transfer curves are take from devices at the same channel length (L = 10 µm).

Noteworthy, while very small amounts of DH4T added to the larger molecule DH6T is very beneficiary to the charge transport (just as it was observed for the DH2T/DH4T pair), addition of small quantities of DH6T into the DH4T solution (2%, 10%) reduced the mobility of devices. This can be explained either by reduced crystallinity of the DH4T due to DH6T implementation, or by DH6T acting as a charge trap. The first proposition tested using a Grazing Incident X-Ray Diffraction setup. These experiments were performed at Stanford University and are reported in. GIXD confirms that just as it was seen about DH4T/DH2T blends, various amounts of either component do not affect the crystallinity of the other. In order to determine the structural characteristics of blended films, UPS measurements were carried out. It was found that the Ionization Energy (IE) of DH4T was largely different from the IE of DH6T, with respective values of 5.2 eV and 4.85 eV. The values of the Ionization Energy as a function of the amount of each material in the blend are reported in **Figure 6.27**. The IE was found to be constant between 100% DH4T and the 50:50 blend, indicating that at such ratio DH4T forms a film over the DH6T. This can be explained by the lower solubility of DH6T than DH4T, leading to the formation of DH6T aggregates first, that sink to the bottom of the film. Furthermore, it was demonstrated via AFM in section *6.3*. that DH4T forms films over the electrodes, and does not grow within the channel. Unfortunately, due high roughness in DH6T films deposited from a chloroform solution, the TOF-SIMS analysis could not be performed. The fact that the DH6T is at the interface between dielectric and the semiconductor explains the observed drop in mobility for small percentages of DH6T reported in **Figure 6.25**. The IE of DH6T being lower than that of DH4T, charges are trapped in the DH6T at the interface. At small quantities of DH4T, the large error bars are due to the disparity on the x/y-scale of the layer within each tested sample. Nevertheless, the DH4T seem to affect the observed IE even when present in small quantities, due to its position over the DH6T. The observed improvement in electrical characteristics is attributed to the effect of DH4T binding the DH6T crystallites leading to better paths between source and drain electrodes. Furthermore, these areas of DH4T separating DH6T are sufficient to inhibit charge transport when I_{DS} is below $V_{Th,DH4T}$. These observations reveal crucial as this method of blending two materials with different electrical properties for combination of a positive aspect of each material could be transposed to a series of other materials and other properties, as will be demonstrated in chapters 7 and 8.

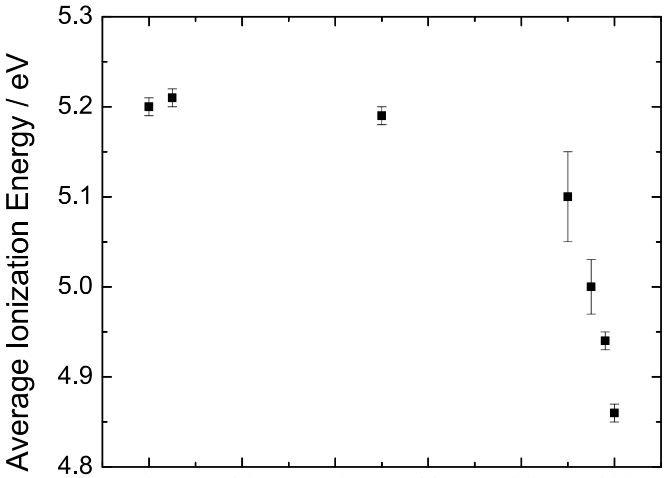

Figure 6.27: Ionization energy as a function of the amount of DH6T added to DH4T.

6.5. Conclusions

In summary, our comparative study on the structure vs. function relationship in solution processed DH4T based OFETs revealed that by optimizing the conditions of film formation via judicious choice of processing method, solvent type, interfaces functionalization and in particular by tuning the rate of evaporation of the solvent it is possible to drive the molecular self-assembly towards the formation of highly ordered low-dimensional architectures exhibiting enhanced electrical characteristics. Significantly, their use as electroactive components in OFETs led to device performances that are beyond the state-of-the-art for DH4T-base transistors, even when compared to vacuum processed OFETs made with the same molecule. In particular, *p*-type mobilities as high as 0.10 cm²/Vs and I_{on}/I_{off} currents exceeding 10^7 were achieved. Our results unambiguously confirm that the tailoring of interfaces is key. Counter intuitively, the functionalization of the injecting electrodes to render them more hydrophobic thus optimize the surface energies via optimal interaction of the alkyl chains of the DH4T for the SAM is found being more important than adjusting the energy match with the HOMO of the semiconductor. In addition, we showed how the different silicon oxide treatment can impact directly the assembly of the semiconductor in highly boiling point solvents leading to interfaces with a lower number of interfacial traps which result in enhanced electrical performances.

We have demonstrated that when a low-boiling point solvent was used (chloroform), the mobility of DH4T could be improved by two orders of magnitude through simple blending with another similar-performing small molecule from the same family (DH6T). By careful analysis of the electrical characteristics of transistors based on bi-component blends, the structure of the blend could be determined, as was controlled through IE measurement with a UPS setup. Addition of very small quantities of a non-semiconducting molecule (DH2T) was proven to be an effective way of increasing the electrical performances of the tested transistors. While most methods relying on multiple semiconducting materials in the same devices focus on separate layers, with multiple processing difficulties, our approach of blending proved to be simple and effective. Our processing method, based on drop-casting, a technique similar to ink-jet printing, as a means to achieve high mobility devices is compatible with large-area applications thus providing a pathway towards organic electronics that satisfies the needed balance between performance and processability.

6.6. References

1 Halik, M. *et al.* Relationship Between Molecular Structure and Electrical Performance of Oligothiophene Organic Thin Film Transistors. *Adv. Mater.* **15**, 917-922 (2003).

2 Payne, M. M., Parkin, S. R., Anthony, J. E., Kuo, C. C. & Jackson, T. N. Organic field-effect transistors from solution-deposited functionalized acenes with mobilities as high as 1 cm2/V-s. *J. Am. Chem. Soc.* **127**, 4986-4987 (2005).

3 Sergeyev, S., Pisula, W. & Geerts, Y. H. Discotic liquid crystals: A new generation of organic semiconductors. *Chem. Soc. Rev.* **36**, 1902-1929 (2007).

4 Leufgen, M. *et al.* High-mobility tetrathiafulvalene organic field-effect transistors from solution processing. *Org. Electron.* **9**, 1101-1106 (2008).

5 Mas-Torrent, M. *et al.* Organic field-effect transistors (OFETs) of highly oriented films of dithiophene-tetrathiafulvalene prepared by zone casting. *Org. Electron.* **9**, 143-148 (2008).

6 Gao, P. *et al.* Dithieno 2,3-d;2 ',3 '-d ' benzo 1,2-b;4,5-b ' dithiophene (DTBDT) as Semiconductor for High-Performance, Solution-Processed Organic Field-Effect Transistors. *Adv. Mater.* **21**, 213-216 (2009).

7 Cavallini, M. *et al.* Ambipolar Multi-Stripe Organic Field-Effect Transistors. *Adv. Mater.* **23**, 5091-5097 (2011).

8 Minemawari, H. *et al.* Inkjet printing of single-crystal films. *Nature* **475**, 364-367 (2011).

9 Kobayashi, H. *et al.* Hopping and band mobilities of pentacene, rubrene, and 2,7-dioctyl[1]benzothieno[3,2-b][1]benzothiophene (C8-BTBT) from first principle calculations. *J. Chem. Phys.* **139** (2013).

10 Yuan, Y. B. *et al.* Ultra-high mobility transparent organic thin film transistors grown by an off-centre spin-coating method. *Nat. Commun.* **5** (2014).

11 Horowitz, G., Peng, X. Z., Fichou, D. & Garnier, F. Organic Thin-Film Transistors Using Pi-Conjugated Oligomers - Influence of the Chain-Length. *J. Mol. Electron.* **7**, 85-89 (1991).

12 Garnier, F., Horowitz, G., Peng, X. Z. & Fichou, D. Structural Basis for High Carrier Mobility in Conjugated Oligomers. *Synth. Met.* **45**, 163-171 (1991).

13 Dodabalapur, A., Torsi, L. & Katz, H. E. Organic Transistors - 2-Dimensional Transport and Improved Electrical Characteristics. *Science* **268**, 270-271 (1995).

14 Katz, H. E., Torsi, L. & Dodabalapur, A. Synthesis, material properties, and transistor performance of highly pure thiophene oligomers. *Chem. Mater.* **7**, 2235 (1995).

15 Horowitz, G., Fichou, D., Peng, X. Z., Xu, Z. G. & Garnier, F. A Field-Effect Transistor Based on Conjugated Alpha-Sexithienyl. *Solid State Commun.* **72**, 381-384 (1989).

16 Biscarini, F., Zamboni, R., Samorì, P., Ostoja, P. & Taliani, C. Growth of Conjugated Oligomer Thin-Films Studied by Atomic-Force Microscopy. *Phys. Rev. B* **52**, 14868-14877 (1995).

17 Leclere, P. *et al.* About oligothiophene self-assembly: From aggregation in solution to solid-state nanostructures. *Chem. Mater.* **16**, 4452-4466 (2004).

18 Barbarella, G., Melucci, M. & Sotgiu, G. The versatile thiophene: An overview of recent research on thiophene-based materials. *Adv. Mater.* **17**, 1581-1593 (2005).

19 Dinelli, F. *et al.* High-mobility ambipolar transport in organic light-emitting transistors. *Adv. Mater.* **18**, 1416-1420 (2006).

20 Duhm, S., Xin, Q., Koch, N., Ueno, N. & Kera, S. Impact of alkyl side chains at self-assembly, electronic structure and charge arrangement in sexithiophene thin films. *Org. Electron.* **12**, 903-910 (2011).

21 Ashizawa, M. *et al.* Improved stability of organic field-effect transistor performance in oligothiophenes including β-isomers. *Tetrahedron* **68**, 2790-2798 (2012).

22 Anokhin, D. V. *et al.* Effect of Molecular Structure of α,α′-Dialkylquaterthiophenes and Their Organosilicon Multipods on Ordering, Phase Behavior, and Charge Carrier Mobility. *J. Chem. Phys. C* **116**, 22727-22736 (2012).

23 Katz, H. E., Lovinger, A. J. & Laquindanum, J. G. α,ω-Dihexylquaterthiophene: A Second Thin Film Single-Crystal Organic Semiconductor. *Chem. Mater.* **10**, 457-459 (1998).

24 Generali, G. *et al.* Correlation among Morphology, Crystallinity, and Charge Mobility in OFETs Made of Quaterthiophene Alkyl Derivatives on a Transparent Substrate Platform. *J. Chem. Phys. C* **115**, 23164-23169 (2011).

25 Song, D. H., Choi, M. H., Kim, J. Y., Jang, J. & Kirchmeyer, S. Process optimization of organic thin-film transistor by ink-jet printing of DH4T on plastic. *Appl. Phys. Lett.* **90** (2007).

26 Garnier, F. *et al.* Dihexylquaterthiophene, A Two-Dimensional Liquid Crystal-like Organic Semiconductor with High Transport Properties†. *Chem. Mater.* **10**, 3334-3339 (1998).

27 Moret, M. *et al.* Structural characterisation of single crystals and thin films of [small alpha],[small omega]-dihexylquaterthiophene. *J. Mater. Chem.* **15**, 2444-2449 (2005).

28 Palermo, V. & Samorì, P. Molecular self-assembly across multiple length scales. *Angew. Chem. Int. Ed.* **46**, 4428-4432 (2007).

29 Granstrom, E. L. & Frisbie, C. D. Field effect conductance measurements on thin crystals of sexithiophene. *J. Phys. Chem. B* **103**, 8842-8849 (1999).

30 Someya, T., Katz, H. E., Gelperin, A., Lovinger, A. J. & Dodabalapur, A. Vapor sensing with alpha,omega-dihexylquarterthiophene field-effect transistors: The role of grain boundaries. *Appl. Phys. Lett.* **81**, 3079-3081 (2002).

31 Dabirian, R. *et al.* The Relationship between Nanoscale Architecture and Charge Transport in Conjugated Nanocrystals Bridged by Multichromophoric Polymers. *J. Am. Chem. Soc.* **131**, 7055-7063 (2009).

32 De Luca, G. *et al.* Non-conventional Processing and Post-processing Methods for the Nanostructuring of Conjugated Materials for Organic Electronics. *Adv. Funct. Mater.* **21**, 1279-1295 (2011).

33 Tanase, C., Meijer, E. J., Blom, P. W. M. & de Leeuw, D. M. Local charge carrier mobility in disordered organic field-effect transistors. *Org. Electron.* **4**, 33-37 (2003).

34 Dinelli, F. *et al.* Spatially correlated charge transport in organic thin film transistors. *Phys. Rev. Lett.* **92** (2004).

35 Chua, L. L. *et al.* General observation of n-type field-effect behaviour in organic semiconductors. *Nature* **434**, 194-199 (2005).

36 Moret, M. *et al.* Structural characterisation of single crystals and thin films of alpha,omega-dihexylquaterthiophene. *J. Mater. Chem.* **15**, 2444-2449 (2005).

37 Mannebach, E. M. *et al.* High Hole Mobility and Thickness-Dependent Crystal Structure in α,ω-Dihexylsexithiophene Single-Monolayer Field-Effect Transistors. *Adv. Funct. Mater.* **23**, 554-564 (2013).

38 Han, D. H. & Park, B. E. Characteristics of OTFTs based on alpha - omega - Dihexyl-sexithiophene(DH6T) using Organic Molecular Beam Deposition. *AIP Conf. Proc.* **1399** (2011).

39 Gidron, O. *et al.* Oligofuran-containing molecules for organic electronics. *J. Mater. Chem. C* **1**, 4358-4367 (2013).

40 Facchetti, A., Mushrush, M., Katz, H. E. & Marks, T. J. n-type building blocks for organic electronics: A homologous family of fluorocarbon-substituted thiophene oligomers with high carrier mobility. *Adv. Mater.* **15**, 33 (2003).

Chapter 7. Ambipolarity on demand: polymer blends

7.1. Introduction

Ambipolar transistors are field-effect transistor (FET) devices in which the charge carriers can be both electrons and holes.[1,2] The key merit of ambipolar transistors emerging from the capability to operate with both types of carriers is that they can operate in three different states: the hole current on state, the off state, and the electron current on state, which can be beneficial for the construction of C-MOS logic circuits with a lower number of device components.[3] While inorganic semiconductors are unipolar (with selection of polarity by doping), organic semiconductors should fundamentally allow transport of both holes and electrons.[4] However, this only happens in ideal cases, or at low temperature [5,6] While most organic semiconductors for OFET feature *p*-type or *n*-type mobility, ambipolarity is still a rare and most sought-after propriety of organic materials.

In order to obtain ambipolar performances, the go-to approach usually is the use of two separate layers of the *p*- and *n*-type semiconductor, leading to ambipolar films. Regrettably, this approach requires complex processing methods (such as vacuum evaporation of the separate films) since the choice of solvent would be tricky if one was to process the films from the solution. Another approach is the use of ambipolar molecules. In most cases of ambipolar molecules, the I_{on}/I_{off} was found to be much weaker than in the case of hole or electron conducting molecules, due to high off current. Furthermore, there is very little control over the ratio between *p*-type and *n*-type mobilities, leading to often very unbalanced ambipolarity. [7]

The possibility to obtain ambipolar behavior in organic field-effect transistors by combining two different semiconductors (*n*-type and *p*-type materials) in the active layer was first demonstrated in systems in which both layers were deposited by co-sublimation. Dodabalapur and co-workers combined layers of two small molecules, the hole-conducting α-sexithiophene and the electron-conducting C60, and observed both hole and electron transport in these devices, although with lower mobility values than those of the single-component. [8] More recently, Dinelli et al. demonstrated a device based on separate layers of DH4T and and N,N′-ditridecylperylene-3,4,9,10-tetracarboxylic di-imide, reaching ambipolar balanced mobilities of 0.03 cm²/Vs. While this result is impressive, among the highest mobilities reported for bilayer transistors, the procedure based on the evaporation of the small molecules is inapplicable for the real-world application, and the I_{on}/I_{off} was found to be very low, i.e. below 10. [9]

In order to circumvent the processability issue, several attempts to layered semiconductors from the solution have been tried. They include using an intermediate layer (TiO_x) that is inserted between the semiconductor materials, thus electronically separating the p- from the n-channel. [10] Another alternative is to use the contact-film-transfer method, [11] in which two different polymer films are deposited on two different substrates and one of them is transferred afterwards on top of the other. The sequential spin-coating from orthogonal solvents has been investigated as well; [12] in this way, it is possible to deposit one layer directly on top of the other without affecting the performance of the first layer.

To date, the best ambipolar blends using polymers and small molecules have been obtained by Shkunov et al., with a mixture of thieno[2,3-b]thiophene terthiophene polymer and phenyl C61 butyric acid methyl ester on OTS-treated SiO_2 substrates. These devices displayed electron mobility of 9×10^{-3} cm²/Vs and hole mobility of 4×10^{-3} cm²/Vs. [3,13] Regrettably, while the processing technique is simple and adapted to the industry, the unbalanced mobilities, relatively low I_{on}/I_{off} (below 10^3) and shifted threshold voltage ($I_{DS,min}$ at V_{GS} over 20V), disqualify these devices for future applications.

Ambipolar polymer/polymer blends have been produced, with balanced mobilities up to $3x10^{-3}$. [14,15] While these results point to the great potential of this approach, the relatively low mobilities and I_{on}/I_{off} (10^3) show that the full potential of these blends have not yet been reached. Furthermore, almost all these studies rely on a single blend at fixed ratio, making it difficult to establish the correlation between ambipolar performances, film structure, molecular structure and blending ratio. The ambition of our study is therefore double. We aim at the fabrication of very high performance balanced ambipolar transistors, with a large threshold voltage window ($V_{Th,n} – V_{Th,p}$) and I_{on}/I_{off}, while trying to establish which *p*-type polymer shows the best compatibility with P(NDI2OD-T2). We will explore the correlation between blending ratio and ambipolar behavior, and compare the structure at the surface of blended materials with pure films. These studies will be accompanied by careful investigation of the *p*-

type and *n*-type electrical performance dependence on the OFET geometry as a tool of determination of the structure of the film and enhancement of the performances.

7.2. Methods

7.2.1. Semiconductors

P(NDI2OD-T2) and the four *p*-type semiconductor candidates for blending; P3HT, IIDDT-C3, PDVT-8 and PCD-TPT (**Figure 7.1**) have been described in chapter 3. All the semiconductor solutions were prepared using chloroform as solvent. The semiconductors were purchased from Polyera (P(NDI2OD-T2)), BASF-Rieke Metals Inc. (P3HT) and 1-material (PCD-TPT, PDVT-8 and IIDDT-C3). Molecular weights, polysdispersity and monomer weights are reported in **Table T7.1**.

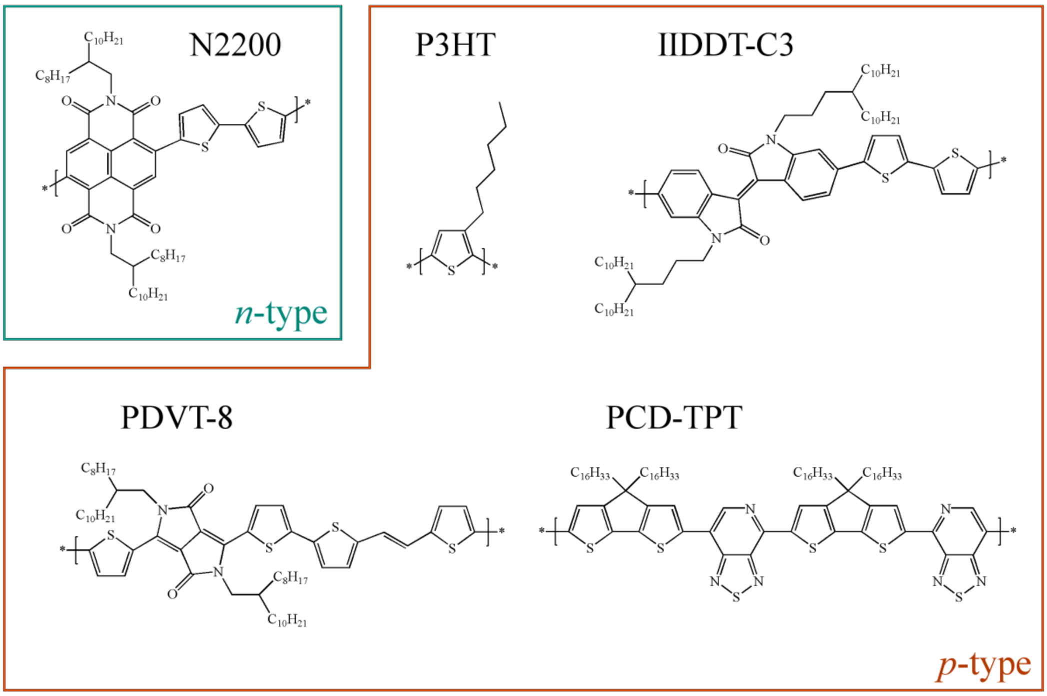

Figure 7.1: Molecular structures of the *n*-type semiconductor P(NDI2OD-T2) and the *p*-type semiconductors P3HT, PCD-TPT, PDVT-8 and IIDDT-C3.

Table T7.1: Average molecular weights and polydispersity of the studied polymers.

Polymer	Molecular weight / kDa	Polydispersity	Monomer weight / Da	Estimated average number of monomers
P(NDI2OD-T2)	28	2.3	989.5	28
P3HT	50	2.4	166.3	300
PCD-TPT	79	2.5	1520.5	52
PDVT-8	51	2.4	1049.7	49
IIDDT-C3	58	2.4	1097.8	53

All values are extracted from the certificate of analysis provided by the supplier of the molecules.

7.2.2. Fabrication of the devices

Bottom-contact bottom-gate configuration transistors purchased from IPMS Fraunhofer Institute were used. They consisted of on *n*$^{++}$-Si substrates with 230 nm of thermally grown SiO_2 as the gate dielectric (15 nF capacitance) and pre-patterned pairs of gold electrodes with interdigitated geometry as the source and drain. All solutions, samples and devices were prepared and measured in a N_2 filled glovebox to avoid oxidative doping of the materials and ensure reproducibility of the experiments. All wafers were treated with OTS before use. All samples were fabricated by spin-coating of the semiconductor solution at a total concentration of 5 mg/mL, at 2500 RPM (acceleration 4000 RPM/s). Bi-component blends were produced by mixing 5 mg/mL solutions of P(NDI2OD-T2) and the other semiconductors, at the desired ratio. The final sample is illustrated in **Figure 7.2**.

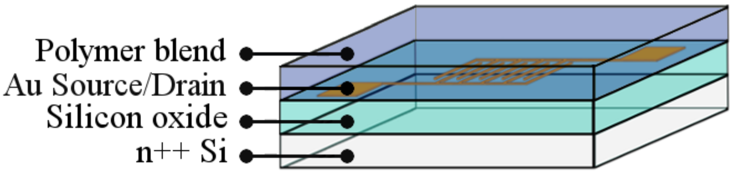

Figure 7.2: Bottom-gate devices on silicon oxide. Schematic representation of the bottom-gate bottom-contact polymer-blend devices on a silicon oxide substrate.

For top-gate transistor fabrication, interdigitated gold source and drain electrodes were evaporated (40 nm thickness) on top a silicon dioxide substrate, using a shadow mask. The 5 mg/mL semiconductor solution was subsequently spin-coated over the electrodes at 2500 RPM (acceleration 4000 RPM/s). A layer of Cyop was spin-coated over the sample at 2300 RPM (acceleration 1150 RPM/s), and annealed 4 hours at 70 °C. The Al gate electrode was vacuum-deposited on the dielectric through shadow mask (layer thickness = 150 nm). The final sample is illustrated in **Figure 7.3**.

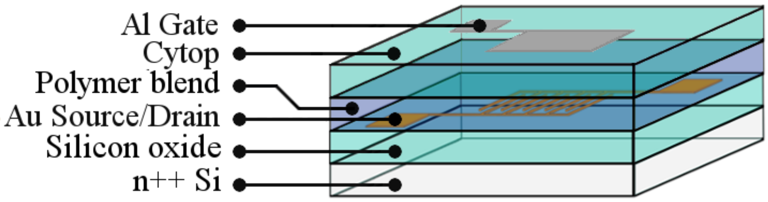

Figure 7.3: Top-gate devices. Schematic representation of the top-gate polymer-blend devices on a silicon oxide substrate.

7.2.3. *Device characterization*

OFET properties were evaluated under positive or negative gate bias to explore the majority charge carrier type and device performance. Experimental data were analyzed using standard field-effect transistor equations described in chapter 4. Unless specified otherwise, the mobilities were determined in the saturation regime, *i.e.* at V_{DS} = ±60 V from the slope of plots of $(I_{GS})^{1/2}$ versus V_{GS}. The reported *p*-type and *n*-type mobilities (μ_p and μ_n) in the bottom-contact bottom-gate geometry were an average of 8 devices, two for each channel length L (L = 2.5, 5, 10 and 20 µm). The reported mobilities for top-gate devices were an average of up to 8 devices, two for each channel length (L = 60, 80, 100 and 120 µm).

7.3. Single-component films

7.3.1. *Energetic levels and electrical performances of the single polymers*

Before any blending was performed, transistors based on single-component semiconductors were fabricated and characterized. The HOMO and LUMO levels of the polymers used in this study have been reported in the literature and are compiled in **Table T7.2**. From the values of the energetic levels we notice that P3HT has a large band gap of almost 2 eV, and very high HOMO and LUMO levels compared to the other polymers, making it optimal for hole injection from gold (the work function of Au, as measured in chapter 6, is around 4.8 eV). Conversely, the HOMO levels of the other *p*-type semiconductors (IIDDT-C3 in particular) are detrimental for hole injection, and a higher contact resistance is to be expected. Since P(NDI2OD-T2) has the lowest HOMO and LUMO levels, both hopping of electrons from P(NDI2OD-T2) towards one of the *p*-type semiconductors and hopping of holes from one semiconductor to P(NDI2OD-T2) are never energetically favored. The large gap between the work function of the gold electrodes and the LUMO level of P(NDI2OD-T2) could lead to a high injection barrier for electron injection.

Table T7.2: HOMO and LUMO levels of the polymers P(NDI2OD-T2), P3HT, PCD-TPT, PDVT-8 and IIDDT-C3.

Polymer	HOMO / eV	LUMO / eV	Band gap / eV
P(NDI2OD-T2) [16,17]	-5.60	-3.94	1.66
P3HT [18,19]	-4.96	-3.04	1.92
PCD-TPT [20]	-5.16	-3.70	1.46
PDVT-8 [21]	-5.30	-3.78	1.52
IIDDT-C3 [22]	-5.52	-3.74	1.78

All values obtained from cyclic voltammetry.

In order to confirm the presence of injection barriers in the polymers, single-component bottom-contact bottom-gate transistors were fabricated for each polymer and the output curves were plotted at positive V_{DS} range for P(NDI2OD-T2) (**Figure 7.4**) and negative V_{DS} range for the other semiconductors (**Figure 7.5**). The shape of the output curve is a strong indicator of the injection barrier. In the case of P3HT, as expected from the energy levels, the curves were ideal for *p*-type charge carrier transport, with a linear increase of the I_{DS} with V_{DS} in the linear regime. While the output curves of PDVT-8 and PCD-TPT seem to indicate the presence of a minor injection barrier, the greatest injection problems are observed for P(NDI2OD-T2) and particularly IIDDT-C3.

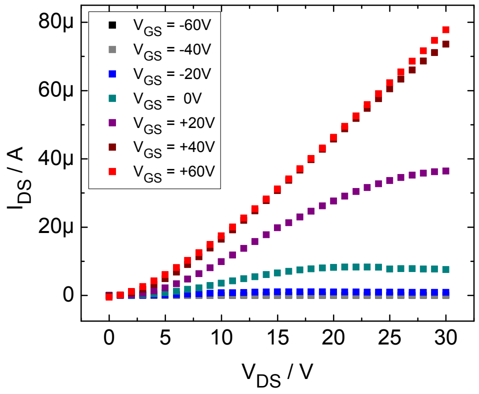

Figure 7.4: Output curves of a P(NDI2OD-T2) based transistor. Measurements performed on a transistor with L = 20 µm.

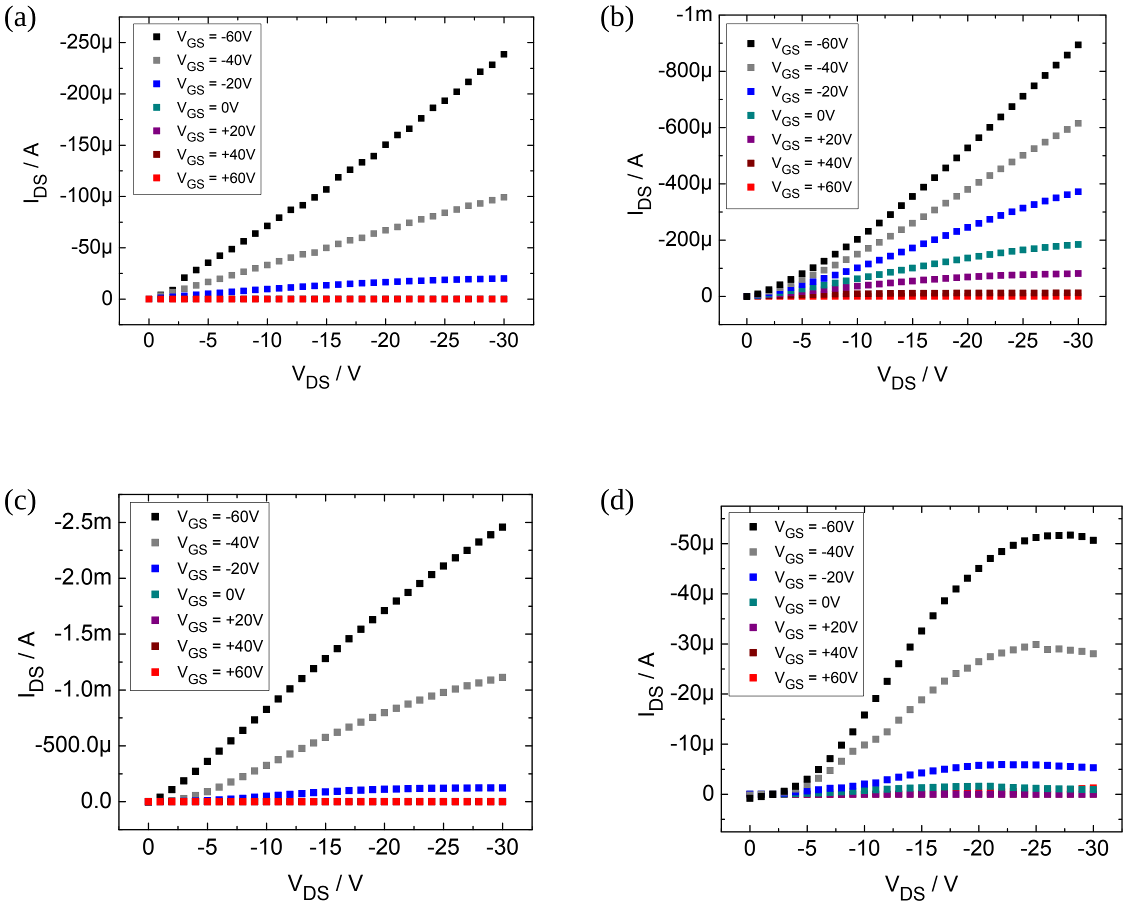

Figure 7.5: Output curves of devices produced with *p*-type semiconductors (a) P3HT (b) PCD-TPT (c) PDVT-8 (d) IIDDT-C3. In all cases, the drain voltage was swept from 0V to -30V, and the channel length was 20 µm.

Transfer curves were plotted for a bottom-contact bottom-gate transistor based on each semiconductor in order to determine their electrical characteristics. In the case of P(NDI2OD-T2) (**Figure 7.6**), the transfer curve revealed a large I_{on}/I_{off} exceeding 10^6 both in linear and saturation regime. The *n*-type mobility was extracted and amounted to an average of 0.016 cm²/Vs in saturation regime, and very low *p*-type mobility was observed ($< 10^{-6}$ cm²/Vs). P3HT behaved as a typical *p*-type semiconductor with high I_{on}/I_{off} ($>10^6$ in linear and saturation regime) and good *p*-type mobilities, but without *n*-type charge transport ability ($<10^{-7}$) (**Figure 7.7, a**). Interestingly, the other 3 polymers, PCD-TPT, PDVT-8 and IIDDT-C3 all featured high *p*-type mobilities (respectively 0.066, 0.60 and 0.080 cm²/Vs), but also decent *n*-type mobilities (**Figure 7.7, b-d**). PDVT-8 and IIDDT-C3 featured *n*-type mobilities around 10^{-4} cm²/Vs, making them very unbalanced yet ambipolar semiconductors with respective mobility ratios (μ_p/μ_n) of 10^4 and 10^3. PCD-TPT was the *p*-type polymer with the highest *n*-type mobility (5.4×10^{-3} cm²/Vs) leading to a mobility ratio around 10. While all these polymers exhibited good I_{on}/I_{off} over 10^6 in linear regime, the I_{on}/I_{off} of PCD-TPT was found to somewhat lower in saturation regime (10^4). The mobility was plotted as a function of the channel length in linear regime (**Figure 7.8**), in order to determine the contribution of the contact resistance to the total resistance. In the case of P(NDI2OD-T2) and IIDDT-C3, the contact resistance was determined to greatly impact the measured mobility in linear regime, with 3 orders of magnitude improvements of mobilities with wider channel lengths (20 µm). In general, mobilities extracted from transfer curves in the linear regime were lower than in saturation regime.

In summary, we have characterized P(NDI2OD-T2) and different *p*-type semiconductors. Among them, P3HT was found to be the only exhibiting pure *p*-type transport whereas PDVT-8 and IIDDT-C3 mostly *p*-type and PCD-TPT ambipolar with a *p*-type mobility only one order of magnitude above *n*-type mobility. All polymers performed properly as semiconductors, with high I_{on}/I_{off} ratios.

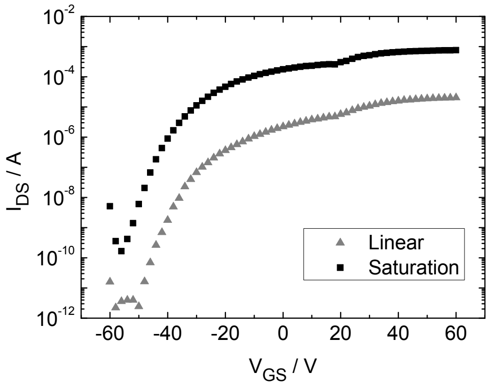

Figure 7.6: Transfer curves of a P(NDI2OD-T2) based transistor. Measurements performed on a transistor with L = 20 µm.

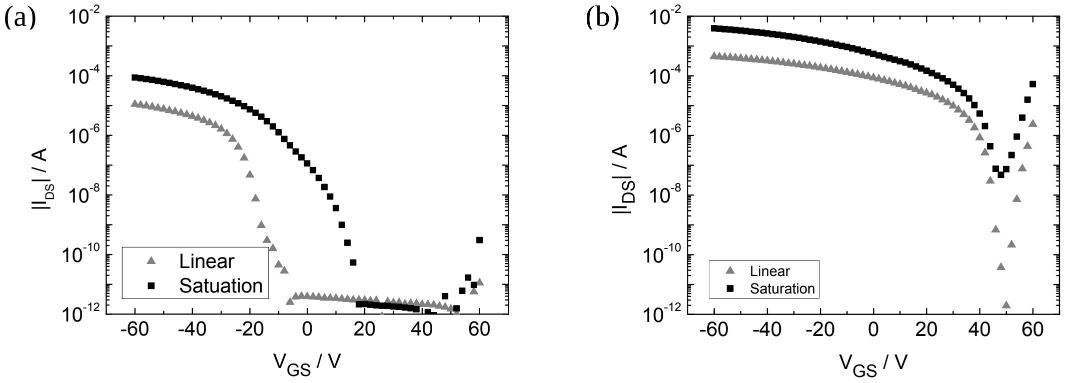

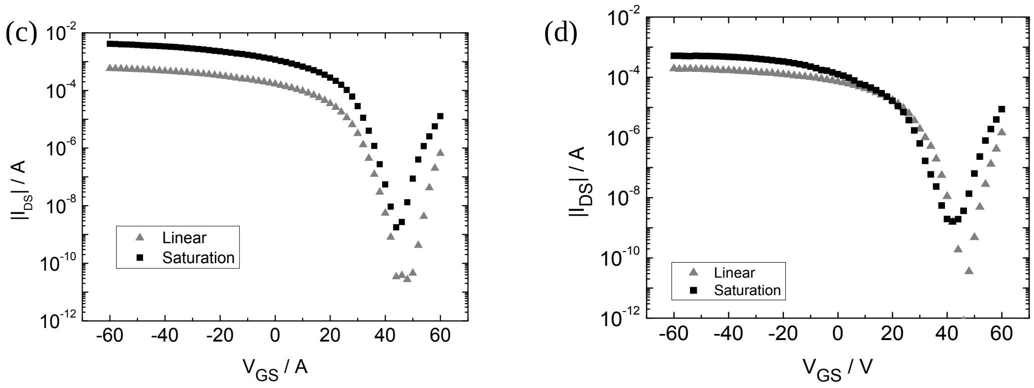

Figure 7.7: Transfer curves of devices produced with *p*-type semiconductors (a) P3HT, (b) PCD-TPT, (c) PDVT-8 and (d) IIDDT-C3. The x and y axis were kept the same in all graphs for easier comparison. In all cases, the gate voltage was swept from +60V to -60V, and all the plots represent measurements performed on devices with L = 20 µm.

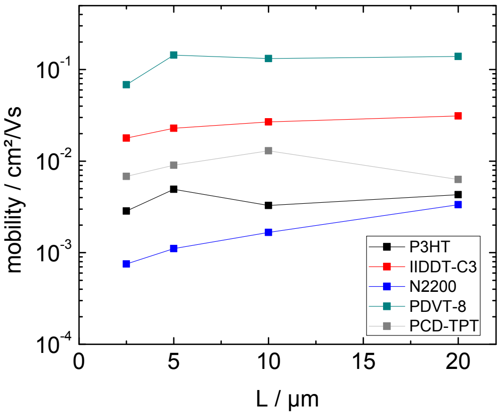

Figure 7.8: Mobility in linear regime as a function of the channel length L of devices produced with P(NDI2OD-T2) and the *p*-type semiconductors P3HT, PCD-TPT, PDVT-8, and IIDDT-C3. The *n*-type mobility is given for P(NDI2OD-T2), and the *p*-type mobility is given for the other polymers.

7.3.2. Film morphology

The existence of a strong correlection between structure/morphology and electrical characteristics in organic material is notorious. The morphology of the surface of transistors based on single-component films was investigated by means of atomic force microscopy imaging. **Figure 7.9** displays the topographical AFM images of the thin-films of the organic/polymeric semiconductor placed in the channel, i.e. between source and drain electrodes. The root-mean-squared roughness (R_{RMS}) extracted from each plot using the formula presented in chapter 5 is summarized in **Table T7.3**. Each semiconductor film, prepared by spin-coating, exhibited a different morphology. P(NDI2OD-T2) shows a very smooth film. The film consisted of stacks of rigid elongated domains, hundreds of nm long, with a R_{RMS} of 0.64 nm, consistently with morphologies observed in literature. [23] P3HT films were very smooth (R_{RMS} = 0.51 nm) and consisted of small bridged aggregates. PDVT-8 films revealed similar morphological structure at the surface, albeit rougher and with smaller and less connected aggregates. The surfaces of PCD-TPT and IIDDT-C3 were characterized by elongated domains, but not as tightly stacked as in the case of P(NDI2OD-T2). IIDDT-C3 films in particular were very rough (R_{RMS} = 1.78 nm).

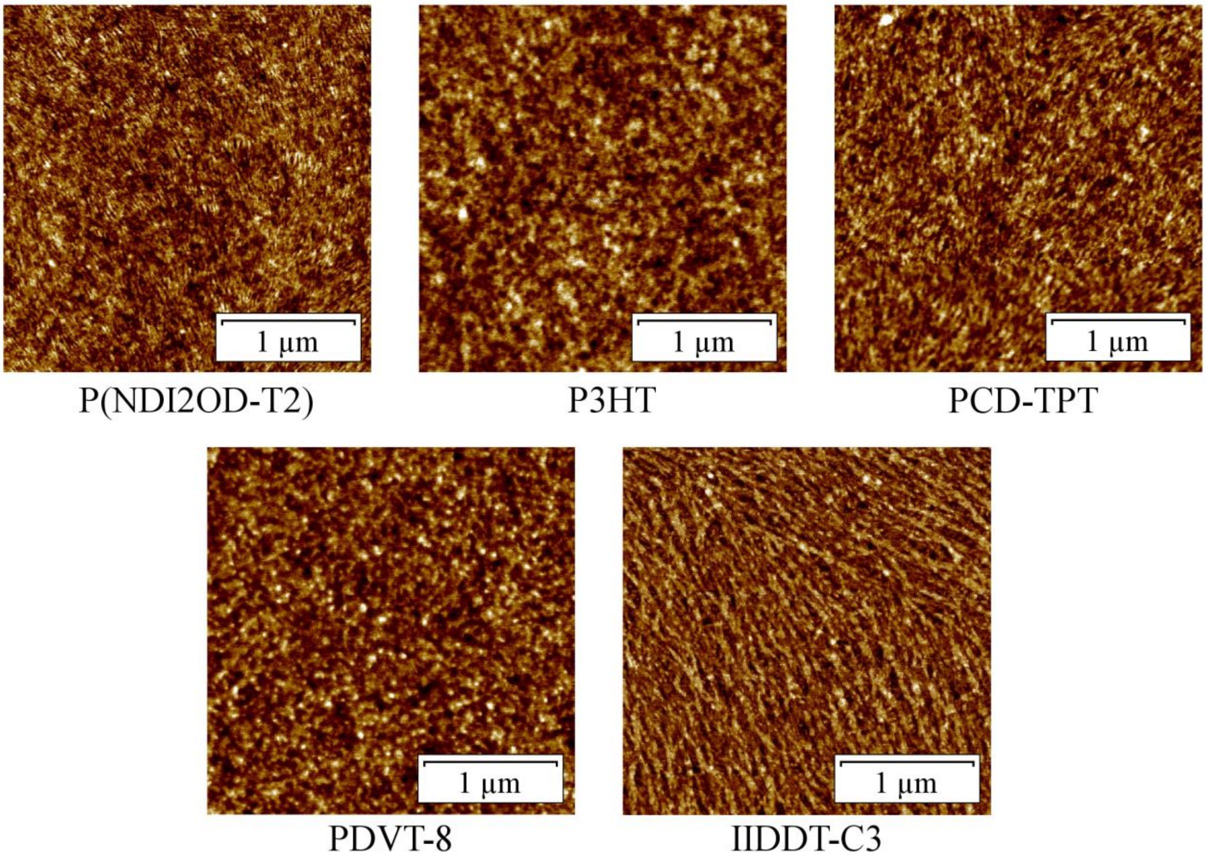

Figure 7.9: Tapping Mode AFM topography images of polymer films. *z*-scales: P(NDI2OD-T2) 4.4 nm, P3HT 3.5 nm, PCD-TPT 5.5 nm, PDVT-8 6.4 nm and IIDDT-C3 12.1 nm.

Table T7.3: Roughness of the polymer films, extracted from the AFM height plots reported in **Figure 7.8**.

Polymer	**R_{RMS} / nm**
P(NDI2OD-T2)	0.637
P3HT	0.512
PCD-TPT	0.795
PDVT-8	0.910
IIDDT-C3	1.783

The R_{RMS} were in all cases determined from images of 10μm × 10μm.

7.4. Bi-component blends

7.4.1. Electrical performances of blends with different polymer-ratios

All the *p*-type semiconductors were individually blended with P(NDI2OD-T2), and bottom-contact bottom-gate transistors were fabricated using these blended solutions. In addition to the single-component devices (blending ratios of 100:0 and 0:100), 3 additional transistors were fabricated for each P(NDI2OD-T2):*p*-type polymer combination. The blending ratios were in each case: 20:80, 50:50 and 80:20. The *p*-type and *n*-type mobilities of each polymer blend as a function of the quantity of P(NDI2OD-T2) in the blend are reported in **Figure 7.10**.

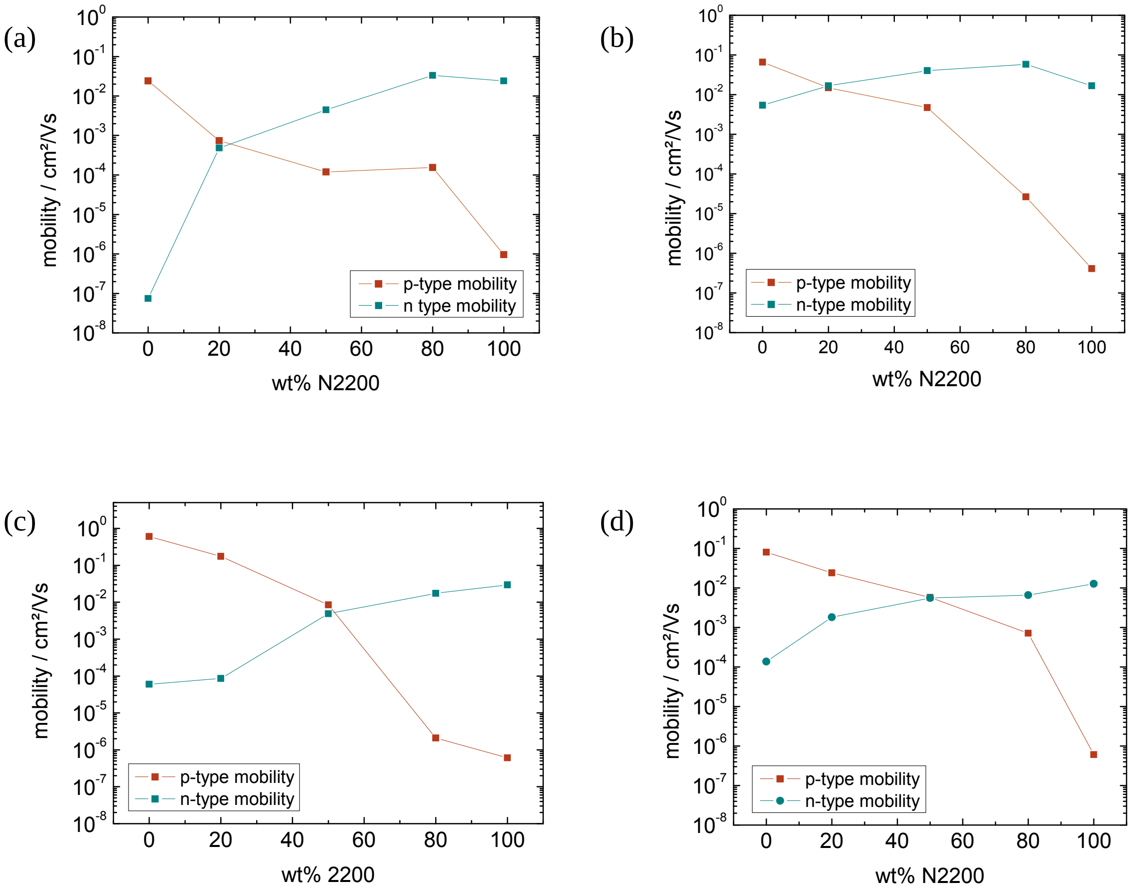

Figure 7.10: Average saturation regime mobility as a function of the percentage in weight of P(NDI2OD-T2) in the semiconductor solution deposited over the electrodes. Blends of P(NDI2OD-T2) with (a) P3HT, (b) PCD-TPT, (c) PDVT-8 and (d) IIDDT-C3.

In every case, the *p*-type mobility decreased with each addition of P(NDI2OD-T2) to the blend. This is easily explained by the poor hole-transport properties of P(NDI2OD-T2). The *n*-type mobility, on the other hand, a minor increase was observed upon addition of 20 wt% of P3HT or PCD-TPT to the P(NDI2OD-T2) solution. These very minor increases are attributed to the slightly different characteristics that can be observed in different samples. In all graphs, a stable decrease of *p*-type mobility and increase of *n*-type mobility was observed and absolutely no strong "break" after addition of small quantities of one material to the solution. Exploiting this feature, it was possible to fabricate transistors with balanced mobilities for each blend. While these balanced mobilities were observed at 20 wt% of P(NDI2OD-T2) when blended with P3HT and PCD-TPT, the "ideal ratio" for PDVT-8 and IIDDT-C3 based transistors was found to be around 50 wt% of P(NDI2OD-T2) in the deposited semiconductor solution. These observed trends are truly remarkable as they pave the way for devices with full control on the ratio between electron and hole transport capabilities. Furthermore, this strategy is most likely applicable to a wide range of *p*-type semiconductors blended with P(NDI2OD-T2), as it was fruitful on all those that were tested here that are structurally and energetically very different.

The largest flaw of ambipolar organic semiconductors is their poor ability to switch off (especially in saturation regime), as the threshold voltage difference between the *p*-type current and *n*-type current tends to be very close. In order to determine the I_{on}/I_{off} of the balanced ambipolar devices based on blends, transfer curves were plotted (**Figure 7.11**). While it was possible to fabricate balanced ambipolar devices using a blend composed of 20 wt% of P3HT, the mobilities below 10^{-3} cm²/Vs and I_{on}/I_{off} below 10^{3} were disappointing. The low mobilities are partially explained by the poor electrical characteristics of the single-component film in comparison to the other tested polymers. Nevertheless, a very high drop in *p*-type mobility (almost two orders of magnitude) is observed upon addition of 20 wt% of P(NDI2OD-T2), combined with a steep increase in *n*-type charge transport. This can be explained by the strong contribution of P(NDI2OD-T2) to the electrical performances and possibly the loss of crystallinity of P3HT upon addition of the second polymer.

Similarly to P3HT, PCD-TPT featured balanced mobilities when blended with 20 wt% P(NDI2OD-T2), but unlike P3HT, the electrical performances were impressive: ambipolar transistors with perfectly balanced mobilities over 10^{-2} cm²/Vs ($\mu_p = 0.015$ cm²/Vs $\approx \mu_n = 0.017$ cm²/Vs) and I_{on}/I_{off} exceeding 10^{4} both in linear and saturation regime were fabricated. These remarkable performances are attributed to the strong mobilities of PCD-TPT, and demonstrate that our approach can be used to "correct" ambipolar polymers featuring unbalanced mobilities. While these characteristics are notable, the threshold voltage is strongly shifted towards positive V_{GS} ($I_{DS,min}$ at V_{GS} = 34V when the voltage is swept from -60V to +60V). This effect tends to further prove that PCD-TPT has a higher impact on the electrical characteristics of the blended film in the bottom-contact, bottom-gate configuration.

IIDDT-C3 and PDVT-8 devices were ambipolar with balanced mobilities when blended in equivalent weight quantities with P(NDI2OD-T2). The extracted mobilities were slightly below 10^{-2} cm²/Vs, and the minimal I_{DS} current was found to be close to 0V. Transfer curves plotted from PDVT-8 devices exhibited a high I_{on}/I_{off} in linear regime (>10^5), but lower in saturation regime (10^3). Transfer curves 50:50 IIDDT-C3:P(NDI2OD-T2) devices displayed an outstanding feature: I_{on}-I_{off} ratios were over 10^5 in saturation regime and up to 10^7 in linear regime, the highest reported values to date for ambipolar organic field-effect transistors. These very high I_{on}/I_{off} stem from a threshold voltage "window" ($\Delta V_{Th} = V_{Th,n} - V_{Th,p}$) over 40V, leaving a large area were the devices are off (the threshold voltage values are reported in **Table T7.4**). The energy levels of P(NDI2OD-T2) and IIDDT-C3 are very close, with respective HOMO levels of -5.60 and -5.52 eV, and respective LUMO levels of -3.94 and -3.74 eV. The injection from one molecules into the other could therefore be possible, leading to possible trapping at low V_{GS}, decreasing the off current, explaining the impressive I_{on}/I_{off}.

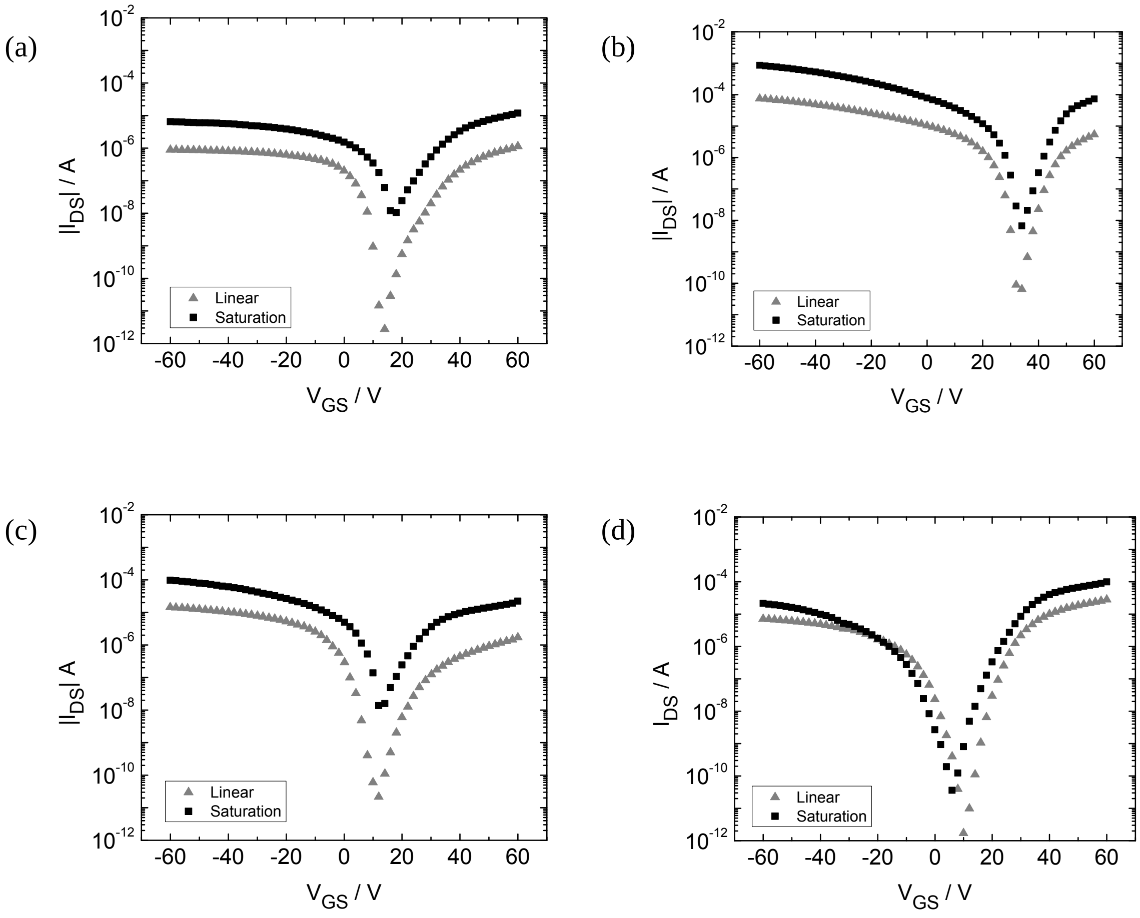

Figure 7.11: Transfer curves of devices produced from blends of P(NDI2OD-T2) and *p*-type semiconductors: (a) 80:20 P3HT:P(NDI2OD-T2), (b) 80:20 PCD-TPT:P(NDI2OD-T2), (c) 50:50 PDVT-8:P(NDI2OD-T2) and (d) 50:50 IIDDT-C3:P(NDI2OD-T2). The x and y axis were kept the same in all graphs for easier comparison. In all cases, the gate voltage was swept from +60V to -60V, and all the plots represent measurements performed on devices with L = 20 µm.

Table T7.4: Threshold voltages of the devices based on blended polymers, extracted from the transfer curves reported in **Figure 7.10**.

Polymer blend	**$V_{Th,p}$**	**$V_{Th,n}$**	**$\Delta V_{Th,p}$**
P3HT:P(NDI2OD-T2) 80:20	8	35	27
PCD-TPT:P(NDI2OD-T2) 80:20	24	46	22
PDVT-8:P(NDI2OD-T2) 50:50	0	25	25
IIDDT-C3:P(NDI2OD-T2) 50:50	-15	26	41

All threshold voltage values extracted from the curves in the linear regime.

7.4.2. Correlation between molecular structure and electrical performances

The molecular structures of the polymers were given in **Figure 7.1** and the molecular weights of each polymer are presented in **Table T7.1**. The molecular structure of P3HT is markedly different from the other polymers. It simply consists of a long flexible chain of thiophene units with hexyl chains, and is very different from P(NDI2OD-T2), a smaller chain consisting of large naphatalene diimide cores separated by non-functionalized thiophene units. The big difference in molecular structure and chemical functions could lead to phase segregation in the formed film, explaining the major impact on electrical characteristics of the presence of 20 wt% of P(NDI2OD-T2) in the blend.

PCD-TPT was the studied polymer possessing the highest molecular weight. The polymer consists of an alternation of dihexadecylcyclopentadithiophene groups and thiadiazolopyridine units, forming a thin and rigid conjugated system with two long and non-branched alkyl chains ($C_{16}H_{33}$) for each thiadiazolopyridine group. The *p*- and *n*-type mobilities are only slightly affected by addition of P(NDI2OD-T2) up to 50%, which could be either due to phase segregation with mostly PCD-TPT at the semiconductor-dielectric interface, or the ambipolar nature of PCD-TPT, leaving little room for improvement of the *n*-type mobility upon blending.

IIDDT-C3 and PDVT-8 share many similarities: they have a similar molecular weight and monomer weight, and their structure includes bithiophene units and branched alkyl chains. Their main differences are the pyrrolopyrroledione unit of PDVT-8 that is replaced by an isoindigo core in IIDDT-C3, and the length of the polymer that is increased in the case of PDVT-8 by one additional bithophene unit and carbon-carbon double-bond. They share more similarities with P(NDI2OD-T2) than the other polymers (unsubstituted thiophene groups, ketone functions, branched alkyl chains) and are thus less likely to phase segregate upon solvent evaportation. This could explain why balanced ambipolarity was found at a 50:50 blending ratio.

7.4.3. Correlation between film morphology and electrical performances

7.4.3.1. Surface morphology

AFM analysis was performed on the polymer blends at a 50:50 blending ratio in order to investigate the effect of blending on the surface of the films. The obtained images are displayed in **Figure 7.12** and the corresponding roughness measurements are reported in **Table T7.5**. In section *7.3.2.*, we observed that all single-component films formed smooth surfaces with $R_{RMS} < 1$ nm, except IIDDT-C3 with a roughness of 1.78 nm.

Films produced from P3HT and P(NDI2OD-T2) blends did not display any of the tight piles of elongated domains observed in the P(NDI2OD-T2) single-component film, but instead large domains with increased roughness compared to both of the single-component blends. This could be due to P3HT aggregating into larger domains and mostly covering P(NDI2OD-T2), P(NDI2OD-T2) losing its structure once blended with P3HT, or both. The measured electrical performances at the bottom of the film (with μ_n two orders of magnitude over μ_p, and very low μ_p of 10^{-4} cm²/Vs) seem to confirm the first explanation.

Concerning PCD:TPT 50:50 blends, the morphology of the surface of the film is similar to that of PCD-TPT, with a roughness value of 0.8 nm in both cases. Nevertheless, due to the close resemblance of P(NDI2OD-T2) and PCD-TPT single-component films, it is difficult to determine if the observed surface is composed of PCD-TPT, P(NDI2OD-T2) with slightly larger domains, or a blend of the two.

Regarding PDVT-8:P(NDI2OD-T2) 50:50 blends, the resulting surface was a bit rougher than in the case of PDVT-8, but the structure of the surface was very similar to PDVT-8. Therefore, it is very likely that the surface is almost only made of PDVT-8. The semiconductor-dielectric interface, however, should not consist of only P(NDI2OD-T2), since blended films at that ratio exhibit balanced mobilities. Furthermore, the presence of 20 wt% P(NDI2OD-T2) in the blend did not modify much the electrical performances of the device, definitively ruling out the presence of a pure P(NDI2OD-T2) layer at the interface.

Finally, films produced from 50:50 IIDDT-C3:P(NDI2OD-T2) blended solutions featured the most interesting surface. Unlike the other *p*-type polymers that displayed higher or similar roughness upon blending, the surface of the films had a reduced roughness when IIDDT-C3 was blended with P(NDI2OD-T2) (from 1.78 to 0.85 nm). This structure could be due to aggregates consisting of both polymers, with a similar blend at the interface, explaining the strong effect of the presence of 20% of one polymer with the other.

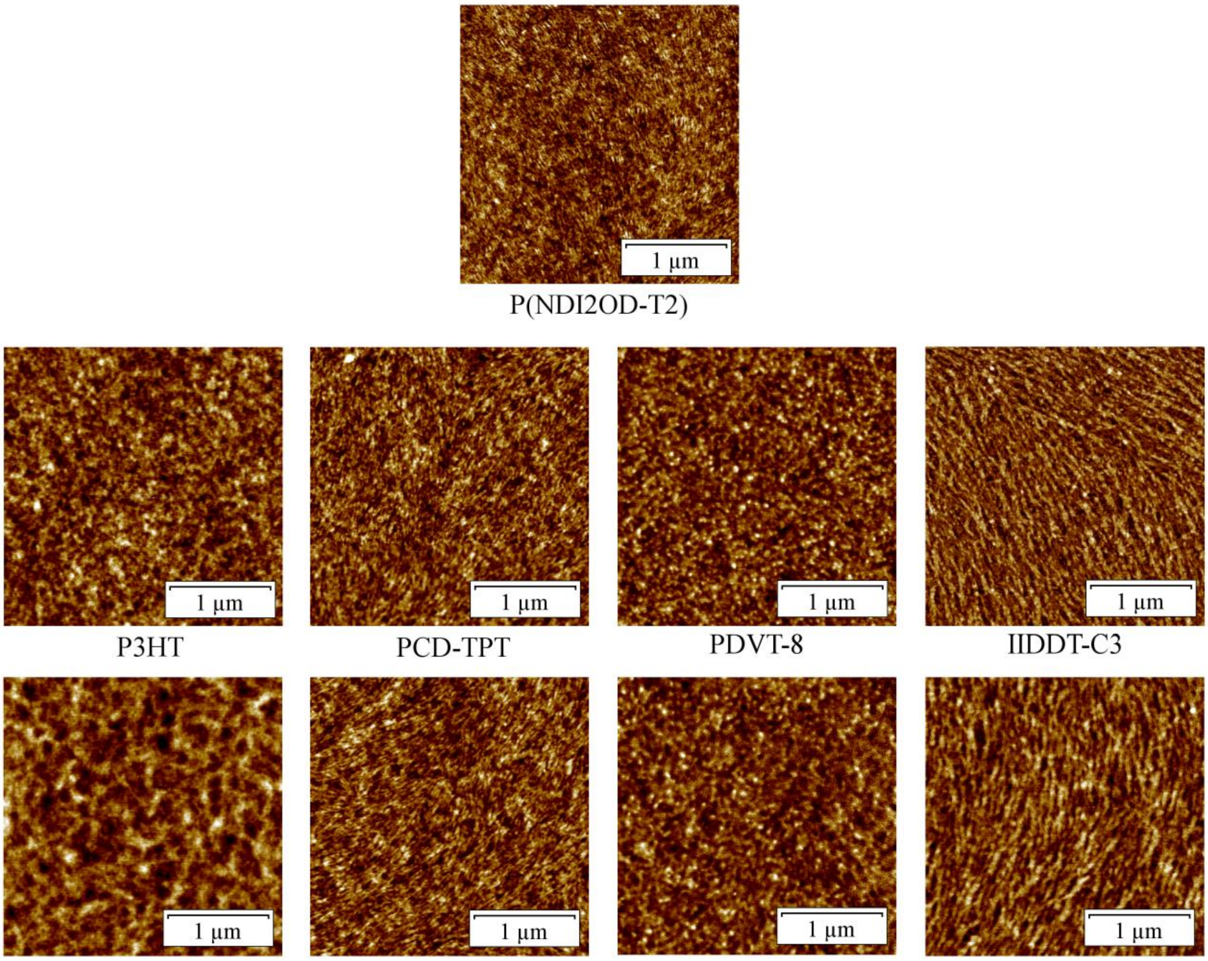

P(NDI2OD-T2)

P3HT

PCD-TPT

PDVT-8

IIDDT-C3

P3HT + P(NDI2OD-T2)

PCD-TPT + P(NDI2OD-T2)

PDVT-8 + P(NDI2OD-T2)

IIDDT-C3 + P(NDI2OD-T2)

Figure 7.12: Tapping Mode AFM topography images of 50:50 blended polymer films. *z*-scales: P(NDI2OD-T2) 4.4 nm, P3HT 3.5 nm, PCD-TPT 5.5 nm, PDVT-8 6.4 nm, IIDDT-C3 12.1 nm, 50:50 P3HT:P(NDI2OD-T2) 5.7 nm, 50:50 PCD-TPT:P(NDI2OD-T2) 5.8 nm, 50:50 PDVT-8:P(NDI2OD-T2) 5.4 nm and 50:50 IIDDT-C3:P(NDI2OD-T2) 5.8 nm.

Table T7.5: Roughness of the polymer films, extracted from the AFM height plots reported in **Figure 7.11**.

Polymer	**R_{RMS} / nm**	**R_{RMS} (50% blend with P(NDI2OD-T2)) / nm**
P(NDI2OD-T2)	0.637	/
P3HT	0.512	0.839
PCD-TPT	0.795	0.809
PDVT-8	0.910	1.192
IIDDT-C3	1.783	0.854

All measurements over 10µm × 10µm surfaces.

7.4.3.2. Top-gate transistors

In order to further investigate the surface of the blended films, top-gate transistors were fabricated for two polymer blends that exhibited completely different surfaces when probed with the AFM: PDVT-8 and IIDDT-C3 blended each time with P(NDI2OD-T2). It is noteworthy to mention that while top-gate transistors based on single-component IIDDT-C3 performed similarly to their bottom-contact bottom-gate counterparts, top-gate P(NDI2OD-T2) transistors featured mobilities one order of magnitude higher, while PDVT-8s *p*-type mobility was decreased by one order of magnitude compared to the performances observed in the bottom-gate configuration. These changes in mobilities are explained by the different electrode-semiconductor and dielectric-semiconductor interfaces. P(NDI2OD-T2) and IIDDT-C3 seemed to have benefitted the most from the increased injection area, while the OTS-treated dielectric allowed higher mobilities for PDVT-8, that did not display much injection difficulties from the output curves reported previously in section *7.3.1.*. Unlike the single-component bottom-gate devices described before, their top-gate counterparts did not display any observable ambipolar behavior. In both cases, the blending of polymers made it possible to fabricate ambipolar transistors. Nevertheless, the electrical characterization revealed large differences in mobilities (**Figure 7.13**). Films produced from blends of PDVT-8 and P(NDI2OD-T2) lead to a sharp decrease in *n*-type mobility, while maintaining very high *p*-type mobility. Therefore, both the electrical measurements and the AFM analysis seem to conclude that the surface of that film is mostly composed of PDVT-8. Transistors fabricated using blends of IIDDT-C3 and P(NDI2OD-T2), on the other hand, performed very well at the 50:50 ratio, with very balanced mobilities over 10^{-2} cm²/Vs in both cases ($\mu_p/\mu_n \approx 2$). These results can be explained by the well blended nature of the film, and the good performances of each separate polymer in the top-gate configuration. However, transfer curves in the saturation regime reported in **Figure 7.14** did not indicate the same ability to switch off as in the bottom-gate geometry, with I_{on}-I_{off} ratios of 10^3 for IIDDT-C3:P(NDI2OD-T2) 50:50 blends. Since a large ΔV_{Th} was observed in that case, the most likely reason for that decreased I_{on}/I_{off} is the dielectric leakage.

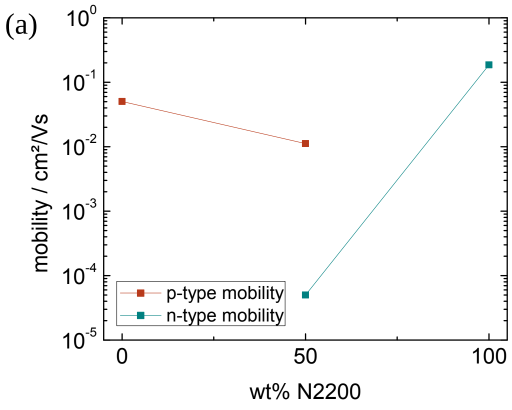

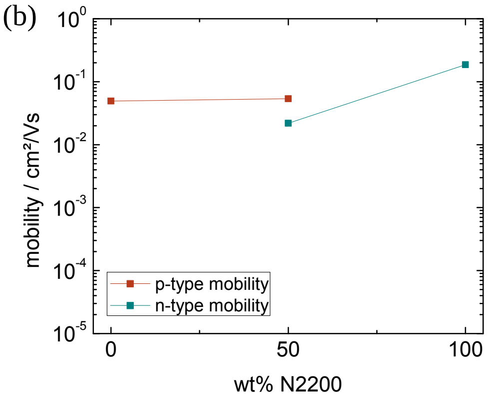

Figure 7.13: Average saturation regime mobility of devices in the top-gate geometry as a function of the percentage in weight of P(NDI2OD-T2) in the semiconductor solution deposited over the electrodes. Blends of P(NDI2OD-T2) with (a) PDVT-8 and (b) IIDDT-C3.

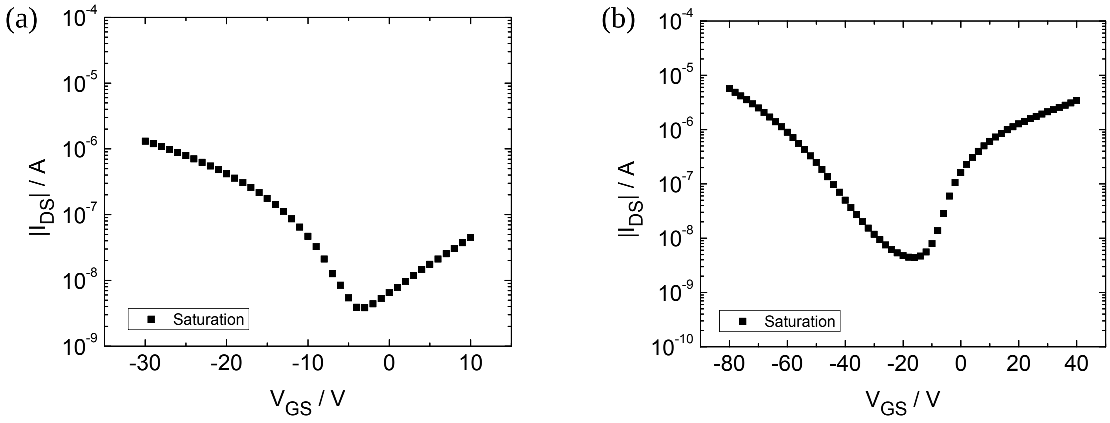

Figure 7.14: Transfer curves of devices produced from blends of P(NDI2OD-T2) and *p*-type semiconductors: (a) 50:50 PDVT-8:P(NDI2OD-T2) and (b) 50:50 IIDDT-C3:P(NDI2OD-T2).

7.4.3.3. Crystallinity

X-Ray diffraction and reflectivity experiments were performed with Rigaku Smartlab at IMM-CNR in Bologna in order to investigate the crystallinity of the single-component and bi-component films (**Figure 7.15**). They found that P(NDI2OD-T2) and PCD-TPT did not demonstrate any particular stacking features, while P3HT aggregated in edge-on configurations. Once blended with P(NDI2OD-T2), no significant features could still be observed, validating the assumption that P(NDI2OD-T2) is detrimental to the crystallinity of P3HT. Regarding PDVT-8, lamellar stacking peaks are observed in the single-component film. When blended with P(NDI2OD-T2), a new peak appears indicating a modified crystalline structure. Finally IIDDT-C3 is highly crystalline and both lamellar and π–π stacking peaks are observable. Films produced from the 50:50 IIDDT-C3:P(NDI2OD-T2) blend maintains a structural order only along the lamellar stacking.

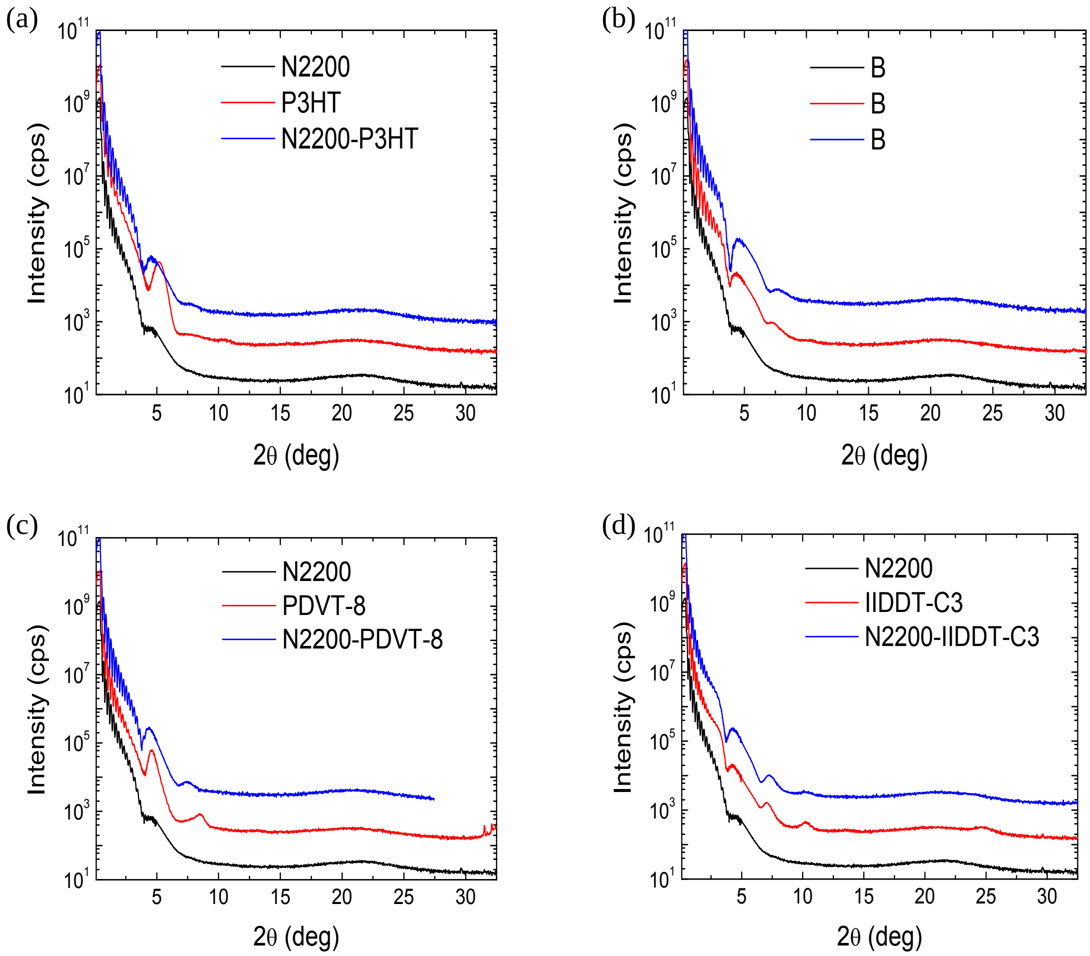

Figure 7.15: X-ray reflectivity (XRR) plots of single-component films and blends. (a) P(NDI2OD-T2), P3HT and 50:50 P(NDI2OD-T2):P3HT blend. (b) P(NDI2OD-T2), PCD-TPT and 50:50 P(NDI2OD-T2):PCD-TPT blend. (c) P(NDI2OD-T2), PDVT-8 and 50:50 P(NDI2OD-T2):PDVT-8 blend. (d) P(NDI2OD-T2), IIDDT-C3 and 50:50 P(NDI2OD-T2):IIDDT-C3 blend.

7.5. Conclusions

We have demonstrated that ambipolar transistors could be fabricated using blends of *n*-type and *p*-type polymers. P(NDI2OD-T2) was blended with 4 different *p*-type polymers, and each time it was possible to fabricate devices with balanced *p*- and *n*-type mobilities. In particular, devices with mobilities over 10^{-2} cm²/Vs and linear regime I_{on}/I_{off} over 10^5 were produced with a blend of P(NDI2OD-T2) and PCD-TPT. Impressive electrical performances obtained with PDC-TPT demonstrate that our approach can be used to adjust the electrical performances of ambipolar polymers featuring unbalanced mobilities. Furthermore, devices produced from P(NDI2OD-T2) blended with IIDDT-C3 featured mobilities up to 10^{-2} cm²/Vs and I_{on}/I_{off} of 10^{7}, unprecedented values for ambipolar organic transistors. While the mobilities of 0.01 cm²/Vs were not superior to some performances reported in literature for single component films, the fine control of the ratio between *p*- and *n*-type mobility and state-of-the-art I_{on}/I_{off} would be particularly suited for logic applications that rely on transistors with different polarities with good capacities to switch off. The morphology and structure of the films were investigated by means of AFM and X-ray diffraction, respectively. AFM was used as a tool to explore the in-plane phase-segregation while XRD data was used to probe the crystallinity of the bi-component films. It was found that P(NDI2OD-T2) and PCD-TPT films were amorphous both as single-component and blended films, yet still resulted in impressive results. These findings demonstrate that long-range order is not required for good charge transport in polymer films, in accordance to recent findings reported in literature. [24] The electrical performances were investigated in function of the geometry of the transistors (top-gate vs. bottom-gate), and it was found that the phase segregation can be probed by electrical testing. In particular, it was demonstrated that IIDDT-C3 and P(NDI2OD-T2) did not phase-segregate upon solvent evaporation, and high-performance balanced ambipolar top-gate devices could be produced from that blend.

7.6. References

1 Pfleiderer, H. & Kusian, W. Ambipolar field-effect transistor. *Solid State Electron.* **29**, 317-319 (1986).

2 Chesterfield, R. J. *et al.* High electron mobility and ambipolar transport in organic thin-film transistors based on a pi-stacking quinoidal terthiophene. *Adv. Mater.* **15**, 1278 (2003).

3 Bisri, S. Z., Piliego, C., Gao, J. & Loi, M. A. Outlook and Emerging Semiconducting Materials for Ambipolar Transistors. *Adv. Mater.* **26**, 1176-1199 (2014).

4 Meijer, E. J. *et al.* Solution-processed ambipolar organic field-effect transistors and inverters. *Nat. Mater.* **2**, 678-682 (2003).

5 Martel, R. *et al.* Ambipolar electrical transport in semiconducting single-wall carbon nanotubes. *Phys. Rev. Lett.* **87** (2001).

6 Podzorov, V., Gershenson, M. E., Kloc, C., Zeis, R. & Bucher, E. High-mobility field-effect transistors based on transition metal dichalcogenides. *Appl. Phys. Lett.* **84**, 3301-3303 (2004).

7 Xue, G. B. *et al.* Ambipolar charge transport of TIPS-pentacene single-crystals grown from non-polar solvents. *Mater. Horiz.* **2**, 344-349 (2015).

8 Dodabalapur, A., Katz, H. E., Torsi, L. & Haddon, R. C. Organic field-effect bipolar transistors. *Appl. Phys. Lett.* **68**, 1108-1110 (1996).

9 Dinelli, F. *et al.* High-mobility ambipolar transport in organic light-emitting transistors. *Adv. Mater.* **18**, 1416 (2006).

10 Cho, S. *et al.* Multilayer bipolar field-effect transistors. *Appl. Phys. Lett.* **92** (2008).

11 Wei, Q. S., Tajima, K. & Hashimoto, K. Bilayer Ambipolar Organic Thin-Film Transistors and Inverters Prepared by the Contact-Film-Transfer Method. *ACS Appl. Mater. Inter.* **1**, 1865-1868 (2009).

12 Kim, F. S., Ahmed, E., Subramaniyan, S. & Jenekhe, S. A. Air-Stable Ambipolar Field-Effect Transistors and Complementary Logic Circuits from Solution-Processed n/p Polymer Heterojunctions. *ACS Appl. Mater. Inter.* **2**, 2974-2977 (2010).

13 Shkunov, M., Simms, R., Heeney, M., Tierney, S. & McCulloch, I. Ambipolar field-effect transistors based on solution-processable blends of thieno[2,3-b]thiophene terthiophene polymer and methanofullerenes. *Adv. Mater.* **17**, 2608 (2005).

14 Earmme, T., Hwang, Y. J., Murari, N. M., Subramaniyan, S. & Jenekhe, S. A. All-Polymer Solar Cells with 3.3% Efficiency Based on Naphthalene Diimide-Selenophene Copolymer Acceptor. *J. Am. Chem. Soc.* **135**, 14960-14963 (2013).

15 Fabiano, S. *et al.* Charge Transport Orthogonality in All-Polymer Blend Transistors, Diodes, and Solar Cells. *Adv. Energy Mater.* **4** (2014).

16 Yan, H. *et al.* A high-mobility electron-transporting polymer for printed transistors. *Nature* **457**, 679-U671 (2009).

17 Steyrleuthner, R. *et al.* The Role of Regioregularity, Crystallinity, and Chain Orientation on Electron Transport in a High-Mobility n-Type Copolymer. *J. Am. Chem. Soc.* **136**, 4245-4256 (2014).

18 Hou, J. H., Tan, Z., He, Y. J., Yang, C. H. & Li, Y. F. Branched poly(thienylene vinylene)s with absorption spectra covering the whole visible region. *Macromolecules* **39**, 4657-4662 (2006).

19 Lee, T. *et al.* Synthesis, Structural Characterization, and Unusual Field-Effect Behavior of Organic Transistor Semiconductor Oligomers: Inferiority of Oxadiazole Compared with Other Electron-Withdrawing Subunits. *J. Am. Chem. Soc.* **131**, 1692-1705 (2009).

20 Ying, L. *et al.* Regioregular Pyridal[2,1,3]thiadiazole pi-Conjugated Copolymers. *J. Am. Chem. Soc.* **133**, 18538-18541 (2011).

21 Chen, H. J. *et al.* Highly p-Extended Copolymers with Diketopyrrolopyrrole Moieties for High-Performance Field-Effect Transistors. *Adv. Mater.* **24**, 4618-4622 (2012).

22 Lei, T., Dou, J. H. & Pei, J. Influence of Alkyl Chain Branching Positions on the Hole Mobilities of Polymer Thin-Film Transistors. *Adv. Mater.* **24**, 6457-6461 (2012).

23 Luzio, A. *et al.* Synthesis, Electronic Structure, and Charge Transport Characteristics of Naphthalenediimide-Based Co-Polymers with Different Oligothiophene Donor Units. *Adv. Funct. Mater.* **24**, 1151-1162 (2014).

24 Wang, S. H. *et al.* Experimental evidence that short-range intermolecular aggregation is sufficient for efficient charge transport in conjugated polymers. *P Natl Acad Sci USA* **112**, 10599-10604 (2015).

Chapter 8. Optical memory TFT device based on an organic bi-component blend

8.1. Introduction

While silicon-based technology is still effectively leading today's electronic industry, the development of high-performance organic semiconducting materials has been the topic of important research efforts in the past two decades. [1-3] Such materials unambiguously represent an interesting alternative since their properties can readily be tuned via *ad-hoc* chemical synthesis and they allow for mild processing from solution using approaches which can be up-scaled and applied to "soft" substrates, thereby making them ideal candidates for the low-cost fabrication of large-area electronic devices. These materials have shown exceptional versatility, enabling integration on flexible and/or transparent substrates for a new generation of electronics. [4-7] Among the plethora of applications of semiconducting organic materials and more generally of π-conjugated (macro)molecules, memories have attracted a special interest because they combine high switching ratios, [8-10] and long retention times [11] as well as low operating voltages [12-14] and the possibility to be integrated onto flexible substrates. [15-18]

In order to increase data storage capabilities in electronic devices (i.e. hard drives, random access memories, etc.), the most popular approaches thus far rely on the continuous scaling down to enable integration of an increasing number of memory cells per area unit. These strategies have shown their limits, as scaling down is hampered by photolithography while fabrication complexity has increased dramatically over the years.[19,20] An alternative method is based on the development of memory cells with increased storage capabilities for multilevel memories. In the case of 1-bit storage devices, a finite yet limited degree of volatility is not detrimental to the overall storage capacity as long as the two states, typically represented by a current maximum and minimum, are still distinguishable. The main challenge is to obtain the highest possible difference in current between an “on-state” and an “off-state”. When multilevel memories are considered, the conundrum shifts dramatically to the stability of states, as each state will necessarily be close to others. In the example of a 4-bit memory cell (16 current levels), one order of magnitude difference between each level is unachievable, since this would mean a switching ratio as high as 10^{15}. Importantly, all those methods where a high switching ratio is simply based on a threshold voltage shift (i.e. not characterized by a change in charge carrier mobility or current) with the "read voltage" within the threshold voltage window are prone to data loss and incorrect reading of the levels in multilevel storage. [21,22]

Previously in this thesis work, it was demonstrated that bi-component blends could prove an effective approach to electrical properties tuning, for improved performances and new functionalities. Among polymers, P3HT was chosen because it is easy to process and able to form homogenous blends efficiently integrated into field-effect transistors. While the previous chapters focused on the improvement of charge-transport performances, this last chapter will step into the realm of practical applications, with the fabrication of a fully functional photo-switchable memory. As canvas for this study, a previous work, reported by Orgiu et al. in 2012, will be exploited. Through this research article, the authors highlighted how a photochromic diarylethene unit, DAE-Me, blended into a P3HT polymer matrix, could be exploited for the fabrication of photo-tunable devices for a fine control of the I_{DS} current. [23] In this chapter we will first demonstrate how this feature can be exploited for the production of non-volatile multilevel memories. Secondly, we will investigate the integration of these memory-units onto a flexible PET substrate, focusing on the structural design of the device and the adequate choice of dielectric for the highest quality of flexible TFT-memories.

8.2. Methods

8.2.1. Transistors on SiO$_2$

Bottom-contact bottom-gate configuration transistors purchased from IPMS Fraunhofer Institute were used. They consisted of on *n*$^{++}$-Si substrates with 230 nm of thermally grown SiO_2 as the gate dielectric (15 nF capacitance) and pre-patterned pairs of gold electrodes with interdigitated geometry as the source and drain. All solutions, samples and devices were prepared and measured in a N_2 filled glovebox to avoid oxidative doping of the materials and ensure reproducibility of the experiments. OTS was purchased from Sigma-Aldrich. OTS treatment consisted of a 12-hours immersion of the ozone-treated wafer into a 10 mM solution of OTS in toluene with 30 min of heating at 60 °C at the beginning of the immersion. The samples were afterwards rinsed with toluene and heated for 60 min at 60 °C. Subsequently, 100 µL of the P3HT-DAE-Me_o solution was spin-coated onto the OTS treated wafer at 1500 RPM (acceleration: 4000 RPM.s^{-1}). The DAE-Me/P3HT solution consisted of a blend of 0.4 mg of DAE-Me_o and 1.6 mg of P3HT in 1mL of chloroform. The final sample is illustrated in **Figure 8.1**.

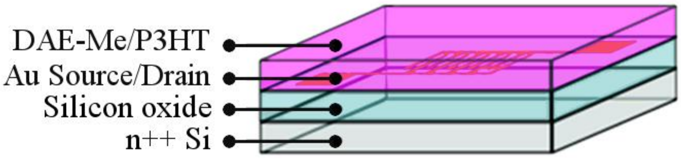

Figure 8.1: Bottom-gate devices on silicon oxide. Schematic representation of the bottom-gate bottom-contact P3HT/DAE-Me devices on a silicon oxide substrate.

8.2.2. Transistors on PET

Independent on the configuration, a square PET film (thickness = 175 µm) was attached to a glass substrate using thermal tape, in order to ensure ease of process for the future steps (especially spin-coating). Unless specified, the DAE-Me_o/P3HT solution consisted of a blend of 0.4 mg of DAE-Me_o and 1.6 mg of P3HT in 1 mL of chloroform (20 wt% DAE-Me solution), and a volume of 150µL was spin-coated at 1500 RPM (acceleration: 4000 RPM.s^{-1}).

8.2.2.1. Top-gate transistors on PET

Interdigitated gold source and drain electrodes were evaporated (60 nm thickness) on top of the PET film, using a shadow mask. The P3HT/DAE-Me blend was subsequently spin-coated over the electrodes. A layer of PMMA (at 70mg/mL, filtered using 0.2 µm filters) was spin-coated on the sample, and annealed 4 hours at 70 °C. The low annealing temperature was chosen for protection of the photochromic molecules. This step was repeated to form a second layer. The Al gate electrode was vacuum-deposited on the dielectric through shadow mask (layer thickness = 60 nm). The final sample is illustrated in **Figure 8.2**.

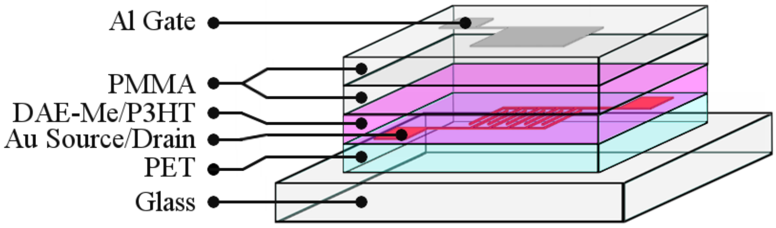

Figure 8.2: Top-gate devices on flexible PET substrate. Schematic representation of the top-gate P3HT/DAE-Me devices on a PET substrate.

8.2.2.2. Bottom-gate transistors on PET, Cytop dielectric

Using a shadow mask, 60 nm of Al were evaporated on top of the PET in order to form the gate electrode. A layer of Cytop was spin-coated onto the gate electrode, and annealed 2 hours at 120 °C. The interdigitated gold source and drain electrodes were vacuum-deposited on the dielectric through shadow masks (layer thickness = 60 nm). The semiconducting P3HT/DAE-Me blend was spin-coated as the final layer of the sample. The final sample is illustrated in **Figure 8.3**.

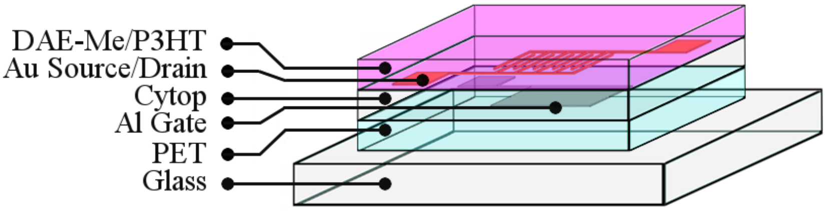

Figure 8.3: Bottom-gate devices on flexible PET substrate. Schematic representation of the bottom-gate P3HT/DAE-Me devices on a PET substrate, using Cytop as dielectric.

8.2.2.3. Bottom-gate transistors on PET, PMMA-PVP dielectric

60 nm of Au were evaporated over the PET layer in order to form the gate electrode. A whole layer was used in order to provide a contactable area outside of the dielectric for future testing of the device, as the hardened PVP was impermeable to piercing with the needle of the probe station. One side of the sample was protected from the next steps of the procedure with a small strap of thermal tape. A layer of the dielectric poly(methyl methacrylate) (PMMA) was spin-coated onto the gate electrode, and annealed one hour at 120 °C. An additional dielectric, poly(4-vinylphenol) (PVP) was spin-coated on the PMMA and annealed two hours at 150 °C. The interdigitated gold source and drain electrodes

were vacuum-deposited on the dielectric through shadow masks (layer thickness = 60 nm). Finally, the semiconducting P3HT/DAE-Me blend was spin-coated as the final layer of the sample. The final sample is illustrated in **Figure 8.4**.

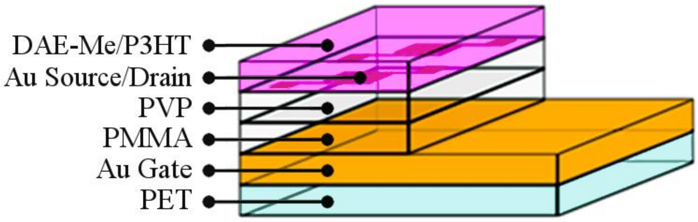

Figure 8.4: Bottom-gate memory unit onto a flexible PET substrate, using a hybrid PMMA/PVP dielectric.

8.2.3. Device characterization

The device characteristics were measured by contacting the source, drain and gate electrodes and applying different voltages in order to get I_{DS}-V_{GS} graphs. In the case of I_{DS}-V_{GS} graphs (transfer curves) each was made by sweeping the gate voltages from +40 V to -60 V, with one measurement every 2 V. The drain voltage was either -10V (linear regime) or -60 V (saturation regime). The I_{DS} current was measured each time. Experimental data were analyzed using standard field-effect transistor equations (for *p-type* semiconductors) for the saturation regime (see chapter 4):

$$I_{DS} = -\frac{W}{2L}\mu C_{TOT}(V_{GS} - V_{Th})^2 \qquad \textbf{Eq. 8.1}$$

with C_{TOT} the total capacitance of the dielectric. The total capacitance in a bilayer PMMA/PVP dielectric is given by:

$$C_{TOT} = \frac{C_{PMMA} \times C_{PVP}}{C_{PMMA} + C_{PVP}} \qquad \textbf{Eq. 8.2}$$

The thickness of each layer was measured using a profilometer. The values of the relative permittivity used for mobility are presented in **Table T8.1**.

Dynamic switching was observed by tracing of I_{DS}-time curves at constant Gate-Source voltage and constant Drain-Source voltage. The samples were illuminated while being biased and I_{DS}-current was measured.

Table T8.1: Relative permittivities of the dielectrics used in chapter 8.

Dielectric	Relative permittivity (ε_r)
SiO_2	3.9 [24]
PVP	3.5 [25]
Cytop	2.1 [26]
PMMA	4.9 [27]

8.2.4. Illumination setups

Depending on the configuration of the devices, different illumination setups were designed. In the case of bottom-gate geometry, the device is directly illuminated from the top, using either a monochromator or a short-pulse laser setup, as illustrated on **Figure 8.5a**. In the case of top-gate geometry, the sample cannot be illuminated from the top, as the gate electrode is not transparent. Therefore, the illumination has to be performed from underneath the device. This can be achieved either through direct illumination which requires the light source to be moved to underneath the device (**Figure 8.5b**) or with a setup relying on two mirrors pointing the light beam underneath the device, starting from a light source on top of the sample (**Figure 8.5c**).

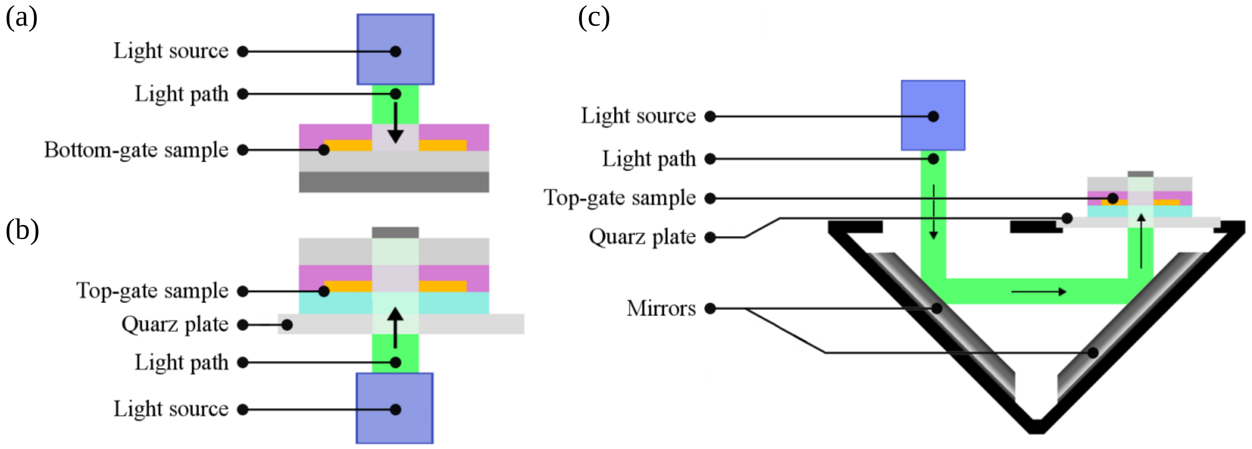

Figure 8.5: Illumination setups. (a) Direct illumination, from the top for bottom-gate devices. (b) Direct illumination, from the bottom for top-gate devices. (c) Double mirror setup for illumination from the bottom. On both setups, the light beam is represented in green.

Illumination was performed using either a laser setup (incident power: 85±17 µJcm^{-2} for each 3 ns pulse at full transmittance, memories on SiO_2 and PET) or a monochromator setup (incident power: 74 µJcm^{-2} per second of irradiation at 313 nm, memories on PET). All the experiments using a monochromatic light source were performed in Strasbourg, while experiments using the short-pulse laser setup were performed at the University of Nova Gorica, with the help of Profs. Egon Pavlica and Gvido Bratina.

8.3. *Three-terminal memory devices on SiO_2.*

We first explored bottom-gate bottom-contact field-effect transistors using a SiO_2 layer as the gate dielectric. The bi-component active layer comprising the photochromic moiety DAE-Me in a P3HT polymer matrix (**Figure 8.6, a,b**) was spin-coated from a solution in chloroform and then electrically characterized in a nitrogen-saturated atmosphere of a glove box. In order to confer a high starting crystallinity to the polymer active layer and enhance its electrical performances, octadecyltrichlorosilane (OTS, **Figure 8.6, c**) chemisorbed self-assembled monolayers were formed on the SiO_2 dielectric surface. [28] Optical microscope images of the channel between source and drain electrodes are presented in **Figure 8.7**, underlying a homogenous coating of the surface within the electrodes. Furthermore, AFM height plots were recorded as a means of investigation of the surface roughness (**Figure 8.8**). It was found that substrate treatment with OTS reduced the roughness (R_{RMS} = 0.54 as compared to 0.74 for an untreated substrate, **Table T8.2**).

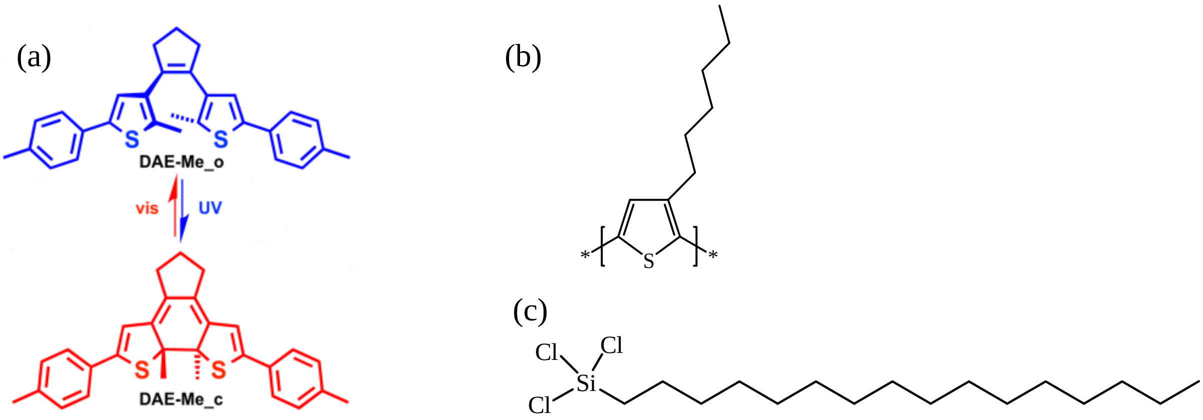

Figure 8.6: Molecular structures. (a) Chemical formulae of the employed diarylethene in its open and closed form, (b) Chemical formula of the *p*-type semiconductor P3HT, (c) Chemical formula of the self-assembled monolayer octadecyltrichlorosilane (OTS).

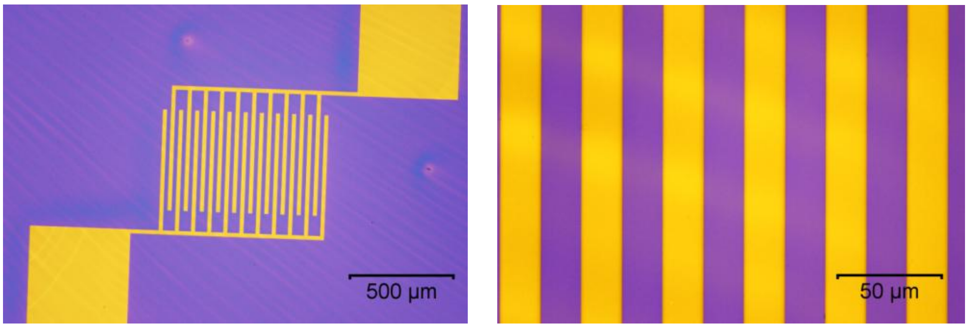

Figure 8.7: Optical microscopy images. Images of P3HT/DAE-Me layer on SiO_2 (channel length = 20 µm).

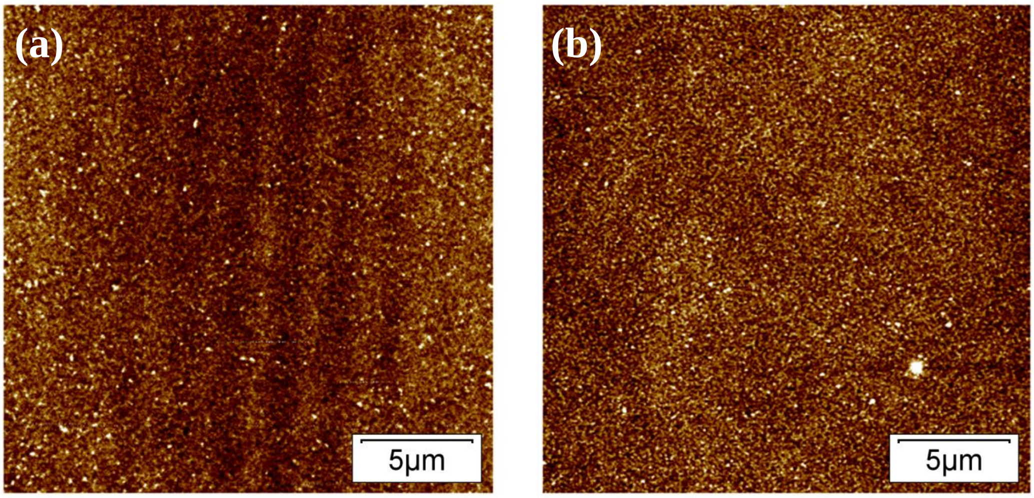

Figure 8.8: Atomic Force Microscopy height plots. Images of (a) a P3HT/DAE-Me layer on SiO_2 without surface treatment (z-scale: 5 nm) and (b) a P3HT/DAE-Me layer on OTS SiO_x treated surface (z-scale: 4 nm).

Table T8.2: Root mean squared values of the roughness (R_{RMS}) as calculated from the AFM height plots presented in Figure 4. Data is presented in nm. The roughness was estimated from 100 nm^2 surfaces.

Surface	Root mean squared roughness (R_{RMS}) / nm
SiO_x / no OTS[1]	0.74
SiO_x / OTS[1]	0.54

[1] OTS treatment

Transfer curves (I_{DS}-V_{GS}) were used to quantify the devices' field-effect mobility (μ_{FET}), threshold voltage (V_{Th}), and I_{on}/I_{off} ratio (**Figure 8.9, a-c**). The electrical characterization revealed devices featuring classical *p*-type transfer characteristics and high field-effect mobilities for P3HT (10^{-3} $cm^2V^{-1}s^{-1}$ for an untreated device and 10^{-2} $cm^2V^{-1}s^{-1}$ for an OTS treated device). OTS treatment was found to generally improve electrical characteristics. The current ratio between the on and off state of the transistor (I_{on}/I_{off}) was found to be over 10^5 in both open and closed form, indicating excellent ability to perform as a field effect-transistor. The current ratio measured in the active layer comprising the photochromic unit either in the open or the closed form ("switching ratio") was extracted from the I_{DS}-V_{GS} curves. In particular, the I_{DS} was measured in the dark once the diarylethene isomer in the bi-component film is turned into its open (DAE-Me_o) or in majority into its closed (DAE-Me_c) isomer upon irradiation with monochromatic light at λ = 546 nm (*erase*) or 313 nm (*write*), respectively. To better compare our results with the scientific literature, we employed the ratio $I_{DS,DAE\text{-}Me\_o}$ /$I_{DS,DAE\text{-}Me\_c}$ (measured at the same V_{DS} and V_{GS}) as a figure of merit (**Figure 8.9d**). As evident from **Figure 8.9b,c** a threshold voltage shifts towards negative bias (ΔV_{Th} amounting to ca. to -15 V) was observed when the DAE-Me molecules were converted from their open to their closed isomer, while OTS was used as a silicon oxide (SiO_2) surface treatment. The resulting difference in threshold voltage between the open and closed forms enables a switching ratio over 10^5 for V_{Th} (open form) < V_{GS} < V_{Th} (closed form). Nevertheless and contrary to single level memories, their multilevel counterparts require fine-tuning of each current-level. Therefore, in order to increase the reliability of the device, the "dynamic range" between the extreme off and on levels ($I_{DS,DAE\text{-}Me\_o}$ - $I_{DS,DAE\text{-}Me\_c}$ at a fixed V_{DS} and V_{GS}) should be maximized. Hence, further measurements have been performed at V_{GS} = - 60 V.

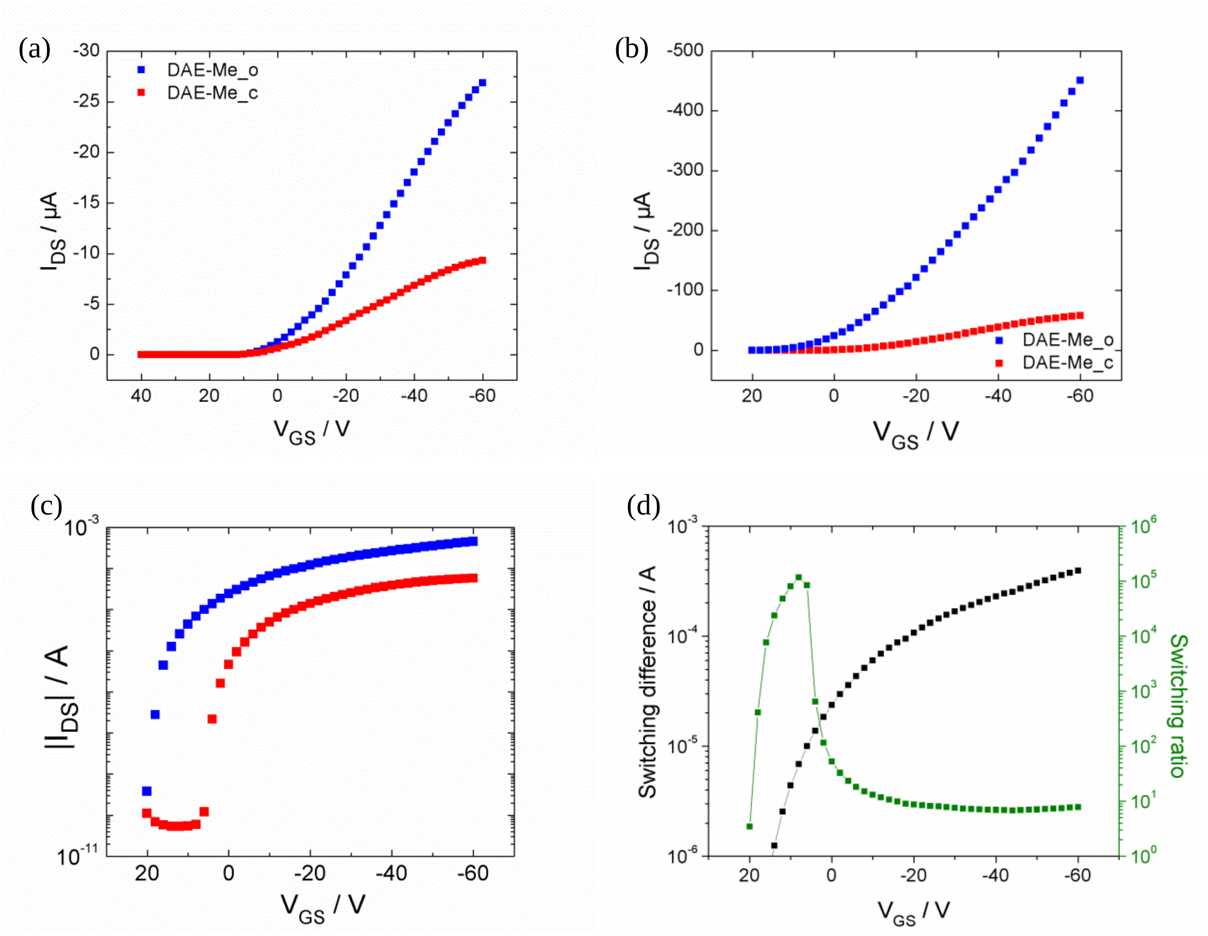

Figure 8.9: Electrical characterization of the bottom-gate/bottom-contact P3HT/DAE-Me devices. (a) I_{DS}-V_{GS} of an untreated device in the open and the closed form (after 10 minutes of irradiation at λ = 313 nm), at V_{DS} = - 60 V. (b) I_{DS}-V_{GS} of an OTS-treated device in the open and the closed form (after 10 minutes of irradiation at λ = 313 nm), at V_{DS} = - 60 V. (c) The same curve as (b) is represented in logarithmic scale. (d) Switching ratio ($I_{DS,DAE\text{-}Me\_o}/I_{DS,DAE\text{-}Me\_c}$) and switching difference ($I_{DS,DAE\text{-}Me\_o}$ - $I_{DS,DAE\text{-}Me\_c}$) as a function of the gate voltage. [All graphs from devices with L = 20 μm, W = 10 mm, C = 1.5 nF cm^{-2}]

Different amounts of DAE-Me added to P3HT (wt%) were tested in order to explore the effect of the mutual ratio on the electrical performances and switching capabilities (**Figure 8.10**). We have found that mobilities decreased when the amount of DAE-Me in the blend was increased (both in open and closed form). On the other hand, the amplitude of the light-induced switching process (in terms of μ_{FET}) of the devices was improved when a superior amount of DAE-Me was introduced in the blend spin-coated onto the device. The threshold voltage difference remained constant up to 20% DAE-Me similarly to the I_{on}/I_{off}. A good compromise between mobility and switching ratio was found with 20 wt% DAE-Me in the blend. It is noteworthy to mention that our blending approach is versatile as it allows for tailoring to any desired DAE-Me/polymer pair depending on the application at hand and the materials in use, [23,29-31] contrary to the separate layer approach that is typically used in the context of organic two- and three-terminal memories. [32,33]

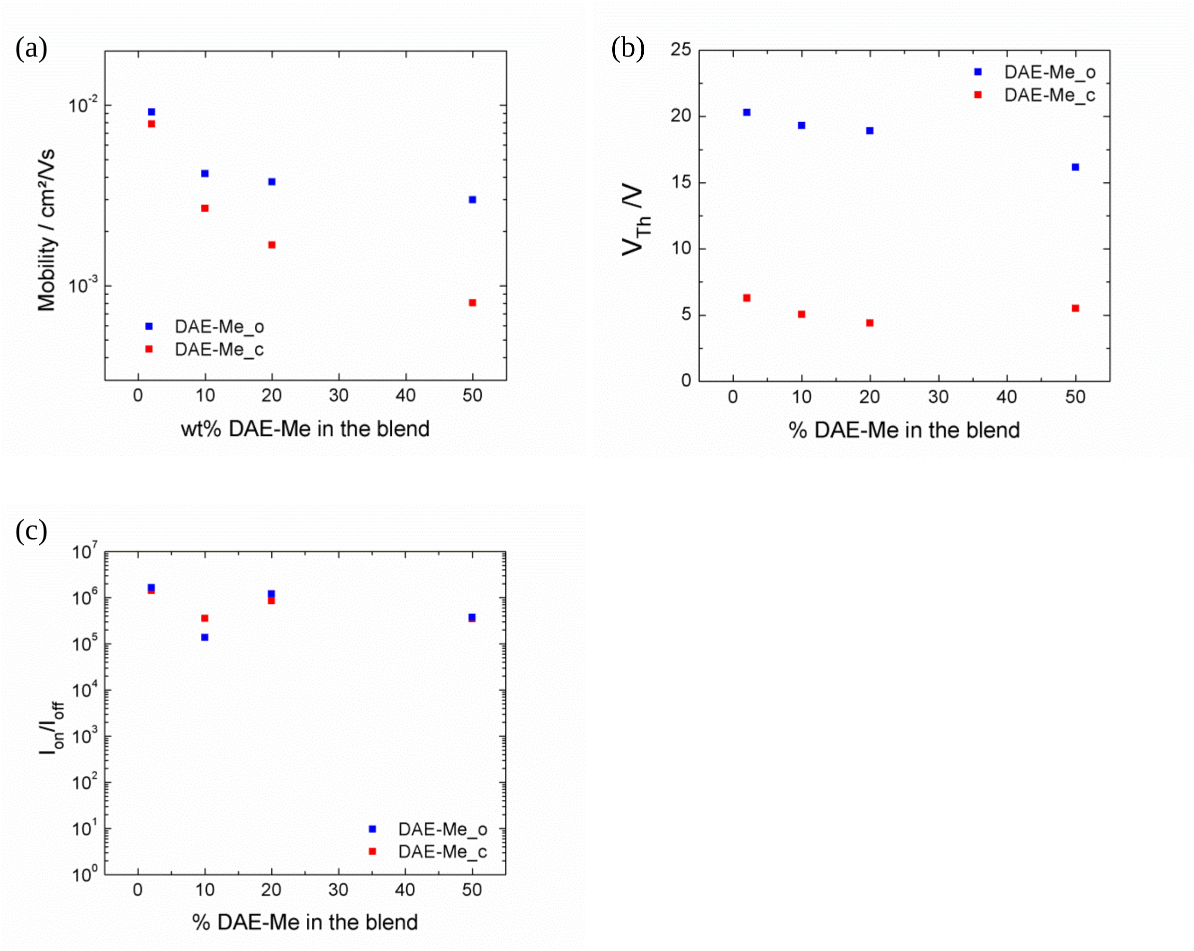

Figure 8.10: Impact of the amount of DAE-Me in the DAE-Me/P3HT blend on the electrical performances. (a) Average μ_{FET} of the devices as a function of the weight percentage of diarylethenes in the blend. (b) Threshold voltages of OTS treated SiO_2 transistors in the open and closed form for different amounts of diarylethene in the blend. (c) I_{on}/I_{off} ratio of the same devices in the open and closed form at V_{DS} = - 60 V. [All graphs from OTS-treated devices with L = 20 µm, W = 10 mm, C = 1.5 nF cm^{-2}]

The endurance of the semiconductor-DAE-Me blend was tested by dynamic write-erase cycles at constant bias. On this occurrence and throughout the entire chapter, continuous measurement of the I_{DS} current as a function of time will be referred to as dynamic characterization. In order to determine the sole contribution of the DAE-Me to the I_{DS} current change, the decay observed due to bias stress on P3HT was estimated from the curve before illumination, and deduced from the I_{DS}-time plot. On over 70 write-erase cycles (10 s cycles after 20 min of measurement without illumination), the switching fatigue was found to be negligible. This is a good indication for the stability of the devices as they can undergo a large number of write-erase cycles with minor impact on their switching ability (**Figure 8.11a**). The retention capabilities of the devices have been tested by measuring the I_{DS} current at a fixed V_{DS} of - 10 V and V_{GS} of - 60 V in the open and the closed form after different storage times in the dark. No modification of the currents was found after 64 days in the dark, providing clear evidence for excellent retention capabilities reaching 100 days (10^7 s, **Figure 8.11b**).

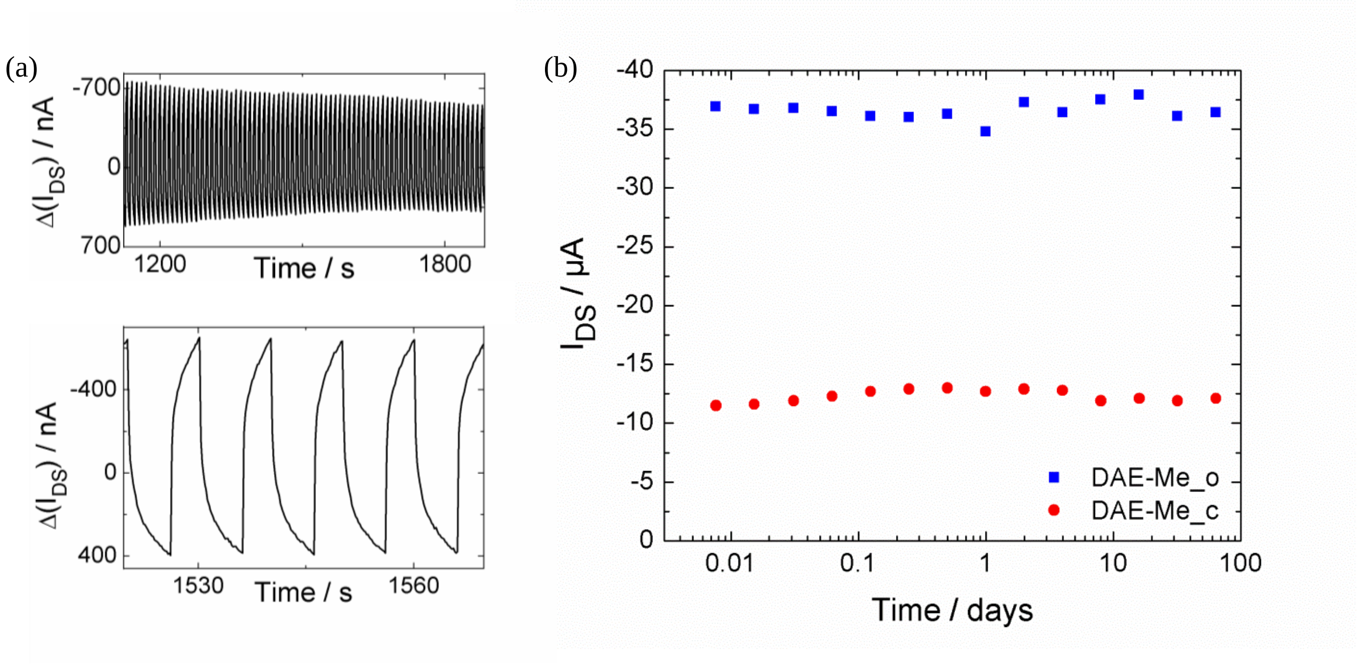

Figure 8.11: Data Retention of the memory device. (a) Experimental dynamic I_{DS}-time curves, corrected for bias stress, at V_{DS} = -10 V and V_{GS} = -60 V: writing for 1 second at 313 nm and erasing for 5 seconds at 546 nm. 70 cycles are shown in the main figure while only 5 of them are to be seen in the inset. ΔI_{DS} is defined by $\Delta I_{DS} = I_{DS} - I_{DS,t(initial)}$; (b) Measurement of the I_{DS} current after different times of storage of the device in the dark at fixed V_{DS} = -10 V and V_{GS} = -60 V to illustrate the retention capability of the devices in the open and the closed form.

8.4. Switching with ultrafast light irradiation.

A laser-setup with ultra short time pulses was used in order to investigate the photo-induced switching upon illumination times associated with modern optics and electronics. The device was exposed to a 3 ns laser pulse (λ = 313 nm) at tunable intensity in intervals of ten seconds leading to a progressive current decrease controlled by the number of pulses. Each pulse generated a ΔI_{DS} step decrease owing to the increasing amount of photogenerated hole traps, i.e. DAE-Me_c. Each current step has a certain height and this allowed us to estimate the *signal-to-noise* ratio (SNR) calculated from the RMS amplitude of the noise over 3×80 consecutive points. Within the first current levels SNR exceeds 50, and decreases to 2.8 in the final steps. The decrease results from the graduate reduction of the step height with a noise value that remains constant. We have successfully built a 400 current-intensity level device (**Figure 8.12**), reaching a data storage capacity over 8 bit (256 levels). By reduction of the light intensity using filters, we have shown that the step in height is dependent on the areal power density: the pulsed light was attenuated to transmittance of 33%, 11.5% and 1.3% in order to determine the minimum number of photons, which can close/open enough DAE-Me molecules to modulate the drain-source current. The step height dependency on the areal power density is explained by the number of molecules undergoing photoisomerization being proportional to the density of the photons hitting the device area (**Figure 8.13**). In particular, our device can already operate at incident power < 1 μJ cm^{-2}s^{-1}. The number of steps and hence the storage density is therefore only limited by the noise in the signal (leading to a maximum of 5000 steps in the presented experiment) with a theoretical maximum given by the number of steps equal to the number of DAE-Me molecules in the channel.

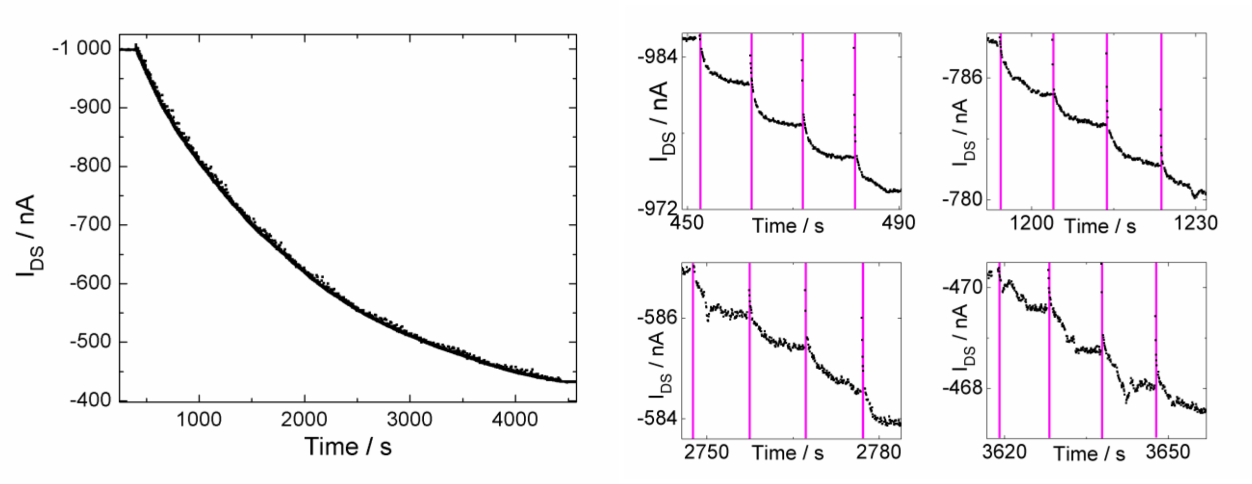

Figure 8.12: I_{DS}-time curves (corrected for bias stress) under irradiation of the device with 3 ns laser pulses (313 nm) every 10 s, underlining the ability to behave as a multilevel memory. Curves were plotted at V_{GS} = -60V and V_{DS} = -10V. Current-spikes in the curve are attributed to photo-generated carriers during irradiation. Given their short duration (3 ns) illumination steps are not represented to scale.

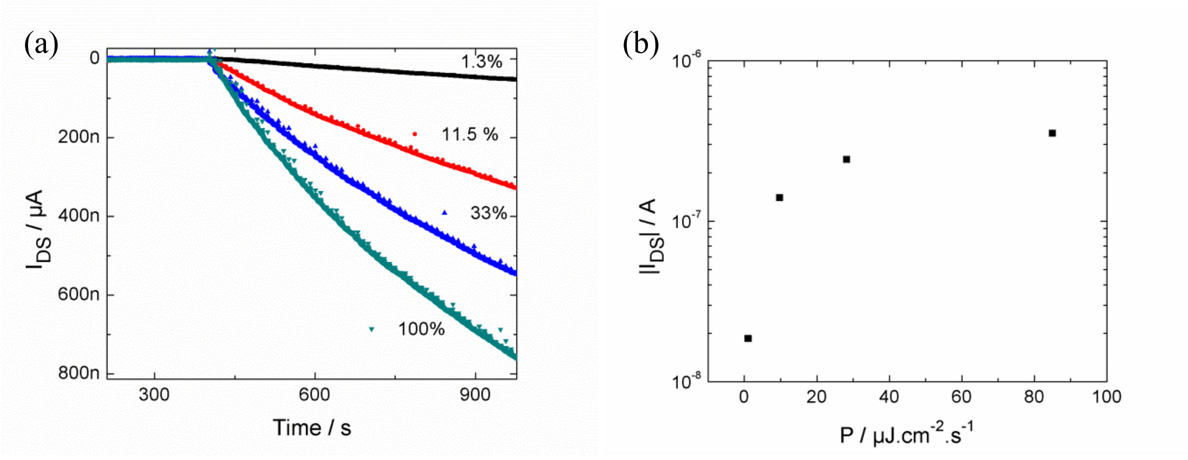

Figure 8.13: Devices illuminated with a laser light-source with filters of different transmittance values. All measurements were performed at V_{DS} = -10 V and V_{GS} = -60 V. (a) I_{DS}-time curves of the tested device. Switching ability was evaluated by dynamic I_{DS}-time curve for unfiltered laser-pulses and laser-pulses with 33%, 11.5% and 1.3% transmittance (100% transmittance corresponds to 85±17 μJcm^{-2} for each 3 ns pulse). All curves were corrected for bias stress and aligned at I_{DS} = 0 A for better appreciation of the effect of the filters on the I_{DS} current. (b) Plot representing the I_{DS} current as a function of the incident power, after twenty 3 ns pulses (Time = 600 s) at 313 nm.

8.5. Three-terminal device memories on a flexible PET substrate.

In view of the ultimate goal of demonstrating the possible implementation of the memory-devices into novel electronic applications, the whole procedure was adapted to a flexible substrate, trading the rigid inorganic silicon based dielectric layer for a polymeric sheet, with a flexible polyethylene terephthalate (PET, **Figure 8.14, a**) substrate. PET was selected for its flexibility, transparency and presence in the industry, underlying ease of use and affordable prices for future large-scale applications.

The three candidates as dielectrics were Poly(methyl methacrylate) (PMMA), Cytop and Poly(4-vinylphenol) (PVP), each with advantages and setbacks (**Figure 8.14, b-d**). PMMA is a widely used polymer and has shown very good performances as dielectric. Being highly soluble in chloroform, it could only be used for top-gate devices, spin-coated on top of the DAE-Me/P3HT blend. This setup has the advantage of encapsulating the blend, enhancing the air-stability of the device. The major setback is that the illumination has to be performed from underneath the device and through the PET film. Cytop has also demonstrated very high dielectric performances (with an excellent dielectric constant between 2.0 and 2.1), and lower solubility in chloroform. Therefore, it can be used in both top- and bottom-gate geometries, bottom-gate devices having the advantage of top illumination directly on the DAE-Me/P3HT blend. Unfortunately, the surface of the cytop layer is very hydrophobic due to its fluorinated moieties, and solutions in chloroform spin-coated on the surface did not produce films of the highest quality in terms of surface coverage, with results displaying low reproducibility. PVP was found to be a poorly performing polymer, in terms of current leakage. Once crosslinked, it did not dissolve in chloroform and could be used for bottom-gate devices. Furthermore, the surface was not hydrophobic as observed with Cytop: a uniform P3HT/DAE-Me film could be spin-coated onto a cross-linked PVP layer.

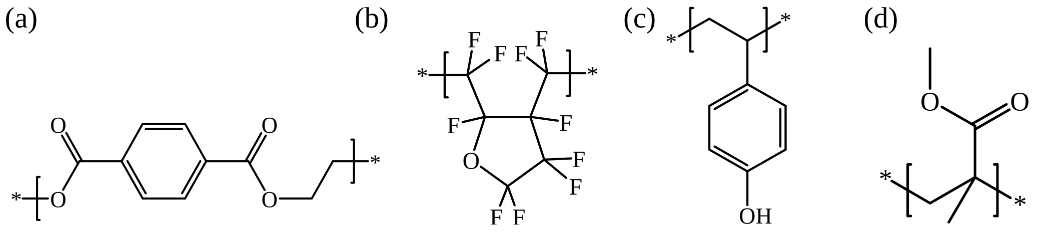

Figure 8.14: Molecular structures. Chemical formulaes of (a) the PET used as a flexible substrate, (b) the dielectric Cytop, (c) the dielectric Polyvinylpyrrolidone (PVP) and (d) the dielectric Poly(methyl methacrylate) (PMMA).

8.5.1. Top-gate geometry

The top-gate geometry was investigated at first, due to its promising semiconductor encapsulation feature, and potential for electrical performances, as OTS is not suitable for growth on a polymeric dielectric. A top-gate field effect transistor using PMMA as a gate dielectric was deisgned. A double layer of PMMA was deposited on the DAE-Me/P3HT blend in order to ensure good dielectric performance after gate deposition and bending tests. As a result, a working flexible transistor was produced, as illustrated in the photograph in **Figure 8.15, a**. The thickness of the PMMA was measured via profilometer and amounted to 860 nm, implying good electrical insulation (**Figure 8.15, b**). The devices were tested for electrical performances through $I_{DS}V_{DS}$ and $I_{DS}V_{GS}$ plots (**Figure 8.16**). The transistors performed very well, with no signs of charge-injection issues. A mobility value of $8x10^{-3}$ cm^2/Vs was found both in linear and saturation regime, the expected value for the top-gate transistor, due to the absence of OTS or HMDS treatment. The I_{on}/I_{off} was of $2x10^3$. The devices were bent at a bending radius of 6 mm for one minute, and were found to operate properly afterwards, without impact on electrical performances.

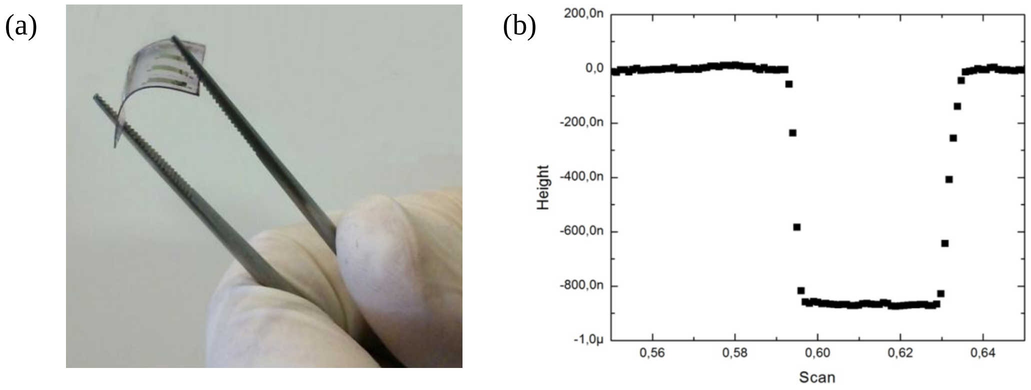

Figure 8.15: Top-gate devices on flexible PET substrate. (a) Photograph of a PET substrate with 8 devices (2 of each of the following channel lengths: 60 µm, 80 µm, 100 µm and 120 µm). (b) Thickness profile of the PMMA dielectric double layer. The height is given in meters, while the scan path is presented in centimeters.

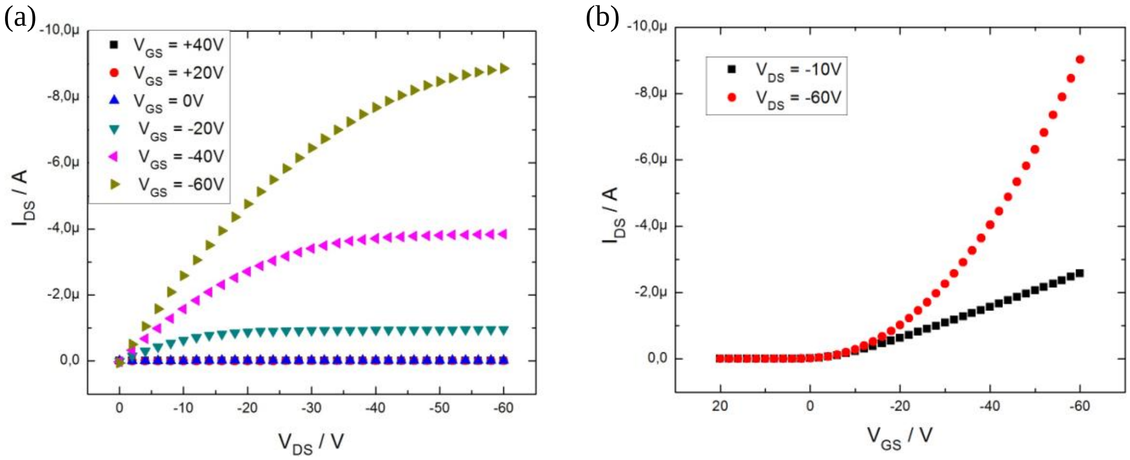

Figure 8.16: Electrical characterization of the top-gate devices on flexible PET substrate. (a) Output characteristics of the PMMA based transistor. (b) Transfer characteristics of the PMMA based transistor.

In order to measure the switching capabilities of the devices, a mirror setup was designed, with the help of Thomas Mosciatti. The available monochromator in the glovebox was designed for illumination from the top. Unfortunately, due to the presence of an opaque Al Gate over the photochromic DAEs in the channel, the illumination needed to be performed from "underneath" the sample (through the PET). No significant switching behavior was observed upon illumination both at 313 nm and 546 nm (**Figure 8.17, a**). This could be explained by the long light-path in the case of the mirror setup. Therefore, the setup was adapted with a direct illumination from under the sample. A slight change of the I_{DS} was observed upon illumination (**Figure 8.17, b**). These low switching capabilities are explained by the PET substrate that cuts most of the UV irradiation. We decided to produce bottom-gate devices in order to circumvent this issue.

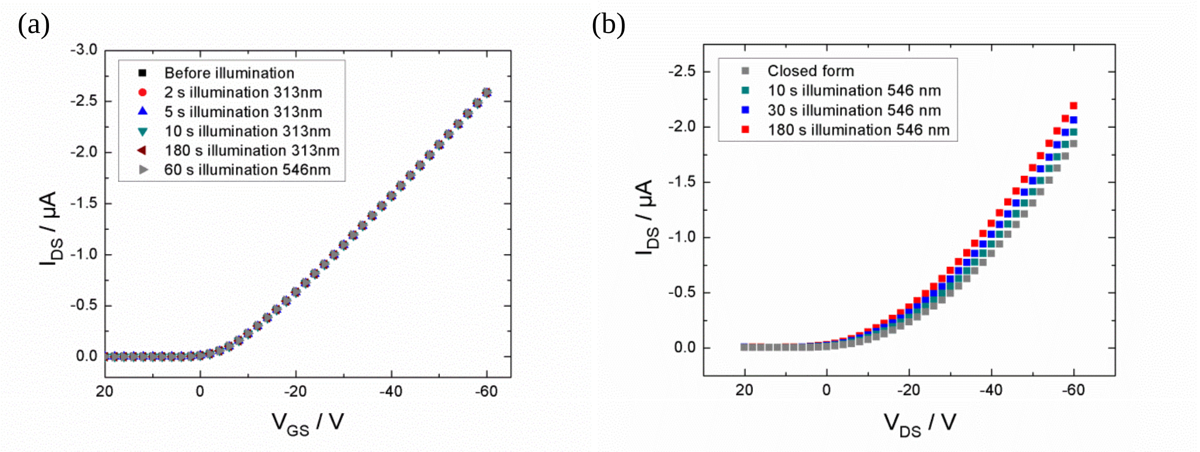

Figure 8.17: Transfer curves before and after illumination. $I_{DS}V_{GS}$ curves of devices illuminated through (a) the double mirror setup and (b) the direct illumination setup.

8.5.2. Bottom-gate geometry

Devices in the bottom-gate geometry were fabricated, using Cytop as a dielectric. The devices were tested and a mobility of 7.9×10^{-3} cm²/Vs was found in the open form, a value comparable to those obtained on an untreated SiO_2 dielectric. In the closed form, the mobility was found to be 5.6×10^{-3} cm²/Vs. This amounts to a low switching ratio of 1.4 (**Figure 8.18, a**). This is explained by observed wetting issues due to the use of Cytop as a dielectric. Dynamic switching curves were traced in order to determine if multi-level devices could be obtained on a flexible substrate. A device with six current steps was obtained at constant reading (**Figure 8.18, b**).

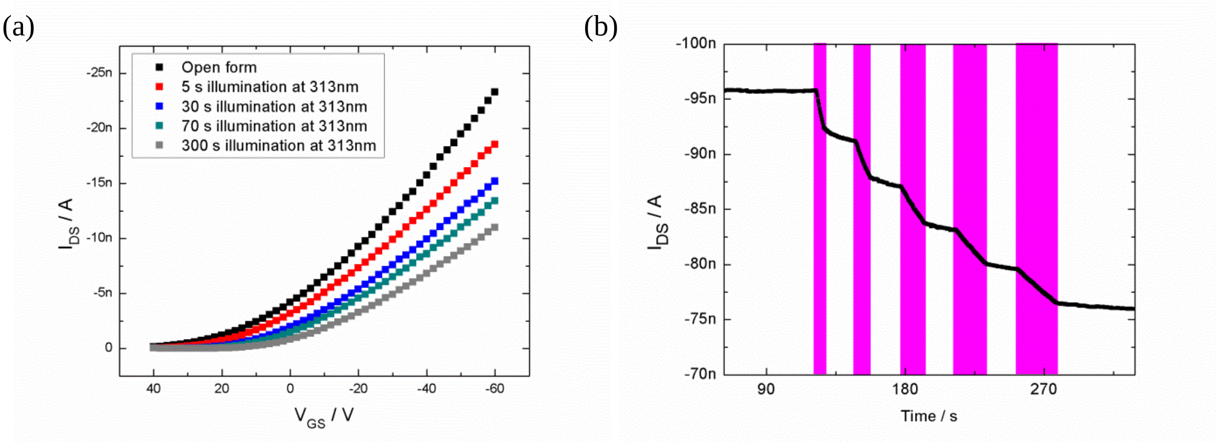

Figure 8.18: Bottom-gate memory unit onto a flexible PET substrate, using Cytop as dielectric. (a) $I_{DS}V_{GS}$ curves of devices illuminated at 313 nm. (b) Experimental dynamic I_{DS}-time curves, corrected for bias stress, showing small irradiation steps at 313 nm underlining the ability to behave as a multilevel memory (5 to 30 seconds incremental irradiation steps).

PVP was used as a dielectric, in order to achieve smooth films in bottom-gate configuration, and to avoid wettability issues as compared to Cytop-based bottom-gate devices. Very thick dielectric films were fabricated, leading to low currents (comparable to those reported above with cytop) (**Figure 8.19, a**). PVP proved to be a bad dielectric with leakage currents of 10% of the I_{DS} current, even at a thickness of 1.5µm (as observed on the transfer curves). Nevertheless, dynamic I_{DS}-time curves have shown good ability to produce multilevel memories (**Figure 8.19, b**).

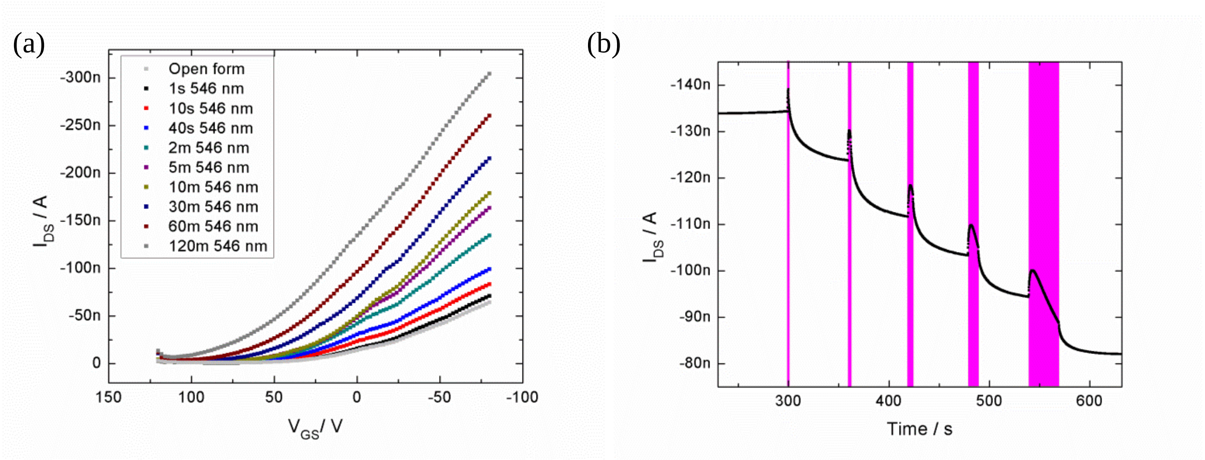

Figure 8.19: Bottom-gate memory unit onto a flexible PET substrate, using PVP as dielectric. (a) $I_{DS}V_{GS}$ curves of devices illuminated at 546 nm. (b) Experimental dynamic I_{DS}-time curves, corrected for bias stress, showing small irradiation steps at 313 nm underlining the ability to behave as a multilevel memory (1 to 20 seconds incremental irradiation steps).

In order to produce well-performing devices, one layer of both poly(methyl methacrylate) (PMMA) and poly(4-vinylphenol) (PVP) were used simultaneously. The objective was to combine the good insulating properties of PMMA with the solvent-robustness and adequate wettability of the PVP. The procedure was found to be successful, even as the gate modulation was highly reduced due to the very thick dielectric layers (540 nm PVP and 400 nm PMMA). The devices were electrically characterized and the field-effect mobilities were comparable to those on SiO_2 without OTS (over 10^{-3} $cm^2V^{-1}s^{-1}$, **Figure 8.20**). Optical microscope images of the channel between source and drain electrodes are presented in **Figure 8.21**, highlighting smooth films at the scale of the electrodes. Furthermore, AFM height plots were recorded as a means of investigation of the surface roughness (**Figure 8.22**). While the roughness increased by a factor of five as compared to films on silicon oxide, it was found that bending of the device at at bending radius of 6 mm for 1 minute did not dramatically change the roughness at the surface (R_{RMS} = 5.09 as compared to 3.22 before bending, **Table T8.3**).

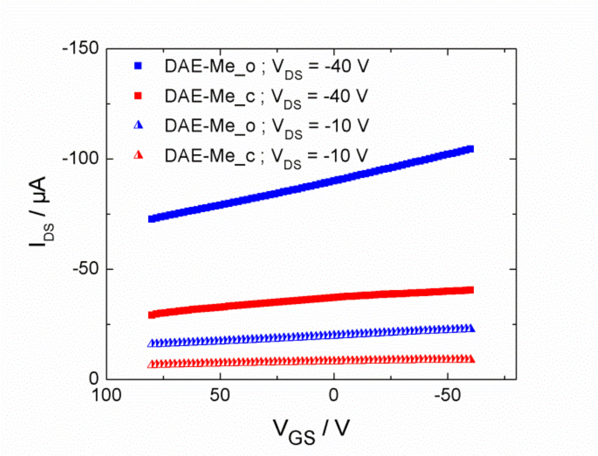

Figure 8.20: Bottom-gate memory unit onto a flexible PET substrate, using a hybrid PMMA/PVP dielectric. $I_{DS}V_{GS}$ curves of a device with a non-treated PVP/PMMA dielectric surface at V_{DS} = - 10 V and - 40 V, with DAE-Me in the open and the closed form.

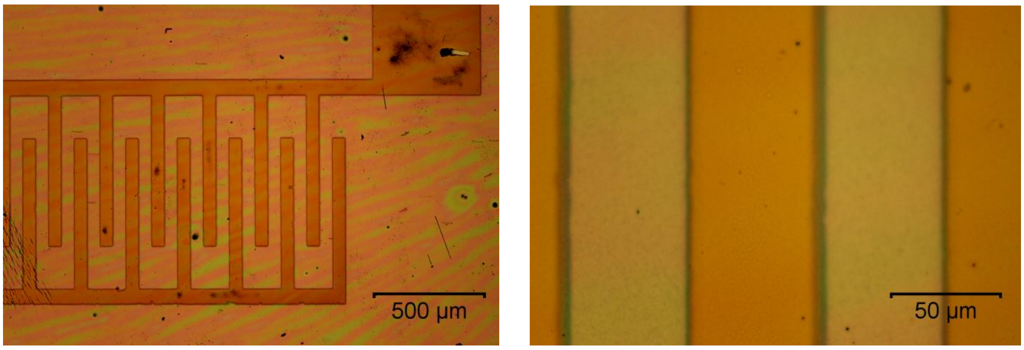

Figure 8.21: Optical microscopy images. Images of P3HT/DAE-Me layer on SiO_2 (channel length = 60 µm).

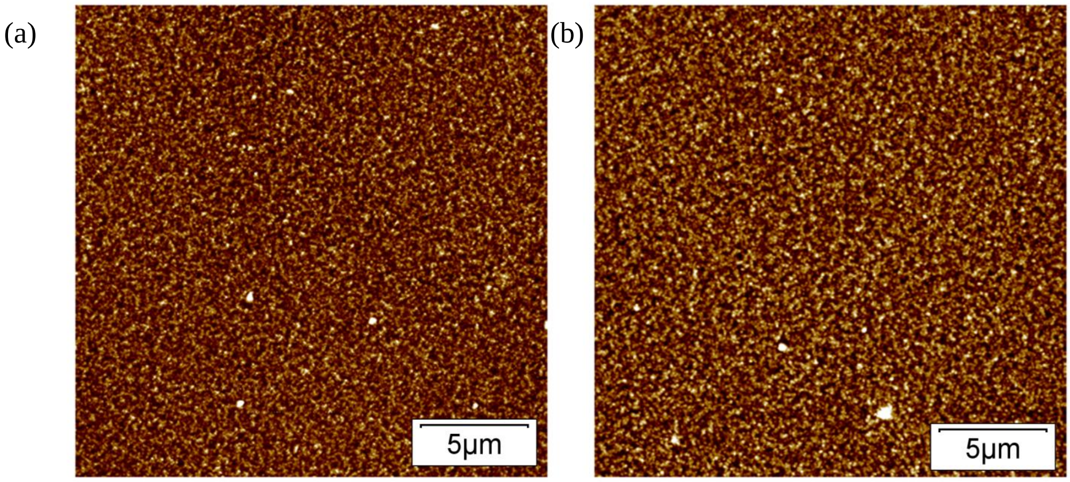

Figure 8.22: Atomic Force Microscopy height plots. Images of (a) a P3HT/DAE-Me layer on PET before bending (z-scale: 25 nm); (b) a P3HT/DAE-Me layer on PET after bending 1 min at a bending radius of 6 mm (z-scale: 35 nm).

Table T8.3: Root mean squared (R_{RMS}) values of the roughness as calculated from the AFM height plots presented in Figure 4 and Figure 20. Data is presented in nm. The roughness was estimated from 100 nm² surfaces.

Surface	Root mean squared roughness (R_{RMS})
SiO_x / no OTS[1]	0.74
SiO_x / OTS[1]	0.54
PVP	3.22
PVP bent[2]	5.09

[1] OTS treatment

[2] bending for 1 minute at a bending radius of 6 mm

Switching capabilities were tested over multiple dynamic switching cycles. We have found that the devices could be switched between closed and open states, albeit at slower pace when compared to devices on SiO_2 (**Figure 8.23, a**). The small increases of drain current during switching are attributed to photogenerated carriers. Dynamic I_{DS}-time curves with small illumination steps at 313 nm indicate the ability of the device to work as a 4-bit multilevel memory (16 distinct levels, **Figure 8.23, b**). Furthermore, electrical characterization was performed on the device after successive bending steps (bending radii amounting to 29.0 mm, 17.5 mm, 10.0 mm, 8.0 mm, and 6.0 mm, **Figure 8.24, a**). Post-bending performances were still comparable to those observed before bending at each bending radius for 60 seconds (**Figure 8.24, b**), with only minor losses in terms of charge carrier mobility and a slight shift in the threshold voltage, proving that with further optimization, the studied organic 3-terminal memory devices could be introduced into flexible electronics.

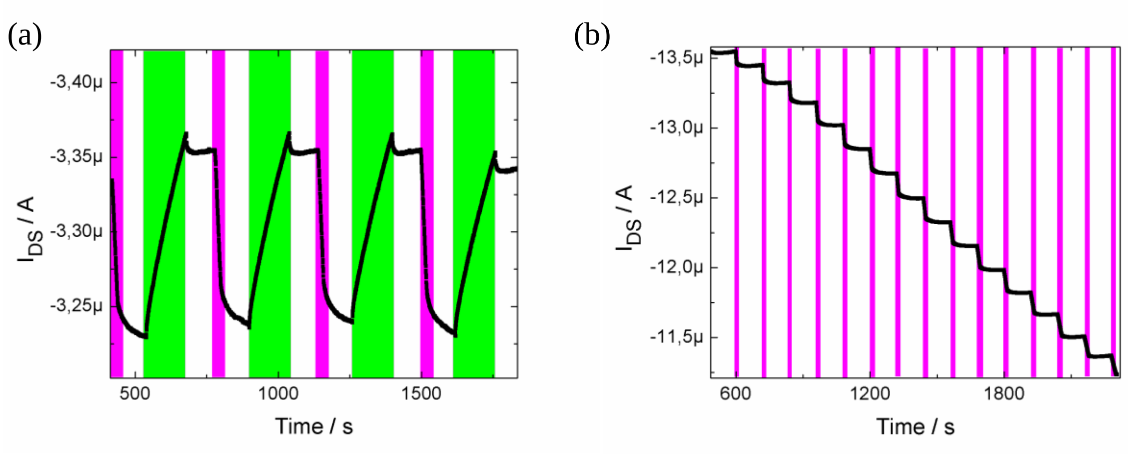

Figure 8.23: Dynamic characterization of the devices. (a) Experimental dynamic I_{DS}-time curves, corrected for bias stress, with write-erase cycles (313 nm for 20 s /546 nm for 140 s) at V_{GS} = - 60 V and V_{DS} = - 10 V; (b) I_{DS}-time curve corrected for bias stress showing small irradiation steps at 313 nm underlining the ability to behave as a multilevel memory (5 to 20 seconds incremental irradiation steps);

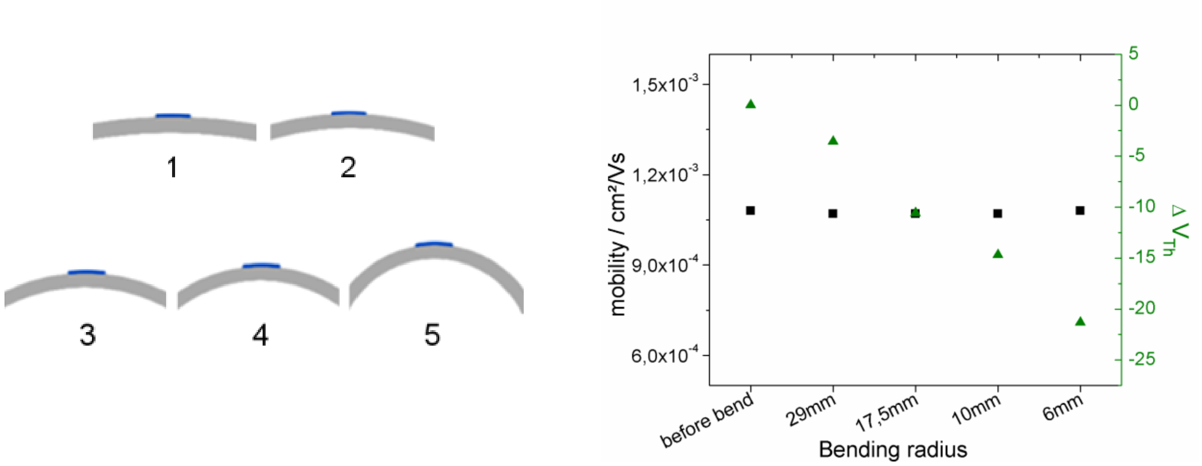

Figure 8.24: Integration of the memory unit onto a flexible PET substrate. (a) Cartoon depicting the bending radii (1: 29.0 mm, 2: 17.5 mm, 3: 10.0 mm, 4: 8.0 mm, and 5: 6.0 mm). (e) Field-effect mobility and threshold voltage after each bending step on a device with diarylethenes in the closed form (after 5 min irradiation at 313 nm).

8.6. Conclusions

We have shown that it is possible to build 3-terminal memory-devices with unprecedented features. Above all, the ability to define many distinct current levels paves the way for high-density memories with 8-bit memory units (256 levels). Illumination times using a laser setup are on the nanosecond time scale, giving rise to a fast response that is necessary for real-life electronics. Transistors were successfully produced in the top-gate configuration on a flexible PET substrate, using PMMA as a dielectric, demonstrating strong electrical performances but no convincing memory behavior. Memories were successfully transferred onto a flexible PET substrate in the bottom-gate configuration, using cytop and PVP as dielectrics. Cytop proved to be a superior dielectric but did not allow for smooth films with strong memory behavior, while films produced on PVP were homogenous but PVP-based devices showed high current-leakage. Therefore, hybrid PMMA/PVP dielectric-based devices were produced and featured good electrical performances, as well as satisfying switching capabilities, demonstrating that this approach can be successfully applied also on flexible substrates. Furthermore, the excellent data retention capabilities of the devices (retention times of 10^7 s) and the reliability after many write-erase cycles make this method ideal for the future applications in (flexible) electronics. Due to the versatile nature of our blending approach, the air-sensitive P3HT could be replaced by an alternative air-stable *p*-type semiconductor with similar energy levels, leading to potentially higher currents (hence an increased possible number of steps) without the need for encapsulation. Our findings are of paramount importance for the realization of a light-controlled cognitive devices where the irradiation history represents the learning process and the non-volatile state retention ensures that the data are preserved over time in a given memory state.

8.7. References

1 Kelley, T. W. *et al.* Recent progress in organic electronics: Materials, devices, and processes. *Chem. Mater.* **16**, 4413-4422 (2004).

2 Braga, D. & Horowitz, G. High-Performance Organic Field-Effect Transistors. *Adv. Mater.* **21**, 1473-1486 (2009).

3 Han, S. T., Zhou, Y. & Roy, V. A. L. Towards the Development of Flexible Non-Volatile Memories. *Adv. Mater.* **25**, 5425-5449 (2013).

4 Benight, S. J., Wang, C., Tok, J. B. H. & Bao, Z. A. Stretchable and self-healing polymers and devices for electronic skin. *Prog. Polym. Sci.* **38**, 1961-1977 (2013).

5 Pang, C., Lee, C. & Suh, K. Y. Recent advances in flexible sensors for wearable and implantable devices. *J. Appl. Polym. Sci.* **130**, 1429-1441 (2013).

6 Baeg, K. J., Caironi, M. & Noh, Y. Y. Toward Printed Integrated Circuits based on Unipolar or Ambipolar Polymer Semiconductors. *Adv. Mater.* **25**, 4210-4244 (2013).

7 Ahmad, S. Organic semiconductors for device applications: current trends and future prospects. *J. Polym. Eng.* **34**, 279-338 (2014).

8 Chiu, Y. C. *et al.* High-Performance Nonvolatile Organic Transistor Memory Devices Using the Electrets of Semiconducting Blends. *ACS Appl. Mater. Inter.* **6**, 12780-12788 (2014).

9 Smithson, C. S., Wu, Y., Wigglesworth, T. & Zhu, S. A More Than Six Orders of Magnitude UV-Responsive Organic Field-Effect Transistor Utilizing a Benzothiophene Semiconductor and Disperse Red 1 for Enhanced Charge Separation. *Adv. Mater.* **27**, 228-233 (2015).

10 Yoon, S. M. *et al.* Fully Transparent Non-volatile Memory Thin-Film Transistors Using an Organic Ferroelectric and Oxide Semiconductor Below 200 degrees C. *Adv. Funct. Mater.* **20**, 921-926 (2010).

11 Radha, B., Sagade, A. A. & Kulkarni, G. U. Metal-organic molecular device for non-volatile memory storage. *Appl. Phys. Lett.* **105** (2014).

12 Liu, X. H. *et al.* The effect of oxygen content on the performance of low-voltage organic phototransistor memory. *Org. Electron.* **15**, 1664-1671 (2014).

13 Nougaret, L. *et al.* Nanoscale Design of Multifunctional Organic Layers for Low-Power High-Density Memory Devices. *ACS Nano* **8**, 3498-3505 (2014).

14 Lee, S. *et al.* Overcoming the "retention vs. voltage" trade-off in nonvolatile organic memory: Ag nanoparticles covered with dipolar self-assembled monolayers as robust charge storage nodes. *Org. Electron.* **14**, 3260-3266 (2013).

15 Kim, S. J. & Lee, J. S. Flexible Organic Transistor Memory Devices. *Nano Lett.* **10**, 2884-2890 (2010).

16 Cosseddu, P., Lai, S., Casula, G., Raffo, L. & Bonfiglio, A. High performance, foldable, organic memories based on ultra-low voltage, thin film transistors. *Org. Electron.* **15**, 3595-3600 (2014).

17 Kim, R. H. *et al.* Non-volatile organic memory with sub-millimetre bending radius. *Nat. Commun.* **5** (2014).

18 Sekitani, T. *et al.* Organic Nonvolatile Memory Transistors for Flexible Sensor Arrays. *Science* **326**, 1516-1519 (2009).

19 Liu, X. *et al.* Advancements in organic nonvolatile memory devices. *Chin. Sci. Bull.* **56**, 3178-3190 (2011).

20 Bez, R., Camerlenghi, E., Modelli, A. & Visconti, A. Introduction to Flash memory. *Proc. IEEE* **91**, 489-502 (2003).

21 Sala, F., Gabrys, R. & Dolecek, L. Dynamic Threshold Schemes for Multi-Level Non-Volatile Memories. *IEEE T. Commun.* **61**, 2624-2634 (2013).

22 Pirovano, A. *et al.* Reliability study of phase-change nonvolatile memories. *IEEE T. Device Mat. Re.* **4**, 422-427 (2004).

23 Orgiu, E. *et al.* Optically switchable transistor via energy-level phototuning in a bicomponent organic semiconductor. *Nat Chem* **4**, 675-679 (2012).

24 Robertson, J. High dielectric constant oxides. *Eur Phys J-Appl Phys* **28**, 265-291 (2004).

25 Chen, F. C., Chu, C. W., He, J., Yang, Y. & Lin, J. L. Organic thin-film transistors with nanocomposite dielectric gate insulator. *Appl Phys Lett* **85**, 3295-3297 (2004).

26 Walser, M. P., Kalb, W. L., Mathis, T. & Batlogg, B. Low-voltage organic transistors and inverters with ultrathin fluoropolymer gate dielectric. *Appl Phys Lett* **95** (2009).

27 Thomas, P., Ravindran, R. S. E. & Varma, K. B. R. Dielectric properties of Poly(methyl methacrylate) (PMMA)/CaCu3Ti4O12 Composites. *I C Prop Appl Dielec* (2012).

28 Chua, L. L. *et al.* General observation of n-type field-effect behaviour in organic semiconductors. *Nature* **434**, 194-199 (2005).

29 Orgiu, E. & Samori, P. 25th Anniversary Article: Organic Electronics Marries Photochromism: Generation of Multifunctional Interfaces, Materials, and Devices. *Adv. Mater.* **26**, 1827-1845 (2014).

30 El Gemayel, M. *et al.* Optically switchable transistors by simple incorporation of photochromic systems into small-molecule semiconducting matrices. *Nat. Commun.* **6** (2015).

31 Borjesson, K. *et al.* Optically switchable transistors comprising a hybrid photochromic molecule/n-type organic active layer. *J. Mater. Chem. C* **3**, 4156-4161 (2015).

32 Shallcross, R. C., Korner, P. O., Maibach, E., Kohnen, A. & Meerholz, K. Photochromic Diode With a Continuum of Intermediate States: Towards High Density Multilevel Storage. *Adv. Mater.* **25**, 4807-4813 (2013).

33 Korner, P. O., Shallcross, R. C., Maibach, E., Kohnen, A. & Meerholz, K. Optical and electrical multilevel storage in organic memory passive matrix arrays. *Org. Electron.* **15**, 3688-3693 (2014).

Chapter 9. Conclusions

9.1. Conclusions

In this thesis we have mastered the controlled self-assembly of well-known semiconducting small molecules and polymers such as oligothiophenes and P3HT in order to achieve high electrical performances in organic field-effect transistors, and we have shown that new functions could arise in solution processed thin-films by combining multiple materials each one conferring a well-distinct function to the ensemble.

First, we focused on dihexylquaterthiophene, a well-established small molecule known to possess good field-effect mobility in vacuum sublimed thin-films. By using drop-casting from the solution as deposition method, we were able to fabricate devices with a field-effect mobility exceeding state-of-the-art of 0.10 cm²/Vs and I_{on}/I_{off} currents over 10^7. These remarkable performances were achieved through optimization of the conditions of film formation via judicious choice of processing method, solvent type, interfaces functionalization and in particular by tuning the rate of evaporation of the solvent. We proved that it is possible to drive the molecular self-assembly towards the formation of highly ordered low-dimensional architectures exhibiting enhanced electrical characteristics. In particular, we demonstrated the particular importance of interface tailoring by careful analysis of the semiconductor-electrode and semiconductor-dielectric interfaces. It was found that different SiO_2 treatments can affect directly the assembly of the semiconductor in high boiling-point solvents leading to interfaces with a lower number of interfacial traps which result in enhanced electrical performances. The same oligomer was blended with similar molecules, dihexylbithiophene and dihexylsexithiophene with respectively two and six thiophene units in the main chain instead of four. While none of the three molecules performed well when deposited from chloroform on their own, we have demonstrated that it is possible to obtain semiconducting films with enhanced electrical characteristics when blended solutions are used instead of single components. The morphology of the resulting film was investigated and it was found that tuning phase segregation by solvent selection can lead to dramatic changes in electrical performances.

The blending strategy was pushed further with blends of semiconducting polymers. The study was conducted using a high-performing *n*-type polymer, P(NDI2OD-T2), which was blended with four different *p*-type polymers: P3HT, PDV-TPT, PDVT-8 and IIDDT-C3. The five polymers were radically different in terms of molecular structure, electrical characteristics and energy levels. Nevertheless, we demonstrated that it was possible to fabricate ambipolar field-effect transistors using P(NDI2OD-T2) blended with any of the four *p*-type semiconductors, with balanced *p*-type and *n*-type mobilities. In particular, bottom-contact, bottom-gate transistors with mobilities over 10^{-2} cm²/Vs and linear regime I_{on}/I_{off} over 10^5 were produced from a solution consisting of a blend of P(NDI2OD-T2) and PCD-TPT. Devices fabricated using a solution of P(NDI2OD-T2) and IIDDT-C3 featured mobilities up to 10^{-2} cm²/Vs and I_{on}/I_{off} of 10^7, unprecedented values for ambipolar organic transistors. The ability to produce ambipolar transistors using a unipolar semiconductor (P3HT) demonstrated that this approach could potentially be applied to a wide variety of semiconductors. The ability to “balance out” an unbalanced ambipolar semiconductor (PCD-TPT) proved that the blending strategy could also be applied as mobility correction in unbalanced materials. Individual experimental results obtained for each polymer blend was explained by morphological characterization of each blended film (AFM, XRD). It was demonstrated that while some films were prone to undergo high phase-segregation, such as PDVT-8 blended with P(NDI2OD-T2), the films involving IIDDT-C3 and P(NDI2OD-T2) were well blended allowing good *p*- and *n*-type mobilities in both top-gate and bottom-gate geometry.

Finally, P3HT was blended with a photochromic small molecule (DAE-Me) for the fabrication of a three-terminal multilevel memory. The devices proved to switch between levels at nanosecond rate, giving rise to a fast response that is necessary for real-life electronics. Above all, the ability to define many distinct current levels was demonstrated, paving the way for high-density memories with 8-bit memory units (256 levels). Furthermore, excellent data retention capabilities of the devices (retention times of 10^7 s) and excellent reliability after many write-erase cycles were established. The procedure was successfully transferred onto a flexible transparent PET substrate, and was proved to operate properly after bending. The strategy relying on a pair of organic semiconductor and photochromic small molecule is generally applicable and could be extended to a wide range other systems featuring the desired properties. For example, P3HT could be replaced by a better performing polymer, in terms of electrical characteristics, air stability or mechanical resistance, leading to further improved multilevel memories.

In summary, we demonstrated that the combination of different (macro)molecular system via blending is a very promising approach as it allows to realize new materials with increased performances and new characteristics, such as data storage and ambipolarity.

Vacuum deposition is often used as standard procedure for small molecule film fabrication, but it is unpractical for industrial applications, due to the high costs and low fabrication speeds that are incompatible with production lines. We proved that focusing on solution processing can be a winning strategy for fabrication of high performance transistors based on organic small molecule semiconductors. This approach is highly applicable for future low-cost applications depending on ink-jet or roll-to-roll (R2R) printed devices. The study of the electrical performances of blended oligomer films are of particular interest as they were produced from a solvent that yielded disappointing results on single component films. In most cases, the best performing solvent is not a viable option in the industry due to high costs and ecological issues. [1] Therefore, relying on blends of semiconducting small molecules for improved performances can lead to new possibilities in terms of device fabrication.

Among all the synthesized organic semiconducting polymers to date, only a fraction of them displayed the ability to transport holes and electrons, [2] and so far, none of them featured absolutely balanced *p*- and *n*-type mobilities. Furthermore, the I_{on}/I_{off} was very poor in most cases, underlining a weak capacity of the device to properly turn off. [3] Unfortunately, ambipolar organic materials are of paramount importance for the fabrication of organic light-emitting transistors and complementary circuits. Our approach demonstrated that semiconducting films could be produced with the desired ratio between hole and electron transport. The general nature of the study validates this approach for future applications involving simple fabrication of ambipolar films, with high capability to switch off and ambipolarity on demand. The control of the ratio between *p*- and *n*-type mobility would be particularly suited for logic applications that rely on transistors with different polarities with good capacities to switch off.

The fabricated multilevel memories displayed exceptional features, such as multilevel operation and non-volatile state retention, making them particularly well suited for reliable miniaturized data drives. [4] An 8-bit memory cell was produced, only revealing the surface of the results that could be reached through this approach. Upon selection of the optimal polymer-photochromic molecule blend, devices with many more current-levels could be produced, with a theoretical limit equal to the number of photochromic molecules in the blend. Furthermore, these light-controlled devices performed well as field-effect transistors indicating the possibility to introduce them into logic applications, providing multiple functions in a single device, leading to new possibilities in terms of circuit architecture. Combined with their easy processing and ability to perform in flexible devices, the memories could easily be integrated into everyday objects, such as flexible data drives and RFID tags. [5]

In conclusion, organic electronics have already proved to be superior to its inorganic counterparts for multiple applications due to its impressive features and versatility, but there is still a lot of research and optimization to be performed in many areas to supersede silicon based technologies. While the constant appearance of novel synthesized molecules have paved the way for major milestones in terms of electrical characteristics, these materials can only reveal their full potential upon careful optimization. The blending approach seems particularly interesting as it proves to be universal: features present in different materials are combined to form new materials with multiple functions and tremendous potential for future applications. The implementation of multiple functions within the same device opens the door for new circuit architecture and miniaturization. [6] Furthermore, the blending approach could be extended beyond organic molecules. Blends of organic materials with carbon-based materials and metal nano-particles are already studied [7-9] and the combination of the peculiar characteristics of these soluble materials with the wide variety of properties of organic materials could lead to very interesting developments in the field of electronics.

9.2. References

1 Anastas, P. T., Wasserscheid, P. & Stark, A. *Handbook of Green Chemistry, Green Solvents, Ionic Liquids*. (Wiley-VCH, 2013).

2 Zhao, Y., Guo, Y. L. & Liu, Y. Q. 25th Anniversary Article: Recent Advances in n-Type and Ambipolar Organic Field-Effect Transistors. *Adv. Mater.* **25**, 5372-5391 (2013).

3 Sonar, P., Singh, S. P., Li, Y., Soh, M. S. & Dodabalapur, A. A Low-Bandgap Diketopyrrolopyrrole-Benzothiadiazole-Based Copolymer for High-Mobility Ambipolar Organic Thin-Film Transistors. *Adv. Mater.* **22**, 5409 (2010).

4 Bandyopadhyay, A. & Miki, K. Fabrication of a memory chip by a complete self-assembly process using state-of-the-art multilevel cell (MLC) technology. *Adv. Funct. Mater.* **18**, 1173-1177 (2008).

5 Fiore, V. *et al.* An Integrated 13.56-MHz RFID Tag in a Printed Organic Complementary TFT Technology on Flexible Substrate. *IEEE T. Circuits-I* **62**, 1668-1677 (2015).

6 Lu, W. & Lieber, C. M. Nanoelectronics from the bottom up. *Nat. Mater.* **6**, 841-850 (2007).

7 El Gemayel, M. *et al.* Leveraging the Ambipolar Transport in Polymeric Field-Effect Transistors via Blending with Liquid-Phase Exfoliated Graphene. *Adv. Mater.* **26**, 4814 (2014).

8 Mosciatti, T. *et al.* A Multifunctional Polymer-Graphene Thin-Film Transistor with Tunable Transport Regimes. *Acs Nano* **9**, 2357-2367 (2015).

9 Mosciatti, T., Orgiu, E., Raimondo, C. & Samori, P. The role of size and coating in Au nanoparticles incorporated into bi-component polymeric thin-film transistors. *Nanoscale* **6**, 5075-5080 (2014).

LIST OF PUBLICATIONS

Solution-Processed Field-Effect Transistors Based on Dihexylquaterthiophene Films with Performances Exceeding Those of Vacuum-Sublimed Films – T. Leydecker, D. T. Duong, A. Salleo, Emanuele Orgiu, and P. Samorì, ***ACS Appl. Mater. Interfaces***, 2014, **6**, 21248-21255

Flexible non-volatile optical memory TFT device with an unprecedented number of distinct levels based on an organic bi-component blend – T. Leydecker, M. Herder, E. Pavlica, G. Bratina, S. Hecht, E. Orgiu and P. Samorì, submitted manuscript.

Organic small molecules with varying number of thiophene groups blended as a tool of investigation of packing and electrical characteristics among similar molecules – Leydecker et al., manuscript in preparation

Ambipolarity on demand: correlation between electrical performances, film structure, molecular structure and blending ratio – Leydecker et al., manuscript in preparation.

Croconanines as molecular materials for organic electronics: synthesis, solid state structure and transistor devices – M.A. Capozzi, C. Carlucci, V. Fino, E. Mesto, R.Musio, T. Leydecker, S. Bonacchi, E. Orgiu, A. Punzi, P. Samorì, E. Schingaro, M. Suriano and G.M. Farinola, submitted.

Thienopyrrolyldione center-capped oligothiophene ambipolar semiconductors for thin film-transistors, manuscript in preparation.

LIST OF COMMUNICATIONS

Poster presentation: T. Leydecker, D. T. Duong, A. Salleo, Emanuele Orgiu, and P. Samorì, *High mobility field-effect transistors from solution processed di-hexylquarterthiophene* at ICOE (International Conference on Organic Electronics) – Grenoble, 2013

Poster presentation: T. Leydecker, D. T. Duong, A. Salleo, Emanuele Orgiu, and P. Samorì, *Optimization of electrical performances of solution processed di-hexylquaterthiophene field-effect transistors* at SUPERIOR meeting – Strasbourg, 2013

Poster presentation: T. Leydecker, M. Herder, E. Pavlica, G. Bratina, S. Hecht, E. Orgiu and P. Samorì, *Multilevel Memory TFT based on a Polymer/Diarylethene blend integrated on a flexible substrate* at ELECMOL – Strasbourg, 2014

Contributed talk: T. Leydecker, M. Herder, E. Pavlica, G. Bratina, S. Hecht, E. Orgiu and P. Samorì, *Flexible Optical memory TFT device with distinct levels based on an organic bi-component semiconductor blend* at ICOE (International Conference on Organic Electronics) – Modena, 2014

STATEMENT OF WORK

All the experiments and data analysis reported in this thesis have been carried out by myself except for those listed below:

Chapter 6: DH6T synthesis was performed by Prof. Melucci's group (ISOF- CNR, Bologna, Italy). GIXD was performed by Prof. Salleo's group (Stanford University, U.S.A.). ToF SIMS experiments were performed by Prof. Licciardello's group in (Università degli Studi di Catania, Italy).

Chapter 7: XRR and XRD measurements and analysis were performed by Dr. Fabiola Liscio (Istituto per la Microelettronica e Microsistemi, Università di Bologna). AFM measurements were performed by Marco Squillaci (Nanochemistry Lab, Strasbourg, France).

Chapter 8: DAE-Me synthesis was performed by Dr. Martin Herder under the supervision of Prof. Hecht (Humbolt Universität zu Berlin, Germany). Experiments involving a laser setup were performed Egon Pavlica, Emanuele Orgiu and I at Univerza v Novi Gorici, Slovenia. AFM measurements were performed with the help of Marco Squillaci.

Dr. Emanuele Orgiu helped with helpful discussions on experimental design and data analysis. The interns under my supervision Maryam Frizi and Quentin Lamy helped performing various experiments during their short stays.

ACKNOWLEDGEMENTS

As we arrive at the end of the thesis, it is time to let the credits roll onto the silver screen. A thesis over three years in the making yet still finished at the last minute; there are many amazing people to thank for their help and support.

First I wish to thank Paolo Samorì. Paolo accepted me in his group for an internship almost four years ago, and welcomed me again six month later for my PhD. He is a great scientist and was a fantastic advisor, always helpful and invested, relentlessly correcting and improving, discussing and suggesting for the best possible results. While I was still a master student, Emanuele Orgiu let me have a glimpse at the mysterious world of charge transport in organic electronics, immediately convincing me to apply to the Nanochemisty Lab. Brilliant mind and remarkable teacher, he always pushed for actual science, understanding rather than guessing.

I would like to thank my collaborators from Berlin and Bologna, synthesizing molecules with interesting features and a degree of purity that Sigma could not achieve. Thank you my dear colleagues from Stanford, Bologna and Catania for taking good care of the countless samples I have sent to you, providing me with great insight that made the understanding of my results possible. Thank you Egon for welcoming us to Slovenia and helping us out with the laser setup.

Being part of the Nanochemistry Lab was incredible, as everyone was ready to help me out. In particular Thomas, Olly, Artur, Marco, Marc-Antoine, Lei, Karl, Sara, Laura, Wassima, Alexander, Mirella and Chiara who helped me out with instruments, did a quick experiment for me or gave me great scientific advice. Naturally, I would also like to thank everyone else at the lab for being kind and welcoming to me, making me feel at work, at home and on vacation in Italy at the same time.

I was not the only PhD student to start in the summer of 2012. With me, the amazing Thomas, who would soon become my friend. Together, we travelled the world to exotic places (such as France and Italy) and took on the hardest challenges (such as deciding on where to eat on Friday evening). Probably born with toque on the head, you taught me how to cook ragù and carbonara, how to choose the best mozzarella, and how to organize a dinner for 50. Thank you, Thomas!

While I did spend quite some time 8 allée Gaspard Monge, I also managed to enjoy the support of other wonderful people. My parents, who I dedicate my thesis to, immediately come to my mind. Loving, caring and supportive every second of my life, I owe them everything and I wish to deeply thank them. Also, I thank my brothers who mean the world to me, and my friends and successive roommates who made sure that there was something fun to do when I came home after a long day at work. Finally, I would like to thank Morgane, octopus-queen and high-level healer of all wounds. You are the life of my love.

Tim

Tim Leydecker

Multiresponsive and supramolecular field-effect transistors

Résumé

Cette thèse a exploré comment, en mélangeant des matériaux avec des propriétés électriques différentes, il est possible de fabriquer des transistors avec des performances accrues. Des transistors organiques à effet de champ basés sur un oligothiophène (DH4T) ont été fabriqués et optimisés jusqu'à ce que les mobilités mesurées fussent supérieures à celles observées dans des films évaporés. Ces résultats ont été obtenus par le contrôle précis des interfaces et de la vitesse d'évaporation. Des polymères de type p ont été mélangés à des polymères de type n. Chaque solution obtenue a été utilisée pour la fabrication de transistors ambipolaires. Les transistors ont été caractérisés et il a été possible de fabriquer des transistors avec des mobilités équilibrées pour chaque paire de polymères. Des transistors à effet de champ basés sur un mélange de P3HT et d'une molécule photochromique (DAE-Me) ont été fabriqués. Le courrant a été mesuré pendant et entre les irradiations et il a été démontré qu'une mémoire non-volatile à multiple niveaux peut être fabriquée.

Mots-clés: Transistors organiques à effet de champ, Interfaces, transistors ambipolaires, molécules photochromiques.

Résumé en anglais

This thesis explored how, by blending of materials with different electrical characteristics, it is possible to fabricate transistors with new or improved performances. First, organic field-effect transistors based on a single oligothiophene, DH4T, were fabricated and optimized until the measured mobility was superior to that observed in vacuum deposited films. This was achieved through careful tuning of the interfaces using self-assembled monolayers and by strong control of the solvent-evaporation rate. P-type polymers were blended with an n-type polymer. Each resulting solution was used for the fabrication of ambipolar field-effect transistors. These devices were characterized and it was found that for each pair of p- and n-type polymers, a transistor with balanced mobilities and high I_{on}/I_{off} could be fabricated. Finally field-effect transistors based on a blend of P3HT and a photoswitchable diarylethene (DAE-Me) were fabricated. The current was measured during and between irradiations and it was demonstrated that a non-volatile multilevel memory could be fabricated.

Keywords: Organic field-effect transistors, Interfaces, ambipolar transistors, Photochromic molecules.